Experimental Investigation and Numerical Modelling of a Concentrating Photovoltaic/Thermal System (CPVT) Based on Point Focus Fresnel Lenses (PFFL)

by

© Rida Ali Hmouda

A Thesis submitted to the School of Graduate Studies in partial fulfillment

of the requirements for the degree of

Doctor of Philosophy

Department of Mechanical Engineering

Faculty of Engineering and Applied Science

Memorial University of Newfoundland

October 2023

St. John's, Newfoundland and Labrador, Canada

Abstract

Climate change is one of the biggest environmental, political, economic, technological, and social challenges of the 21st century. The increasing cost of fossil fuels further exacerbates this. To mitigate greenhouse gas emissions to a tolerable level, the world energy system needs to transition to renewable energy sources. Solar energy is one of the most suitable alternatives in this regard. Solar photovoltaic (PV) and solar thermal technologies are the two most widely available solar technologies. However, one of the main drawbacks of PV technology is its relatively low energy conversion efficiency and land use requirements. Multi-junction photovoltaic (MJPV) solar cells have been developed to overcome these limitations. These cells are a new generation of PV technology that offers higher efficiency, better response to high solar concentration, and lower temperature coefficients. However, they tend to be more expensive.

Concentrator photovoltaic (CPV) systems can address these challenges and replace expensive MJPV materials with cost-effective concentrator optics elements. However, high solar radiation concentrations can lead to an increase in cell temperature, necessitating cooling. Concentrated photovoltaic thermal (CPVT) systems have emerged as a solution, enabling the simultaneous production of electrical and thermal energy.

This dissertation focuses on the theoretical and experimental evaluation of a CPVT system's electrical and thermal performance. An indoor prototype CPVT model was designed, built, and tested at the Thermofluid Laboratory. The model incorporates a sun simulator, point-focus Fresnel lenses (PFFL), MJPV cells, copper heat sinks, and a copper pipe flow loop.

The design aims to reduce MJPV module temperature and enhance heat transfer to the heat transfer fluid (HTF) in the flow channel, enabling high electrical and thermal energy production. A numerical model was developed to simulate the performance of the CPVT design and validated using experimental data from indoor test campaigns. The CPVT model was tested and simulated under various design parameters.

The experimental results indicated that the prototype CPVT model achieved electrical and thermal efficiencies of 34.73% and 54.7%, respectively. The corresponding electrical and thermal energy outputs were measured at 42.75 W and 67.89 W, respectively.

The results obtained from Computational Fluid Dynamics (CFD) simulations showed that the highest electrical efficiency of 36.47% was recorded at a mass flow rate of 0.025 *kg/s* and a concentration ratio (*CR*) of 100X. Conversely, the lowest electrical efficiency of 25.56% was observed at a mass flow rate of 0.0029 *kg/s* and a *CR* of 500X. The CFD analysis also highlighted that the highest thermal efficiency of 73.0% was achieved at a mass flow rate of 0.0029 *kg/s* and a *CR* of 500X, while the lowest thermal efficiency of 61.5% was observed at a mass flow rate of 0.025 *kg/s* and a *CR* of 100X.

Regarding power output, the highest recorded electrical energy output was 389.3 W, obtained with a mass flow rate of 0.5 *kg/s* and a *CR* of 1000X. Similarly, the highest thermal energy output was 1028.5 W, attained with a mass flow rate of 0.1 *kg/s* and a *CR* of 1000X. The CFD results also revealed that the outlet temperatures varied between 18.1 to 72.5 $°C$, depending on the mass flow rate and *CRs*. This temperature range makes the CPVT system suitable for various applications such as swimming pool water heating, domestic hot water, and space heating.

The numerical model used in this study was validated with indoor experimental data, and demonstrated good agreement in the average cell temperature with a maximum deviation of 4.58% at a flow rate of 0.0029 *kg/s* and a minimum deviation of 1.14% at a flow rate of 0.025 *kg/s*. These validation results indicate that the model is accurate and reliable and can be used for further optimization and analysis of the CPVT system.

Acknowledgements

All praises are due to Allah (whom we praise, seek his help and ask for his forgiveness) for his guidance, blessing and helping me to complete this thesis. May his mercy and blessing be upon the noble Prophet Mohamed (SAWA), his households and his companions.

I would like to express my deep gratitude to my supervisor Dr. Yuri S. Muzychka, for his guidance, support, patience and immense knowledge throughout this work. Also, I would like to express my sincere gratitude to my second supervisor Dr. Xili Duan for his advice, support, and valuable suggestions.

My sincere thanks also go to all of the technicians in the Heat Transfer Lab, Technical service, and mechanical engineering workshop for their help while building up my experimental setup.

My truthful appreciation goes to my parents, Ali Hmouda and Fatima Shalfuh (May Allah has mercy on them), and my brothers, sisters and my friends for their moral support during my Ph.D. study.

Finally, thanks to my family for supporting me through this long journey, especially my wife, who had to endure endless days and weeks of frustration during my obsessive engagement in research; this would not have been possible without you.

Dedication

To the soul of my beloved father (May Allah has mercy on him)

To the soul of my beloved mother (May Allah has mercy on her),

To my beloved wife, children, and the whole family

Table of Contents

List of Figures

List of Tables

Nomenclature

Roman Symbols

$(I_T)_{max}$	=	maximum measured values of the irradiance W/m^2
$(I_T)_{min}$	=	minimum measured values of the irradiance W/m^2
$\bar{C}_l, C_t^U$	=	approximately universal function of Prandtl number
$\dot{V}$	=	volume flow rate, m^3/s
A	=	contact area between the inner pipe surface and HTF, m^2
A_{Fr}	=	Fresnel lens area, m^2
A_{pv}	=	solar cell area, m^2
c	=	velocity of light in vacuum ($c = 3\times10^8$ m/s)
C_p	=	heat capacity, J/kgK
D	=	pipe diameter, m
$E_{eq,ele}$	=	equivalent electrical energy
E_g	=	Width of the semiconductor bandgap, eV
E_{ph}	=	Energy of the photon J
f	=	Fanning friction factor, $16/Re$
FF	=	fill factor
g	=	gravitational acceleration, m/s^2
h	=	Plank's constant ($h = 6.626\times10^{-34}$ $J\,s$)
h	=	forced convection heat transfer coefficient inside the pipe, W/m^2K
h	=	heat transfer coefficient, W/m^2K
I	=	current of the solar cell, A
I_D	=	diode's current, A
I_L	=	light-generated current, A
I_m	=	maximum current, A
I_O	=	reverse saturation current, A
I_{SC}	=	short circuit current, A

k	=	thermal conductivity, W/mK
k	=	Boltzmann constant (=1.3806503×10^{-23} J/K)
k_t	=	thermal coefficient
L_c	=	characteristic length, m
n	=	diode ideality factor
Nu	=	Nusselt number, hD/k
Nu_l	=	average Nusselt number taken over MJPV, assuming laminar heat transfer dominates
Nu^T	=	average "thin-layer-solution" Nusselt number for laminar flow
Nu_t	=	average Nusselt number taken over MJPV, assuming turbulent heat transfer dominates
P	=	perimeter, m
P_{ele}	=	amount of energy that is converted to electrical power, W
P_m	=	maximum power, W
q	=	charge of an electron (=1.60217646×10^{-19} C)
Q_{cond}	=	conduction heat transfer rate, W
Q_{heat}	=	amount of energy that is converted to heat, W
Q_{in}	=	heat transfer rate into the system, W
q_{irr}	=	solar radiation flux, W/m^2
$Q_{n/c}$	=	natural convection heat transfer rate, W
Q_{out}	=	heat transfer rate out of the system, W
Q_{rad}	=	surface-to-ambient radiation energy, W
Q_{th}	=	thermal energy absorbed by HTF, W
R	=	thermal resistance between consecutive nodes, K/W
R_a	=	Rayleigh number
Re	=	Reynolds number, DU/v
R_S	=	series resistance, Ω
T_a	=	ambient temperature, K
T_c	=	solar cell temperature, $°C$

T_{IE}	=	temporal instability %
T_{in}	=	inlet temperatures of the HTF, $°C$
T_m	=	average mean temperature of HTF, K
T_{out}	=	outlet temperatures of the HTF, $°C$
T_s	=	surface temperature, K
T_w	=	average wall temperature of the pipe, K
U	=	average velocity, m/s
V	=	voltage of the solar cell and the diode, V
V_D	=	voltage of the diode, V
V_m	=	maximum voltage, V
V_{OC}	=	open-circuit voltage, V
$\dot{m}$	=	mass flow rate, kg/s

Subscripts

a	=	ambient
cond	=	conduction
D	=	diode
ele	=	electrical
irr	=	irradiation
n/c	=	natural convection
OC	=	open circuit
rad	=	radiation
ref	=	reference
SC	=	short circuit

Greek Symbols

ε	=	emissivity of the solar cell material
α	=	thermal diffusivity, m^2/s
β	=	coefficient of volumetric thermal expansion K^{-1}
β_{ref}	=	temperature coefficient of the MJPV solar cell, $\%/K$
δ	=	electrical-to-thermal ratio
ΔP	=	pressure drop, Pa
ΔT	=	temperature difference between HTF and surface $℃$
η	=	efficiency
η_{ele}	=	electrical efficiency
η_m	=	module efficiency
η_{opt}	=	optical efficiency of the concentrator
η_{PES}	=	primary energy saving efficiency
η_{ref}	=	cell's electrical efficiency at the reference temperature T_{ref}
η_{sc}	=	electrical efficiency of the MJPV cell
η_{th}	=	thermal efficiency
λ	=	wavelength m
μ	=	dynamic viscosity, Ns/m^2
ν	=	kinematic viscosity, m^2/s
ρ	=	fluid density, kg/m^3
σ	=	Stefan Boltzmann constant (5.67×10^{-8} $W/m^2.K^4$)

Acronyms

CFD	=	computational fluid dynamics
CPVT	=	Concentrating Photovoltaic Thermal
CR	=	maximum concentration ratio
DAQ	=	data acquisition system
FVM	=	Finite Volume Method

GCR	=	geometrical concentration ratio
HS	=	Heat sink
HTF	=	heat transfer fluid
InGaP/InGaAs/Ge	=	Gallium indium phosphate/Indium gallium arsenide/Germanium
MJPV	=	multi junction photovoltaic
MPP	=	maximum power point
OGF	=	oval gear flowmeter
PES	=	primary energy saving
PFFL	=	point focus Fresnel lens
PMMA	=	Polymethyl Methacrylate

List of Publications

1. Hmouda, R. A., Muzychka, Y. S., Duan, X. (2022). Experimental and Theoretical Modelling of Concentrating Photovoltaic Thermal System with Ge-Based Multi-Junction Solar Cells. Energies, 15(11), 11. https://doi.org/10.3390/en15114056.
2. Hmouda, R. A., Muzychka, Y. S., Duan, X. (2022). A Numerical Investigation of the Feasibility of a Concentrating Photovoltaic Thermal System based on Point-Focus Fresnel Lens. Proceedings of the 9th International Conference on Fluid Flow, Heat and Mass Transfer (FFHMT'22) Niagara Falls, Canada – June 08-10, 2022 Paper No. 215 DOI: 10.11159/ffhmt22.215.
3. Hmouda, R. A., Muzychka, Y., Duan, X. (2022). Assessment of Concentrated Photovoltaic Thermal (CPVT) Systems Using CFD Analysis. Journal of Fluid Flow, Heat and Mass Transfer (JFFHMT), 9(1), 165.
4. Hmouda, R. A., Muzychka, Y., Duan, X. (2022). Electrical Characteristics Analysis of High Concentrated Multi-Junction Solar Cells. The 31st Annual Newfoundland Electrical and Computer Engineering Conference (NECEC) November 15, 2022, St. John's, NL, Canada.
5. Hmouda, R. A., Muzychka, Y., Duan, X. (2023). Development and Performance Characterization of a Novel CPVT System. Journal of Solar Energy Engineering, ASME. (Under submission).

Chapter 1

Introduction

1.1 Background

Energy is necessary for human societies to achieve their social, economic, and environmental objectives. Energy enables people to access health care, education, clean water, and sanitation. It also supports industrialization, innovation, and infrastructure development. In the last few decades, energy consumption has rapidly increased due to the rapid growth in the global population, economic development, and technological developments. Figure 1.1 shows the primary energy consumption around the world during the period from 1965 to 2021. It can be seen that the total primary energy consumption has increased by almost four times since the year 1965, reaching 165,320 TWh in 2021.

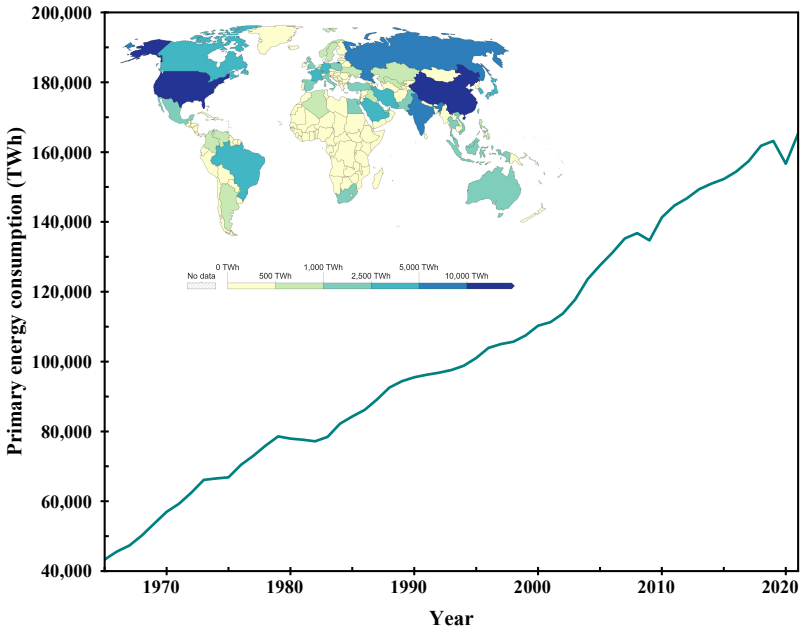

Fig. 1.1: Primary energy consumption, re-produced from (Ritchie et al., 2022)

Further, the world map depicts the primary energy consumption distribution according to country. It's important to note that energy consumption is closely tied to a country's population and economic activity. Hence, countries with larger populations and more developed economies tend to consume more energy. The energy resources include coal, crude oil, gas, nuclear, and modern renewables (Ritchie et al., 2022).

Furthermore, only some of these forms of energy are equally sustainable. Fossil fuels contribute to greenhouse gas emissions and climate change. They also cause air pollution and health problems. Consequently, increasing primary energy consumption can have significant and far-reaching environmental impacts. Figure 1.2 displays the growth of global CO_2 emissions from fossil fuels from the 19th century to today.

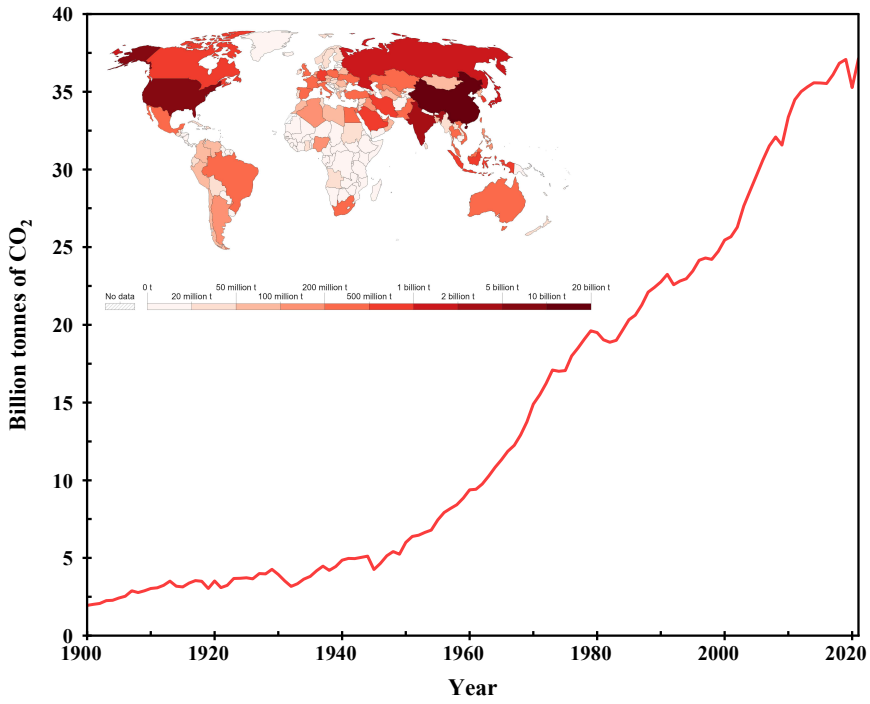

Fig. 1.2: Global CO2 emissions from fossil fuels, re-produced from (Ritchie et al., 2020)

It can now be seen that the world emits over 34 billion tonnes each year. Therefore, improving energy efficiency, switching to more sustainable energy sources that are renewable, efficient, and affordable, and applying emission-reduction technologies can help mitigate these effects, reduce the environmental footprint of energy consumption, and improve people's quality of life.

According to the latest data from various sources, around 700 to 800 million people worldwide still lack access to electricity. Most of them live in sub-Saharan Africa and Asia. The COVID-19 pandemic has slowed down the progress toward universal energy access and worsened the situation for many households in developing countries (IEA, 2022a; Ritchie et al., 2022; The World Bank, 2022).

Many remote communities in Canada are cut off from the North American power grid. In the last decade, there were 292 such communities with an approximate population of 195,000, 171 of which were indigenous communities with an approximate population of 126,000. Some of these communities have their own local power grids that mainly use hydropower, while 144 remote indigenous communities with a population of roughly 90,000 people rely solely on diesel-generated electricity. Using diesel-generated electricity in these communities can limit economic development, resulting in poor quality services, increasing CO_2 emissions, and leading to fuel spills and leaks. With rising fuel prices, electricity costs are high, and transportation costs add to the expense of electrification. These communities would benefit from switching to low-carbon, sustainable power systems that can improve their environmental and economic situations by connecting to

local or provincial power grids, using renewable energy sources, or combining both (Karanasios, 2018).

Besides the facts mentioned above, in Canada, the main consumer of energy overall is the industrial sector, while space heating ranks as the highest end-use residentially. Additionally, more than 17.4% of the energy consumed in the residential sector is used to heat water, which makes it the second-highest end-use of energy in this sector. About 98% of this energy is supplied from conventional sources, such as the general electrical grid, heating oil, and gas (Elliott, 2012). Although fossil fuels have greatly enhanced human living standards, an increase in their cost and increased awareness of their environmental impact make it imperative to reduce fossil fuel consumption. As per the Paris Agreement signed in 2015, the use of fossil fuels must be decreased by 20% to achieve target gas emission reductions (Bos & Gupta, 2018). In addition, according to the European Union's 2050 road map, approximately two-thirds of energy should come from renewable sources, and electrical energy must be produced using zero-emission techniques (European Commission, 2012).

1.2 Renewable Energy Sources

Renewable energy is harnessed from sustainable and clean resources, unlike traditional fossil fuels. Renewable energy production has been increasing rapidly in recent years, and this trend is expected to continue. According to the International Energy Agency (IEA), renewable energy was the largest source of new power capacity additions in 2020, accounting for 90% of the total. In 2020, the world added more renewable power capacity than fossil fuel-based power capacity for the first time (IEA, 2022a). The most common

renewable energy sources include solar, wind, hydropower, bioenergy, geothermal, and ocean energy. The following is a brief description of these sources.

1.2.1 Solar Energy

Solar energy has become a promising renewable energy source that could meet a big part of our energy needs in the future. The technology to collect and use solar energy has been improving quickly, making it cheaper and more efficient. Two main methods to exploit solar energy are photovoltaic solar cells, which convert sunlight directly into electricity. They can be installed on roofs, walls, or ground-mounted arrays. They are the most common and widely used way to exploit solar energy for residential and commercial purposes. The second method is solar thermal or concentrating solar power (CSP), which uses mirrors or lenses to concentrate sunlight onto a receiver that heats a fluid such as water or oil. They can be used for water desalination, space heating, water heating, and power generation. However, solar energy also has some drawbacks that need to be considered, such as the high initial cost and the intermittency of solar power. The intermittency of solar power means that it depends on the availability and intensity of sunlight, which varies with time, season, weather, and location.

1.2.2 Wind Energy

Wind energy is a promising renewable energy source that can provide clean and sustainable electricity for various applications. Wind energy is produced by using wind turbines that capture the wind's kinetic energy and convert it into mechanical power that drives a generator. Wind energy has many advantages over other energy sources, such as no water requirement for power generation, which is a growing concern in the case of

thermal power plants. Also, it is emissions-free, abundant, inexhaustible, and cost-effective. Wind energy can also reduce reliance on fossil fuels and enhance energy security and independence for remote communities. However, wind energy also faces challenges like variability, intermittency, environmental impacts, and social acceptance. Therefore, wind energy requires careful planning, integration, storage, and management to optimize its benefits and minimize its drawbacks.

1.2.3 Hydropower Energy

Hydropower energy is one of the oldest and largest forms of renewable energy that utilizes flowing water to generate electricity. In hydropower plants, falling water is turned into mechanical energy by turbines. Generators then turn this mechanical energy into electricity. Hydropower is a clean energy source that does not produce greenhouse gas emissions or air pollutants, making it a favourable alternative to fossil fuel-based electricity generation. Hydropower also has the added benefit of providing energy storage capabilities through reservoirs, which can help balance out fluctuations in electricity demand and supply. Despite these advantages, hydropower can have a negative environmental impact, including the potential disruption of aquatic ecosystems and the displacement of communities where dams are built. Therefore, careful planning and management are necessary to ensure that the benefits of hydropower are balanced with the potential impacts.

1.2.4 Bioenergy

Bioenergy is a renewable energy source that converts biomass, such as plant materials or organic waste, into electricity, heat, and transportation fuels. This can be done through various processes, including combustion, gasification, and fermentation. Bioenergy is

considered a renewable energy source because it relies on continuously growing and replenishing organic matter. Additionally, bioenergy has the potential to be carbon neutral or even negative, as the carbon dioxide released during combustion or other processes can be offset by the carbon absorbed during the growth of new biomass. Bioenergy also has the advantage of being a decentralized energy source, as it can be produced locally from various sources, including agricultural waste and forestry residues. However, bioenergy does have some environmental and social impacts that need to be carefully considered, including land use and competition for resources such as water and fertilizer. Therefore, the sustainable production of bioenergy requires careful planning and management to ensure that the benefits of bioenergy are maximized while minimizing any potential negative impacts.

1.2.5 Geothermal Energy

Geothermal energy is a renewable energy source that utilizes the earth's natural heat to generate electricity or heat buildings. This energy source is obtained by drilling wells into the earth's crust and extracting the hot water or steam naturally produced by the earth's heat. Geothermal energy has several advantages for the environment and society. It can provide clean and reliable power with low greenhouse gas emissions and reduce dependence on fossil fuels by utilizing local heat resources. However, the development of geothermal energy does have some potential environmental impacts, including the potential for land subsidence, increased seismic activity, and the release of greenhouse gases and other pollutants from geothermal fluids. Therefore, careful planning and management are

necessary to ensure that the benefits of geothermal energy are balanced with the potential impacts.

1.2.6 Ocean Energy

The ocean is a vast and largely untapped renewable energy source that has the potential to play a significant role in meeting our energy needs. The most well-known forms of ocean energy are tidal and wave power, which harness the kinetic energy of ocean currents and waves to generate electricity. Unlike solar and wind energy, which depend on weather conditions, tidal and wave power can be predicted with a high degree of accuracy, making them reliable power sources. In addition, ocean energy has a relatively low environmental impact, as it produces no greenhouse gas emissions or other pollutants. However, the development of ocean energy technologies is still in its early stages, and significant research and development are needed to make them economically competitive with traditional energy sources. Nevertheless, with continued investment in research and development, ocean energy has the potential to provide a significant source of clean and renewable energy in the future.

1.3 The Share of Renewables in Global Energy

Recently, renewable energy sources have gained increasing attention as the world seeks to transition to a more sustainable energy mix. According to the International Energy Agency (IEA, 2022b), in 2020, renewables accounted for approximately 29% of global electricity generation. However, the share of renewable energy in primary energy consumption, including electricity, transportation fuels, and heat, remains much lower. In fact, as of 2019, renewables only accounted for around 11% of total primary energy

consumption worldwide, with the majority still coming from fossil fuels. Nonetheless, the trend toward greater use of renewable energy sources is expected to continue in the coming years as countries worldwide set ambitious goals to reduce their carbon emissions and mitigate the impacts of climate change. Figure 1.3 shows the change in each renewable source from 1965 to 2021. It should be noted that hydropower is by far the most significant modern renewable source. However, we can also see that wind and solar power are both growing quickly (Ritchie et al., 2022).

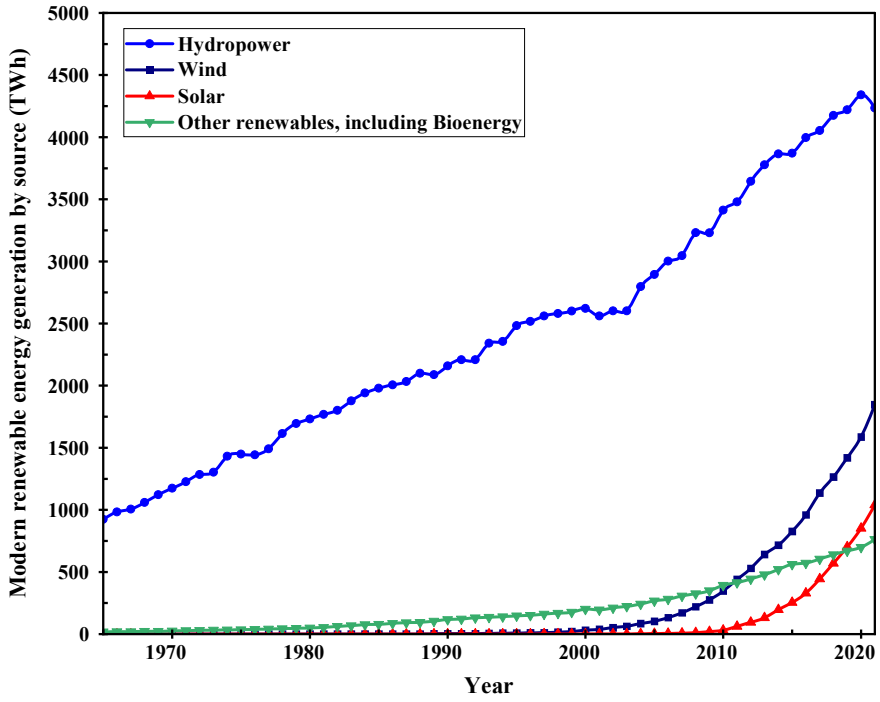

Fig. 1.3: Share of primary energy from renewable sources, re-produced from (Ritchie et al., 2022)

1.4 Motivation and Problem

Over the past centuries, most of the world's energy needs have been met by fossil fuels, which are more convenient and cheaper than other energy sources. However, in the last 20 years, climate change has become a significant concern on a global scale, requiring the

energy sector to address the resulting challenges. The risk and potential impact of climate change have led to greenhouse gas emissions reduction becoming a core issue in energy policy. Additionally, fossil fuels are non-renewable resources projected to be exhausted in the long term, and they are also the primary source of CO_2 emissions into the atmosphere. Furthermore, nuclear energy has been viewed as an attractive solution to the challenge of climate change due to its zero greenhouse gas emissions. However, concerns have been raised over the safety of nuclear facilities and the storage and disposal of highly hazardous radioactive waste. Additionally, nuclear weapon proliferation is possible, further complicating matters. As a result, the current challenge is balancing the need to address the threat of climate change while meeting the energy requirements of established and developing economies. Efforts now should be directed toward renewable energy sources that are abundant, affordable, safe, and environmentally benign. Such sources should be sustainable and able to replace fossil fuels when they eventually become depleted.

In the last ten years, solar energy has been used all over the world as an alternative source of energy. Solar energy is an up-and-coming renewable resource that is widely distributed throughout the globe. Unlike wind and biomass, solar energy is relatively evenly distributed across all regions of the planet. Moreover, its ability to be directly converted into electricity and heat without requiring additional steps makes it a more convenient renewable energy source than other alternatives. Even though the amount of energy that hits the earth's surface in one hour is estimated to be greater than the amount of energy consumed by the entire earth's population in one year (Hurley, 2021), the most significant drawback of solar energy is its low energy density. It requires large collector surfaces to harvest substantial amounts, meaning many materials are needed, making their cost high

and their dissemination low worldwide. As a result, solar energy penetration technology is continuously developed to increase the efficiency of equipment converting sunlight into usable energy.

Solar photovoltaic (PV) and solar thermal (ST) are currently the most commonly available solar technologies, whereas in PV technology, solar radiation is converted directly into electrical power. Solar thermal technology can generate thermal power from dissipative heat from solar radiation and be utilized in practical applications. Even though PV is considered a promising technology for electricity generation, the high cost, low efficiency, and long payback periods for wide-scale energy generation are hindrances to their more comprehensive applications. Conventional solar thermal technology is more cost-effective than PV panels, but it only produces low-quality heat with limited direct uses. A complex and costly system is required to convert this heat into high-quality electricity. One of the technological innovations to achieve better overall efficiency is to use the co-generation principle, where waste heat is captured and used as an additional energy product. Integrating these two techniques enables the exploitation of the most significant amount of solar radiation. This combination has led to a hybrid system called the Photovoltaic/Thermal System (PV/T), which includes a heat exchanger or flow channel underneath the PV cells to collect heat dissipated from the cells.

One of the major challenges of PV/T technology is that it generates heat at a relatively low operating temperature and has a high cost of PV cells. To produce more energy, conventional PV arrays require large areas. However, PV panels for large-scale energy generation are expensive and have long payback periods. A possible solution is to concentrate solar radiation on PV cells using inexpensive concentrator optics elements such

as lenses and mirrors instead of expensive PV cells. This technology is known as concentrator photovoltaic (CPV) technology. CPV has attracted the interest of the scientific community due to its ability to increase efficiency and reduce the cost of solar electricity (A. Luque & Hegedus, 2011a). Point-focus Fresnel lens (PFFL) concentrator is a widely used component in CPV systems due to its numerous advantages, such as being lightweight, low-cost, and effectively increasing energy density. PFFL concentrates light onto a small, high-efficiency solar cell. Thus, using high-efficiency but expensive solar cells, such as multi-junction photovoltaic cells (MJPV), is counterbalanced by the low-cost optical elements employed. Nevertheless, the main drawback of CPV is that concentrated solar radiation increases the PV surface temperature, often necessitating active cooling. Furthermore, CPV systems are a relatively new technology, so their potential applications and long-term reliability and durability still need to be fully established. This can be a concern for investors and users who are looking for a long-term investment.

These issues can be overcome by adopting a Concentrator Photovoltaic Thermal (CPVT) system, which uses water as a coolant. CPVT harvests and converts the excess heat produced by PV cells into thermal energy. In this way, the PV cells are maintained at a moderate temperature, and both electrical and thermal outputs are increased, which can be utilized in different applications.

1.5 Statement of the Problem

Solar energy is a promising, sustainable, clean energy source that can meet increasing global energy demand and reduce greenhouse gas emissions. However, solar energy technologies such as photovoltaic (PV), solar thermal (ST), concentrated photovoltaic

(CPV), and hybrid photovoltaic/thermal (PV/T) systems have some limitations, such as low energy conversion efficiency, high cost, and land use requirements. Concentrated photovoltaic thermal (CPVT) systems are a novel type of solar energy technology that can overcome these limitations. Additionally, CPVT systems that combine MJPV solar cells and PFFL with active cooling are an emerging technology. This area of research is still not mature enough. More studies, analyses, and development work on design considerations are still required.

This work presents an experimental study on an indoor prototype model of CPVT that was designed and built at the Thermofluid Laboratory of the Mechanical Engineering Department, Memorial University of Newfoundland. The CPVT model includes a sun simulator that was specially designed and manufactured for this experiment to emulate sunlight in an indoor environment. Moreover, copper heat sinks (adapters) were machined to provide a flat surface for cell mounting and a round shape on the backside for attachment to a copper pipe flow loop. The proposed design aims to reduce the MJPV module temperature and increase heat transfer to the heat transfer fluid (HTF) in the flow channel to produce high electrical and thermal energy. A numerical model is developed to simulate the performance of the CPVT design and validated against the experimental data collected in the indoor test campaigns.

1.6 Objectives

This research aims to propose an efficient integrated CPVT model based on a point-focus Fresnel lens concentrator equipped with high-efficiency GaInP/InGaAs/Ge multi-junction photovoltaic cells, a copper heat sink, and an absorber tube as an active cooling

system. The performance of the CPVT model needs to be improved by increasing the generated electrical power and the extracted heat from the MJPV. To achieve this aim, experimental and numerical investigations were conducted to analyze the heat transfer and fluid flow of the proposed model under different operating conditions. The specific objectives of the study can be summarized as follows:

- To investigate the feasibility of using concentrated photovoltaic thermal (CPVT) systems as a sustainable and cost-effective solution to meet the increasing global energy demand and reduce greenhouse gas emissions.
- To design and build an indoor prototype model of CPVT that combines multi-junction photovoltaic (MJPV) solar cells and point-focus Fresnel lenses (PFFL) with active cooling, which includes:
    - Designing and fabricating a sun simulator that can emulate sunlight in an indoor environment for testing the proposed CPVT model.
    - Designing and manufacturing copper heat sinks to provide a flat surface for cell mounting and a round shape on the backside for attachment to an absorber tube.
    - Designing and fabricating a movable lenses holder for adjusting a proper focal length.
- To experimentally investigate the performance of the CPVT prototype model and evaluate its energy conversion efficiency in terms of both electrical and thermal energy.
- To develop a three-dimensional computational fluid dynamics (CFD) model using Ansys software to analyze the heat transfer in the CPVT model. Due to the limitations of experimental testing, the CFD model is capable of performing extensive parametric

studies with different heat transfer fluid (HTF) flow rates, HTF inlet temperatures, and incident irradiance levels. The numerical model will be validated against the experimental data collected in the indoor test campaigns.

- To develop an electrical model capable of analyzing the electrical characteristics of the MJPV solar cell under different concentration ratios (*CR*) and surface temperatures.
- To bridge the technological gap and advance the implementation of CPVT systems by providing a comprehensive and in-depth analysis of their electrical and thermal performance. The study will investigate the effects of various parameters, such as *CR*, mass flow rate, inlet temperature, and cell surface temperature, on the efficiency and output of the CPVT system. The study will also compare the numerical simulation results with the experimental data and validate the accuracy and reliability of the models. The study will contribute to the existing knowledge base and aid in successfully deploying and optimizing CPVT technology.
- To provide recommendations for further research and development of CPVT systems and suggest areas for improvement and innovation. Also, to enhance the understanding of the CPVT systems that will help the companies to improve this technology and increase the percentage of energy demand which is met through solar energy sources.

1.7 Scope

To successfully achieve the above objectives, this thesis' focus will be on the following particular points:

- Conduct a comprehensive literature review to investigate existing research on CPVT technologies, including their thermal and electrical performance, feasibility, and potential for sustainability and cost-effectiveness.
- Focus on CPVT systems that use MJPV solar cells, PFFL, and heat sinks with active cooling as the main components. Other components, such as tracking systems, PV analyzer kits, and maximum power point tracking (MPPT), will not be included in this study.
- Perform a series of experiments to evaluate the electrical and thermal performance of the CPVT prototype under various operating conditions.
- Perform a series of parametric studies using the developed CFD model to assess the impact of different HTF flow rates, HTF inlet temperatures, and incident irradiance levels on the heat transfer during the CPVT model.
- Validate the CFD model against the experimental data collected during the indoor test campaigns.
- Discuss the technical and environmental benefits of the novel CPVT model.

1.8 Thesis Structure

This thesis is structured into eight main chapters, references and four appendices, and the content of the thesis is organized as follows:

Chapter One: The first chapter of this thesis provides a comprehensive introduction to the research. It begins by presenting the general background of the energy scenario, highlighting the significance of addressing primary energy consumption and its impact on

climate change. The growing importance of renewable energy sources, particularly solar energy, is emphasized. The chapter outlines the motivation behind this study and identifies the research problem. Clear and well-defined objectives of the research are stated, along with the specific scope of the study. Furthermore, the chapter provides an overview of the Concentrated Photovoltaic Thermal (CPVT) system, setting the stage for the rest of the thesis.

Chapter Two: Presents a detailed literature review covering various aspects of solar energy conversion technologies. It delves into the principles of photovoltaic cells, explaining their different types and classifications. Concentrated Photovoltaic (CPV) and CPVT systems are thoroughly discussed, along with Multi-junction Photovoltaic cells (MJPV) and concentrator optics. The chapter also reviews heat extraction methods and heat transfer fluids utilized in CPVT systems. The chapter concludes with a comprehensive summary and analysis of existing literature on CPVT systems.

Chapter Three: The design of the proposed CPVT model is presented in detail. It describes the indoor CPVT model and its key components, including the solar simulator, Fresnel Lenses, and MJPV solar cell. The measurement equipment used in the experiments, such as data acquisition systems, radiation, and temperature measurements, are discussed. The chapter elaborates on the experimental procedures and includes a benchmark test to confirm the accuracy of the apparatus. Moreover, it addresses the evaluation of experimental uncertainties, ensuring the reliability of the results.

Chapter Four: This chapter provides the theoretical background of the proposed CPVT model. It introduces energy balance equations and discusses the thermal and electrical

characteristics of the CPVT system. The theory and governing equations that underlie the system's operation are explained in detail.

Chapter Five: Revolves around the Computational Fluid Dynamics (CFD) analysis of the proposed CPVT model. It presents the numerical modelling approach using the Finite Volume Method for CFD simulations. The software ANSYS Fluent and a comprehensive explanation of the computational methodology are introduced. Key topics covered include mesh generation, governing equations of fluid flow, solver settings, and mesh independence study. The chapter also addresses uncertainties and errors in CFD simulations, ensuring the accuracy of the numerical results.

Chapter Six: This chapter is dedicated to analyzing the electrical characteristics of the MJPV cells. It investigates the behaviour of MJPV solar cells, providing a detailed examination of I-V characteristics and electrical parameters. A mathematical lumped diode model of a single-junction solar cell is presented and verified. The chapter concludes with a comprehensive discussion and analysis of the electrical characteristics of the MJPV cells.

Chapter Seven: This pivotal chapter presents and thoroughly discusses the research findings. It begins with a justification and motivation for using the CPVT model. The chapter showcases and validates both experimental and numerical simulation results. A wide array of parameters is examined, including the effect of mass flow rate on temperature, efficiencies, and power output of the CPVT model.

Chapter Eight: The final chapter draws comprehensive conclusions from the research findings. It summarizes the key insights from the experimental and numerical analyses, highlighting the achievements in fulfilling the research objectives. Additionally, the chapter

provides recommendations for future work to enhance the performance of CPVT systems and explores new research areas.

Chapter 2

Literature Review

2.1 Introduction

Concentrated photovoltaic thermal (CPVT) systems are hybrid solar systems that use both concentrated photovoltaic (CPV) and solar thermal (ST) technologies to obtain energy from the sun. This means that the same system can produce both electricity and heat. CPVT systems use concentrated sunlight to generate electricity through high-efficiency multi-junction photovoltaic (MJPV) cells and simultaneously recover heat from the cells for various applications. CPVT is a relatively nascent technology. Many aspects of CPVT are still under research and development. In the present chapter, an attempt has been made to review the state-of-the-art CPVT technology and its historical development, types, and performance.

This chapter also discusses concentrator optics, heat extraction methods, and heat transfer fluid (HTF). Further, the chapter introduces the basic concepts and classifications of PV and CPVT systems. It then reviews the potential applications of CPVT systems in various sectors. The chapter concludes by summarizing the key insights derived from the literature review. It highlights the significance of CPVT systems, and the identified research gaps are also briefly discussed, setting the stage for further exploration in the subsequent chapters.

2.2 Solar Energy Conversion Technologies

The search for sustainable and renewable energy sources has become an increasingly important area of research in recent years. Solar energy has emerged as the most promising energy source among the various exploitable alternatives. This is primarily because solar energy is abundant and widely exploited for power generation compared to other renewable energy sources. The expansion in this sector is reflected in the growing number of solar installations worldwide. The utilization of solar energy has the potential to address the increasing energy demands of the world's growing population while simultaneously reducing the environmental impact of non-renewable sources. Therefore, continued efforts must be made toward developing and deploying solar technologies for a sustainable future.

Solar energy can be directly converted into useful forms of energy using two main categories of technologies: thermal systems and photovoltaic systems. Thermal systems convert solar energy into heat energy using a working fluid, usually water or air. Photovoltaic systems convert solar energy into electrical energy using semiconductors that produce an electric current when exposed to light. Typically, these two systems are used as individual units separately, but a more recent idea is to combine them to form hybrid PV/T systems, which may be regarded as the third way for direct solar energy conversion.

2.3 Energy from the Sun

One of the essential factors for the cost-effective use of solar energy is the amount of solar radiation that reaches the earth's surface, as it determines the performance of any solar system. However, solar energy is intermittent and diffuse, limiting its use and requiring large surface areas to collect and store energy for practical applications. The challenges of

solar energy are its diffuse and variable nature, which increases the cost of manufacturing solar collectors and storage systems. Even though sunlight is seemingly free, society has to invest in the material and infrastructure to convert solar energy into proper forms of energy. Its high cost limits its widespread use compared to conventional fuels. According to Planck's quantum theory of 1900, solar radiation has wave and particle (photon) characteristics, known as wave-particle duality in physics. Each photon of wavelength λ has an energy E_{ph} given by:

$$E_{ph}(\lambda) = \frac{hc}{\lambda} \tag{2.1}$$

Where h is the Plank's constant ($h = 6.626\times10^{-34}\ J\,s$) and c is the velocity of light in vacuum ($c = 3\times10^{8}\ m/s$).

As shown in Eq (2.1) the energy of the photons emitted by the sun depends on the wavelength of the radiation, and their distribution over different wavelengths is called a solar spectrum, which is given by Planck's distribution law (Bergman et al., 2020; Duffie et al., 2020). The total solar irradiance and its spectral distribution affect the efficiency of any solar device used for terrestrial applications (Nann & Emery, 1992). Solar thermal collectors tend to convert solar energy with a relatively constant efficiency over the entire solar spectrum; this conversion depends only on the optical properties of the front cover and/or coating of the absorber plate used, selective or non-selective. On the other hand, PV panels are very sensitive to the wavelength of solar radiation, and different types of cells have different spectral responses (Gottschalg et al., 2005; van Dyk et al., 2002).

2.4 Photovoltaic Cells

As previously stated, PV cells convert sunlight or artificial light into electricity using the photovoltaic effect, in which materials absorb photons and emit electrons. PV cells are currently one of the most efficient and widely used technologies for converting sunlight directly into electrical energy. The following subsections will highlight their principles of operation, classifications, the current state of technology, and efficiency.

2.4.1 Principle of Operation of a PV Solar Cell

The basic principle of a PV solar cell is to convert sunlight into direct current (DC) electricity using a large surface diode (slab) with a p-n junction. The diode has two contacts on the top and rear sides that can be connected to a load, such as a lamp, to collect the current. The diode is made of semiconductor material with two energy levels, the valence and conduction bands, separated by an energy gap (*Eg*). When light with enough energy hits the diode, it breaks the covalent bonds of the semiconductor and frees electrons from the valence band to the conduction band, creating holes in the valence band. The holes act like positive charges that can move and carry current within the material. The electric field of the p-n junction separates the electrons and holes and drives them to the contacts, creating an electric current. However, not all the light can be used for this process. Only light with photon energy equal to or higher than *Eg* can create electron-hole pairs, and any extra energy is lost as heat. Light, which has photon energy lower than *Eg* cannot excite electrons and is also lost as heat. These are some of the reasons why the theoretical conversion efficiencies of PV solar cells are limited to 20-30% (Hovel, 1975; Tonui, 2006).

Figure 2.1 depicts the PV effect, which occurs when a semiconductor is exposed to sunlight and produces electrical energy.

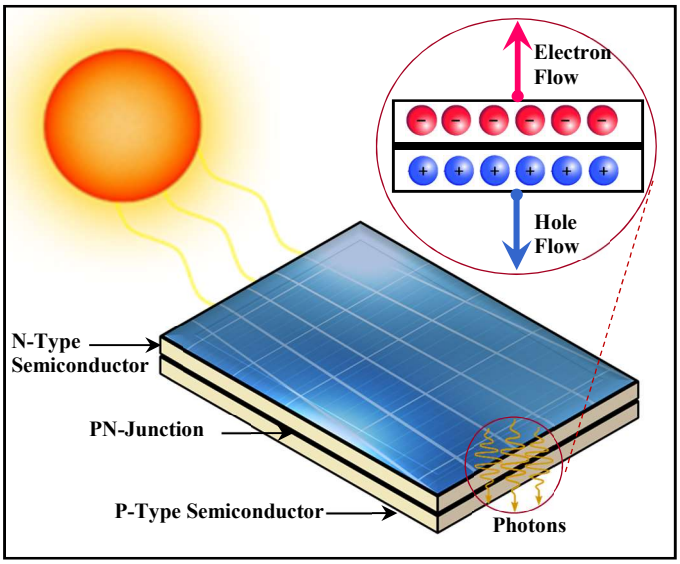

Fig. 2.1: Schematic diagram showing the photovoltaic effect

2.4.2 Types and Classifications of Photovoltaic Cells

The photovoltaic effect is a process that converts light (photons) into electricity, and it is the basis of solar PV energy conversion. The electricity output is influenced by various factors, such as the cell's material, the cell's size, and the light source's quality and intensity (Ibn-Mohammed et al., 2017). PVs can be classified differently, such as by the active materials (i.e., the primary light-absorbing materials) used for the solar cells, as shown in Fig. 2.2, or by the material complexity (Jean et al., 2015). Another way to categorize PVs is based on their device structure and architecture, which can be either wafer-based or thin-film. Wafer-based PVs are made from slices of semiconducting wafers derived from ingots (Zhou, 2015). On the other hand, thin-film cells utilize insulating substrates such as glass

or flexible plastics to deposit layers of semiconducting materials that form the device structure (Kilner et al., 2012).

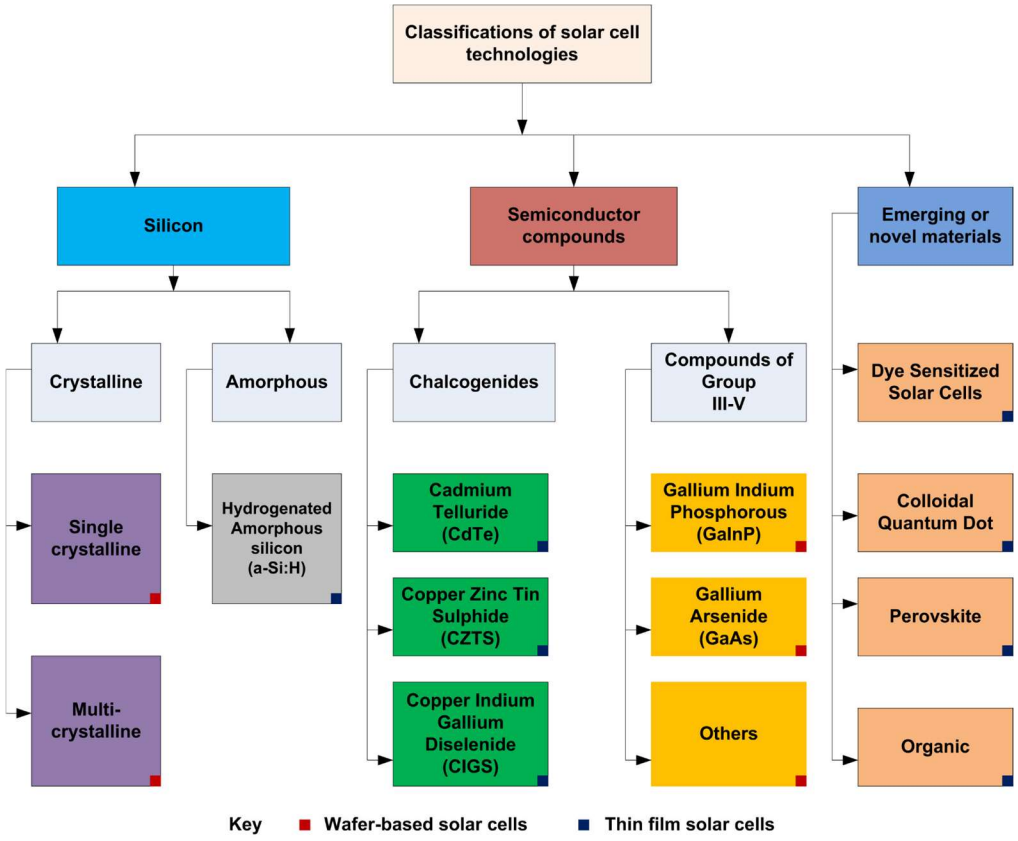

Fig. 2.2: Classification of solar cells based on the primary active material (Ibn-Mohammed et al., 2017).

Furthermore, PV cells can be classified into four generations based on their historical development and technological advancement (Pastuszak & Węgierek, 2022). However, the classification into generations is not strictly defined, and there can be some overlap between them. The four generations of PV cells are:

First generation: These are the conventional crystalline silicon (c-Si) cells, which can be either monocrystalline (mono-Si) or polycrystalline (poly-Si). They have high efficiency

and a long lifetime but are also expensive and require a lot of energy and material to produce (Sampaio & González, 2017).

Second generation: These are the thin film (TF) cells, which use thin layers of materials such as amorphous silicon (a-Si), cadmium telluride (CdTe), or copper indium gallium selenide (CIGS). They have lower efficiency and shorter lifetime than c-Si cells but are also cheaper and easier to manufacture. They can be flexible and integrated into various applications (Altuwairgi, 2022).

Third generation: These emerging PV technologies aim to overcome the limitations of the first and second-generation cells. They include multi-junction (MJ) cells, which use multiple layers of different materials to capture a broader range of the solar spectrum and achieve higher efficiencies (Nishioka et al., 2006; Yamaguchi, 2003); dye-sensitized solar cells (DSSC), which use organic dyes to absorb light and transfer electrons (Swami, 2012); organic photovoltaic (OPV) cells, which use organic polymers or molecules as the active materials (Hong et al., 2019); and perovskite solar cells, which use a hybrid organic-inorganic material with a perovskite crystal structure(Niu et al., 2015). These cells could be low-cost, high-efficiency, and environmentally friendly but face stability, scalability, and toxicity challenges.

Fourth generation: These are the future PV technologies that aim to incorporate novel concepts and approaches to enhance the performance and functionality of PV cells. They include quantum dot solar cells, which use nanoscale semiconductor particles to manipulate light absorption and emission (Hu & Mandelis, 2021); plasmonic solar cells, which use metallic nanostructures to enhance light trapping and scattering (Atwater & Polman, 2010;

Green & Pillai, 2012); thermophotovoltaic cells, which use thermal radiation from a heat source to generate electricity (Bauer, 2011); and luminescent solar concentrator cells, which use fluorescent materials to collect and concentrate sunlight (van Sark, 2013). These cells have the potential to achieve ultra-high efficiencies, low cost, and novel applications, but they also require further research and development.

2.4.3 Photovoltaic Efficiency (State-of-the-Art)

Different PV cell technologies are available nowadays, with different conversion efficiencies and costs. The National Renewable Energy Laboratory (NREL) maintains a chart of the highest confirmed conversion efficiencies for research cells for a range of PV technologies, plotted from 1976 to the present, as illustrated in Fig. 2.3. The chart is updated regularly with data from independent, recognized test labs and reported on a standardized basis. The chart covers 28 different subcategories of PV technologies, such as crystalline silicon cells, multijunction cells, thin films, and emerging PV. The chart also highlights each technology's most recent world record and the company or group that fabricated the device. The chart is a valuable tool for tracking the progress and trends of PV research and development. It also allows for comparing the performance and potential of different PV technologies. The latest version of the chart, released on April 5, 2023, shows that multijunction cells have achieved the highest efficiency of 47.6%, followed by single-junction GaAs cells with 30.8% and crystalline Si cells with 27.6%. Among thin-film technologies, CdTe cells have reached 22.1%, while CIGS cells have reached 23.6%. Among emerging PV technologies, perovskite solar cells have achieved 25.8%, while organic solar cells have achieved 19.2%. The chart also shows that some PV technologies

have experienced rapid improvements in efficiency over time, while others have reached a plateau or slowed down (NREL, 2023).

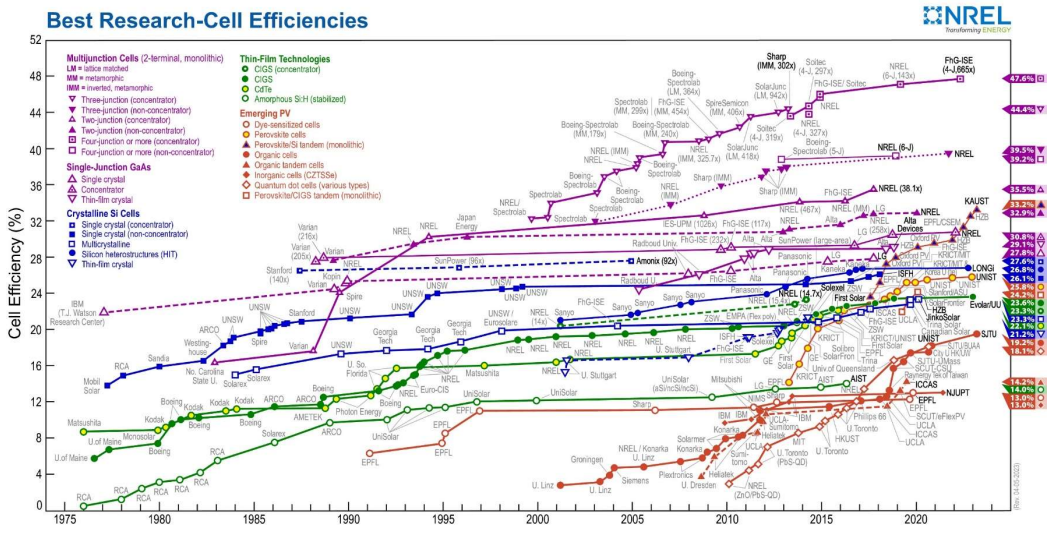

Fig. 2.3: Best Research-Cell Efficiencies chart (NREL, 2023)

2.5 Concentrating Photovoltaic (CPV) Systems

Photovoltaic technology can be divided into two categories: non-concentrated and concentrated. The former is the widely used type of PV that has a high initial cost compared to other sources of electricity. To improve the efficiency and cost-effectiveness of solar power generation, some methods have been proposed and studied, such as sun tracking (Mousazadeh et al., 2009) and concentrating photovoltaic (CPV) technology (Garboushian et al., 1997). CPV systems use lenses or mirrors to direct more sunlight onto a smaller solar cell, which reduces the amount of expensive semiconductor material needed in a PV system (Almonacid et al., 2017). The concentration ratio of CPV systems is defined as the ratio of the lens area to the solar cell area. It indicates how many times the sunlight has been concentrated. It is usually measured in 'suns.'

According to Shanks et al., (2016), CPV systems can be classified into four groups based on the concentration ratio: low (<10 suns), medium (10–100 suns), high (100–2000 suns), and ultrahigh (>2000 suns). Besides, CPV systems can be classified into two types based on the optical devices they use, which are point-focus and line-focus systems. Point-focus systems use devices such as paraboloid dishes, Fresnel lenses or heliostats to concentrate sunlight. In contrast, line-focus systems use parabolic mirrors and linear Fresnel lenses or mirrors (A. L. Luque & Viacheslav, 2007). Figure 2.4 shows the most common concentrator configurations, which are also used by some solar thermal systems (Karathanasis, 2015). Furthermore, CPV systems have several advantages and disadvantages, which are listed below:

Advantages:

- High Efficiency: CPV systems can achieve higher efficiency than traditional PV systems because they use lenses or mirrors to concentrate sunlight onto small, high-efficiency solar cells.
- Reduced Cost: CPV systems use less semiconductor material than traditional PV systems, which can reduce the overall cost of the system.
- Scalability: CPV systems can be easily scaled up to generate more electricity by adding more concentrators and solar cells.
- Reduced Land Use: CPV systems require less land than traditional PV systems to generate the same amount of electricity because they use smaller solar cells.

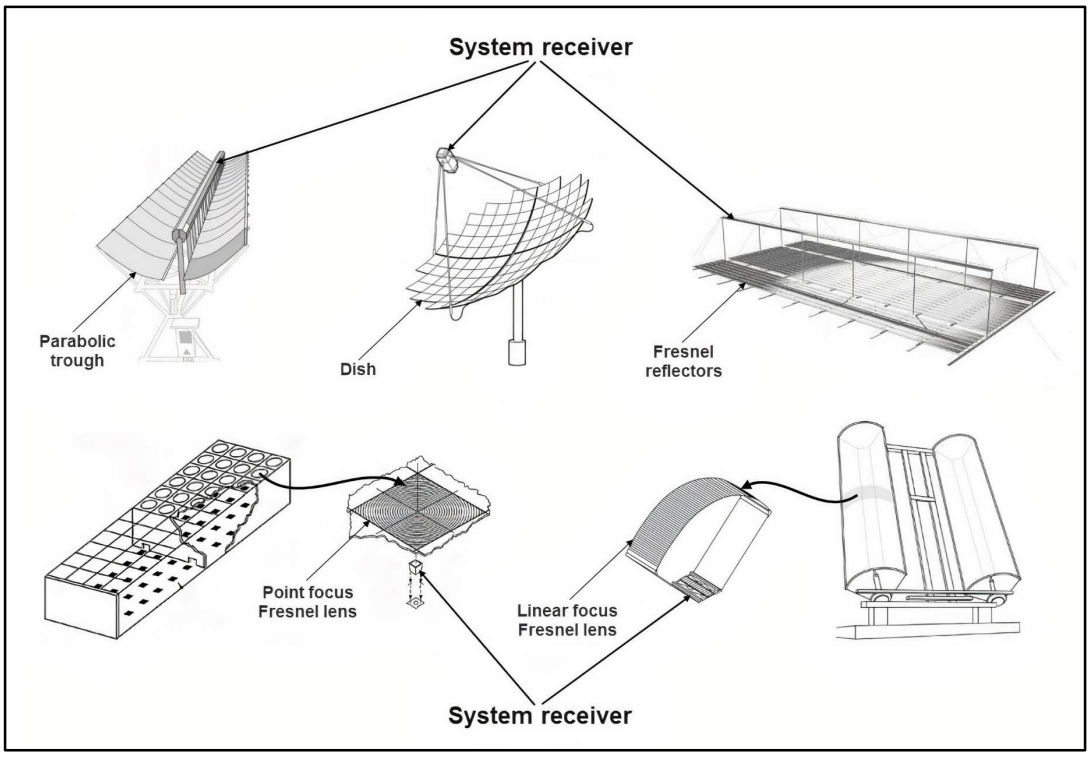

Fig. 2.4: Typical optical devices used in concentrated solar power applications (Karathanasis, 2015)

Disadvantages:

- Sun Tracking: CPV systems can only concentrate direct sunlight, not diffuse light, so they require sun tracking systems to keep the sunlight aligned with the concentrator optics, which adds complexity and maintenance costs.
- Heat Dissipation: CPV systems can generate much heat, especially at high concentration ratios, which can reduce the efficiency of solar cells and cause hot spots that can damage the solar cells. Therefore, they require heat management and additional cooling systems to prevent overheating.
- Limited Application: CPV systems are most effective in areas with high direct sunlight, which limits their application in areas with cloudy or overcast weather.

- Limited Geographic Applicability: Because CPV systems require direct sunlight, they are most effective in areas with high levels of direct sunlight, which may limit their geographic applicability.

2.6 Concentrated Photovoltaic Thermal (CPVT) Systems

As stated in Chapter 1, CPVT systems are a novel type of solar energy technology that can overcome the limitations of CPV systems. They are a hybrid technology that combines CPV and solar thermal to generate electricity and heat simultaneously. CPVT systems use optical concentrators to focus sunlight on photovoltaic cells and thermal receivers, increasing energy conversion efficiency. In recent years, CPVT systems have gained significant attention as a promising solution for meeting energy demands while reducing carbon emissions. The following sections will present a detailed review of CPVT components.

2.6.1 Multi-junction Photovoltaic Cells

Multi-junction photovoltaic cells are becoming increasingly popular in concentrated photovoltaic systems due to their superior efficiency. MJPV solar cells are PV cells that consist of a stack of three or more single-junction solar cells with different bandgaps, enabling them to capture a broader range of the solar spectrum and achieve higher conversion efficiencies than conventional single-junction PV cells. They are a third-generation technology and have been studied since the 1960s (Wolf, 1960; Yastrebova, 2007). A common MJPV is schematically shown in Fig. 2.5 (Nishioka et al., 2006). They are made of III-V semiconductor compounds (these semiconductor materials are alloys that are composed of elements from Groups III and V in the periodic table), such as gallium

indium phosphide (GaInP), indium gallium arsenide (InGaAs), and germanium (Ge), which have high optical absorption coefficients and long minority carrier lifetimes (Wiesenfarth et al., 2017). The bandgaps of the layers decrease from top to bottom.

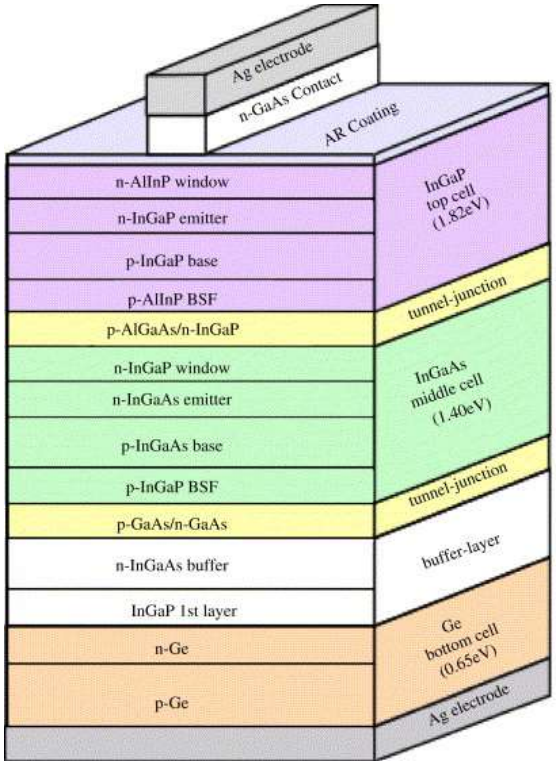

Fig. 2.5: A structure of a MJPV cell made of InGaP/InGaAs/Ge layers (Nishioka et al., 2006)

The comparison of single-junction silicon PV and multi-junction solar cells in terms of their solar spectrum utilization is shown in Fig. 2.6. A MJPV solar cell typically consists of three layers of semiconductors with different bandgaps: Ge (0.67 eV), InGaAs (1.18 eV), and GaInP (1.70 eV). These materials are chosen for their high optical absorption coefficients and good values of minority carrier lifetimes and mobility (A. Luque & Hegedus, 2011b; Miles et al., 2005).

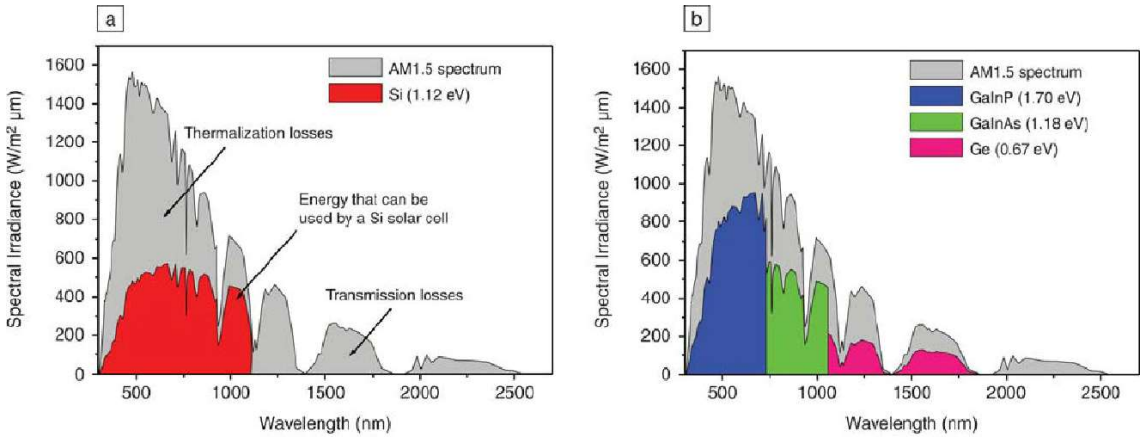

Fig. 2.6: Spectral response of (a) Si solar cells and (b) GaInP/GaInAs/Ge solar cells (Yastrebova, 2007).

The top layer (GaInP) converts the photons with the highest energies in the short wavelength range, while the middle layer (InGaAs) converts the photons with medium energies in the near-infrared range, and the bottom layer (Ge) converts the photons with the lowest energies in the infrared range. MJPV solar cells are especially suitable for CPV systems, which focus sunlight onto a small cell area, as they respond better to high concentrations and a lower temperature coefficient. They are ideal for applications that require high power generation and long-term performance under extreme conditions, such as point-focused systems. Henry, (1980) concluded that multi-junction solar cells could achieve higher theoretical efficiencies than other PV technologies. The maximum theoretical efficiency of a multi-junction solar cell under 1000 suns concentration and at room temperature increases with the number of bandgaps, ranging from 37% for one bandgap to 72% for 36 bandgaps.

2.6.2 Types of Concentrator Optics

Solar concentration is a crucial aspect of various established and potential solar technologies. The primary aim of solar concentration is to direct and concentrate solar radiation onto a particular location to create an area with high energy flux. This high energy flux is used for various purposes, including generating electricity in the CPVT system, where the heat generated is used as a secondary energy source. Solar concentrators collect and concentrate solar radiation using reflective or refractive surfaces. They are widely used in CPVT systems, which aim to reduce the cost and material of solar cells by using high-concentration ratios.

Solar concentrators can be divided into two main types: reflective and refractive. Reflective concentrators use mirrors or lenses to reflect and focus light onto the solar cell, while refractive concentrators use lenses to bend and direct light onto the solar cell. As previously mentioned, Fresnel lenses can be classified into two types based on their symmetry: point-focus or linear-focus lenses. Point-focus lenses have circular symmetry around their axis and concentrate light into a point. On the other hand, linear-focus lenses have a constant cross-section along a transverse axis and focus light into a line. Typically, point-focus lenses use one cell, while a linear array of cells is used for linear-focus lenses. Fresnel lenses are usually made of Acrylic plastic, specifically Polymethyl methacrylate (PMMA), which can be moulded well and has demonstrated good weatherability when combined with UV stabilizers (Swanson, 2003). They are generally integrated into modules with a lens or multiple lenses, a housing intended to secure the back side of the lens from dust and dirt, and a solar cell. Figure 2.7 shows various configurations of Fresnel lenses.

The main advantages of solar concentrators are increased intensity of solar energy; reduced heat loss due to the smaller area used for concentrating solar energy; high delivery temperature; and reduced cost as they can replace the large receiver. These advantages make solar concentrators suitable for the thermal utilization of solar energy; however, optical losses, dependence on beam radiation only, and the complexity of design and proper maintenance are the challenges associated with solar concentrators (Kashyap et al., 2022).

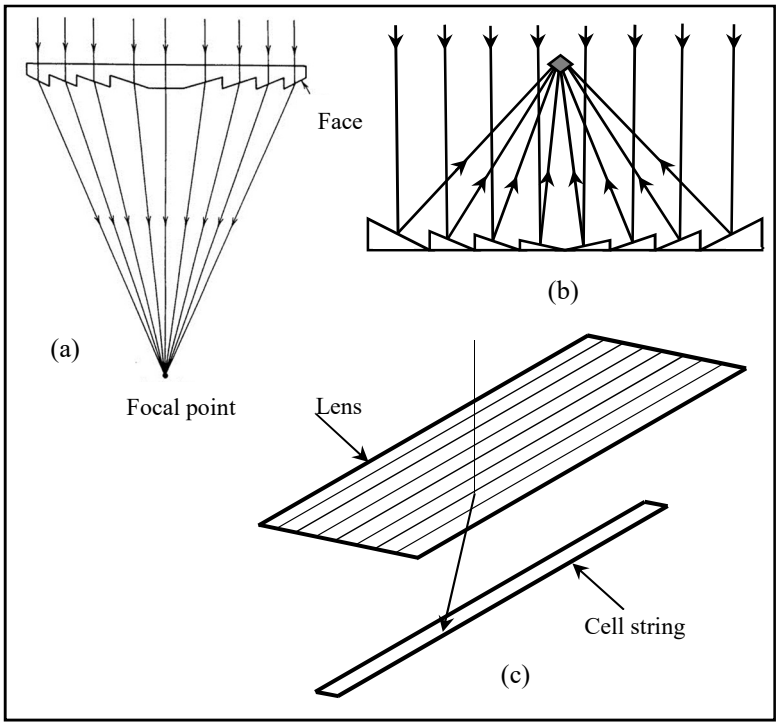

Fig. 2.7: Fresnel lens configurations (a) Point-focus Fresnel lens (b) Reflective Fresnel lenses (c) Linear Fresnel lens

2.7 Heat Extraction Methods for a CPVT System

Heat extraction methods are crucial for the design and performance of CPVT systems, as they can enhance heat dissipation and reduce the temperature of the PV cells. According to Sharaf and Orhan, (2015a), heat extraction methods can be classified into pre-

illumination and post-illumination methods. Pre-illumination methods employ filters that split and block some wavelengths of the solar spectrum before they reach the PV cells, but this technology is still under development. Post-illumination methods use heat receivers that capture the excess heat from the PV cells after receiving solar radiation. The efficiency of heat extraction depends on the operating temperature of the cell and the contact quality between the PV cell and the cooling unit (Alzahrani et al., 2021). Figure 2.8 illustrates the energy flow in both pre-and post-illuminating techniques (Papis-Frączek & Sornek, 2022).

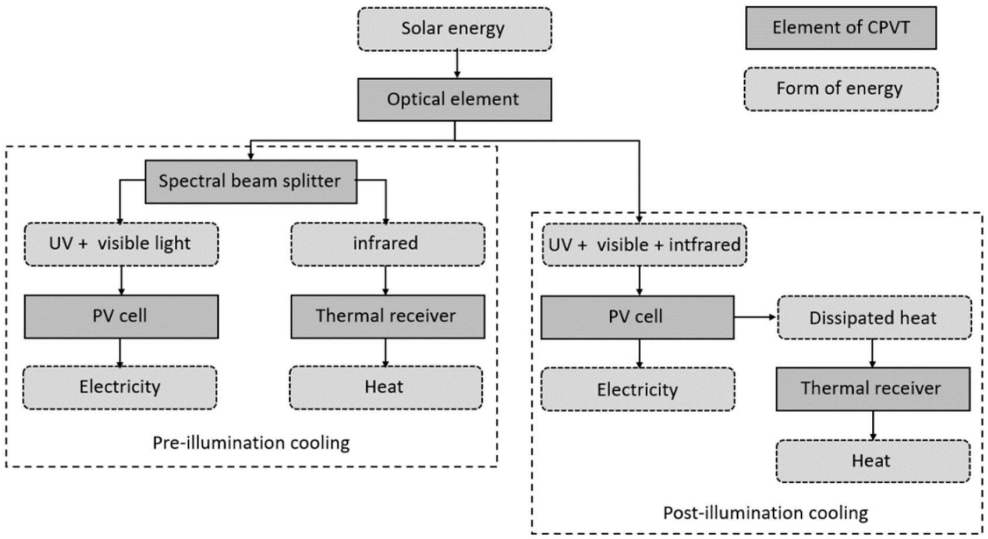

Fig. 2.8: Energy flow in both pre-and post-illuminating techniques (Papis-Frączek & Sornek, 2022).

Two main approaches are commonly used for thermal regulation of CPVT systems: passive and active cooling (Al Siyabi, 2019). Passive cooling methods use natural convection phenomena and do not need any mechanical equipment. They include various techniques such as heat spreading (Araki et al., 2002), cooling fins (Lv et al., 2015), heat pipe (Y. A. Cengel, 2003), and phase change material (PCM) (Wang et al., 2008). In

contrast, active cooling methods use mechanical equipment such as fans and pumps to force the circulation of a heat transfer fluid (HTF) through the heat receiver, such as microchannel heat sinks (Ohadi et al., 2013), jet impingement heat sinks (Barrau et al., 2011), liquid immersion (Zhu et al., 2011), and multi-layered microchannel (MLM) technique(Vafai & Zhu, 1999). Active cooling methods have higher convective heat transfer coefficients and are more efficient than passive cooling (AlFalah et al., 2022).

2.8 Heat Extraction Devices for a CPVT System

In CPVT systems, the heat receiver is a crucial component that plays a vital role in the thermal management system. The performance of CPVT systems is heavily dependent on the heat extraction devices used to dissipate excess heat from the PV cells. Heat extraction devices regulate the temperature of the PV cells and prevent thermal degradation, which can result in reduced energy output and a decreased system lifespan. Developing efficient and effective heat extraction devices is essential to enhance the performance and durability of CPVT systems.

There are different types of heat extraction devices for CPVT systems with active liquid cooling (Papis-Frączek & Sornek, 2022). These devices can be classified into two main groups depending on the scale of their internal channels: macro- and micro-. Macro-scale devices have large channels with diameters ranging from 1 to 10 mm, while micro-scale devices have small channels with diameters less than 1 mm. Macro-scale channel/duct devices include rectangular, circular, triangular ducts, metal blocks with inner channels, serpentine ducts, and flow between two flat plates. Rectangular ducts are simple in design and to manufacture but they can suffer from increased pressure drop and reduced heat

transfer performance. Circular ducts have a more uniform flow distribution and lower pressure drop, but they can be more difficult to fabricate. Triangular ducts have the advantages of both rectangular and circular ducts, but their design can be more complicated. Metal blocks with inner channels efficiently transfer heat, but their production costs can be high. Serpentine ducts enhance heat transfer performance by creating turbulent flow and can be fabricated with a low-pressure drop. The flow between two flat plates is an efficient heat extraction method but requires more space. Microchannel devices include single-layered microchannel devices, multi-layered microchannel devices, microchannels with internal features, and microchannels with pin fins. Microchannel devices can provide higher heat transfer performance and reduced size and weight than macro-scale channel/duct devices. However, they can also be more complicated to manufacture and more susceptible to clogging.

Each type of device has advantages and disadvantages in terms of thermal performance, pressure drop, fabrication cost, and reliability. More details about heat extraction techniques may be found in (Sharaf & Orhan, 2015a), (Papis-Frączek & Sornek, 2022). Figure 2.9 shows the percentage of different shapes of heat receivers for heat extraction devices with macro- and microscale channels. For the macro-scale devices, the most common shape is circular ducts (25%), followed by rectangular ducts and serpentine ducts (both 15%). Triangular ducts and metal blocks with internal channels are slightly less common (both 13%). For the micro-scale devices, single-layered receivers are the most prevalent (50%), followed by multi-layered receivers (18%). Pin fins and internal features are less frequent (9% and 5%, respectively). There is also a significant group of other shapes that are not classified (18%).

2.9 Heat Transfer Fluid for a CPVT System

Heat transfer fluid (HTF) is an essential component of CPVT systems. For active cooling, the most common HTFs are air, water, nanofluids, and oils (Krishna et al., 2020). Air and water are cheap, abundant, and eco-friendly fluids. However, water is better for cooling because it has a high heat capacity. Sometimes, pure water is unsuitable and can be mixed with glycols or nanofluid particles (Al-Amri & Mallick, 2013). Water-nanofluid solutions can transfer heat more effectively because they have a higher heat capacity, improving thermal and electrical efficiency. The higher the concentration of nanoparticles, the higher the viscosity and, therefore, the higher the pumping power (Hamzat et al., 2022).

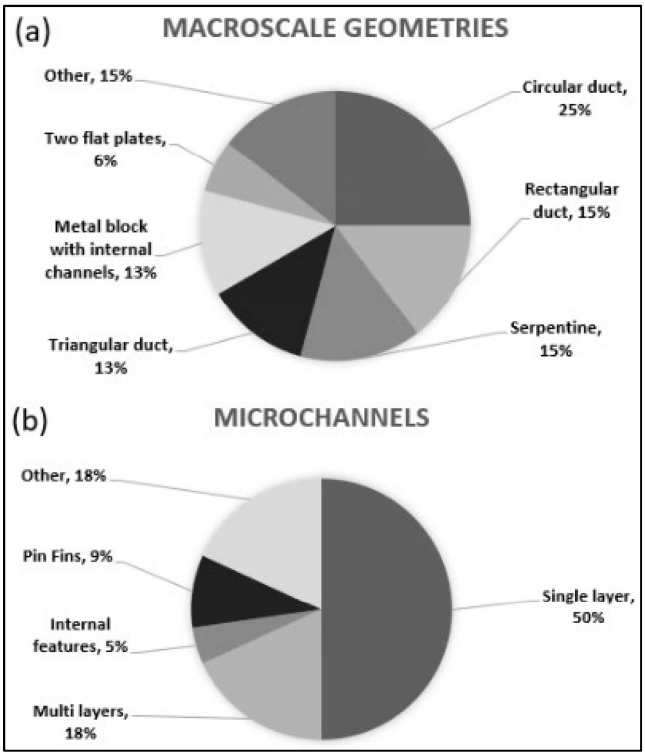

Fig. 2.9: Pie chart showing the percentage of different shapes of heat receivers for heat extraction devices with (a) macroscale channels and (b) microscale channels (Papis-Frączek & Sornek, 2022).

Research on hydrophobic coatings has been conducted to overcome this issue, and the results showed a reduction in pressure drop of 17% (Motamedi et al., 2019). Moreover, using nanofluids may cause corrosion of aluminum channels due to the pH of the fluid (Campos et al., 2019). Furthermore, Ahmed et al., (2020) investigated the performance and temperature limits of a CPVT system. They used three different types of HTFs: water, ethylene glycol and water mixture (60:40), and syltherm oil 800. They found that water was the best cooling fluid in terms of temperature distribution. Therefore, selecting an appropriate HTF is essential to ensure the efficient and reliable operation of CPVT systems.

2.10 Concentration Ratio (*CR*)

A review of previous studies demonstrates that there is no unique definition of the concentration ratio. However, the concentration ratio is often classified into two categories. The first is the geometric concentration ratio. This is defined as the entrance aperture (area of the primary lens) divided by the exit aperture (area of the receiver). The second is the intensity of concentration (suns). This is defined as the ratio of the average intensity of the concentrated light on the active cell area divided by 1000 W/m^2 (0.1 W/cm^2) since peak solar irradiance is usually set at 1000 W/m^2. For example, if 10 W of radiation is focused on a solar cell with a 1 cm^2 active area, the intensity concentration is 100 suns (Swanson, 2003).

2.11 Tracking Systems for CPVT Systems

Although this study focused on the performance of CPVT systems under static concentrators in a controlled indoor environment, the tracking system is an essential component of CPVT systems in real-world applications. CPVT systems often use tracking

systems to increase their energy output and efficiency. A tracking system adjusts the angle of the solar collector to follow the sun's path and maximize the amount of solar radiation collected. There are two main types of tracking systems: single-axis and dual-axis. Single-axis trackers rotate the collector along one axis (usually an east-west axis), while dual-axis trackers adjust the collector's angle horizontally and vertically. Dual-axis trackers are more complex and expensive but can increase electrical energy output by up to 40% compared to a fixed-tilt system (David, 2023). Some tracking systems use sensors and control systems to optimize the collector's angle and minimize shading from nearby objects. However, tracking systems also have disadvantages, including higher installation and maintenance costs and increased susceptibility to wind damage. The choice of tracking system depends on factors such as the local climate, energy demands, and available space.

2.12 Classification of the CPVT Systems

The CPVT system is relatively complex and has not been clearly classified. Sharaf and Orhan, (2015a) proposed three types of CPVT systems based on their focus: CPVT-focused, system integration-focused, and component improvement-focused, as shown in Fig. 2.10. The same figure also shows that the CPVT system can be divided into high-concentration and low-concentration systems.

High-concentration CPVT systems can be further categorized by their concentration shape and level into linear-focus and point-focus systems, as shown in Fig. 2.11. The system can use different types of concentrators depending on the shape of the concentration. For linear focus, the system can use linear Fresnel reflectors, linear Fresnel

lenses, or parabolic trough collectors. For point focus, the system can use parabolic dish collectors, heliostat field central receivers, or point-focus Fresnel lenses.

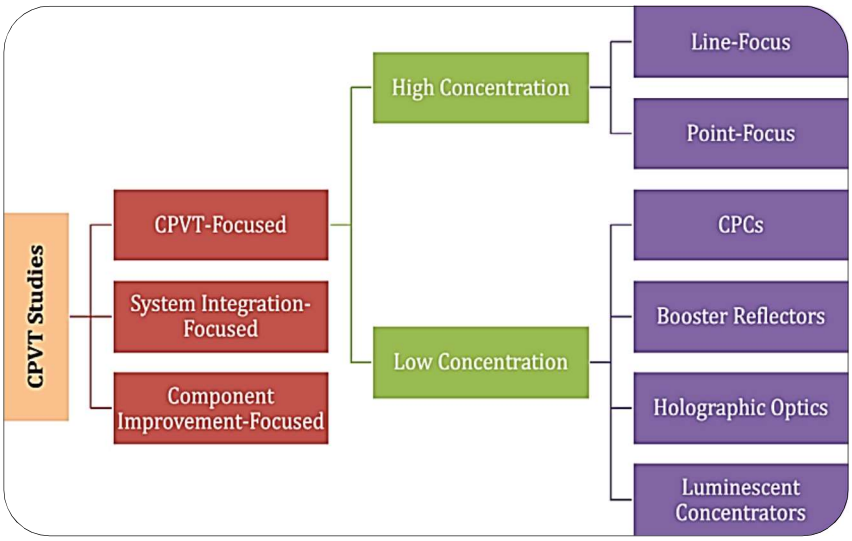

Fig. 2.10: Classification of CPVT systems (Sharaf & Orhan, 2015a)

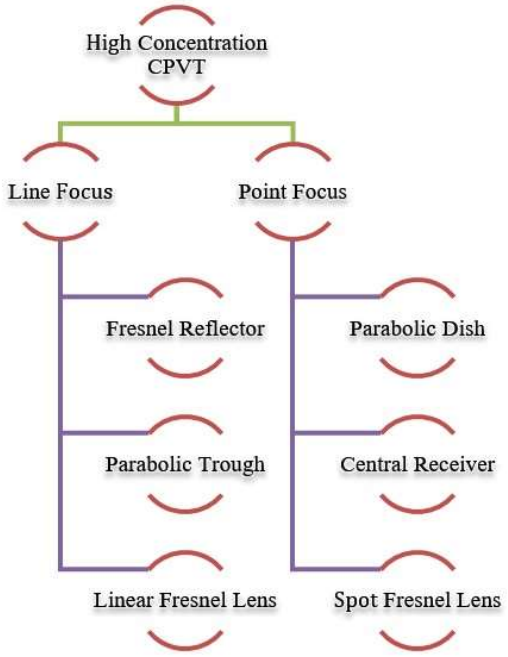

Fig. 2.11: Flowchart illustrating the categories for high-concentration CPVT systems

This study will focus on high-concentration CPVT systems with a point focus. A brief overview of high-concentration CPVT systems with a linear focus will also be provided to enhance understanding and avoid confusion or ambiguity when comparing these systems.

2.12.1 High-Concentration Linear-Focus CPVTs

High-concentration CPVT systems with linear focus include CPVTs based on linear Fresnel reflectors (LFRs), parabolic trough collectors (PTCs), and linear Fresnel lenses (LFLs). These systems use either mirror (reflection) or transparent lenses (refraction) to concentrate solar radiation. LFRs use segments of mirrors to focus solar radiation on a fixed receiver placed at a common focal point of the reflectors. LFLs use lenses that bend (refract) incoming solar radiation to converge toward a common point. LFRs and LFLs can achieve concentration ratios up to 30 times the normal radiation (Dey, 2004; Kaplan et al., 1985).

2.12.1.1 CPVT Based on Linear Fresnel Reflector (LFR)

Researchers at the Australian National University (ANU), in collaboration with Chromasun Inc., have developed an integrated micro-concentrator (MCT) system based on LFRs, as an advancement of the CPVT system concept (MCT, 2011; Vivar, Everett, et al., 2012), as depicted in Fig. 2.12. The MCT has a distinctive feature of being enclosed, which makes it suitable for rooftop integration. The enclosure also protects the internal components of the MCT from environmental factors such as rain, wind, dust, snow, and other weather conditions. This enhances durability, reduces maintenance costs, and prevents optical misalignments (Walter et al., 2010). Moreover, the MCT uses commercially available monocrystalline PV cells to lower costs. The results for the prototype of the MCT installed on the rooftop of a building at the ANU campus showed

that the average electrical and thermal efficiencies were 8% and 50%, respectively, in a full-day test. Similarly, for the instantaneous test, the average electrical and thermal outputs were 280 W and 2400 W, respectively (Vivar et al., 2013).

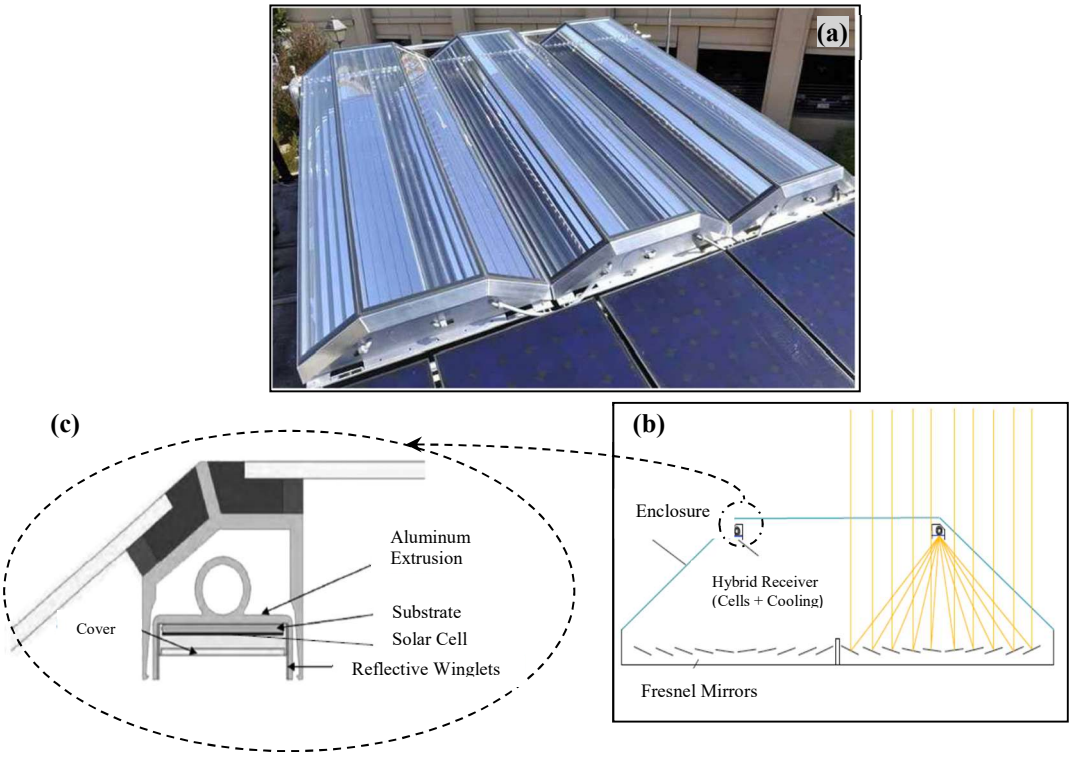

Fig. 2.12: Micro-concentrator MCT-CPVT system: (a) prototype units; (b) schematics of the MCT system with glass enclosure; and two sets of Fresnel mirrors, and (c) a cross-section of the MCT receiver design with PVT details (Vivar et al., 2013)

2.12.1.2 CPVT Based on Parabolic Trough Collector (PTC)

The team of researchers at the Australian National University (ANU) has also developed a hybrid CPVT system, called Combined Heat and Power Solar (CHAPS), based on a parabolic trough collector, as presented in Fig. 2.13. The CHAPS system uses monocrystalline cells attached to aluminum extrusion receivers. The heat transfer fluid (HTF) used is water with anti-corrosion and anti-freeze additives, which is pumped through

an extruded aluminum receiver to cool the PV and produce thermal energy. An outdoor model experiment of the system showed that the outlet HTF temperature is 65 $°C$ while the electrical and thermal efficiency is 11% and 58%, respectively (Coventry, 2005).

Fig. 2.13: Prototype of a CPVT based on PTC at the ANU (Coventry, 2005)

Furthermore, Buffet, (1983) and Gibart, (1981) conducted one of the earliest studies to evaluate the technical feasibility and economic potential of CPVT based on a PTC system. With variable concentration ratios, the results revealed that the electrical efficiency ranged from 6% to 8%, while the thermal efficiency ranged from 46% to 70% (Gibart, 1981). The study also included an expense analysis per year performed on a 500 model (2000 m^2/year), which predicted that the system would have a short payback time of 10.5 to 12.8 years (Buffet, 1983).

2.12.1.3 CPVT Based on Linear Fresnel Lenses (LFL)

A CPVT system based on linear Fresnel lenses, as illustrated in Fig. 2.14, was studied theoretically and experimentally by Kong et al., (2013). They used monocrystalline silicon PV cells and water as the HTF. The researchers found that on a sunny day, the electrical

efficiency was roughly 10%, and the thermal efficiency was roughly 56%. Another CPVT system based on LFL was designed, developed and deployed at Dallas-Fort Worth (DFW) airport in Texas, USA, between 1978 and 1982. O'Neill, (1985) reported on the performance of the system for the first three years of operation. The system consisted of 110 individual concentrator modules and a roof-mounted 245 m^2 concentrator array. It also used a one-axis tracking system to track the sun's motion from east to west, with weekly north-south tilting to decrease the solar declination angle. The system produced 27 kW of DC electricity converted to AC and 120 kW of thermal energy. The electrical energy was mainly used for lighting and running the circulation pump, and the thermal energy was used to provide hot water to a nearby hotel. Moreover, the CPVT system used a glycol/water solution as HTF and had a steel housing to support the lens and receiver and provide an environmental enclosure. The recorded data over three years showed that the electrical efficiency was 7.7%, whereas the thermal efficiency was 39.2%.

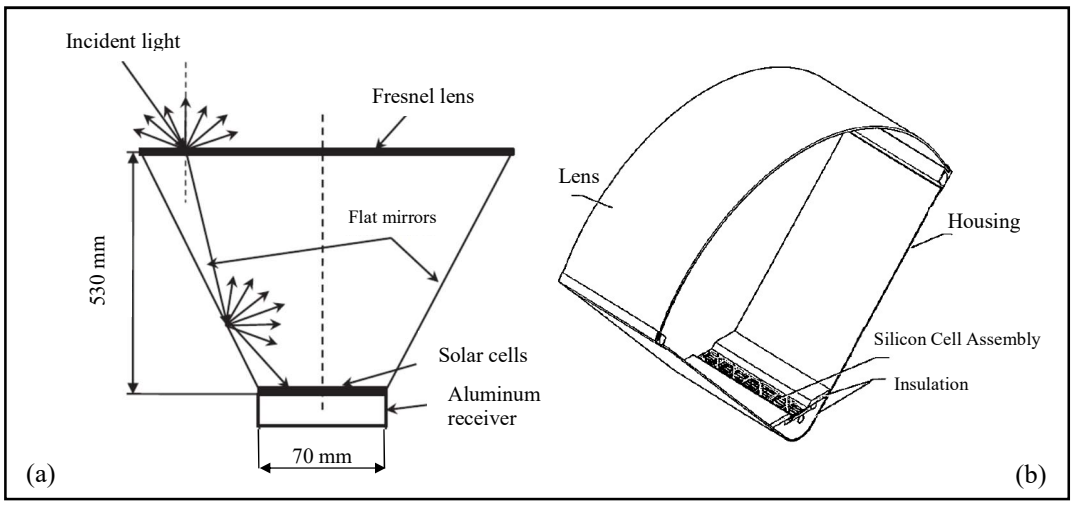

Fig. 2.14: Schematic of a CPVT based on LFL, (a) with two booster mirrors (Kong et al., 2013), and (b) the module that was used at DFW airport (O'Neill, 1985)

2.12.2 High Concentration Point Focus (CPVTs)

High-concentration CPVT systems with point focus include those based on parabolic dish collectors (PDCs), heliostat field central receivers (HFCRs), and spot Fresnel lenses (SFLs).

2.12.2.1 CPVT Based on Parabolic Dish Collectors (PDCs)

A CPVT based on PDC was designed and simulated by Buonomano et al., (2013), which differed from the CPVT based on the parabolic trough concept. The design included a two-axis tracking system to achieve a higher outlet temperature, thus expanding the number of possible applications. The proposed CPVT used multi-junction PV and diathermic oil as HTF. The results showed that the thermal efficiency for the proposed design ranged from 50% to 60%, whereas the electrical efficiency ranged from 19% to 25%. Another design of a CPVT based on PDCs was implemented by (Jiang et al., 2009). They suggested using four parabolic dishes, spectral beam splitters, heat recovery units, and PV receivers with heat sinks, as shown in Fig. 2.15. They developed an electrical and optical model to evaluate the spectral and spatial concentrated flux distribution. The results revealed that the concentrating and beam-splitting optical efficiencies were 66.1% and 78.0%, respectively, while the net electrical efficiency was approximately 18%.

2.12.2.2 CPVT Based on Heliostat Field Central Receivers (HFCRs)

A CPVT based on HFCRs was studied by Segal et al., (2004) ; Segal and Epstein, (1999). They illustrated and analyzed two optical approaches for a large-scale system using beam splitting and pre-illumination PV heat extraction. In the first configuration, a hyperboloidal mirror served as the receiver and beam splitter, which let part of a selected

spectral band reach a PV cell array mounted near the aim point of the heliostat field while reflecting the remaining part of the spectrum and directing it to a series of compound parabolic concentrators (CPCs) placed at the second focal zone below the mirror, equipped with ground thermal receivers, as demonstrated in Fig. 2.16 (a). In the second configuration, the tower consisted of standard mirrors that reflected the solar radiation down into the ground thermal receiver, as depicted in Fig. 2.16 (b) (Imenes & Mills, 2004).

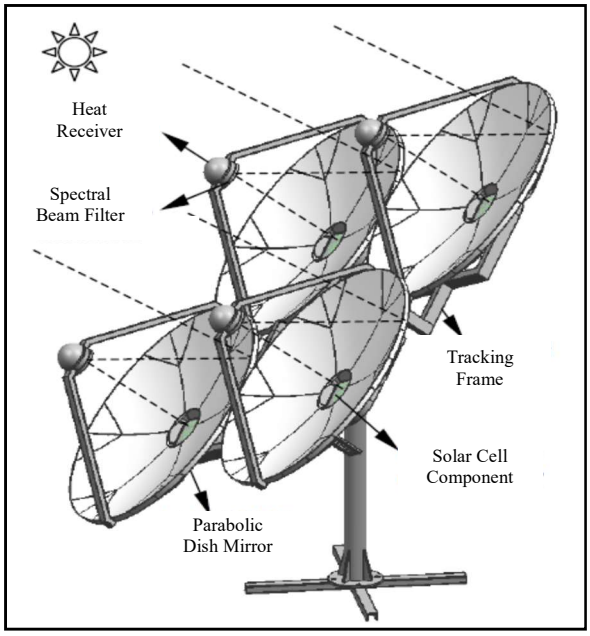

Fig. 2.15: Schematic view of a CPVT based on a PDC system (Jiang et al., 2009)

The solar spectrum was split and filtered through an additional paraboloidal selective mirror before reaching the focal plane. A portion of the spectral band was reflected and directed laterally to a side PV receiver, and the rest of the spectrum was transmitted to the ground receiver. The results show that 55.6 *MW* of solar radiation hit the heliostat field. About 11.4 *MW* that reached the PV cells for the first approach could be converted into

electrical energy. Moreover, about 27.6 *MW* that reached the thermal receiver was available for conversion to thermal energy. In the second configuration, roughly 11.45 *MW* was convertible to electrical energy, and about 26 *MW* could be converted into thermal energy.

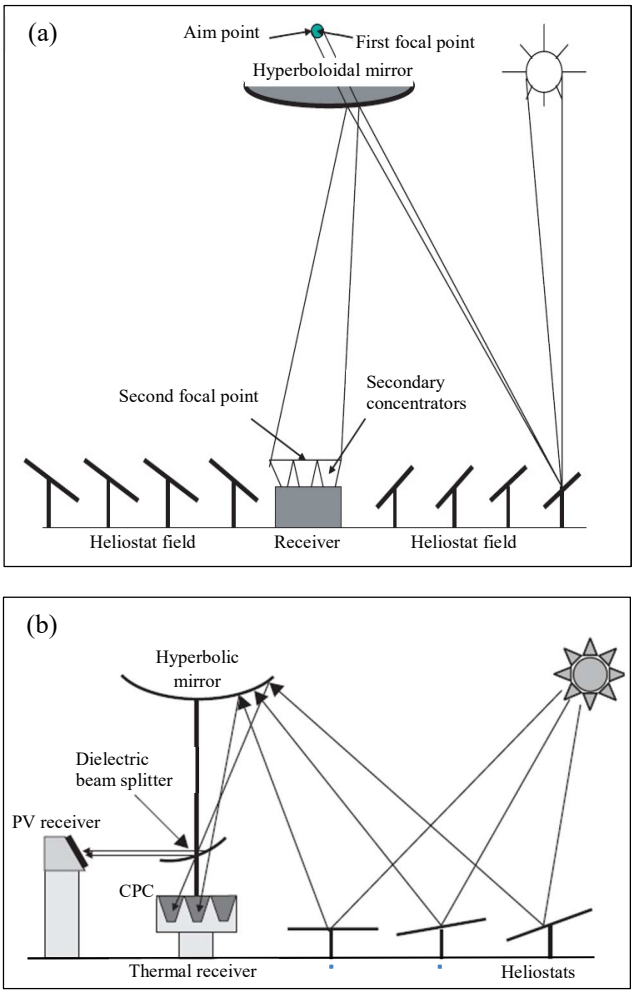

Fig. 2.16: CPVTs based on HFCRs with (a) a hyperboloidal tower reflector system (Segal et al., 2004) and (b) an additional paraboloidal mirror as the beam splitter and a PV array located laterally (Imenes & Mills, 2004)

One of the early studies of the CPVT based on spot Fresnel lenses (SFLs) was conducted by Nakata et al., (1982). They aimed to build a hybrid CPVT with a capacity of 30 *kWp* (5 *kWp* electric and 25 *kWp* thermal energies) for practical applications such as

DHW and air conditioning of a commercial building. The system included a turntable with three concentrator arrays, and a unique design of circular Fresnel lenses with high transmissivity and optical efficiency, to achieve a uniform light distribution on the silicon PV. Water flowed through a copper tube underneath the metal substrate.

Besides, a simplified semi-empirical electrical model for a CPVT based on the spot Fresnel lens system was developed and validated by Mbewe et al., (1985). This model aimed to assess silicon PV cells' performance in both CPV and hybrid CPVT systems. The receiver of the proposed model consisted of a PV cell connected to a flow channel, where an HTF flowed to extract the thermal energy that could be used for industrial or residential applications. The proposed design included several receivers with the same heat removal unit, sun-tracking technique, and a Fresnel lens for each receiver. This study did not address thermal performance, but the electrical model was demonstrated and analyzed under concentrated radiation for the general silicon PV cell. The results showed that the electrical efficiency varied from about 15% to 18% depending on the cell temperature and concentration ratio. The difference between theoretical and experimental results was about 10%.

Ju et al., (2012) developed a simulation model to evaluate the electrical and thermal performance of a hybrid pre-illumination CPVT system. As shown in Fig. 2.17, the proposed design consisted of a Fresnel lens, a spectral beam splitter, a GaAs PV receiver, a thermoelectric generator (TEG) receiver, and two heat sinks. The Fresnel lens concentrated the radiation and directed it to a dichroic mirror, which split the concentrated radiation into two bands based on the wavelengths. The long wavelengths were directed to

a TEG receiver, while the short wavelengths were directed to a GaAs PV receiver. One of the heat sinks was connected to the PV receiver to keep it at a moderate temperature, while the other heat sink attached to the TEG receiver created a significant temperature gradient.

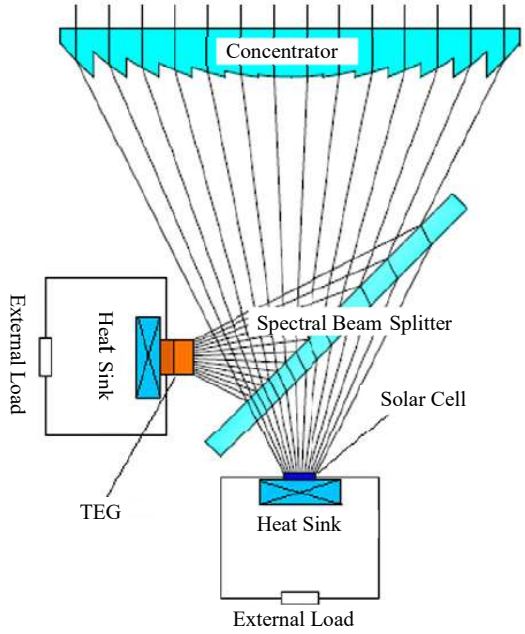

Fig. 2.17: Schematic diagram of a CPVT based on SFLs with a spectral beam splitter and TEG (Ju et al., 2012)

To simulate the system, a one-dimensional (1D) numerical model was established to determine the electrical and thermal performance of the hybrid system. The researchers also studied the effects of specific parameters such as concentration ratio, operating temperatures of the PV and TEG components, spectral response, and heat transfer coefficients on the performance of the entire hybrid system. The results showed that the system's electrical efficiency ranged from 26.62% to 27.49%, depending on the concentration ratio. The researchers concluded that under high concentration ratios, the performance of the new hybrid design was better than that of a PV-only system.

2.13 Applications Areas of CPVT Systems

CPVT systems have emerged as a promising technology for simultaneously generating electricity and thermal energy. The system offers several potential applications catering to various sectors, including commercial buildings, industrial processes, agriculture, remote off-grid areas, solar cooling, and hybrid systems. The following are brief descriptions of a variety of possible applications:

Commercial building: CPVT systems have been installed in various commercial buildings to provide hot water and air conditioning. These systems are cost-effective and efficient in meeting the energy demands of commercial spaces and reducing energy consumption significantly (Cai et al., 2020; Jacob et al., 2022; Lozano-Medina et al., 2019).

Industrial processes: CPVT systems have been integrated into industrial processes, such as food processing, textile, chemical industries, and manufacturing, to provide process heat and steam. These applications have resulted in significant energy savings and reduced greenhouse gas emissions (Ben Youssef et al., 2018; Calise et al., 2014).

Agriculture: CPVT systems have been used in the agricultural sector to provide process heat and dry crops. These systems help to increase crop yield and reduce post-harvest losses (Hussain & Lee, 2023; G. Wu et al., 2019).

Remote off-grid areas: CPVT systems have provided electricity and hot water in remote off-grid areas. These systems are a reliable and cost-effective source of energy for these communities (Abdelhady et al., 2014; Jamal et al., 2020).

Solar cooling: CPVT systems have been used to provide cooling in hot climates. These systems have shown promising results in reducing energy consumption for air conditioning (Buonomano, Calise, & Palombo, 2013; Lin et al., 2020).

Hybrid systems: CPVT systems have been integrated with other renewable energy systems, such as wind and biomass, to provide a more reliable and efficient energy source. These hybrid systems have proven effective in meeting various applications' energy demands (Bamisile et al., 2020; Hosseini & Butler, 2021).

Desalination: Another important application area of the CPVT system is desalination, which is the process of removing salt and other minerals from saltwater to produce fresh water for drinking, irrigation, and industrial use. Desalination is especially important in arid and semi-arid regions with limited or inadequate freshwater resources. CPVT systems can provide electrical and thermal energy for various desalination methods, such as reverse osmosis, multi-effect distillation, or membrane distillation. CPVT systems can also reduce the environmental impact of desalination by reducing greenhouse gas emissions and brine waste (Santana et al., 2023; Z. Zhang et al., 2019).

2.14 Literature Review on CPVT Systems

CPVT technology is not a recent innovation and has been around for several decades. It emerged in the late 1970s and early 1980s (Evans et al., 1978), (Gibart, 1981), (Nakata et al., 1982), (Buffet, 1983), and since then, many CPVT systems have been developed and tested theoretically and experimentally (Kandilli, 2013). The results showed the system has great potential in the energy market sector. However, the system has not advanced beyond the laboratory level worldwide, and more RD&D is needed. Research and development

activities have been conducted on CPVT systems regarding concentrator design, system optimization and performance evaluation. As mentioned before, CPVT systems can be categorized based on the type of concentrator, such as parabolic trough type (PTC) (Coventry, 2005; M. Li et al., 2011), compound parabolic concentrator type (CPC) (Brogren, 2004; G. Li et al., 2014), parabolic dish type (PDC) (Chen et al., 2014; Kribus et al., 2006), linear Fresnel lens type (LFL) (Liu et al., 2014; Rosell et al., 2005), and point-focus Fresnel lens type (PFFL) (Kong et al., 2013; Y. Wu et al., 2012).

There are many review articles on PVT technology and CPV technology in the literature. Zhang and his co-workers wrote a review paper on low-concentration CPVTs. Their article mainly reviewed and discussed PV/T, CPVs, cooling of PVs, beam splitting systems and the effect of non-uniform illumination on PVs (L. Zhang et al., 2012). Vivar et al. reviewed the standards for evaluating the active cooling of CPVs and CPVT and suggested some changes to these standards to suit the hybrid integration of the electrical and thermal components in a CPVT (Vivar, Clarke, et al., 2012). Sharaf and Orhan also conducted an excellent review of CPVT systems (Sharaf & Orhan, 2015a, 2015b). Their study focused on the design considerations and the characteristics of CPVTs and reviewed the essential elements that make up a CPVT.

Furthermore, Amanlou et al., (2016) comprehensively reviewed uniform solar illumination in low-concentration photovoltaic systems. Their paper focuses on how the uniformity of solar illumination on the photovoltaic panel affects the system's electrical performance. They compare different types of reflectors, such as V-type, cylindrical, compound parabolic and linear Fresnel, and evaluate their optical simulation, concentration

ratio, mirror requirement and flux distribution. They also present an experimental study of a photovoltaic/thermal flat collector with and without a linear Fresnel reflector. The results show that the linear Fresnel reflector has the best irradiance uniformity and can improve the thermal and overall efficiency of the system by 16% and 17.5%, respectively. However, a comparative study between line-focus and point-focus Fresnel lenses as solar concentrating systems showed that the point-focus Fresnel lens has slightly better thermal performance than the line-focus (Imtiaz Hussain & Lee, 2016).

Daneshazarian et al., (2018) also reviewed CPVT technology, which included the basic concepts, design and investigation of CPVT solar collectors. They divided CPVT collectors into system elements to show the functionality and roles of the subsystems in the overall system performance. Jacob et al., (2022) reported the recent advancements in CPVT systems and discussed the different types of CPVT systems, such as low-, medium- and high-concentration systems, and their applications in various sectors, such as residential, industrial and agricultural, in their review article. The article also addressed the challenges and opportunities in the thermal management and storage of CPVT systems, such as heat extraction, heat transfer fluids, heat exchangers, phase change materials and thermal energy storage systems. The article highlighted the potential benefits of CPVT systems for clean energy production, carbon emission reduction and economic development.

Papis-Frączek and Sornek, (2022) conducted another review study on heat extraction devices for CPVT systems with active liquid cooling. They compared different types of heat extraction devices used in CPVT systems, such as heat pipes, microchannels, and water jets, and evaluated their heat transfer and system efficiency performance. The review

also emphasized proper system design to achieve optimal heat transfer and cooling performance in CPVT systems. The study offered valuable insights for designing and optimizing heat extraction devices for CPVT systems with active liquid cooling.

In addition, the number of CPVT-related research publications has increased significantly in the past two decades (Coventry, 2005; Mittelman et al., 2007). These studies have carried out design considerations and theoretical and experimental investigations. The results from these studies show that hybrid CPVT systems have unique advantages in entering the energy market. Kribus et al., (2006) presented and analyzed a novel miniature CPVT system that produces electricity and heat from solar radiation. The system uses a small parabolic dish to concentrate sunlight about 500 times on a photovoltaic cell array. A heat transfer fluid is pumped into the array to remove the excess heat from the cells and deliver it to a heat exchanger and storage tank. The system can provide hot water or other forms of thermal energy to a nearby consumer. The system's total efficiency was high, about 80%, with an electrical efficiency of about 20% at low temperatures. The electrical efficiency was gradually reduced at elevated temperatures, but the lost electrical energy was mostly recaptured as thermal energy. Furthermore, the study showed that if the CPV receiver is actively cooled, the additional thermal energy production is attained at almost no extra cost. Moreover, delivering the output heat to the consumer should add no more than 5% to the overall system cost.

Renno and Petito, (2013) developed a theoretical model of a CPVT system for a domestic application. The proposed system uses a point-focus Fresnel lens to concentrate sunlight onto a high-efficiency triple-junction photovoltaic cell, which is actively cooled to

improve electrical efficiency and simultaneously generate hot water. The mathematical model was designed to evaluate the thermal and electrical performance of the system for different time levels and compare it with a traditional system. The paper shows that the fluid outlet temperature of about 90°*C* allows using an absorption heat pump with a CPVT system.

Su et al., (2014) conducted an experimental and numerical analysis of a solar tracking CPVT system using a novel non-dimensional lattice Boltzmann method. They used a small-scale CPVT system with a parabolic dish, with the heat receiver consisting of two photovoltaic panels - one for concentrated solar radiation and the other for non-concentrated radiation and working fluid flowing between these plates. The experiment demonstrated that the electrical efficiency of the water-cooling system improved by about 2.5 times compared to conventional photovoltaic systems. The authors concluded that the non-dimensional lattice Boltzmann method is valuable for simulating and optimizing CPVT system designs.

Renno and De Giacomo, (2014) developed a dynamic model of a coil circuit receiver connected to triple-junction solar cells to determine the outlet fluid temperature for a constant cell operating temperature of 120 °*C* and for changing irradiance conditions. The results showed that the fluid reached a maximum temperature of 75.4 °*C* with a constant PV cell temperature. In contrast, for high irradiance conditions, the outlet temperatures ranged from 60 - 75 °*C* for *CR* = 500X and exceeded 80 °*C* for *CR* = 1000X. A point-focus Fresnel HCPV/T system with triple junction solar cells was tested outdoors by (Xu et al., 2015). The system generated heat and electricity with an electrical efficiency of 28%, and

the overall system efficiency could reach 80% with a maximum thermal efficiency of 54%. A mathematical model was developed to address the challenge of measuring the cell temperature in the system. The effects of different irradiations and cell temperatures on electrical performance were also investigated. The findings indicated that electrical performance was mainly influenced by direct solar radiation.

Imtiaz Hussain and Lee, (2015) studied the effects of varying the fluid flow rate on the maximum power output of a U-shaped heat receiver in a CPVT system. The system includes eight triple junction solar cells, eight Fresnel lenses, dual-axis tracking, and a forced cooling system. They compared the numerical and experimental results of the thermal and electrical power outputs at different flow rates, irradiations, and ambient temperatures. The results showed an optimum flow rate that maximized the CPVT power output at a given irradiation and ambient temperature, around 0.033 *kg/s*. The study also reported a good agreement between the numerical and experimental results with less than a 7% deviation.

Xu et al., (2016) created numerical models for the electrical and thermal performance of a point-focus Fresnel lens HCPVT module. The electrical model used the Shockley diode equation, and the thermal model used a two-dimensional steady-state heat transfer. The models took irradiance, ambient temperature, wind speed, water temperature and mass flow rate as inputs and produced electrical and thermal efficiency as outputs. Outdoor experimental results validated the simulation results of both models. The results indicated that the HCPVT could reach an overall efficiency of 90%, with an electrical and thermal efficiency of 28% and 60%, respectively. Moreover, it was observed that solar irradiation

mainly affected electrical efficiency, and the thermal efficiency increased with the increase of irradiance, ambient temperature and water mass flow rate. The HCPVT module generated hot water at up to 70 $°C$ without significantly reducing the electrical efficiency. In their study, Renno and Petito, (2016) developed a CFD model using ANSYS-CFX to investigate the energy generation potential of various CPVT configurations. The model estimated 28.9% and 23.2% cell efficiencies for sunny and cloudy days, respectively. The study also found that under favourable weather conditions, the average temperature of the solar cells was 63 $°C$, while the fluid temperature was 55 $°C$. Alzahrani et al., (2021) examined the effect of increasing the concentration ratio and the temperature on CPVT components in terms of MJPV and optical concentrator materials. They also discussed the optical, thermal and economic implications. The results showed that higher concentration ratios increased the temperature, which affected the operation, performance and reliability of the CPVT system.

Askari et al., (2022) performed a parametric and intelligent forecasting study on a dish-concentrating CPVT system's energy and exergy performances using six different nanofluids. Two soft computing paradigms, the adaptive neuro-fuzzy inference system (ANFIS) and genetic programming (GP), were used to develop forecasting models. The study investigated the effects of varying the concentration of nanoparticles and the mass flow rate of the nanofluids on the performance of the CPVT collector. The results showed that using nanofluids improved the energy and exergy performances of the CPVT system, and the increase in the concentration of nanoparticles led to an increase in energy efficiency and pressure drop. Su et al., (2022) conducted research to simulate the nanofluid cooling of a CPVT system that uses a dish-shaped concentrator and Al_2O_3-water nanofluid

as coolant. They used a sub-continuous lattice Boltzmann model that considers the nonlinear effects of nanoparticle concentration and size on the effective thermal conductivity and viscosity of the nanofluid. The study compared the nanofluid cooling efficiency with pure water-cooling efficiency under different solar irradiance. They also analyzed the effects of nanoparticle concentration, Knudsen number and Richardson number on the Nusselt number, drag coefficient, power coefficient and fluid temperature of the system. The paper defined an objective enhancement function as the ratio of Nusselt number to power coefficient and found the optimal values of the parameters that maximize this function. The research provides a practical tool for optimal nanofluid cooling enhancement of CPVT solar receivers.

Besides the previous studies, we summarized and compared more than twenty experimental and theoretical studies on CPVT systems based on point focus in Table 2.1.

Table 2.1: Summarizes and compares experimental and theoretical studies on CPVT systems based on point focus.

Extent of Study (Authors)	Primary Concentrator Optics	PV Type	Primary Heat Extraction Concept[1]	Outlet Temperature (°C)	Concentration Ratio[2]	Energy output (W)		Efficiency (%)		Design Distinguishing Features	Nature of Study
						Electrical	Thermal	Electrical	Thermal		
Test prototype (Nakata et al., 1982)	SFL	Si	Water flows through a copper tube below a metallic substrate (P)	NA	50	5000 (T)	25000 (T)	NA	NA	Grid connected complete system with custom designed Fresnel lenses and a hybrid receiver	Description and preliminary analysis of a built prototype
Test prototype (Wong & Dorney, 1983)	SFL	Si	Water flows through copper tube attached below PVs then through a pre-illumination tube above PV cells (D)	29.4 (E)	230	0.0378 (E)	41.5 (E)	0.032 (E)	35 (E)	Water-filled transparent tube for heat extraction and secondary concentration	Thermal and electrical performance assessment
Conceptual design (Bar-Lev et al., 1983)	PDC	NA	Water flows through a two-section polygonal receiver with PV cells attached on its surface (P)	NA	24	NA	NA	NA	NA	Two-section conical receiver with polygonal cross-section	Modifications description
Conceptual design (a) (Boese et al., 1983)	SFL	GaAs	A HTF flows through a passage above the PV receiver with a filters layer in the passage (S)	200-400 (T)	NA	NA	NA	NA	NA	A combination between direct HTF absorption and spectrally selective filters	Description of a conceptual system

1 (P): Post illumination; (S): Pre-illumination using spectral decomposition; (D): Pre-illumination using direct absorption HTF.

2 Geometric concentration ratios if available; flux or effective concentration ratio if not.

E: Experimental; T: Theoretical; NA: Not Available.

Table 2.1 (continued)

Extent of Study (Authors)	Primary Concentrator Optics	PV Type	Primary Heat Extraction Concept[1]	Outlet Temperature (°C)	Concentration Ratio[2]	Energy output (*W*)		Efficiency (%)		Design Distinguishing Features	Nature of Study
						Electrical	Thermal	Electrical	Thermal		
Conceptual design (b) (Boese et al., 1983)	HFCR	GaAs or Si	A central thermal receiver converts solar energy to thermal energy and a cooling circuit is attached to PV cells (P)	NA	~50	NA	NA	NA	NA	PV cells arranged around the thermal receiver to utilize spillage	Description of a conceptual modification
Conceptual design (Mbewe et al., 1985)	SFL	Si	Water flows through a rectangular channel with PV cells attached above it (P)	NA	1-1000	NA	NA	NA	NA	Receivers share the same heat extraction and tracking mechanisms	Electrical modeling and validation of CPV silicon cells
Conceptual design (a) (Segal et al., 2004)	HFCR	Mono-Si	A ground receiver collects non-PV-suitable radiation (S)	NA	500	6844 (T)	27616 (T)	12.3 (T)	49.6 (T)	Hyperboloidal mirror as receiver and beam splitter and CPC boosters	Ray tracing and optical modeling and simulation
Conceptual design (b) (Segal et al., 2004)	HFCR	Mono-Si	A ground receiver collects non-PV-suitable radiation (S)	NA	500	6869 (T)	25995 (T)	12.4 (T)	46.7 (T)	Hyperboloidal mirror as receiver and paraboloidal mirror as beam splitter and CPC boosters	Ray tracing and optical modeling and simulation
Conceptual design (Kribus et al., 2006)	PDC	MJPV	Water flows below a cooling plate with PV cells above it (P)	58 (T)	500	172 (T)	530 (T)	20 (T)	60 (T)	Compact and economic design	Thermal, electrical and economic modeling and performance assessment

Table 2.1 (continued)

Extent of Study (Authors)	Primary Concentrator Optics	PV Type	Primary Heat Extraction Concept[1]	Outlet Temperature (°C)	Concentration Ratio[2]	Energy output (*W*)		Efficiency (%)		Design Distinguishing Features	Nature of Study
						Electrical	Thermal	Electrical	Thermal		
Conceptual design (Jiang et al., 2009)	PDC	Si	HTF circulates through a cavity receiver that receives non-PV suitable solar radiation (S)	NA	80	NA	NA	18 (T)	NA	Optimized beam splitter coated with 38 layers	Ray tracing and spectral and spatial optical modeling and simulation and electrical performance assessment
Operational prototype (Chayet et al., 2010)	PDC	MJPV	Water flows through a microchannel heat exchanger with PV cells soldered to its top (P)	60-85 (E)	629	4500 (E)	11000 (E)	20.5 (E)	70 (E)	Multiple low cost flat mirrors comprise the parabolic dish and microchannel heat exchanger	Thermal and electrical performance assessment
Test prototype (Helmers et al., 2011)	PDC	MJPV	Water flows through a microchannel heat exchanger with PV cells mounted on it (P)	up to 120 (T)	132 - 795	NA	NA	25 (T)	53 (T)	Microchannel heat exchanger	Optical, thermal and electrical performance assessment
Test prototype (Xia et al., 2011)	SFL	GaAs	Water flows through a copper tube that receives infrared solar radiation (S)	NA	30	0.6 (E)	NA	15 (E)	35 (E)	Dual-film broadband holographic optical element	Optical, thermal, and electrical performance assessment
Conceptual design (Ju et al., 2012)	SFL	GaAs	Receiving only the PV suitable band of solar spectrum, a heat sink attached to a PV receiver dissipates heat (S)	NA	770	0.1905 (T)	NA	27.49 (T)	NA	Beam splitter and solar thermoelectric generator	Thermal and electrical modeling, simulation, and parametric studies

Table 2.1 (continued)

Extent of Study (Authors)	Primary Concentrator Optics	PV Type	Primary Heat Extraction Concept[1]	Outlet Temperature (°C)	Concentration Ratio[2]	Energy output (W)		Efficiency (%)		Design Distinguishing Features	Nature of Study
						Electrical	Thermal	Electrical	Thermal		
Conceptual design (Buonomano, Calise, Dentice d'Accadia, et al., 2013)	PDC	InGaP/InGaAs/Ge	Diathermic oil circulates through a serpentine channel embedded within a rectangular planar receiver (P)	150 (T)	33	556 (T)	1389 (T)	19- 25 (T)	50- 60 (T)	High temperature design meant for integration with a double-effect absorption chiller	Thermal and electrical modeling, simulation, and parametric studies
Test prototype (Helmers & Kramer, 2013)	PDC	GaAs	Water flows through a microchannel heat exchanger with PV cells mounted on it (P)	NA	522	125 (E)	350-450 (E)	19.9 (E)	NA	Micro-channel heat exchanger and kaleidoscope homogenizer	Validation of a developed model using a test prototype
Test prototype (Kandilli, 2013)	PDC	Mono-Si	Water flows through vacuum tubes that receive IR and UV radiation from hot mirrors and radiation directly from sun (S)	55 (E)	1797	18.4 (E)	141.2 (E)	15.2 (E)	49.9 (E)	Miniature design with hot mirrors and vacuum tubes	Optical, thermal, and electrical modeling and performance assessment
Conceptual design (Renno & Petito, 2013)	PDC	GaInP/GaAs/Ge	Glycol solution flows through pipes below a cooling plate with PV cells on top of it (P)	90 (T)	900	550 (T)	2500 (T)	20 (T)	69 (T)	CCHP system	Thermal, electrical and economic modeling, performance assessment and parametric studies

Table 2.1 (continued)

Extent of Study (Authors)	Primary Concentrator Optics	PV Type	Primary Heat Extraction Concept[1]	Outlet Temperature (°C)	Concentration Ratio[2]	Energy output (*W*)		Efficiency (%)		Design Distinguishing Features	Nature of Study
						Electrical	Thermal	Electrical	Thermal		
Test prototype (Aldossary et al., 2016)	SFL	GaInP/GaAs/Ge	Water flows through a rectangular cooling channel with PV cells mounted on it (P)	90 (T)	500	20.03 (T)	29.97 (T)	39.5 (T)	NA	In case of active cooling, the bottom side of the MJPV is attached to a rectangular aluminum cooling channel	technical feasibility of passive and active cooling methods for CPV systems in harsh environments,
Test prototype (Al Siyabi, 2019)	NA	GaInP/GaAs/Ge	Water flows through a multi-layered heat sink with PV cells attached above it (P)	37.88 (E)	500	3.535 (E)	16.4 (E)	16 (E)	82.4 (E)	The HCPV-MLM heat sink performance in indoor and outdoor conditions has been examined	Work provides an extensive study on enhancing the CPVT performance using the multi-layer heat sink technique
Test prototype (Chen et al., 2019)	SFL	GaAs	HCPV/T system based on water spray cooling	30 (T)	1000	NA	NA	20-25 (T)	47 (T)	an HCPV/T system based on water spray cooling that uses a point-focus Fresnel lens under a *CR* up to over 1000X	A dynamic model is developed that can perform complete energy flow analysis on the HCPV/T system
Conceptual design (Ahmed et al., 2020)	SFL	GaInP/GaAs/Ge	HCPVT using a mini-channel heat sink with PV cells attached above it (P)	109 (T)	500-2000	NA	NA	40.8 (T)	65.4 (T)	The HCPV/T system uses a finned mini-channel heat sink to increase the heat transfer area	An actively cooled HCPV/T using three types of coolants to increase & optimize the system's performance
Conceptual design (AlFalah et al., 2022)	SFL	MJPV	UHCPV/T using micro-channel heat sinks with PV cells attached above it (P)	71 (T)	500-2500	78.6 (T)	NA	39.86 (T)	63.6 (T)	The UHCPV/T module uses four-pin fin cooling micro-channel heat sinks to increase the heat transfer area	Thermal and electrical modelling are developed for the performance of actively cooled UHCPV/T

2.15 Conclusions

This chapter comprehensively reviews important, relevant topics on CPVT systems. It is worth noting that while some works in the literature are considered CPVT systems, they are actually CPV systems because the extracted thermal energy is wasted and not utilized; these works fall under the category of CPVs with active cooling mechanisms rather than true CPVTs. However, it is important to acknowledge that studies on CPVs with active cooling have played a significant role in developing the CPVT concept, which focuses on utilizing the extracted thermal energy instead of dissipating it.

CPVT systems have received increasing attention from the scientific community and industrial developers. Numerous CPVT systems have been designed, studied, and demonstrated in the literature. Three types of research work on CPVT systems were identified: theoretical studies to analyze fundamental physical and technical aspects, numerical studies to optimize system design and performance, and experimental studies to validate theoretical and numerical observations in real-world conditions. These studies and demonstrations indicate that CPVT systems possess immense potential for market penetration in the energy sector. They offer unique features such as compactness, flexibility, semi-static operation, multi-output generation, high-grade thermal output, high electrical and thermal efficiencies, and a wide range of applications.

Finally, this literature review shows that most previous research on CPVT systems focused on linear concentration focus, including CPVTs based on LFRs, PTCs, and LFLs. The CPVT system based on PFFLs, MJPV cells, heat sink, and active cooling is still immature. More research, investigation, and development work related to these design

considerations is still necessary. Moreover, there are limited reports on high CPVT systems with geometric concentration ratios exceeding 500X and even fewer studies on PFFLs. To the best of the researcher's knowledge, none of the existing studies experimentally and numerically cover the topic of designing and integrating heat receivers, copper heat sinks, MJPVs, PFFLs, and the sun simulator that were designed and manufactured specifically for the present study.

Chapter 3

Experimental Design of the Proposed CPVT Model

3.1 Introduction

CPVT systems offer an attractive option among solar energy technologies as they convert absorbed solar radiation into electrical and thermal energy. This chapter presents the development of an experimental facility for a CPVT model based on PFFL concentrators as optical elements. The CPVT model is equipped with high-efficiency GaInP/InGaAs/Ge multi-junction solar cells, copper heat sinks, an absorber tube serving as an active cooling system, and a sun simulator to experimentally investigate the thermal and electrical performance under different concentration ratios and at various HTF flow rates. This chapter also discusses the experimental techniques used to perform the above investigations. Moreover, it explains the standard classification for solar simulators, the technical parameters of the PFFLs, and the electrical characteristics of the MJPV solar cell. In addition, it describes the calibration of the measuring devices and the uncertainty analysis.

3.2 Description of the Indoor CPVT Model

As stated in Chapter 1, the experimental model of the CPVT based on PFFLs used in this work was designed and built locally at the Thermofluid Laboratory of the Mechanical Engineering Department, Memorial University of Newfoundland. The schematic diagram

of the experimental setup is shown in Fig. 3.1. Appendix A includes test fixture specifications.

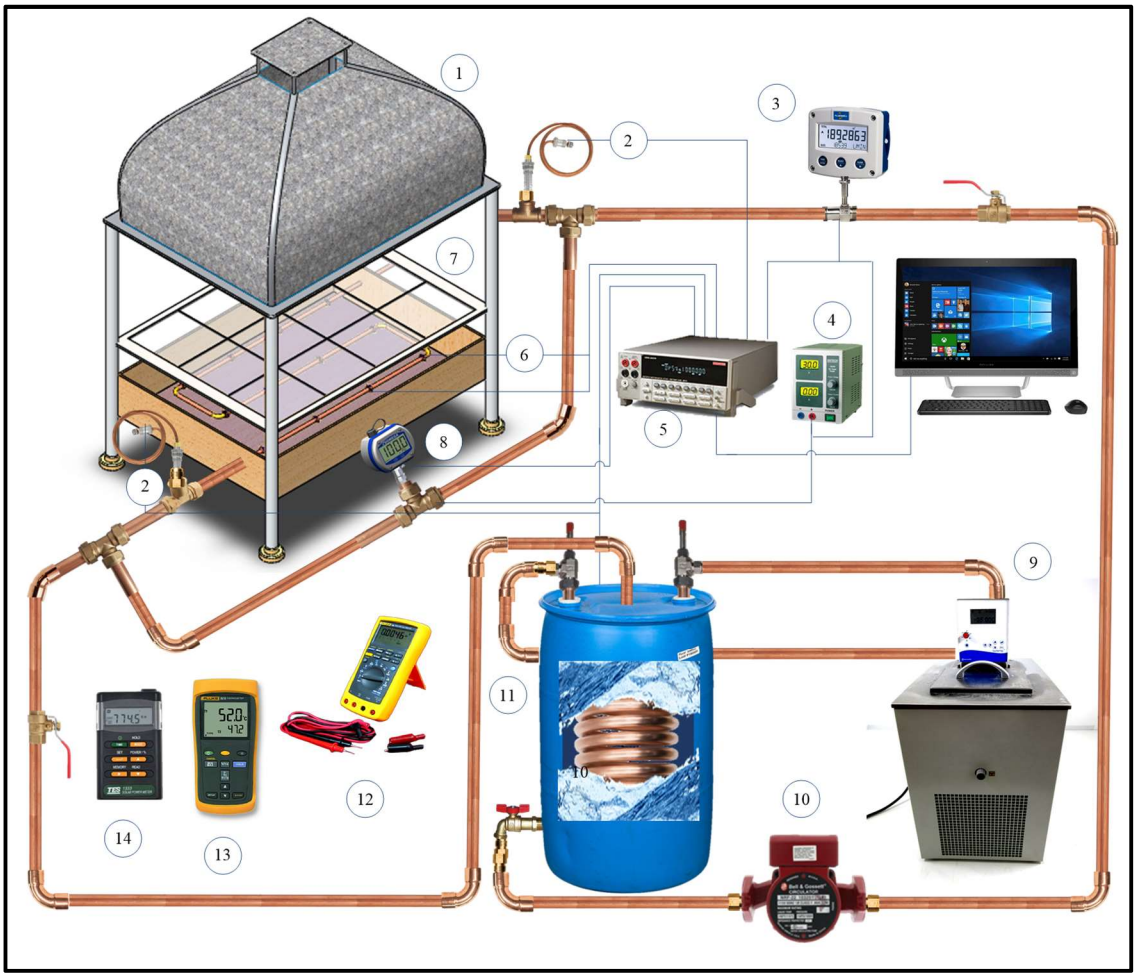

Fig. 3.1: Schematic diagram of the CPVT system based on PFFL. 1: Sun simulator, 2: Thermocouples, 3: Flow meter, 4: Power supply, 5: DAQ, 6: MJPV & Heat sinks, 7: PFFL, 8: Differential pressure transducer, 9: Thermal bath, 10: Pump, 11: Tank and heat exchanger, 12: Multi-meter, 13: Digital thermometer, 14: Solar meter.

The CPVT model mainly consists of a sun simulator, PFFLs, MJPV solar cells, heat sinks, and a flow loop containing a 1/2-inch copper pipe. The researchers also used other instrumentation and materials, such as a data acquisition system (DAQ), a solar meter, a

flow meter, thermocouples, a differential pressure transducer, a thermal bath, a circulation pump, a tank and heat exchanger, a variable resistor, epoxy adhesive glue, a thermal insulator, a multimeter (voltmeter, ammeter), wires, a power supply, and a computer.

3.2.1 Solar Simulator

A solar simulator is an invaluable tool for conducting experimental characterizations of solar systems in a controlled indoor laboratory environment. Indoor testing with a solar simulator helps overcome the challenges of outdoor testing, where parameters such as solar radiation intensity, ambient temperature, and wind velocity can vary significantly with time, affecting repeatability. Indoor testing, which simulates solar radiation intensity and climate, is conducted under controlled environmental conditions that enable researchers to run tests more efficiently and with greater precision and repeatability than outdoor tests. By utilizing indoor testing with a solar simulator, experimental work can be completed in a shorter time, and results can be easily repeated for more accurate analysis and interpretation.

Indoor thermal and electrical testing can be implemented using a continuous solar simulator. However, unlike conventional PV systems, the CPVT system integrating Fresnel lens and MJPV solar cell is very demanding in terms of incident light collimation, uniformity, and spectral match, which makes the commercial solar simulator very expensive for this research. Therefore, we designed and built a solar simulator specifically for this project. We have considered the simplicity and the cost while taking into account the aforementioned characteristics. Figure 3.2 shows a photo of the test facility with the solar simulator and measuring devices.

Fig. 3.2: A photo of the test facility with the solar simulator and measuring devices

Solar simulator light sources can be classified into two main categories: continuous sources and pulsed sources. A continuous light source ensures a consistent and uninterrupted illumination output over a specified period. On the other hand, a pulsed source delivers the desired intensity within a brief duration by intermittently activating the light source. The tungsten halogen lamp has been chosen as the light source for the developed solar simulator. It is widely used in solar beam experiments for solar simulator

applications because it provides a very stable and smooth spectral output (Pedrotti et al., 2017; Skoog et al., 2017; Tawfik et al., 2018). Moreover, their wavelength ranges between 200-2600 *nm* (Esen et al., 2017), which is similar to sunlight, especially in terms of thermal radiation. It is inexpensive and requires only simple power supply units. The experiment utilized an Ushio Lighting FEL $120V$ $1000W$ G9.5 BULB, which belongs to the category of tungsten halogen lamps. These lamps consist of a tungsten filament that emits light when an electric current passes through it. The filament is enclosed within a halogen gas, such as bromine or iodine. Figure 3.3 illustrates the specific halogen lamp employed in the experiment.

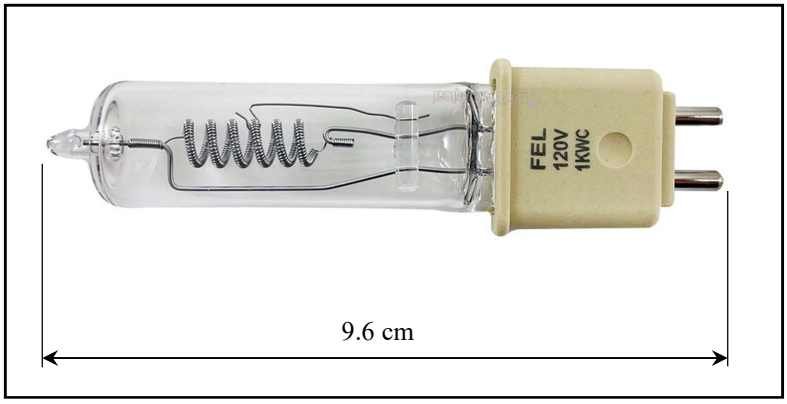

Fig. 3.3: A photo of the tungsten halogen lamp

According to the standard classification for solar simulators for electrical performance testing of photovoltaic devices ASTM E927-19 (ASTM-E927, 2019), the radiation source to be used as a solar simulator should be within four classes, namely: class A, class B, class C, and class U (unclassified) as shown in Table 3.1.These classes are determined based on three main tests: light spectral match, spatial non-uniformity and temporal instability. We

measured the temporal instability of simulator light according to ASTM E927-19 standards by recording the irradiance values over a fixed time interval and using the following equation (ASTM-E927, 2019) to calculate the temporal instability:

Table 3.1: ASTM E927 – 19 Classifications of Solar Simulators (ASTM-E927, 2019)

Classification	Characteristics		
	Spectral Match (All intervals)	**Spatial Non-Uniformity of Irradiance**	**Temporal Instability of Irradiance**
Class A	0.75 - 1.25	≤ 2 %	≤ 2 %
Class B	0.60 - 1.40	≤ 5 %	≤ 5 %
Class C	0.40 - 2.00	≤ 10 %	≤ 10 %
Class U	> 2.00	≤ 10 %	≤ 10 %

$$T_{IE} = \frac{(I_T)_{max} - (I_T)_{min}}{(I_T)_{max} + (I_T)_{min}} \times 100 \tag{3.1}$$

Where T_{IE} temporal instability, $(I_T)_{max}$ and $(I_T)_{min}$ are the maximum and minimum measured values of the irradiance, respectively. Table 3.2 presents the temporal instability calculated using equation (3.1) for three sampling times. The maximum temporal instability is 8.97% when using a sampling time of 30 seconds. Therefore, based on these findings, the light source can be classified as C.

The lamp supplier suggested that the lamp operation temperature should be under 350 $°C$. Therefore, a fan was installed to blow air over the lamp to reduce the lamp surface temperature and ensure effective lamp cooling. The operating lamp surface temperature with cooling was measured using an IR camera, as depicted in Fig. 3.4. From Fig. 3.4, it can be seen that the lamp's surface temperature is approximately 150 $°C$, below the

recommended temperature, ensuring that the experiment was conducted safely. However, using a solar simulator involves various other safety hazards, including electrical hazards due to high voltages during start-up, harmful ultraviolet radiation to the skin and eyes, and high pressure inside some lamps that may cause them to burst. Moreover, handling some lamps carefully and avoiding touching the glass surface with bare hands is important to prevent uneven heating and potentially shorten their lifespan.

Table 3.2: Temporal instability of the solar simulator light at three test sampling times

Data sampling time (10 seconds)			
Irradiance I_T (W/m^2)		Temporal instability T_{IE} (%)	Classification
Max	855.04	8.82 %	C
Min	716.46		
Data sampling time (20 seconds)			
Irradiance I_T (W/m^2)		Temporal instability T_{IE} (%)	Classification
Max	858.63	8.66 %	C
Min	721.78		
Data sampling time (30 seconds)			
Irradiance I_T (W/m^2)		Temporal instability T_{IE} (%)	Classification
Max	862.27	8.97 %	C
Min	720.32		

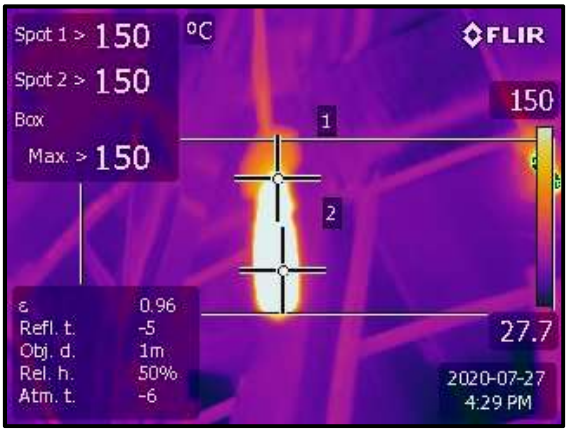

Fig. 3.4: IR image of the lamp within the solar simulator

3.2.2 Fresnel Lenses

Using Fresnel lenses as the primary optical element in the CPVT systems is a promising technology for increasing the solar radiation intensity on solar cells, thus reducing the system's capital cost. As stated in Chapter 2, Fresnel lenses can be classified based on their symmetry into point-focus or linear-focus lenses. Also, they can be classified based on the requirement of image reproduction into Imaging and Non-imaging, as demonstrated in Fig. 3.5. An imaging Fresnel lens creates a clear image of the light source. Still, its production requires high quality and precision, making it more expensive and complex. A non-imaging Fresnel lens focuses the light beam from the source to a target point without making any image of the source. This type of lens has many advantages for CSP technology, such as large acceptance angles, higher tolerances in manufacturing and operation, less need for accurate tracking, and misalignment compensation (Kumar et al., 2015).

Currently, Fresnel lenses have experienced an improvement in quality as a result of advancements in modern plastics, new moulding techniques, and computer-controlled diamond turning. These developments in the manufacturing process have enabled the creation of Fresnel lenses suitable for various applications. It is now possible to produce Fresnel lenses through compression moulding, injection moulding, cutting, or extrusion using various plastic materials (Leutz & Suzuki, 2001). Compression moulding has proven to be the most effective method for creating high-performance point-focus Fresnel lenses (Swanson, 2003).

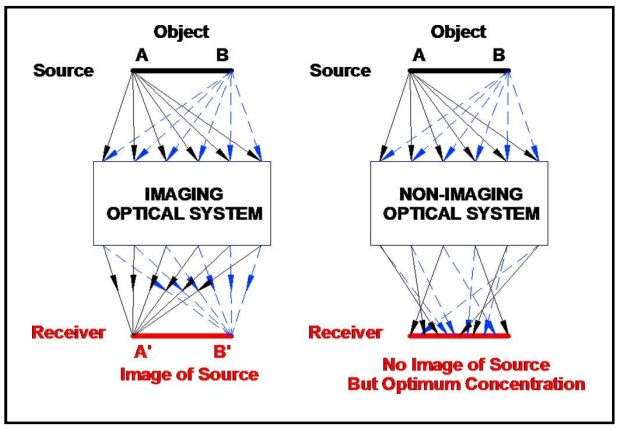

Fig. 3.5: Schematic diagram of an imaging and non-imaging optical system (Kumar et al., 2015)

The PFFLs used in this research were obtained from Fresnel Factory Inc., a company specializing in Fresnel lenses since 2002, formerly known as DiYPRO Co., Ltd. The technical parameters of the lenses are listed in Table 3.3 (Fresnel Factory, 2019). The active area of the Fresnel lens is 0.0784 m^2, while the MJPV (receiver) has an area of 0.0001 m^2. Hence, the resulting geometrical concentration ratio (*GCR*) is 784X representing the maximum concentration ratio (*CR*) achievable without optical losses. We placed 12 PFFLs in an array of 3×4, and to support, align, and adjust the proper focal length of the Fresnel lenses, we designed and fabricated a movable lens holder, as previously shown in Fig. 3.2

Table 3.3: Technical parameters of the PFFLs

Parameter	Value
Fresnel lens size (mm^2)	280×280
Focal length (*mm*)	330
Thickness (*mm*)	4
Groove pitch (*mm*)	0.5
Transmissivity (%)	92%
Material	PMMA

3.2.3 Multi-junction Photovoltaic Solar Cell

12 FULLSUNS Triple-Junction Photovoltaic solar cells, made of GaInP/InGaAs/Ge with an active area of 100 mm^2 for each cell, were employed for indoor experimental testing in the CPVT system. The solar cell had a typical electrical conversion efficiency of about 40.34% under standard controlled lab conditions using a flash simulator, with the following measurement conditions: radiation of 100 W/cm^2, MJPV temperature of 25 $°C$, and air mass (AM) of 1.5G. Table 3.4 reports the performance of the MJPV cell at the indoor flash test with concentration ratios of 500X and 1000X, including the following parameters: I_{SC} (short-circuit current), V_{OC} (open-circuit voltage), I_m (maximum current), V_m (maximum voltage), P_m (maximum power), and FF (fill factor). Figure 3.6 displays the actual MJPV solar cell used in the experiment (FULLSUN, 2020).

Table 3.4: Characteristics of the MJPV solar cell at the indoor flash test

CR	***I_{SC} (A)***	***V_{OC} (V)***	***I_m (A)***	***V_m (V)***	***P_m (W)***	***FF (%)***	***Eff (%)***
500X	7.563	3.121	7.289	2.823	20.577	87.18	41.15
1000X	15.015	3.235	14.502	2.782	40.345	83.06	40.34

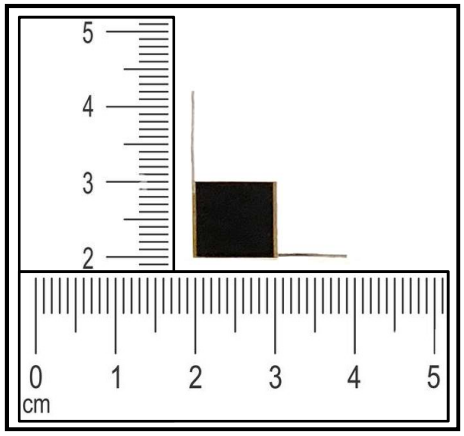

Fig. 3.6: Photograph of the MJPV solar cell used in the experiment

3.2.4 Heat Receiver

The heat receiver is a key component of the thermal management system in the CPVT model. It is widely known that the efficiency of PV cells decreases not only due to the high operating temperature but also because of the non-uniform temperature distribution over the PV cells. The integration of an active cooling system with the backside of the MJPV cells, apart from increasing the system's electrical efficiency, makes the surplus heat available for utilization in other applications. This experiment used a circular cooling channel in a serpentine configuration arrangement to extract the heat from the MJPV cells using distilled water as HTF. The cooling channel is made of a 1/2-inch copper pipe and requires a flat plate absorber to mount the MJPV cells because of its shape. Therefore, 12 copper heat sinks (adapters) were designed and machined to provide a flat surface for cell mounting and a round shape on the backside for attachment to a copper pipe flow loop.

Moreover, we pasted the MJPV cells onto the copper heat sinks using OB-101 Epoxy adhesive (a highly thermally conductive and electrically insulating glue). We also aligned the solar cells with their respective Fresnel lenses at the focal length. Figure 3.7 shows the top-section view of the heat receiver (the cooling channel and heat sinks), along with the MJPV cells and the PFFLs.

3.3 Measurement Equipment

The experimental setup consisted of the required instrumentation for measuring the quantities necessary to characterize the overall performance of the CPVT model. The following sections describe the equipment and instrumentation used to measure the relevant

quantities. However, the measuring devices used were previously illustrated in Figs. 3.1 and 3.2.

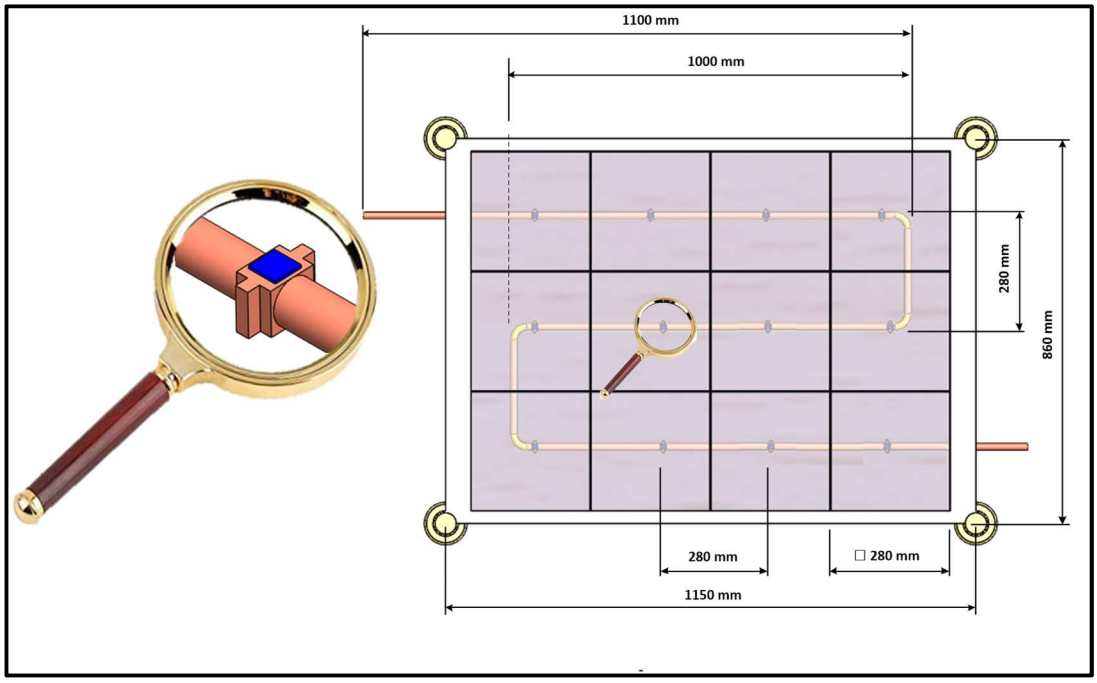

Fig. 3.7: Top-section view of the heat receiver in the CPVT model

3.3.1 Data Acquisition System

The raw data from various sensors/transducers were collected and recorded by a Keithley 2700 data acquisition system (DAQ) and stored in a connected PC. The Keithley 2700 DAQ can measure and control up to 80 channels of signals. It has a built-in multimeter that can measure voltage, current, resistance, frequency, and temperature. It also has a graphical user interface allowing users to configure, monitor, and analyze the data. The thermocouples, flow meters, and pressure transducer were connected to the DAQ.

3.3.2 Radiation Measurements

The solar radiation intensity falling on the Fresnel lens surfaces was measured and stored by a TES 1333 solar power meter. The solar power meter is a compact, rugged and easy-to-operate instrument. It uses a very stable detector as the solar-sensitive component. The meter can display the solar radiation in W/m^2 or $Btu/(ft^2 \cdot h)$ units. It also has data hold, max/min/avg, data memory and RS232 interface functions. Appendix B provides the product features and specifications.

3.3.3 Volumetric Flow Rate Measurements

An oval gear flowmeter (OGF) from FLOMEC (model OM006H513-222RS) was used to measure the volumetric flow rates of the HTF. The flowmeter ranged from 0.0083 to 0.45 *gpm* and was calibrated by the manufacturer. A Tee-Type filter from Swagelok was installed before the flowmeter to protect it from foreign particles that may be suspended in the fluid.

3.3.4 Temperature Measurements

Copper-constantan (Cu- CuNi) or T-type thermocouples from Omega were used for temperature measurements in this experiment. Two rugged pipe plug thermocouples were employed to measure the inlet and outlet temperatures. One thermocouple was used to measure the ambient temperature and another to measure the tank temperature. In addition, 36 thermocouples were used to measure the inlet, outlet, and surface temperatures for each MJPV cell in the model. U-shaped grooves were made on each heat sink to accommodate the thermocouples for measuring the surface temperature of the MJPV cell. The

thermocouple readings were checked for accuracy within ±0.1℃ using a constant temperature bath and an ice/water mixture. Finally, all temperature signals were logged by the DAQ system and monitored by a PC.

3.3.5 Pressure Measurements

The pressure drop on the CPVT model was measured using an Omega differential pressure transducer, DPGM409-350HDWU, which has a range of 0 to 5 *psi* and a corresponding voltage output of 0 to 5 *Vdc*. The manufacturer performed the sensor calibration. All measurements were taken when the CPVT model was in a horizontal position.

3.3.6 Thermal Bath

To regulate the inlet temperature of the HTF, a constant temperature bath was utilized in the testing facility. Specifically, a Fisher brand 6200 R35 constant temperature bath was employed for this purpose. With an impressive cooling capacity of up to 800 *W* and temperature stability of ±0.05℃, this bath ensures a consistently maintained inlet coolant temperature. It is capable of providing volumetric flow rates of up to 5.5 *gpm* and has a fluid capacity of up to 2.27 gallons. The bath was connected to a copper coil that was submerged within the working fluid reservoir, acting as a heat exchanger to sustain a stable inlet temperature for the working fluid.

3.3.7 Thermophysical Properties of the HTF

Due to its tremendous advantages, ordinary water is one of the most popular working fluids in heat engineering. Distilled water was used as the HTF in the experiments. The

equations for water properties are taken from (POPIEL & WOJTKOWIAK, 2007) and are listed below. The temperatures are specified in degrees Celsius, and are within the range from 0 to 150 °C. All fluid properties were evaluated at the average of the measured inlet and outlet temperatures.

$$\rho = a + bT + cT^2 + dT^{2.5} + eT^3 \tag{3.2}$$

$$C_p = a + bT + cT^{1.5} + dT^2 + eT^{2.5} \tag{3.3}$$

$$k = a + bT + cT^{1.5} + dT^2 + eT^{0.5} \tag{3.4}$$

$$\mu = \frac{1}{a + bT + cT^2 + dT^3} \tag{3.5}$$

The values of the constants *a*, *b*, *c*, *d*, and *e* are given in Table 3.5.

Table 3.5: Constants for the formulas of the thermophysical properties of Water.

	a	***b***	***c***	***d***	***e***
ρ	999.79684	0.068317355	-0.010740248	0.00082140905	-2.3030988×10^{-5}
C_p	4.2174356	-0.0056181625	0.0012992528	-0.00011 535353	4.14964×10^{-6}
k	0.5650285	0.0026363895	-0.00012516934	-1.5154918×10^{-6}	-0.0009412945
μ	557.82468	19.408782	0.1360459	-3.1160832×10^{-4}	-

3.3.8 Experimental Procedures

The experiments were performed to obtain data for experimental performance analysis, both thermal and electrical. A typical test run consisted of the following steps:

- The test module was assembled, and all instruments and equipment were connected. The electrical and the flow loop connections were connected, and the focal points of the Fresnel lenses were adjusted and aligned with the MJPVs. All connection tubes and heatsinks were insulated to minimize heat loss to the surroundings.
- The DC power supply, DAQ system, and PC were switched on. The coolant that flows within the heat exchanger was initiated by switching on the thermal bath until it reached the desired initial temperature.
- A Bell & Gossett circulation pump was used to circulate the HTF within the flow channel at a temperature of 15 $°C$ for 30 minutes to ensure the temperature of the pipe, the heat sinks, and MJPVs were uniform at this initial temperature and to remove any trapped air from the loop and ensure there was no leakage before starting the experiments.
- To protect the solar cells from any sudden increase in their temperature, the HTF was circulated at a temperature of 15 $°C$ and at the desired flow rate, then the solar simulator was switched on. The experiment was monitored to reach the temperature steady state condition. The steady-state was achieved when the temperature variations in all thermocouple's measurements were less than 0.2 $°C$ or the test reached a half hour of the run, whichever came first.
- Once the system was stabilized, the TES 1333 solar power meter was used to measure the solar radiation falling on the surfaces of the Fresnel lenses. The data was recorded by switching the DAQ to the scanning mode.

- The HTF flow rate was set to a starting value of 0.00131 *kg/s*, which was then increased incrementally by approximately 0.002 *kg/s*. This procedure was repeated until the maximum flow rate attainable was reached.
- The data consisted of inlet and outlet temperatures of the HTF, inlet and outlet temperatures of each heat sink, the surface temperature of each MJPV, ambient temperature, voltage, current, pressure drops, and mass flow rates. These data were saved in Excel files and then averaged to be used in the data reduction procedure.
- All required HTF properties, such as density, thermal conductivity, heat capacity, and viscosity, were evaluated at the average bulk temperature. Figure 3.8 shows a picture of the flow channel equipped with MJPV cells and heat sinks during the test run.

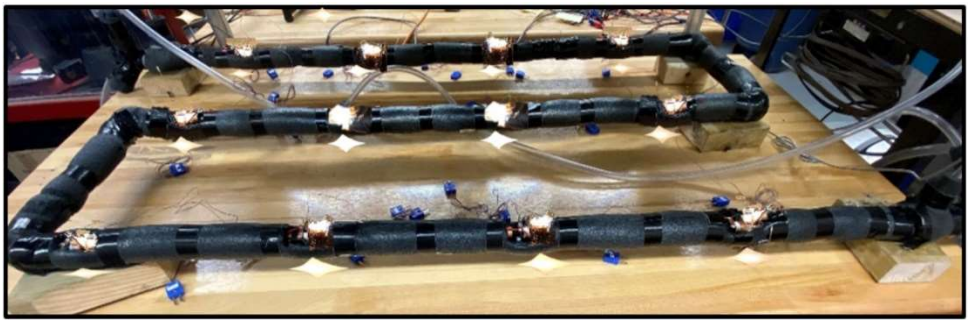

Fig. 3.8: A photo of the heat receiver during the test run

3.4 Benchmark Test

Benchmark tests were conducted to validate the accuracy of the measuring instruments. Benchmarking is a practical way to measure the performance of experimental methods by using theoretical data. We benchmarked the experimental apparatus by obtaining the friction factor in a pipe. This test ensured the accuracy of the pressure transducer, flow

meters, and data acquisition system. The pressure drop tests were performed using distilled water on a 1.81 *m* straight copper pipe with a 7.6 *mm* diameter over a wide range of flow rates. The best-known theoretical Fanning friction factor (*f*) was employed to evaluate the experimental equipment's uncertainty and the measurement setup's quality. The flow regime was laminar and fully developed, considering the operational conditions. Comparing experimental results and well-established theories guaranteed a proper testing procedure. The volumetric flow rate and Reynolds number are defined as follows:

$$\dot{\mathrm{v}} = \frac{\pi}{4} D^2 U \tag{3.6}$$

$$Re = \frac{DU}{\nu} \tag{3.7}$$

Where D is the pipe diameter, U is the average velocity, and ν is the kinematic viscosity. The Hagen-Poiseuille equation, Eq. (3.8), is a physical law that computes the pressure drop of a Newtonian and an incompressible flow through a long and circular tube with a constant cross-sectional area. The pressure drop is a function of friction factor (f), fluid density (ρ), pipe geometries (D and L), and averaged velocity (U) as:

$$\Delta P = 2f \left(\frac{L}{D}\right) (\rho U^2) \tag{3.8}$$

According to Fanning's theory, the friction factor for smooth round tubes is often taken as:

$$f = \frac{16}{Re} \tag{3.9}$$

Figure 3.9 shows the variation of friction factor versus Reynolds number for distilled water at the room temperature of 20 ℃. The results reveal that the collected experimental data are within the ±10% range of the theoretical Fanning model. This precise measurement also shows insignificant effects of surface roughness on the results.

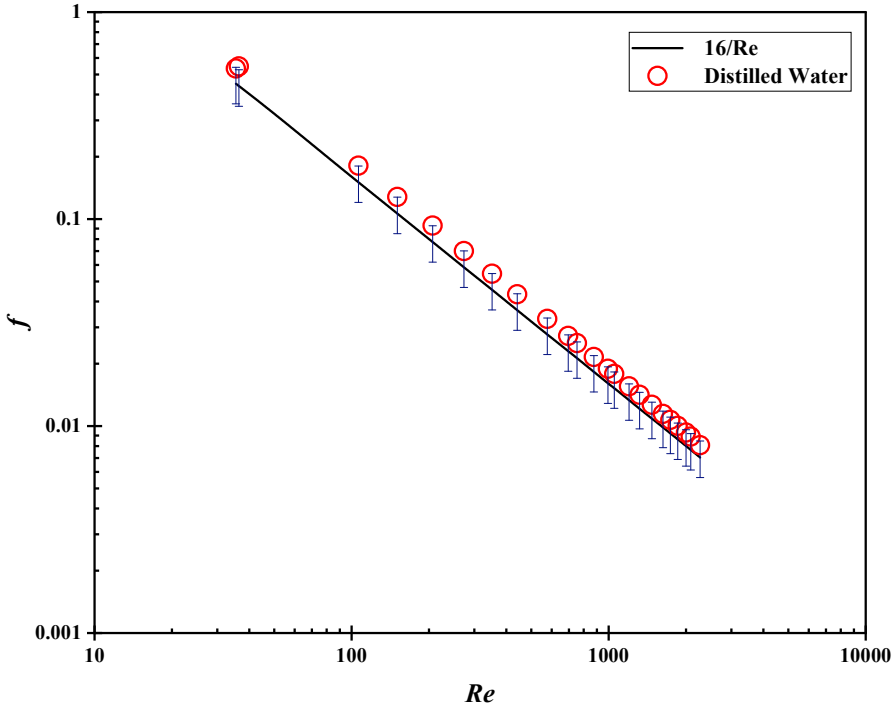

Fig. 3.9: Pressure drop benchmarking test using distilled water with 10% error bars

3.5 Experimental Uncertainty

The uncertainty is a numerical estimation representing the potential error range within a measurement. It is vital in accurately assessing and interpreting experimental data by minimizing discrepancies. Uncertainty encompasses the degree of confidence in experimental measurements, ranging from a lack of certainty to a complete absence of information. Our experiments utilized various measuring equipment, including thermocouples, flowmeter, pressure transducer, solar power meter, digital multimeter, and

thermal bath. The manufacturers of these instruments have specified the uncertainties associated with their measurements, as outlined in Table 3.6.

We employed the method proposed by Kline and McClintock, F. A., (1953) to analyze uncertainty. This approach allows for a comprehensive assessment of the uncertainties present in various parameters such as temperature differentials (ΔT), mean temperature (T_m), flow rates, Reynolds numbers (Re), friction factor (f), heat transfer, and Nusselt numbers (Nu). The uncertainties in these parameters depend on the accuracy of temperature, flow rate, and pressure measurements, as well as uncertainties in the thermo-physical properties of the working fluids.

Table 3.6: Uncertainties of experimental instruments

Equipment	**Measurement**	**Uncertainty**
Thermocouple	Temperature [℃]	± 0.1 ℃
Flowmeter	Flow rate [gpm]	± 1.0 %
Pressure transducer	Pressure [Pa]	± 0.08 %
Solar power meter	Radiation [W/m^2]	± 5.0 %
Digital multimeter	Voltage [V]	± 0.01 %
Digital multimeter	Ampere [A]	± 0.01 %
Thermal bath	Temperature [℃]	± 0.1 ℃

A summary of the uncertainty analysis results can be found in Table 3.7, while detailed information regarding the methodology is provided in Appendix C. These analyses help us to understand the possible errors and uncertainties in our experimental measurements and to interpret the data more accurately. Table 3.7 presents the uncertainty analysis establishing a range of overall uncertainty for each parameter. The results displayed in Table 3.7 reveal that specific parameters exhibit high uncertainty, primarily attributed to

the small temperature difference (less than 1.5 °C) between the inlet and outlet of the HTF. Consequently, this leads to increased uncertainties in ΔT and Nu. Moreover, the low flow rate also had high uncertainty because it was below 10% of the full-scale reading, which was the recommended limit by the manufacturer.

Table 3.7: Relative uncertainties of various parameters

Parameters	Uncertainty	Parameters	Uncertainty
ΔT	0.83/12.29 %	Re	4.64/5.48 %
T_m	0.30/0.41 %	f	5.15/12.90 %
Flow rate	2.55/12.93 %	Q	12.54/13.29 %
Nu	13.89/14.45 %	A_c	0.70 %

3.6 Experimental Limitations

The CPVT model is a novel approach to combining photovoltaic and thermal energy conversion in a single system. However, the model also faces some experimental challenges that must be addressed before practical implementation. One of the main challenges is to ensure the system's integrity and longevity by identifying the maximum working temperature of the materials comprising the system, such as the PV cells, the glues, the insulating materials, and the boiling point of the HTF. These materials have different thermal properties and tolerances and may degrade or fail when exposed to high temperatures. Researchers can effectively assess the system's performance and reliability under various operating conditions by determining these limitations. This knowledge is essential when designing CPVT models, as it allows for the identification of potential weak points and the implementation of appropriate mitigation strategies.

Chapter 4

Theoretical Background of the Proposed CPVT Model

4.1 Introduction

This chapter presents the theoretical background and the heat transfer analytical correlations of the proposed CPVT model, which is a novel hybrid system that combines photovoltaic and thermal energy conversion. We first introduce the theory and governing equations that describe the physical processes involved in the CPVT system, such as solar radiation, heat transfer, and electrical output. Then, we perform thermal and electrical analyses to evaluate the performance and efficiency of the CPVT system under different operating conditions.

4.2 Energy Balance Equations

The steady-state analysis is considered in this study, and thus, the solar flux striking the MJPV surface over a period of time is taken as constant. The model assumes that the absorbed solar radiation in the solar cells that is not converted to electricity is converted to thermal energy. This thermal energy is conveyed between the front and back surfaces of the MJPV cells via conduction. At the front surface, the heat is lost to the surroundings by natural convection and radiation, while at the rear surface, the heat is transferred to the heat sink via conduction. To assess the performance of the CPVT model, conducting an energy balance analysis for each layer of the CPVT components is important. An energy balance

analysis is based on determining the input and output energy flows and the energy content change of an arbitrary control volume. The general three-dimensional energy balance equation is as follows:

$$\frac{\partial Q(x,y,z)}{\partial t} = Q_{in} - Q_{out} \tag{4.1}$$

The energy input for the CPVT model is due to incident solar radiation, while energy output includes thermal losses from the CPVT model, heat flow into the HTF, and electrical energy. Assuming steady-state operation, the energy balance for the CPVT model becomes:

$$Q_{in} = Q_{heat} + P_{ele} \tag{4.2}$$

$$Q_{in} = Q_{th} + Q_{n/c} + Q_{rad} + P_{ele} \tag{4.3}$$

Where $\frac{\partial Q}{\partial t}$ is the change in internal energy, Q_{in} is the heat transfer rate into the system and represents the solar radiation flux that reaches the MJPV cell surface in (W), Q_{out} is the heat transfer rate out of the system, Q_{hea} and P_{ele} are the amounts of energy that are converted to heat and electrical power, respectively in (W). Q_{th} is the thermal energy absorbed by HTF in (W), $Q_{n/c}$ is the natural convection heat transfer rate in (W), and $Q_{rad}$is the surface-to-ambient radiation energy in (W).

Figure 4.1 displays a zero-dimensional CPVT configuration schematic to illustrate the fundamental energy flows for the CPVT model, from input solar radiation to final useful outputs. As we can see, part of the total incident energy q_{irr} on the MJPV solar cell is lost as optical losses, while the remainder is converted into two forms. The first portion is

converted to electrical power, while the remainder is converted into heat. A portion of this heat is transferred to the HTF by convection, while the rest is transferred to the ambient by natural convection and radiation.

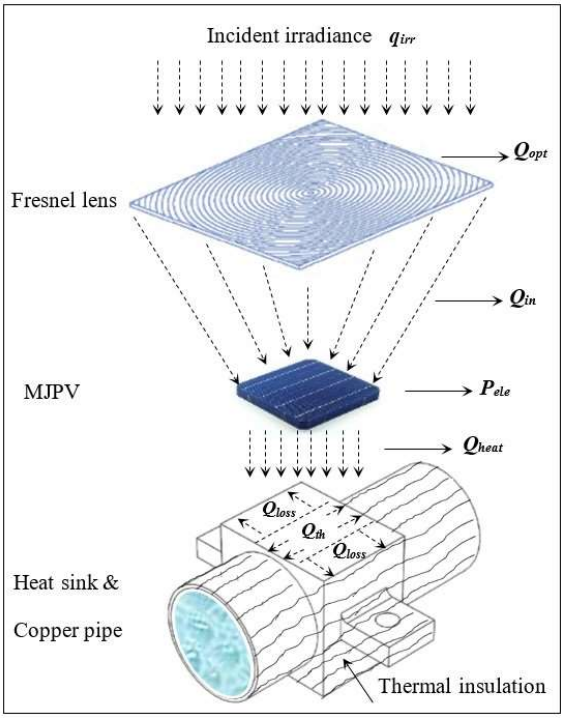

Fig. 4.1: A schematic diagram of the energy flow process in a part of the CPVT model

4.3 Thermal and Electrical Analysis

The thermal analysis is developed by using the applicable heat transfer processes by constituting energy balance equations between the interacting nodes. In this section, a mathematical model that describes the thermodynamic energy performance of the CPVT model was developed. To facilitate the theoretical analysis, we have adopted the following assumptions:

1. The CPVT system is in a quasi-steady state.
2. The material properties of MJPV are homogeneous and isotropic.
3. The MJPV solar cell was modelled as one homogeneous cell, and the other sub cells were not considered.
4. The internal reflections within the transparent layers of the MJPV were neglected.
5. The flow is incompressible.
6. The thermal properties of the HTF are constant.
7. The radiation is concentrated uniformly along the area of the MJPV cells.
8. Fresnel lenses are free from manufacturing errors.

The solar radiation flux can be evaluated from the following relation:

$$Q_{in} = q_{irr} \times CR \times A_{pv} \tag{4.4}$$

Where q_{irr} is the solar radiation flux in (W/m^2), A_{pv} is the solar cell area in (m^2), and CR is the maximum concentration ratio of the CPVT model and is calculated as follows (Renno & Petito, 2016):

$$CR = \frac{A_{Fr}}{A_{pv}} \times \eta_{opt} \tag{4.5}$$

Here A_{Fr} represents the Fresnel lens area in (m^2), and η_{opt} is the optical efficiency of the concentrator, typically around 80%−90% (Shanks et al., 2016).

The following equation can be used to calculate the amount of energy that converts to heat (Aldossary et al., 2016):

$$Q_{heat} = Q_{in} \times (1 - \eta_{sc}) \tag{4.6}$$

Where η_{sc} denotes the electrical efficiency of the MJPV cell, which can be determined using the equation (Evans & Florschuetz, 1977; Skoplaki & Palyvos, 2009):

$$\eta_{sc} = \eta_{ref}[1 - \beta_{ref}(T_c - T_{ref})] \tag{4.7}$$

Where η_{ref} represents the cell's electrical efficiency at the reference temperature T_{ref}, typically taken as the ambient temperature of 25 °C. T_c is the solar cell temperature, and β_{ref} is the temperature coefficient of the MJPV solar cell (β_{ref} = 0.047 %/K). The values of η_{ref} and β_{ref} are usually provided by the solar cell manufacturer.

The thermal energy absorbed by HTF is expressed as:

$$Q_{th} = \dot{m} C_p (T_{out} - T_{in}) \tag{4.8}$$

Where $\dot{m}$, represents the mass flow rate in (*kg/s*), C_p is the specific heat in (*J/kg·K*), and T_{in} and T_{out} are the inlet and outlet temperatures of the HTF, respectively. The forced convection heat transfer coefficient inside the pipe ($W/m^2.K$) can be calculated as follows:

$$h = \frac{Q_{th}}{A(T_w - T_m)} \tag{4.9}$$

Here A is the contact area between the inner pipe surface and HTF (m^2), T_w is the average wall temperature of the pipe (K), and T_m is the average mean temperature of HTF (K). The Nusselt number can be calculated as:

$$Nu = \frac{hD}{k} \tag{4.10}$$

Where D is the pipe diameter (m), and k is the thermal conductivity of the HTF ($W/m.K$). The thermal efficiency can be calculated as follows:

$$\eta_{th} = \frac{Q_{th}}{Q_{in}} \tag{4.11}$$

The electrical efficiency of the MJPV cell is influenced by the concentration ratio and the cell operating temperature, and it can be expressed as (Renno & Petito, 2015):

$$\eta_{sc} = \eta_{ref} + \frac{d\eta}{dT} \times \left(T_c - T_{ref}\right) \tag{4.12}$$

Here η_{ref} is the reference efficiency corresponding to the concentration value, according to the cell manufacturer, and T_{ref} is the reference temperature equal to 25 $°C$. The factor $\frac{d\eta}{dT}$ for $CR > 30$ is equal to:

$$\frac{d\eta}{dT} = -0.09167 + 0.005787 \times \ln(CR) \tag{4.13}$$

The solar radiation flux received by the MJPV cell and converted into electrical power is determined as follows:

$$P_{ele} = Q_{in} \times \eta_{sc} \tag{4.14}$$

Considering the system losses, the electric efficiency of the CPVT system can be calculated as follows:

$$\eta_{ele} = \eta_{sc} \times \eta_m \times k_t \tag{4.15}$$

Where η_m is the module efficiency, which is 0.9 for up to 100 cells, and k_t is the thermal coefficient that shows the percentage reduction of the electricity produced by the system at a given operating temperature, and it can be calculated as:

$$k_t = 1 + \beta_{ref} \times (T_c - 25) \tag{4.16}$$

4.4 Theory and Governing Equations

The thermal performance analysis of the CPVT system involves heat transfer by conduction, convection, and radiation. A fraction of the heat is transferred within the solid layers of the MJPV solar cell by conduction, and the rest of the heat is lost to the surrounding environment by convection and radiation. Figure 4.2 shows a one-dimensional side view of the CPVT assembly, with steady-state energy balance and boundary conditions. The longitudinal section of a single cell consists of incident irradiance, MJPV, adhesive glue layer, heat sink, copper pipe, HTF, and thermal insulator. According to (Chou et al., 2012), the structure of the MJPV has a thin top (GaInP) and middle (GaInAs) subcell compared to the bottom (Ge) substrate. Moreover, the (Ge) layer absorbs long-wavelength photons (870 *nm* - 1950 *nm*) and usually receives the most irradiation. Therefore, the MJPV

solar cell can be modelled as one homogeneous Germanium cell (Ge), which does not affect the junction temperature.

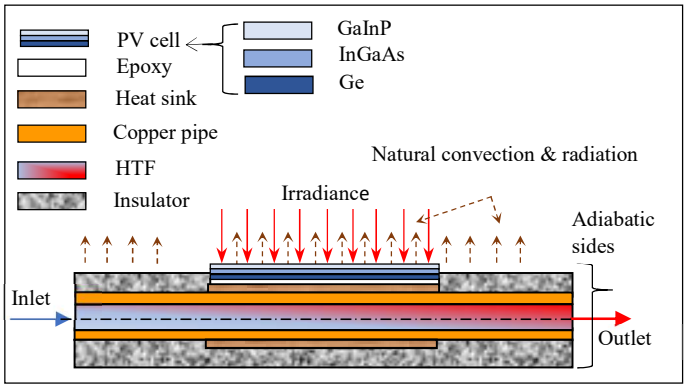

Fig. 4.2: Schematic description of CPVT assembly layers

The steady state heat conduction within the MJPV assembly to the top surface of the copper pipe is defined by Fourier's law as follows (Bergman et al., 2020):

$$Q_{cond} = -kA\nabla T \tag{4.17}$$

Where Q_{cond} is the conduction heat transfer rate (W), A is the layer area (m^2), k is the thermal conductivity of the layer material ($W/m.K$), and ∇T is the temperature gradient. The heat generated by solar energy conversion will be either collected by HTF from the CPVT assembly or lost to the environment by convection and radiation.

According to Theristis and O'Donovan, (2015), the heat transfer by natural convection can be described as:

$$Q_{n/c} = hA\Delta T \tag{4.18}$$

Where $Q_{n/c}$ is the natural convection heat transfer rate (W), h is the natural convection heat transfer coefficient ($W/m^2.K$), and ΔT is the temperature difference between the surface and the ambient (K). The MJPV is placed horizontally, so it can be modeled as a horizontal plate with uniform heat flux facing upward. The concentrated light heats up the fluid near the top surface of the MJPV, creating a natural convection flow. Therefore, the heat transfer by natural convection from the upper surface of the MJPV is correlated for ($1 < Ra < 10^{10}$) by the equations presented below (Warren M. et al., 1998):

$$Nu^T = 0.835\overline{C}_l Ra^{1/4} \tag{4.19}$$

$$Nu_l = \frac{1.4}{ln(1 + \frac{1.4}{Nu^T})} \tag{4.20}$$

$$Nu_t = C_t^U Ra^{1/3} \tag{4.21}$$

$$Nu = ((Nu_l)^m + (Nu_t)^m)^{1/m} \qquad m = 10 \tag{4.22}$$

Where Nu^T is the average "thin-layer-solution" Nusselt number for laminar flow. Nu_l is the average Nusselt number taken over MJPV, assuming laminar heat transfer dominates. Nu_t is the average Nusselt number taken over MJPV, assuming turbulent heat transfer dominates, and $\overline{C}_l, C_t^U$ are approximately universal function of Prandtl number with values of 0.515, 0.14 respectively (Warren M. et al., 1998). R_a is the Rayleigh number, which is defined as follow:

$$R_a = \frac{g\beta\Delta T L_c^3}{\upsilon\alpha} \tag{4.23}$$

Where β is the coefficient of volumetric thermal expansion (K^{-1}), g is the gravitational acceleration (m/s^2), α is the thermal diffusivity (m^2/s), and υ is the kinematic viscosity (m^2/s).

The natural convection heat transfer coefficient h can be expressed as follows:

$$h = \frac{Nu\ k}{L_c} \tag{4.24}$$

Here k is the thermal conductivity of the air ($W/m.K$), and L_c is the characteristic length (m) defined as $L_c = A/P$ where A, and P are the surface area and the perimeter of the MJPV, respectively.

The radiation heat transfer can be calculated from the following relations:

$$Q_{rad} = \varepsilon\sigma A(T_s^4 - T_a^4) \tag{4.25}$$

Where Q_{rad} is the radiation heat-transfer rate (W), ε is the emissivity of the solar cell material, σ is the Stefan Boltzmann constant (5.67×10^{-8} $W/m^2.K^4$), T_s is the surface temperature (K), and T_a is the ambient temperature (K). It is worth noting that A in the equations for natural convection and radiation denotes the area of the MJPV and the area of the exposed part of the heat sink.

The energy flow and the equivalent thermal circuit corresponding to the CPVT assembly layers, and the surroundings are shown in Fig. 4.3.

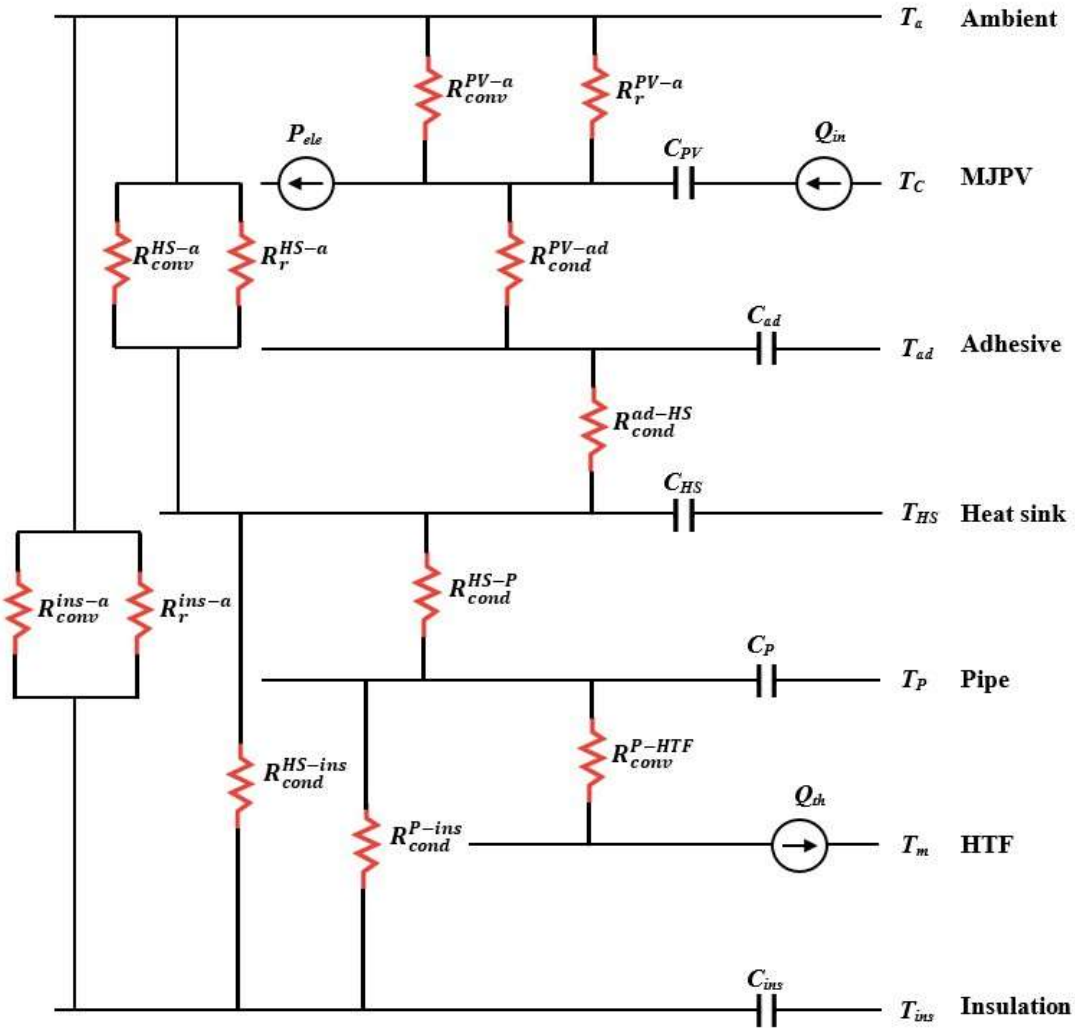

Fig. 4.3: Equivalent thermal resistance circuit for the CPVT assembly layers

Based on the assumptions mentioned earlier, the following dynamic energy balance equations for each layer were derived. For each node of the thermal network, i.e., for each material of the CPVT assembly layers, the thermal-balance equation has the general form:

$$M_i C_i \frac{\partial T_i}{\partial t} = \sum_j Q_{in} - \sum_k Q_{out} \tag{4.26}$$

Where M and C represent the mass and specific heat of the material, respectively, Q_{in} and Q_{out} denote the heat transfer rate into and out of the system, respectively. The heat flows Q is related to the temperatures of consecutive nodes using the equation:

$$Q = \frac{T_i - T_{i+1}}{R_{th,i-i+1}} \tag{4.27}$$

Here, R represents the thermal resistance between consecutive nodes. Each node in the thermal system is positioned at the mid-thickness of the material layer, so the thermal resistance between nodes is calculated as half the sum of the thermal resistances of consecutive layers:

$$R_{i-i+1} = \frac{R_i + R_{i+1}}{2} \tag{4.28}$$

Considering the solar cell as the control volume, the inflow energy flux is caused by the absorbed, concentrated solar radiation. The outflow energy flux consists of heat dissipated to the surroundings by convection and radiation, heat transferred to the thermal adhesive by conduction, and the electric energy output, resulting in:

$$\rho_{PV} A_{PV} \delta_{PV} C_{PV} \frac{\partial T_{PV}}{\partial t} = Q_{in} - \left[\frac{T_{PV} - T_a}{R_r^{PV-a}} + \frac{T_{PV} - T_a}{R_{conv}^{PV-a}} + \frac{T_{PV} - T_{ad}}{R_{cond}^{PV-a}} + P_{ele} \right] \tag{4.29}$$

Considering the thermal adhesive as the control volume, the inflow energy flux is from the solar cell by conduction, and the outflow energy flux is to the heat sink by conduction, resulting in:

$$\rho_{ad} A_{ad} \delta_{ad} C_{ad} \frac{\partial T_{ad}}{\partial t} = \left(\frac{T_{PV} - T_{ad}}{R_{cond}^{PV-ad}}\right) - \left(\frac{T_{ad} - T_{HS}}{R_{cond}^{ad-}}\right) \tag{4.30}$$

Considering the heat sink as the control volume, the energy flux entering the system is from the thermal adhesive by conduction. The energy flux leaving the system consists of heat dissipated from the upper surface to the surroundings by convection and radiation, as well as the heat transferred to the pipe and insulating material by conduction, yielding:

$$\rho_{HS} A_{HS} \delta_{HS} C_{HS} \frac{\partial T_{HS}}{\partial t} = \left(\frac{T_{ad} - T_{HS}}{R_{cond}^{ad-H}}\right) -$$

$$\left[\left(\frac{T_{HS} - T_P}{R_{cond}^{HS-P}}\right) + \left(\frac{T_{HS} - T_{ins}}{R_{cond}^{HS-ins}}\right) + \left(\frac{T_{HS} - T_a}{R_r^{HS-a}}\right) + \left(\frac{T_{HS} - T_a}{R_{conv}^{HS-a}}\right)\right] \tag{4.31}$$

Considering the pipe as the control volume, the inflow energy flux is from the heat sink by conduction, and the outflow energy flux is to the HTF by convection and to the insulating material by conduction, yielding:

$$\rho_P A_P \delta_P C_P \frac{\partial T_P}{\partial t} = \left(\frac{T_{HS} - T_P}{R_{cond}^{HS-P}}\right) - \left[\left(\frac{T_P - T_m}{R_{conv}^{P-HTF}}\right) + \left(\frac{T_P - T_{ins}}{R_{cond}^{P-ins}}\right)\right] \tag{4.32}$$

Taking the HTF as the control volume, the inflow energy flux comes from the pipe through convection, and the outflow energy flux is the heat gained by the HTF flowing through the pipe, resulting in:

$$\rho_{HTF} A_{HTF} \delta_{HTF} C_{HTF} \frac{\partial T_{HTF}}{\partial t} = \left(\frac{T_P - T_m}{R_{conv}^{P-HTF}}\right) - \dot{m}_{HTF} C_{HTF} (T_{out} - T_{in}) \tag{4.33}$$

Taking the insulator as the control volume, the energy flux entering the system is from the heat sink and the pipe by conduction, and the energy flux leaving the system is the heat dissipated to the ambient by convection and radiation, yielding:

$$\rho_{ins} A_{ins} \delta_{ins} C_{ins} \frac{\partial T_{ins}}{\partial t} = \left[\left(\frac{T_{HS} - T_{ins}}{R_{cond}^{HS-i}}\right) + \left(\frac{T_P - T_{ins}}{R_{cond}^{P-ins}}\right)\right] - \left[\left(\frac{T_{ins} - T_a}{R_r^{ins-a}}\right) + \left(\frac{T_{ins} - T_a}{R_{conv}^{ins-a}}\right)\right] \quad (4.34)$$

4.5 Primary Energy-saving Efficiency

One of the challenges of evaluating the performance of the CPVT system is to compare its thermal and electrical outputs, which have different energy grades according to the second law of thermodynamics. Therefore, simply adding the outputs or the efficiencies does not give a meaningful measure of the system's performance (Huang et al., 2001; Sharaf & Orhan, 2015a). Several methods have been suggested to solve this problem, such as using a Carnot factor, an electrical-to-thermal ratio, or a primary-energy saving (PES) efficiency. These methods aim to convert the thermal output or efficiency to an equivalent electrical output or efficiency or to account for the difference between the outputs or efficiencies.

The Carnot factor is based on the system's temperatures and converts the thermal efficiency to an equivalent electrical efficiency. Otanicar et al., (2010) used this method in their CPVT model and assumed a Carnot factor of 0.5. The electrical-to-thermal ratio is based on the energy or exergy analysis of the renewable energy market and converts the thermal and electrical energies to equivalent electrical energy. Coventry and Lovegrove,

(2003) proposed this method and varied the ratio from 1 for a simple energy analysis to 17 for an exergy analysis. They also found that the best method was based on the renewable energy market and used financial data levelized cost of electricity (LCOE) to find the ratio. For a flat plate PV/T system with amorphous silicon solar cells, the ratio was 4.24.

$$E_{eq,ele} = \frac{Q_{th}}{\delta} + P_{ele} \tag{4.35}$$

$E_{eq,ele}$ is the equivalent electrical energy, Q_{th} the thermal and, P_{ele} the electrical energy produced, and δ is the electrical-to-thermal ratio. This method is interesting but complex and not well explained. Moreover, the example of the flat plate PV/T system differs significantly from the CPVT system. Therefore, a third method has been used, which divides the electrical and thermal efficiencies by two factors to give more weight to the electrical output. The term primary energy saving (PES) is used for this method, which considers the difference between thermal and electrical efficiencies. It is defined by Huang et al., (2001) as:

$$\eta_{PES} = \frac{\eta_{ele}}{\eta_{pri\rightarrow e}} + \frac{\eta_{th}}{\eta_{pri\rightarrow th}} \tag{4.36}$$

Where η_{ele} and η_{th} are the electrical and thermal efficiencies of the CPVT system, the term $\eta_{pri\rightarrow e}$ is the electric power generation efficiency of a conventional power plant and equals 0.4. At the same time, $\eta_{pri\rightarrow th}$ is the thermal efficiency of a conventional gas-fired domestic hot water system and was assumed to be 0.65 (Santbergen, 2008).

4.6 Pumping Power in the CPVT System

The pumping power required for various flow rates in CPVT systems is an important aspect to consider in system performance analysis. The pumping power depends on several factors, such as the flow rate, the pressure drop, the pipe diameter, and the HTF properties. Although turbulent flow dissipates heat more effectively than laminar flow, it also causes a pressure drop in the flow channel, ultimately leading to higher power consumption to run the pump. The required pumping power to overcome the pressure loss can be calculated using the following equation (Y. Cengel & Cimbala, 2013):

$$P_{pump} = \dot{V} \times \Delta P \tag{4.37}$$

Where $\dot{V}$ is the volume flow rate, and ΔP is the pressure drop.

Chapter 5

CFD Analysis of the Proposed CPVT Model

5.1 Introduction

Numerical analysis using computational fluid dynamics (CFD) is a powerful tool to investigate the performance and optimization of CPVT systems under various conditions. CFD can provide detailed information on flow patterns, temperature distributions, heat transfer coefficients, pressure drops, and the efficiency of CPVT systems. CFD can also help evaluate the effects of different design parameters, such as concentration ratio, geometry, and material properties. This chapter aims to present the numerical analysis of the proposed CPVT model using the ANSYS Fluent tool, which performs CFD modelling of the CPVT model under steady-state conditions. The performance indicators of the CPVT model are evaluated, and the effects of different input and output parameters on these indicators are also investigated.

5.2 Numerical Modelling

Numerical analysis involves utilizing algorithms and mathematical models to solve complex problems. It provides a highly efficient approach for solving complicated mathematical equations through numerical simulation and modelling. Unlike analytical methods, numerical simulation can handle large equation systems and complex geometries that are often impossible to solve analytically. As a result, numerical simulations have become essential for the mathematical modelling of various natural phenomena. In fields

such as aerodynamics and material sciences, where experimental investigations can be expensive and time-consuming, numerical simulation offers a cost-effective alternative to evaluate the performance of complex systems that are challenging to solve analytically.

Partial differential equations (PDE) are usually used to describe a physical phenomenon mathematically. These PDEs are transformed into a "numerical analog" that can be represented in a computer and processed using a computer program based on a specific algorithm. In order to solve a mathematical model numerically, the physical model needs to be discretized. There are several discretization schemes, such as the finite difference method (FDM), finite volume method (FVM), finite element method (FEM) methods, boundary element method (BEM) method and boundary volume method (BVM). In the present study, the numerical computations are performed using the finite volume method (FVM).

5.3 Finite Volume Method

The Finite Volume Method is a valuable numerical technique for analyzing and simulating CPVT systems' thermal and fluid dynamics aspects. In CPVT systems, the interaction between concentrated solar radiation, heat transfer, and fluid flow is crucial in their performance. The FVM discretizes the integral form of the conservation equations directly in the physical space. It was initially introduced by researchers such as McDonald, (1971) and MacCormack & Paullay, (1972) to solve two-dimensional time-dependent Euler equations. It was later extended to three-dimensional flows by Rizzi and Inouye, (1973). The FVM provides a systematic approach to discretize the CPVT system into a network of control volumes, allowing for the conservation equations of mass, momentum,

and energy to be solved. By dividing the computational domain into discrete cells, the FVM enables the accurate calculation of fluxes at the cell interfaces, capturing the intricate interplay between solar energy absorption, the convective and conductive heat transfer, and the fluid flow behaviour within the CPVT system. The FVM also accommodates complex geometries and unstructured grids, providing flexibility in modelling complicated designs and configurations of CPVT systems.

The FVM can use either structured or unstructured mesh to represent the grid. We use Fig. 5.1 to show an example of structured (quadrilateral) and unstructured (triangle) finite volume elements in two dimensions for the discretization of the partial differential equations. The key idea of the FVM is the integration over the control volume. The discretization of the first- and second-order derivatives for the general flow-field variable depends on the surface areas of the element that bound the control volume. As shown in Fig. 5.1, we decompose the surface areas in the normal direction ($\vec{n}$) to the volume surfaces into their components in the Cartesian coordinate directions, which give us the projected areas A_i^x and A_i^y in the x and y directions, respectively. The projected areas are positive if their outward normal vectors from the volume surfaces point in the same directions as the Cartesian coordinate system; otherwise, they are negative (Tu et al., 2018).

5.4 ANSYS Fluent

ANSYS Fluent is a commercial software that uses the FVM to solve fluid dynamics problems. It is one of the most powerful CFD software, with well-validated physical modelling capabilities for various CFD and multiphysics applications. ANSYS Fluent can handle complex geometries, unstructured meshes, moving boundaries, multiphase flows,

turbulence models, heat transfer models, and chemical reactions. ANSYS Fluent also has various add-ons that provide additional features or capabilities, such as ANSYS Design Modeler and ANSYS Meshing

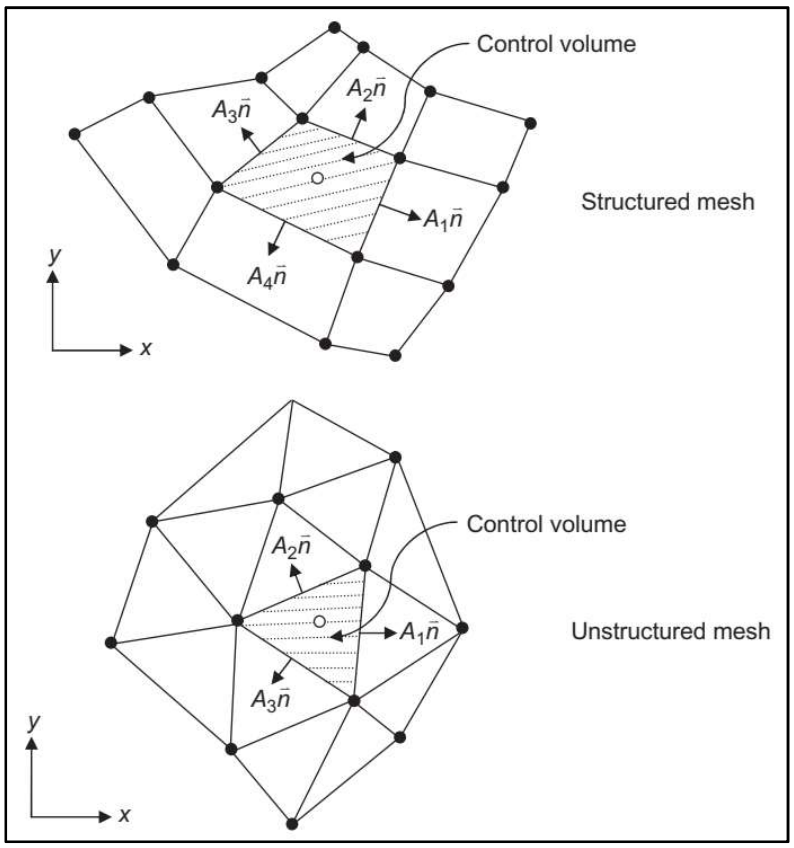

Fig. 5.1: A depiction of a structured and unstructured mesh for the FVM (solid symbols indicate element vertices and open symbols at the centre of the control volumes indicate computational nodes) (Tu et al., 2018).

Alternatively, a third-party computer-aided design (CAD) program, such as SolidWorks, can create the model geometry instead of the ANSYS Design Modeler. The meshing software allows the user to achieve different accuracy levels depending on the mesh quality; the finer the mesh, the more accurate the solution (ANSYS, Inc., 2017). In this study, ANSYS Fluent 19.0 was used to simulate the CPVT system because of the

complexity of the system design and the difficulty of solving the 3D fluid flow and heat transfer equations.

5.5 Computational Methodology

A series of steps were followed in sequential order to simulate the CPVT system using ANSYS Fluent. These steps are summarized below:

1. Creating the geometrical model of the CPVT using either ANSYS Design Modeler or another CAD program. In this research, SolidWorks was used to create the 3-D models.
2. Meshing the domain of the geometrical model using appropriate meshing parameters and techniques with ANSYS Meshing. It is beneficial to have a finer mesh near the points of interest of the model and regions where the physical phenomena of the domain of interest are more significant and relevant.
3. Choosing and applying the appropriate modelling technique available in ANSYS Fluent that best matches the conditions and phenomena of the CPVT model.
4. Defining the boundary conditions and material properties.
5. Iterating the numerical model using the selected solver in Fluent until a converged solution is obtained.

In this study, some sub-programs were needed to set up and run a successful model. These programs include the pre-processor, solver, and post-processor. The pre-processor consists of building and meshing the geometry of the CPVT model, which includes boundaries and solid/fluid domains. This research used SolidWorks, ANSYS Design Modeller, and ANSYS Meshing for modelling and meshing the geometry. After building

the models, ANSYS Meshing generated the mesh. The main program, ANSYS Fluent, performed numerical simulation and post-processing of the results. The solver enables the user to solve the mathematical equations numerically. To model the heat transfer and flow problem mathematically, the user needs to follow three steps:

- Develop the governing equations that describe heat transfer and flow.
- Discretize the governing equations into numerical equations.
- Solve the numerical equations using the solver.

5.5.1 Mesh Generation

Mesh generation, also known as grid generation, is one of the most important and time-consuming steps in CFD simulation. It involves creating a discrete representation of the computational domain for solving the flow and energy equations. Mesh generation is a step that many users tend to overlook, but it can significantly impact the accuracy and reliability of the results. Therefore, special attention should be given to the quality of the mesh.

In this simulation, a hybrid unstructured mesh consisting of tetrahedral and hexahedral elements was used. The meshing was done using the ANSYS Fluent Meshing tool, which allows for generating fine elements in regions of interest. Various metrics, such as skewness, orthogonal quality, and aspect ratio, can assess the quality of the mesh. Skewness measures the deviation of the cell angles from an ideal shape. It ranges from 0 to 1, where 0 indicates a perfect cell, and 1 indicates a degenerate cell. Orthogonal quality measures the alignment of the cell faces with the flow direction. It also ranges from 0 to 1, but in this case, 1 indicates a good alignment, and 0 indicates a poor alignment. The aspect ratio

measures the ratio of the longest to the shortest edge of a cell. To avoid numerical diffusion and instability, it should be as low as possible, preferably less than 100 (ANSYS, Inc., 2017; Thinsurat, 2019).

Figure 5.2 presents the meshed CPVT model viewed from the side and the isometric angles. The mesh consists of more than 8.0 million nodes and 13.6 million elements. The average values of the mesh quality metrics are 0.14 for skewness, 0.93 for orthogonal quality, and 24.0 for aspect ratio, indicating an excellent overall mesh quality for this simulation. Figure 5.3 shows a zoomed-in isometric view of a part of the CPVT model, including the meshed MJPV, epoxy layer, heat sink, and copper pipe. Figure 5.4 displays a zoomed-in side view of the same part, with the addition of the HTF.

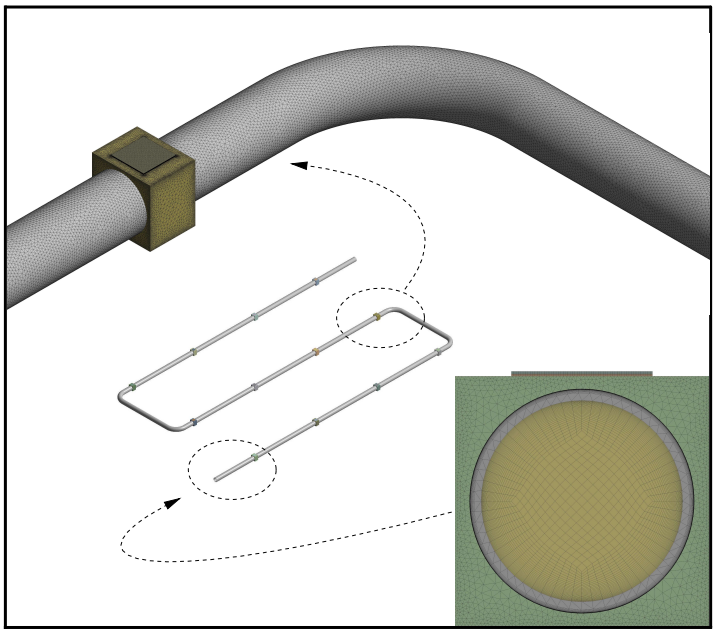

Fig. 5.2: Isometric and side view of the meshed CPVT model

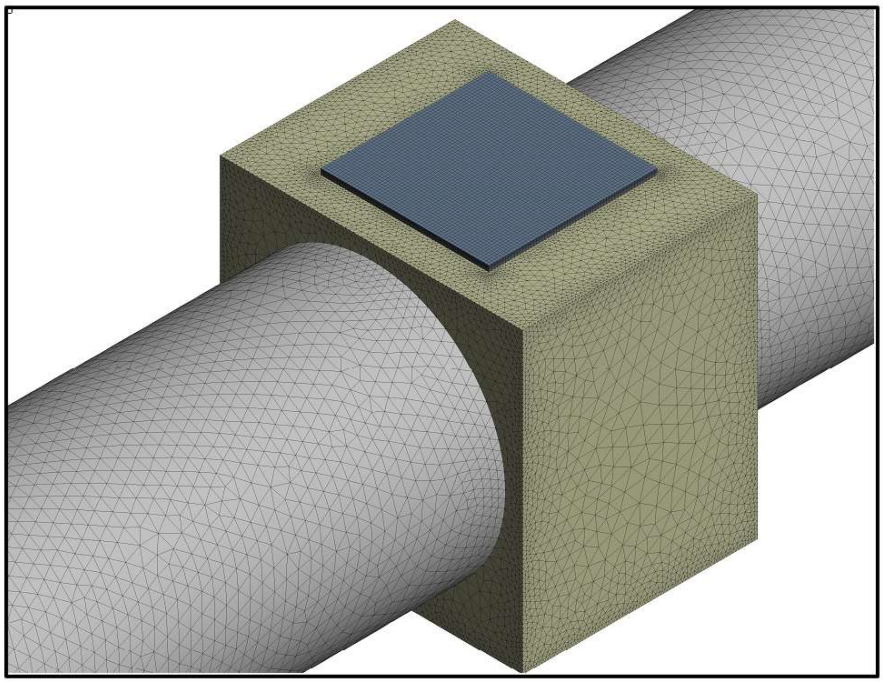

Fig. 5.3: Zoomed-in isometric view of a section of the meshed CPVT model

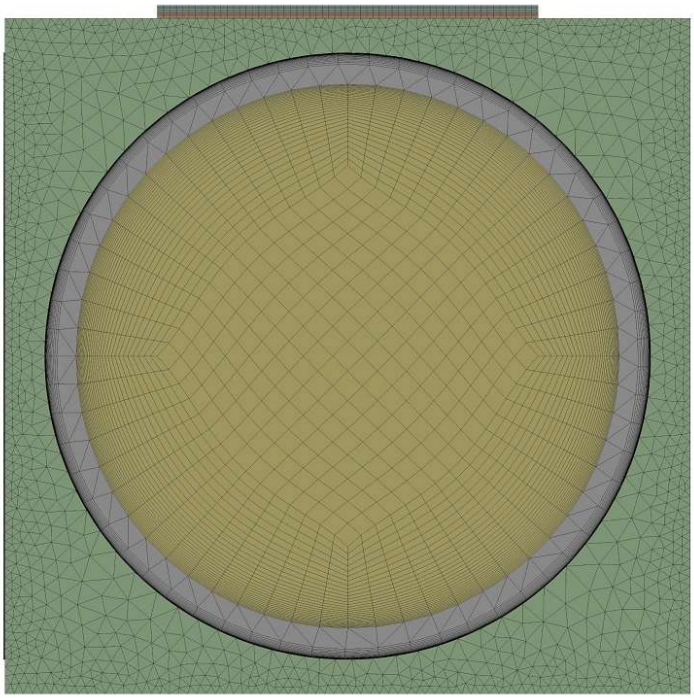

Fig. 5.4: Zoomed-in side view of the meshed CPVT model

5.5.2 Governing Equations of Fluid Flow

The numerical simulations used to analyze the thermal performance of the CPVT model were performed in ANSYS Fluent 19.0, a CFD software that incorporates a set of governing equations to model the physical phenomena in a given fluid domain. The governing equations for fluid flows and heat transfer are based on conservation laws: Conservation of Mass, Conservation of Momentum, and Conservation of Energy. These equations are applied, discretized, and solved within the CPVT geometry by ANSYS Fluent. This study considers both laminar and turbulent flow models. The standard k-ε model is used for the turbulent flow model, as it is one of the most common and widely accepted models for turbulence simulations in CFD. The following assumptions are made for the fluid flow and heat transfer analysis: steady state, incompressible flow, and Newtonian HTF.

5.5.2.1 Conservation of Mass

The law of conservation of mass for fluid flow states that the net rate of mass flow across a control volume is zero. In other words, the mass entering and leaving a control volume is balanced. The continuity equation expresses this principle as (Tu et al., 2018):

$$\frac{\partial u}{\partial x} + \frac{\partial v}{\partial y} + \frac{\partial w}{\partial z} = 0 \tag{5.1}$$

where u,v and w denote to HTF velocity in x, y, and z directions.

5.5.2.2 Conservation of Momentum

Based on Newton's second law, the conservation of momentum states that the net force acting on a fluid element is equal to the rate of change of its momentum. The Navier-Stokes equations govern the motion of fluids, and for a Cartesian frame of reference, the equations for each velocity component become (Tu et al., 2018):

$$\underbrace{\frac{\partial u}{\partial t}}_{local\ acceleration} + \underbrace{\frac{\partial (uu)}{\partial x} + \frac{\partial (vu)}{\partial y} + \frac{\partial (wu)}{\partial z}}_{advection} = \underbrace{\frac{\partial}{\partial x}\left[(\nu + \nu_T)\frac{\partial u}{\partial x}\right] + \frac{\partial}{\partial y}\left[(\nu + \nu_T)\frac{\partial u}{\partial y}\right]}_{diffusion}$$

$$+ \underbrace{\frac{\partial}{\partial z}\left[(\nu + \nu_T)\frac{\partial u}{\partial z}\right]}_{diffusion} + \left(S_u = - \underbrace{\frac{1}{\rho}\frac{\partial p}{\partial x}}_{pressure\ gradient} + S'_u\right) \tag{5.2}$$

$$\frac{\partial v}{\partial t} + \frac{\partial (uv)}{\partial x} + \frac{\partial (vv)}{\partial y} + \frac{\partial (wv)}{\partial z} = \frac{\partial}{\partial x}\left[(\nu + \nu_T)\frac{\partial v}{\partial x}\right] + \frac{\partial}{\partial y}\left[(\nu + \nu_T)\frac{\partial v}{\partial y}\right]$$

$$+ \frac{\partial}{\partial z}\left[(\nu + \nu_T)\frac{\partial v}{\partial z}\right] + \left(S_v = -\frac{1}{\rho}\frac{\partial p}{\partial y} + S'_v\right) \tag{5.3}$$

$$\frac{\partial w}{\partial t} + \frac{\partial (uw)}{\partial x} + \frac{\partial (vw)}{\partial y} + \frac{\partial (ww)}{\partial z} = \frac{\partial}{\partial x}\left[(\nu + \nu_T)\frac{\partial w}{\partial x}\right] + \frac{\partial}{\partial y}\left[(\nu + \nu_T)\frac{\partial w}{\partial y}\right]$$

$$+ \frac{\partial}{\partial z}\left[(\nu + \nu_T)\frac{\partial w}{\partial z}\right] + \left(S_w = -\frac{1}{\rho}\frac{\partial p}{\partial z} + S'_w\right) \tag{5.4}$$

Where ν is the kinematic laminar viscosity ($\nu=\mu/\rho$), and ν_T is the kinematic turbulent or eddy viscosity ($\nu_T=\mu_T/\rho$). S'_u, S'_v, and S'_w are the additional source terms comprise the pressure and non-pressure gradient terms and other possible sources, such as gravity, that influence the fluid motion.

5.5.2.3 Conservation of Energy

According to the first law of thermodynamics, the energy change rate in a fluid element is equal to the sum of the rate of heat addition to and work done on the fluid element. To set up a heat transfer problem in ANSYS Fluent, the energy equation has to be enabled, which reads (Tu et al., 2018):

$$\frac{\partial T}{\partial t}+\frac{\partial (uT)}{\partial x}+\frac{\partial (vT)}{\partial y}+\frac{\partial (wT)}{\partial z}=$$

$$\frac{\partial}{\partial x}\left[\left(\frac{\nu}{Pr}+\frac{\nu_T}{Pr_T}\right)\frac{\partial T}{\partial x}\right]+\frac{\partial}{\partial y}\left[\left(\frac{\nu}{Pr}+\frac{\nu_T}{Pr_T}\right)\frac{\partial T}{\partial y}\right]+\frac{\partial}{\partial z}\left[\left(\frac{\nu}{Pr}+\frac{\nu_T}{Pr_T}\right)\frac{\partial T}{\partial z}\right]+S_T \qquad (5.5)$$

Where T is the temperature, Pr, and Pr_T are the laminar and turbulent Prandtl numbers, respectively. S_T is the heat source (i.e., the solar radiation flux that reaches the MJPV cells). Based on the definition of the turbulent Prandtl number Pr_T, we obtain:

$$Pr_T=\frac{\mu_T}{\Gamma_T} \qquad (5.6)$$

Where Γ_T is the turbulent diffusivity, μ_T is the local turbulent viscosity and can be evaluated as:

$$\mu_T=\rho C_\mu \frac{k^2}{\varepsilon} \qquad (5.7)$$

Where k and ε are the turbulent kinetic energy and the dissipation rate, respectively, C_μ= 0.09 is a model constant used in the ANSYS Fluent when the standard k-ε turbulence model is applied.

5.5.2.4 *k-ε* Two-Equation Turbulence Model

The k-ε model is a widely used two-equation turbulence model that belongs to the Reynolds-averaged Navier-Stokes (RANS) family of models. It is suitable for a wide range of turbulent flows; especially free shear flows with relatively small pressure gradients and confined flows where the Reynolds shear stresses are important. It is robust, economical, and reasonably accurate for most engineering applications. The model is based on the Boussinesq eddy viscosity assumption, which relates the Reynolds stresses to the mean strain rate by a turbulent scalar viscosity (μ_T). The model solves two transport equations, one for the turbulent kinetic energy (k), which represents the turbulence intensity, and one for the dissipation rate (ε), which represents the scale of turbulence. The transport equations are given by (Tu et al., 2018):

$$\frac{\partial k}{\partial t}+\frac{\partial (uk)}{\partial x}+\frac{\partial (vk)}{\partial y}+\frac{\partial (wk)}{\partial z}=$$

$$\frac{\partial}{\partial x}\left[\frac{\nu_T}{\sigma_k}\frac{\partial k}{\partial x}\right]+\frac{\partial}{\partial y}\left[\frac{\nu_T}{\sigma_k}\frac{\partial k}{\partial y}\right]+\frac{\partial}{\partial z}\left[\frac{\nu_T}{\sigma_k}\frac{\partial k}{\partial z}\right]+(S_k=P-D) \qquad (5.8)$$

$$\frac{\partial \varepsilon}{\partial t}+\frac{\partial (u\varepsilon)}{\partial x}+\frac{\partial (v\varepsilon)}{\partial y}+\frac{\partial (w\varepsilon)}{\partial z}=$$

$$\frac{\partial}{\partial x}\left[\frac{\nu_T}{\sigma_\varepsilon}\frac{\partial \varepsilon}{\partial x}\right]+\frac{\partial}{\partial y}\left[\frac{\nu_T}{\sigma_\varepsilon}\frac{\partial \varepsilon}{\partial y}\right]+\frac{\partial}{\partial z}\left[\frac{\nu_T}{\sigma_\varepsilon}\frac{\partial \varepsilon}{\partial z}\right]+\left(S_\varepsilon=\frac{\varepsilon}{k}(C_{\varepsilon 1}P-C_{\varepsilon 2}D)\right) \qquad (5.9)$$

The equations contain four adjustable constants σ_k, σ_ε, $C_{\varepsilon 1}$, and $C_{\varepsilon 2}$. These constants have been arrived at by comprehensive data fitting for various turbulent flows (σ_k =1.0, σ_ε = 1.3, $C_{\varepsilon 1}$ = 1.44, $C_{\varepsilon 2}$ =1.92), (Launder & Spalding, 1974).

The destruction term D is given by ($D=\varepsilon$), and the production term P is formulated as:

$$P = 2\nu_T \left[\left(\frac{\partial u}{\partial x}\right)^2 + \left(\frac{\partial v}{\partial y}\right)^2 + \left(\frac{\partial w}{\partial z}\right)^2 \right]$$

$$+\nu_T \left[\left(\frac{\partial u}{\partial y} + \frac{\partial v}{\partial x}\right)^2 + \left(\frac{\partial v}{\partial z} + \frac{\partial w}{\partial y}\right)^2 + \left(\frac{\partial w}{\partial x} + \frac{\partial u}{\partial z}\right)^2 \right] \quad (5.10)$$

5.5.2.5 *y*+ Values and Near Wall Treatments in CFD Simulations

In CFD, predicting the behaviour of turbulent fluid flow near a solid boundary is crucial for many engineering applications. In the context of near-wall turbulent modelling in CFD and ANSYS Fluent, the parameter known as y+ plays an important role. y+ is a dimensionless parameter representing the distance from the wall to the first node in the near-wall region of a turbulent flow. It is defined as (Ansys, 2020a):

$$y^+ = \frac{u_\tau y}{\nu} \quad (5.11)$$

Where u_τ is the friction velocity, y is the wall-normal distance, and ν is the kinematic viscosity. y^+ is necessary for near-wall turbulent modelling in CFD because it determines the choice of the turbulence model and the wall treatment approach. Different regions of the turbulent boundary layer have different characteristics and require different modelling strategies. The regions are usually classified as (Salim & Cheah, 2009):

- **Viscous sublayer**: $y^+ < 5$, where the flow is laminar and dominated by viscous effects.
- **Buffer layer**: $5 < y^+ < 30$, where the flow is transitional and both viscous and turbulent effects are essential.
- **Logarithmic layer**: $y^+ > 30$, where the flow is fully turbulent and dominated by turbulent effects.

Ansys Fluent offers various approaches for modelling near-wall turbulence based on the near-wall mesh resolution and y^+. These approaches are(Ansys, 2020b):

- **Viscous sublayer resolving approach**: This approach requires a very fine mesh near the wall such that $y^+ < 5$ for all wall-bounded cells. The turbulence model solves the transport equations up to the wall without additional assumptions. This approach is suitable for *k-ω* models and *k-ε* models with enhanced wall treatment (EWT).

- **Wall-function approach**: This approach requires a coarser mesh near the wall such that $y^+ > 30$ for all wall-bounded cells. The turbulence model does not solve the transport equations in the viscous sublayer and buffer layer but uses analytical functions to account for the fluid velocity and other variables in these regions. This approach is suitable for standard *k-ε* models and other models that do not have EWT.

- **Blended approach**: This approach allows a mixed range of y^+ values for the wall-bounded cells, such that some cells have $y^+ < 5$ and some cells have $y^+ > 30$. The turbulence model uses a blending function to switch between the viscous sublayer resolving approach and the wall-function approach depending on the local y^+ value. This approach is suitable for realizable *k-ε* models, RNG *k-ε* models, SST *k-ω* models, and others with EWT.

In this study, the mesh near the wall was properly sized to capture the heat transfer and fluid dynamics in the near-wall region accurately and efficiently, ensuring accurate flow field simulations. The wall y^+ value in this research was $y^+ < 5$ for all simulations.

5.5.3 Solver Settings

The selection of an appropriate solver is crucial for obtaining accurate results and minimizing errors compared to experimental data. The user needs to specify the type of solver, either pressure-based or density-based, and determine if the flow is steady or unsteady. In this research, a pressure-based solver was chosen for a steady flow. Furthermore, the laminar model was selected to simulate the laminar flow in the CPVT model. In contrast, the turbulent k-ε model (Realizable with EWT) was chosen for simulating turbulent flow in the CPVT model. The next step involves defining the material properties for each component of the CPVT model, such as HTF, pipe, heat sinks, epoxy layers, and MJPV cells. The operating and boundary conditions at all boundary zones are also specified.

Moving on to the solution setup, the "Solution Methods" are considered. The chosen Pressure-Velocity Coupling Scheme is SIMPLEC (Semi-Implicit Method for Pressure Linked Equations-Consistent). The SIMPLEC algorithm converges 1.2-1.3 times faster than SIMPLE while maintaining the exact computational cost per iteration (Tamilarasan, 2015).

Second-order discretization is preferred for spatial discretization as it provides more accurate solutions. However, if convergence becomes challenging, first-order discretization is used as it is more likely to produce a converged solution. A least squares

cell-based gradient interpolation method is employed, as it is recommended for regular meshes and offers accuracy while minimizing false diffusion in heat transfer problems (Vodret et al., 2014). Table 5.1 illustrates the selected solution methods, marked in colour.

Table 5.1: Selected solution methods

		Solution Methods				
Pressure-Velocity Coupling	**Scheme**	SIMPLE	SIMPLEC	PISO	Coupled	
Spatial Discretization	**Gradient**	Green-Gauss Cell-Based	Green-Gauss Node-Based		Least Squares Cell-Based	
	Pressure	Second Order	Standard	PRESTO	Linear	Body Force Weighted
	Momentum	First Order Upwind	Second Order Upwind	Power Law	QUICK	Third Order MUSCL
	Turbulent Kinetic Energy	First Order Upwind	Second Order Upwind	Power Law	QUICK	Third Order MUSCL
	Specific Dissipation Rate	First Order Upwind	Second Order Upwind	Power Law	QUICK	Third Order MUSCL
	Energy	First Order Upwind	Second Order Upwind	Power Law	QUICK	Third Order MUSCL

Solution Controls involve under-relaxation factors that govern the solution variables in each iteration based on the current conditions. Default values are typically used but can be adjusted if convergence issues arise. Gradually decreasing these factors aids convergence, while increasing them can reduce computation times. In this case, the values were decreased before switching to second-order schemes to facilitate convergence.

To ensure that the solutions have converged, the residuals of all variables are monitored, with at least one variable chosen to demonstrate convergence towards a single value with minimal changes. By default, the residuals of continuity, x-velocity, y-velocity, z-velocity, Turbulent Kinetic Energy, and Turbulent Kinetic Energy Dissipation Rate equations are set to 10^{-6}. In contrast, the energy equation's residual is set to 10^{-9}.

Before commencing calculations, solution initialization is performed to apply initial values to all variables in all cells of the models. Hybrid Initialization is preferred as it considers initial values specific to the physical models. In contrast, Standard initialization applies a single value to flow and energy variables in all cells.

5.5.4 Mesh Independence Study

A comprehensive mesh independence study was conducted to ensure the reliability and accuracy of the simulation results. This study aimed to assess the mesh resolution's impact on the calculated values, specifically the cell temperature and HTF outlet temperature. Six different mesh configurations were generated, varying the mesh elements from 4.0 to 35.0 million. The results of the mesh independence study, presented in Fig. 5.5, indicate that both the cell and HTF outlet temperatures exhibit minimal variation as the number of grid elements increases. This observation suggests that the solutions have converged and are independent of the mesh resolution. Based on these findings, a mesh configuration with approximately 8.1 million nodes and 13.6 million elements was selected for the subsequent simulations. This mesh configuration balances accuracy and computational efficiency, providing sufficiently accurate results while minimizing simulation run time.

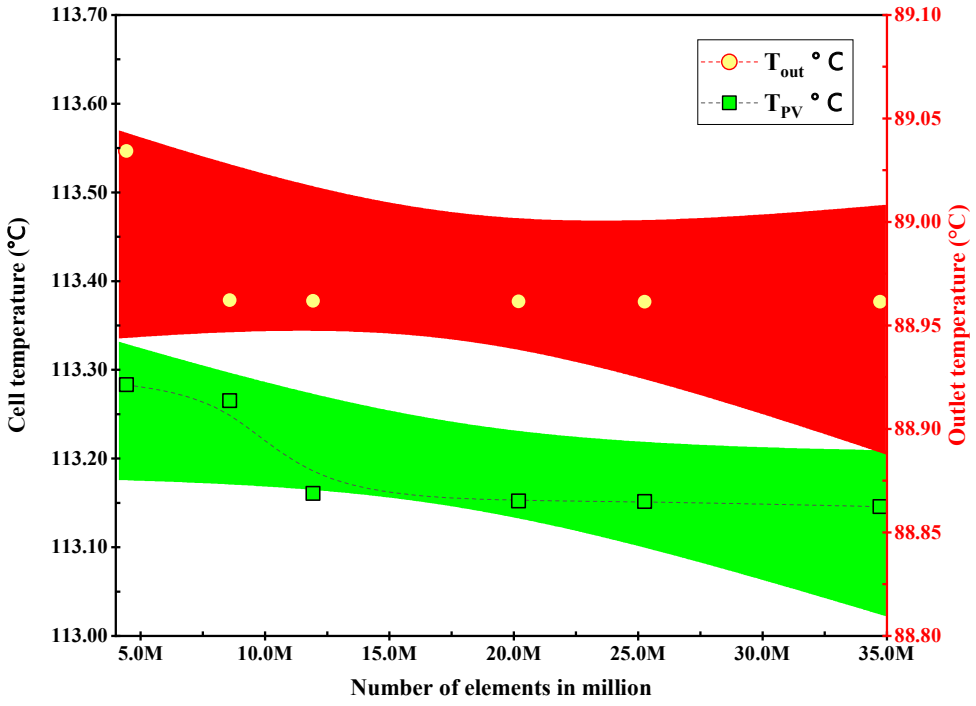

Fig. 5.5: Mesh independence study for solar cell temperature and HTF outlet temperature

The mesh independence study is a critical step in ensuring the robustness and validity of the numerical simulations. By establishing mesh independence, we can have confidence in the results' reliability and consistency, reducing the uncertainties associated with discretization errors and numerical approximations. The chosen mesh configuration guarantees accurate representations of the flow and heat transfer phenomena in the CPVT system, allowing for meaningful analysis and reliable conclusions.

5.6 Uncertainty and Error in CFD Simulations

Computational simulations are powerful tools for studying complex systems and phenomena that are difficult or impossible to observe experimentally. However,

simulations are not exact representations of reality, and they are subject to various sources of uncertainty and error that can affect their accuracy and reliability. Uncertainty refers to the lack of knowledge or information about a system or a model. In contrast, the error is the deviation or discrepancy between a simulation result and the actual value. Uncertainty and error can arise from different phases of the simulation process, such as model formulation, parameter estimation, numerical discretization, solver convergence, and data analysis.

Oberkampf et al. present a general framework for identifying and classifying error and uncertainty in computational simulations that involve the numerical solution of partial differential equations (PDEs). The framework categorizes error and uncertainty into six main phases, which represent a synthesis of the activities recognized in the systems engineering and operations research communities, the risk assessment community, and the computational mathematics community. The phases are (Oberkampf et al., 2002):

1. Conceptual modelling of the physical system
2. Mathematical modelling of the conceptual model
3. Discretization and algorithm selection for the mathematical model
4. Computer programming of the discrete model
5. Numerical solution of the computer program model
6. Representation of the numerical solution

Figure 5.6 illustrates the characteristics and activities of each phase and the relationships between them. In this thesis, ANSYS Fluent was used to perform CFD

simulations and analysis of the CPVT model. Some methods and techniques were applied to evaluate and reduce uncertainty and error in our simulations, such as:

- Mesh independence study: Different mesh sizes were tested and compared to ensure they did not change significantly by increasing the number of grid elements.
- Validation and verification process: The simulation results were compared with the experimental data to assess the agreement and accuracy of our model.
- Mesh quality metrics: Various metrics that assess the quality of the mesh were checked, such as skewness, orthogonal quality, and aspect ratio, to ensure that their values were within the recommended limit.

These methods helped us improve our simulation quality and confidence.

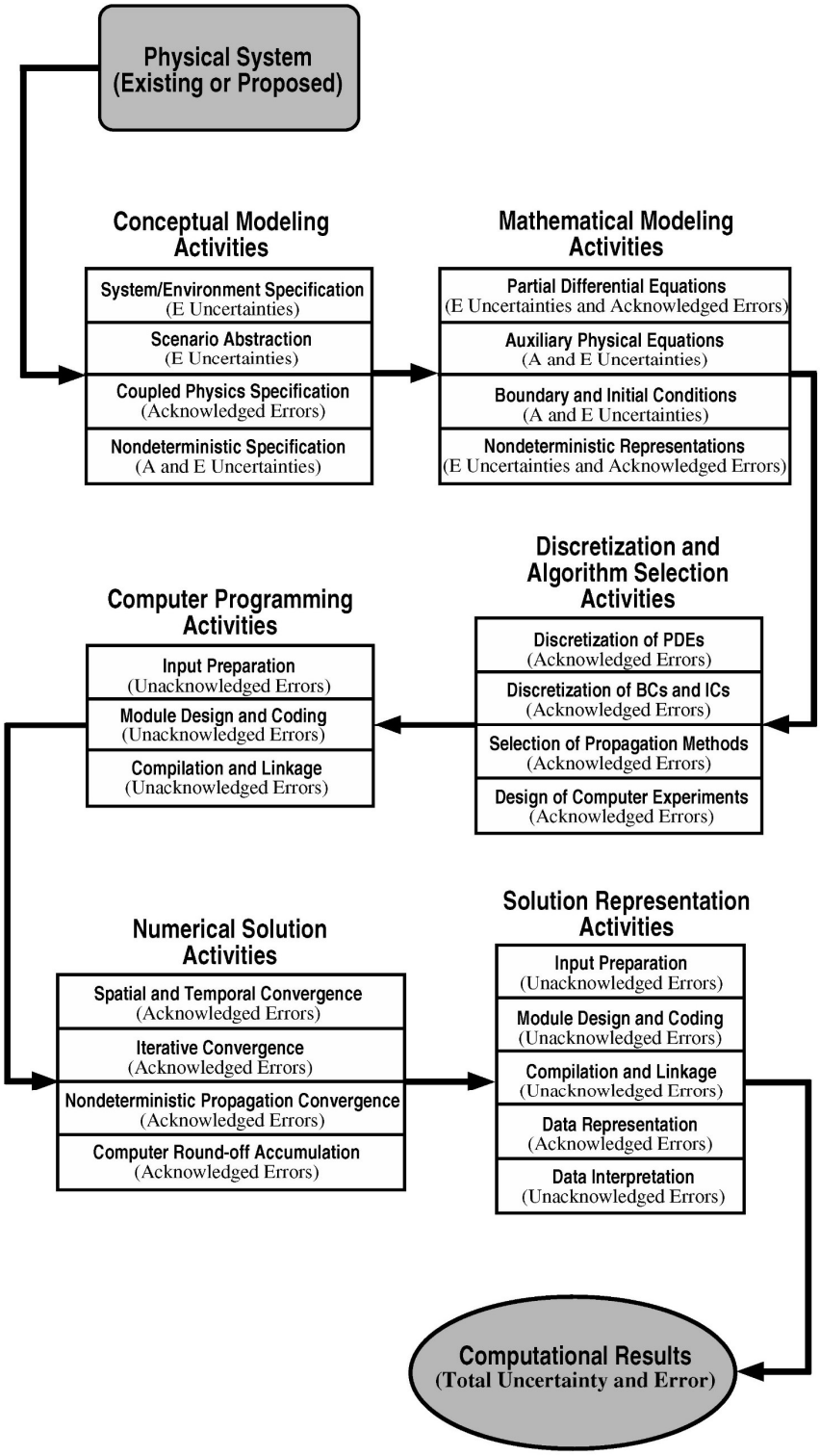

Fig. 5.6: Sources of uncertainty and error in modelling and simulation (Oberkampf et al., 2002).

Chapter 6

Electrical Characteristics Analysis of High-Concentration MJPV Cells

6.1 Introduction

In recent years, MJPV solar cells have attracted much attention due to their high efficiency and potential applications in concentrated photovoltaic systems. However, the electrical characteristics of MJPV cells under high-concentration conditions are not well understood and need to be investigated for optimal design and operation. Designing high-concentration photovoltaic systems requires the characterization of the performance of MJPV solar cells under various operating temperatures and concentrated solar radiation. Even though the manufacturers' data for MJPV cells are available, a calibrated model covering an entire range of different operating conditions still needs to be developed to enhance such a model.

This chapter describes the development of a mathematical model for MJPV based on a lumped diode model circuit. The model was implemented using the MATLAB program to predict the short-circuit current (I_{SC}), open-circuit voltage (V_{OC}), peak power (P_m), fill factor (FF), and conversion efficiency (η_{ele}) under operating conditions extended outside the standard test ranges. The model was calibrated against experimental data published by two MJPV cell manufacturers.

6.2 Analysis of the Behaviour of MJPV Solar Cells

An overview of MJPV solar cells was conducted in Chapter 2, highlighting their unique characteristics compared to conventional single-junction PV solar cells. The internal series connection of MJPV solar cells with different band gaps makes them highly sensitive to incident spectral irradiance. Moreover, the intensity of the irradiance significantly influences the electrical characteristics and temperature dependencies of MJPV cells. Under concentrated irradiance, each subcell exhibits its own I-V curve, determined by its photocurrent. However, due to the MJPV solar cell having only two electrical terminals, it is not possible to independently measure these subcell I-V curves. Instead, the internal I-V characteristics of each subcell combines to form the overall I-V curve of the MJPV solar cell, which can be measured externally. As stated in Chapter 2 (Best Research-Cell Efficiencies Chart), the three-junction solar cell with a concentrator started in 2000 with 28% efficiency, and has now reached 44.4%. Meanwhile, the three-junction solar cell without a concentrator started in 2003 with 28% efficiency, has now reached 39.5%. (NREL, 2023).

6.3 I-V Characteristics of MJPV Solar Cell

One of the most important methods for evaluating the performance and quality of MJPV solar cells is to measure their I-V characteristics under different illumination and temperature conditions. The I-V curve shows the relationship between a solar cell's output current and voltage at a given irradiance and temperature. From the I-V curve, several key parameters can be extracted, such as I_{SC}, V_{OC}, P_m, FF, and η_{ele} of the solar cell. These parameters reflect the electrical behaviour of the solar cell and its response to various

environmental factors. Moreover, the I-V curve can also reveal the effects of parasitic resistances (series and shunt resistances) and degradation mechanisms on solar cell performance. Therefore, I-V characterization is essential for MJPV solar cell research and development, as well as quality control and fault diagnosis. Figure 6.1 shows a typical I-V curve of an MJPV solar cell.

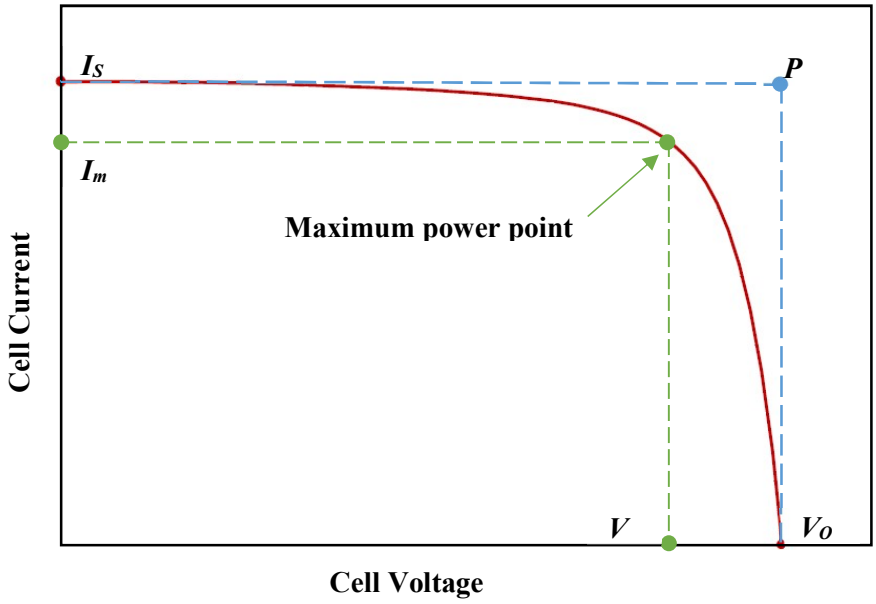

Fig. 6.1: Typical I-V curve of an illuminated MJPV solar cell

6.3.1 Short Circuit Current (I_{SC})

I_{SC} is an important parameter in characterizing the performance of a solar cell. It represents the maximum current obtained from the cell when its terminals are shorted, resulting in zero voltage across the cell. I_{SC} is determined by the amount of light absorbed by the cell and the efficiency of the charge separation process. Mathematically, I_{SC} is the current at zero voltage (I at $V = 0$).

6.3.2 Open Circuit Voltage (V_{OC})

V_{OC} is another key parameter in solar cell characterization. It represents the maximum voltage that can be obtained across the cell when no current is flowing (i.e., the terminals are open-circuited). V_{OC} is primarily influenced by the bandgap energy of the semiconducting materials used in the cell and the level of recombination within the device. Mathematically, V_{OC} is the voltage at zero current (V at $I = 0$).

6.3.3 Maximum Power (P_m), Current at P_m (I_m), and Voltage at P_m (V_m)

P_m is the highest power that can be extracted from a solar cell under a given illumination and temperature. It is equal to the product of the current (I_m) and the voltage (V_m) at the maximum power point (MPP) on the I-V curve of a solar cell, as shown in Fig. 6.1. The MPP is where the slope of the I-V curve is equal to ($-I_m/V_m$). The P_m, I_m, and V_m, which are essential parameters for determining a solar cell's optimal operating point and conversion efficiency. They can be measured experimentally using a variable load resistor or an electronic load device connected to a solar cell under illumination. Alternatively, they can be calculated using the following equation:

$$P_m = I_m \times V_m \tag{6.1}$$

6.3.4 Fill Factor (FF)

The FF measures the quality of a solar cell. It is defined as the ratio of the maximum power (P_m) to the theoretical power (P_T) as shown in Fig. 6.1. The FF ranges from 0 to 1, with higher values indicating better quality and lower losses in a solar cell. The FF depends

on internal and external factors, such as parasitic resistances, light intensity, and temperature. The *FF* is an important parameter for determining the conversion efficiency of a solar cell. It can be calculated using the following equation:

$$FF = \frac{P_m}{P_T} = \frac{I_m \times V_m}{I_{SC} \times V_{OC}} \tag{6.2}$$

6.3.5 Efficiency (η)

Efficiency (η) is a fundamental parameter that quantifies the ability of a solar cell to convert incident sunlight into electrical power. It is defined as the ratio of the maximum power output (P_m) to the incident light power (P_{in}). The η depends on internal and external factors, such as material properties, parasitic resistances, light intensity, spectral distribution, and temperature. The η is an essential parameter for comparing the performance of different types of solar cells and for designing and optimizing PV systems. It can be calculated using the following equation:

$$\eta = \frac{P_m}{P_{in}} \times 100\% \tag{6.3}$$

These parameters play a significant role in characterizing the performance and efficiency of solar cells, providing valuable insights for design optimization and performance evaluation.

6.4 Mathematical Lumped Diode Model of a Single-junction Solar Cell

Equivalent circuit models are practical and widely used methods for simulating solar-cell performance. Several methods have been proposed in the literature to predict the I-V characteristics of the multi-junction solar cell, such as the single-diode model, the double-

diode model, the lumped diode model, and the network cell model. The lumped diode model is more practical and time-saving than the single or double-diode models, as it requires fewer empirical parameters to be estimated. The general equivalent lumped diode circuit model of a single solar cell consists of a PV cell in parallel with a diode (under solar radiation, a PV cell is modelled as a current source). For MJPV cells, this model is often extended to include the voltage drop due to high current flow by adding a series resistance (R_S) (Domínguez et al., 2010). The equivalent circuit of the lumped diode model of the multi-junction solar cell is presented in Fig. 6.2.

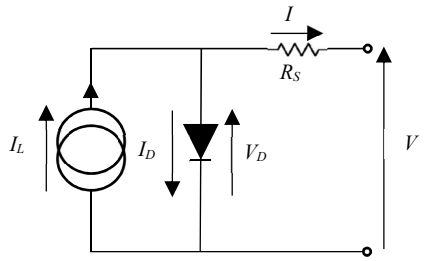

Fig. 6.2: Lumped diode model of the solar cell (Domínguez et al., 2010)

The output current and voltage of the solar cell for a lumped diode model with R_S are represented by I-V characteristics and mathematically expressed as (Domínguez et al., 2010):

$$I = I_L \times I_D \tag{6.4}$$

$$V = V_D - IR_S \tag{6.5}$$

Where I, I_L, and I_D are the current of the solar cell, light-generated current, and diode's current (A), respectively. V and V_D are the voltage of the solar cell and the diode (V),

respectively. R_S is the series resistance (Ω). The Shockley equation calculates the diode current as (Domínguez et al., 2010):

$$I_D = I_O \left[exp\left(\frac{qV_D}{nkT}\right) - 1 \right] \tag{6.6}$$

Where I_O is the reverse saturation current (A), q is the charge of an electron (=1.60217646×10^{-19} C), k is the Boltzmann constant (=1.3806503×10^{-23} J/K), T is the cell temperature (K), and n is the diode ideality factor. According to Kirchhoff's current law, the I-V characteristics of the solar cell, including the series resistance effect, can be written by (Domínguez et al., 2010):

$$I = I_L - I_O \left[exp\left(\frac{q(V + IR_S)}{nkT}\right) - 1 \right] \tag{6.7}$$

The light-generated current depends on the solar radiation and PV cell surface temperature can be computed using the following equation (Singh, 2013):

$$I_L = [I_{SC} + K_i(T - T_C)] \left[\frac{S}{100}\right] \tag{6.8}$$

Where I_{SC} is the short circuit current at the reference temperature and radiation, K_i is the short circuit current temperature coefficient, T_C is the cell reference temperature, and S is the solar irradiation (in mW/cm^2).

The temperature dependence of the reverse saturation current density I_O has the following form (Domínguez et al., 2010; Kinsey et al., 2008):

$$I_O = T^{3+\frac{\gamma}{2}} exp\left(-\frac{E_g}{kT}\right) \quad (6.9)$$

Where E_g is the width of the semiconductor bandgap at temperature T and γ is the third order dependence of the square of the intrinsic carrier concentration on temperature.

To study the characteristics of MJPV solar cells under concentrated radiation, we need to define the concentration ratio (*CR*) factor. The *CR* can be theoretically determined by dividing the I_{SC} under concentrated radiation by the I_{SC} under one sun illumination. That is, if sunlight is concentrated by a factor of X (X suns illumination), the I_{SC} at that concentration is given by (A. Luque & Hegedus, 2011a; Nishioka et al., 2006; Osterwald et al., 2014):

$$I_{SC}^{X_{suns}} = XI_{SC}^{1_{suns}} \quad (6.10)$$

Where X is the concentration ratio factor, which is indicated by the symbol *CR* in the following graphs.

6.5 Model Verification

To verify the accuracy and reliability of the mathematical model, we calibrated the characteristic I-V and P-V curves of the considered module against the available experimental data of triple-junction cells produced by AZURSPACE, (2014) and FULLSUN, (2020). Table 6.1 compares the experimental and modelled I-V and P-V curve parameters: I_{SC}, V_{OC}, I_m, V_m, and *FF* at 500X and 1000X concentration ratios and a PV surface temperature of 25 °*C*. We observed a good agreement between the experimental and computed values. The overall Root-Mean-Square Errors (RMSE) evaluated for the parameters above ranged from 0.45 % to 3.79%.

Table 6.1: I-V curve parameters of the experimental and developed model at *CR* of 500X and 1000X

	Developed Model		**AZURSPACE**			**FULLSUNS**		
CR	***500 X***	***1000 X***	***500 X***	***1000 X***	***RMSE %***	***500 X***	***1000 X***	***RMSE %***
I_{SC} **(*A*)**	7.57	15.16	7.58	15.07	0.5654	7.563	15.015	0.9093
V_{OC} **(*V*)**	3.12	3.18	3.12	3.16	0.4504	3.121	3.235	1.2240
I_m **(*A*)**	7.3	14.6	7.42	14.77	1.3262	7.289	14.502	0.640
V_m **(*V*)**	2.75	2.78	2.79	2.64	3.7921	2.823	2.782	1.8426
FF	0.849	0.839	0.876	0.819	2.8034	0.8718	0.8306	2.0185

6.6 Discussion and Analysis of the Electrical Characteristics of the MJPV Cells

In this section, we present the results of the mathematical model of the MJPV cells under different operating conditions. We discuss how the *CR*, PV surface temperature (T_{PV}), and R_S affect the key parameters of the I-V and P-V curves, such as the I_{SC}, V_{OC}, P_m, *FF*, and η.

6.6.1 Effect of the Radiation Variation on the MJPV Cell

We developed the mathematical model for MJPV to study the effects of the *CR* and T_{PV} on the V_{OC}, the I_{SC}, and P_m of the MJPV cell. Figure 6.3 demonstrates that I_{SC} increases linearly with *CR*, indicating increased solar radiation intensity on the MJPV cell. In contrast, V_{OC} exhibits a logarithmic increase with *CR*. It is important to note that the variation in V_{OC} due to radiation is relatively small compared to the variation in I_{SC}.

Furthermore, the power output of the MJPV cell, P_{out}, increases with higher radiation falling on the solar cell as both I_{SC} and V_{OC} increase. Figure 6.4 illustrates the positive correlation between *CR* and P_{out}, signifying increased radiation on the MJPV cell. These

findings emphasize the importance of using concentrators in solar cell applications. Concentrators enhance the radiation reaching the cells while maintaining the same cell area, thereby boosting the P_{out}.

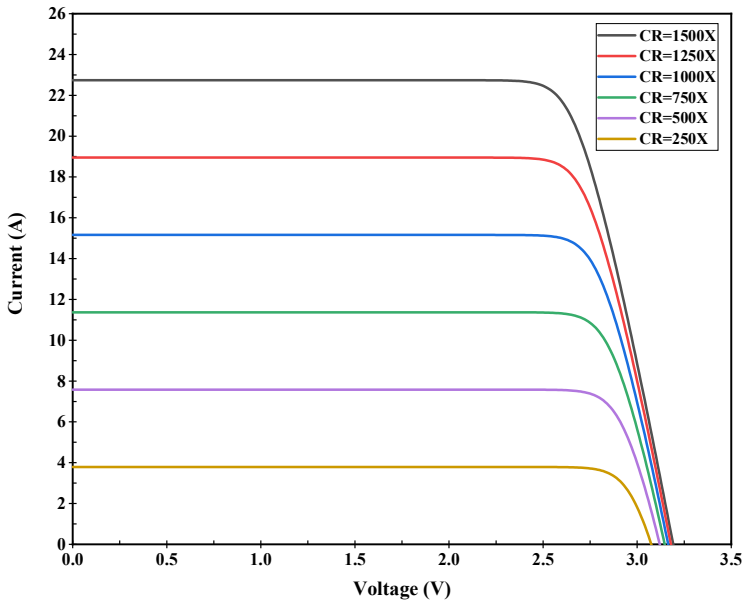

Fig. 6.3: I-V characteristics for various irradiation values at a PV temperature of 25 °*C*.

6.6.2 Effect of the Temperature Variation on the MJPV Cell

Figure 6.5 shows different I-V curves at different PV temperatures, ranging from 25 to 115 ℃, and a *CR* of 750X. It is evident that an increased cell temperature significantly reduces the V_{OC}, thus lowering its performance. On the other hand, the increase in the temperature of the solar cells is accompanied by an increase in the I_{SC}. The I-V curves shown in Fig. 6.5 are represented in power variation as a function of the voltage variation in Fig. 6.6 below. The increase in the I_{SC} and the decrease in V_{OC} due to the increase in the PV surface temperature negatively influence the maximum power output.

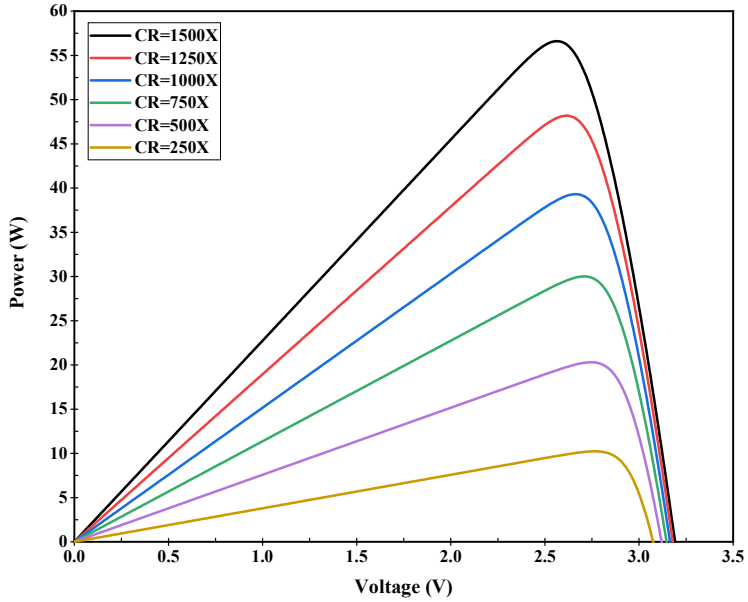

Fig. 6.4: P-V characteristics for various irradiation values at a PV temperature of 25 °*C*.

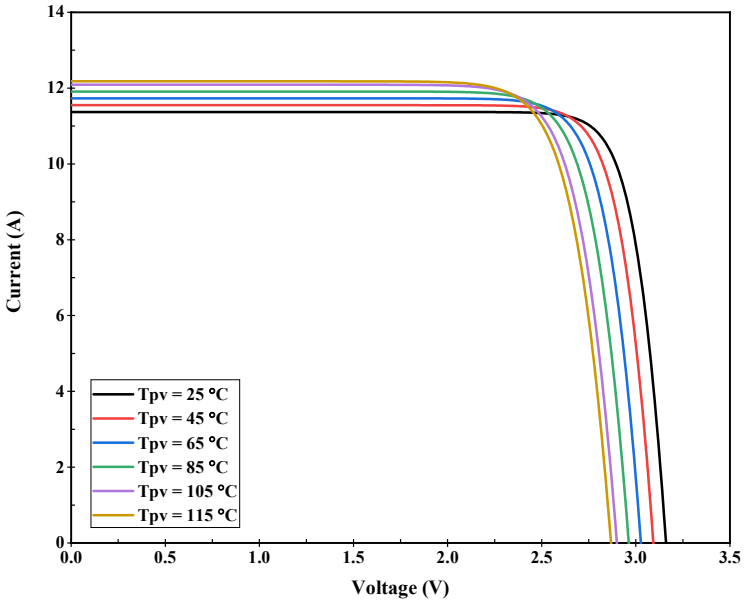

Fig. 6.5: I-V curves at *CR* = 750X and different PV temperatures

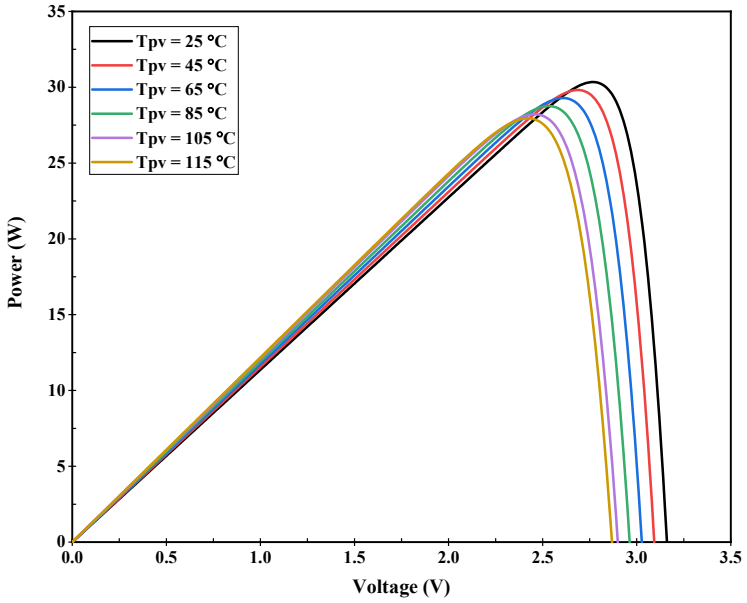

Fig. 6.6: P-V curves at *CR* = 750X and different PV temperatures

6.6.3 Effect of Series Resistance

The influence of the R_S on the I-V characteristics of the MJPV cell is shown in Fig. 6.7, assuming no effect of shunt resistance. As the R_S increases, the I-V characteristic of the MJPV cell bends (reducing the area under the curve), and the *FF* decreases, while the V_{OC} and the I_{SC} remain unchanged. The R_S values range from 0 to 0.08 Ohms, the *CR* = 750X and the PV surface temperature is 25 ℃. Moreover, the effect of the RS on the P-V curve is illustrated in Fig. 6.8. As the value of R_S increases, the power output of the MJPV cell decreases.

6.6.4 Conversion Efficiency

Figure 6.9 depicts the temperature dependence of the η for GalnP/InGaAs/Ge MJPV cells at various *CRs*. As the PV surface temperature increased, η showed a decrease in all

cases. The reduction in efficiency can be attributed to the decrease in the band gap of the MJPV cell with rising cell temperature, leading to an increase in the recombination rate within the depletion region. With an increase in the concentration ratio from 250X to 1500X and a rise in the cell temperature from 25 ℃ to 115 ℃, the theoretical efficiency value dropped from 41.40% to 32.74%.

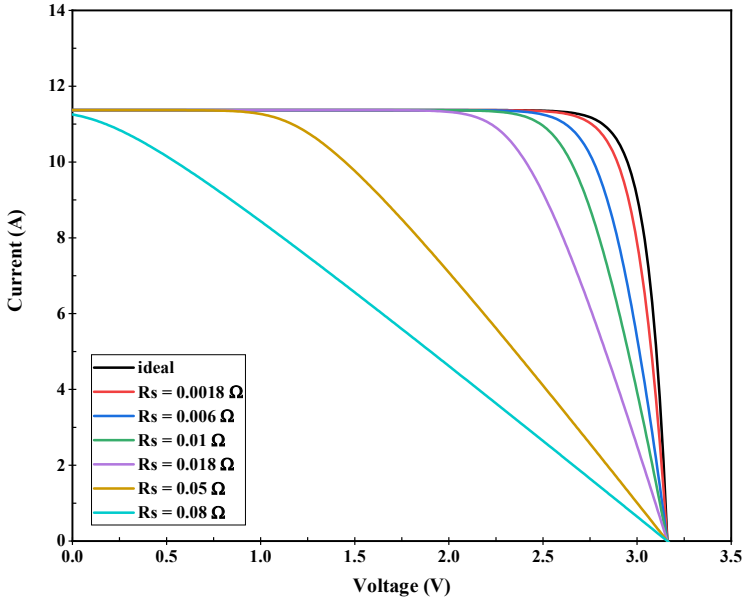

Fig. 6.7: Influence of the series resistances on the I-V characteristics of the MJPV cell

6.6.5 Open Circuit Voltage

Figure 6.10 illustrates the temperature dependence of V_{OC} under various *CRs*. V_{OC} increased as *CR* increased. For all *CRs*, V_{OC} decreased with increasing temperatures. The maximum value of V_{OC} was 3.23 V at a *CR* of 1500X and a surface temperature of 25 ℃. Conversely, the minimum value of V_{OC} was 2.73 V at a *CR* of 250X and a surface temperature of 115 ℃.

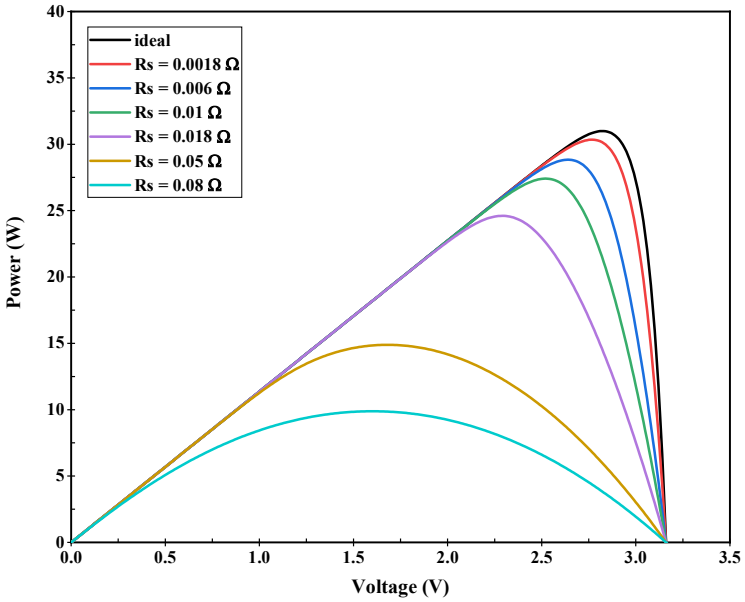

Fig. 6.8: Influence of the series resistances on the P-V characteristic of the MJPV cell

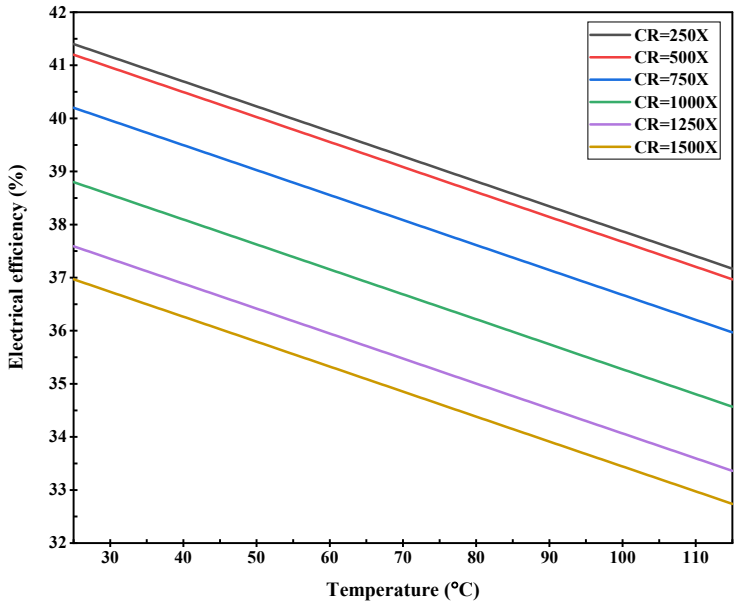

Fig. 6.9: Temperature dependence of the conversion efficiency of a MJPV solar cell

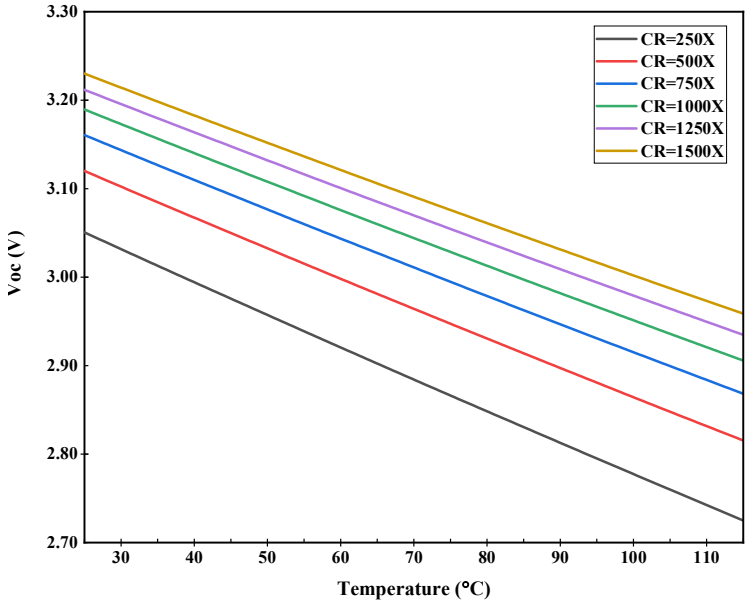

Fig. 6.10: Temperature dependence of the V_{OC} of a MJPV solar cell

6.6.6 Short Circuit Current

Figure 6.11 depicts the temperature dependence of the I_{SC} for MJPV cells at different *CRs*. Across all *CRs*, I_{SC} exhibited a slight increase with rising temperature due to the increased minority-carrier diffusion length. This indicates that the absorption coefficient's change with temperature contributes to an increase in I_{SC}. The maximum I_{SC} recorded was 24.36 A at a *CR* of 1500X and a PV surface temperature of 115 $°C$. Conversely, at a *CR* of 250X and a PV surface temperature of 25 $°C$, the minimum I_{SC} observed was 3.79 A.

6.6.7 Fill Factor

The temperature dependence of the *FF* under different *CRs* is presented in Fig. 6.12. It is observed that *FF* decreases as both the MJPV surface temperature and *CR* increase. The maximum *FF* value of 0.85 was recorded at a *CR* of 250X and a surface temperature of

25 °*C*. On the other hand, the minimum *FF* value of 0.78 was observed at a *CR* of 1500X and a surface temperature of 115 °*C*.

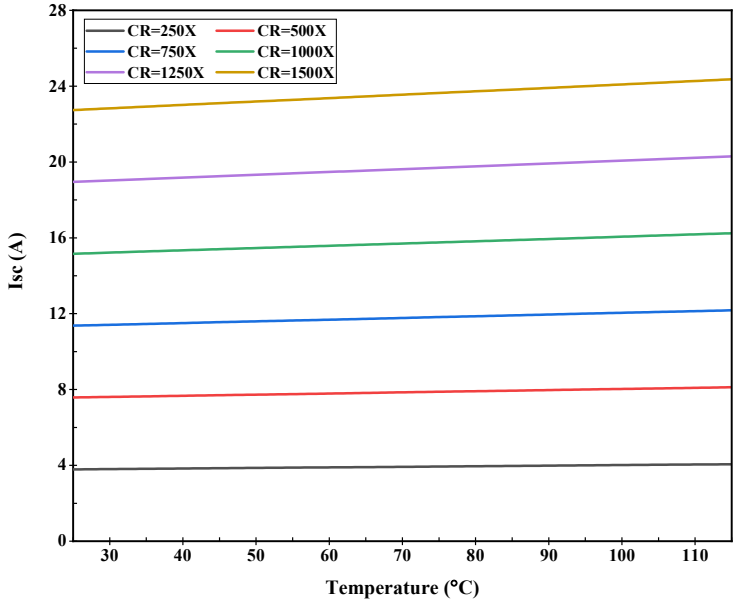

Fig. 6.11: Temperature dependence of the I_{SC} of a MJPV solar cell

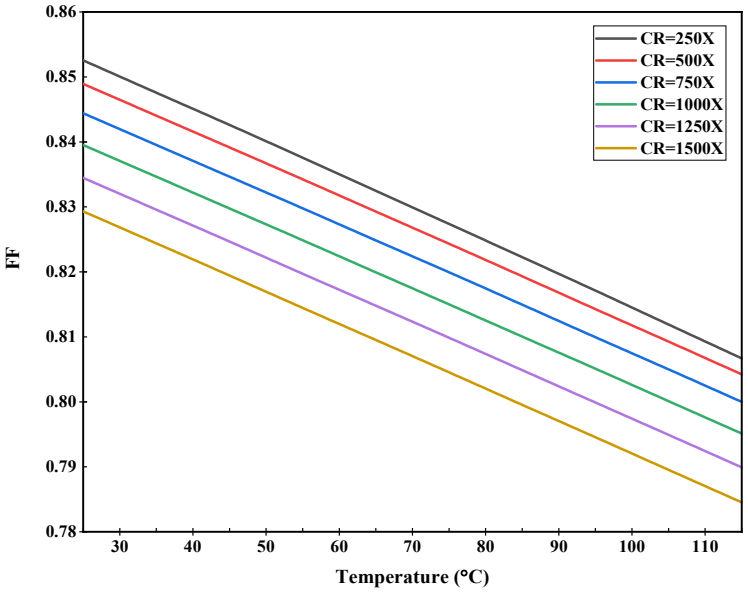

Fig. 6.12: Temperature dependence of the *FF* of a MJPV solar cell

6.7 Summary

This chapter developed a mathematical model for MJPV cells based on a lumped diode model circuit. The temperature dependences of the electrical characteristics of GalnP/InGaAs/Ge triple-junction solar cells under various *CRs*, including I_{SC}, V_{OC}, *FF*, and η, were evaluated under operating conditions extended beyond the standard test ranges. Moreover, experimental data published by two MJPV cell manufacturers were used to validate the accuracy of the proposed model. Based on the presented results, the following observations were made:

- The effect of solar radiation on I_{SC} in MJPV cells was more pronounced than on V_{OC}. I_{SC} and increased linearly with increasing *CR*, while V_{OC} showed a logarithmic increase with increasing *CR*.

- The P_{out} of MJPV cells increased with higher *CR* values due to increased radiation on the cells.

- Elevated cell temperature resulted in a significant reduction in V_{OC}, adversely affecting cell performance. Conversely, I_{SC} increased with rising solar cell temperature.

- The increase in R_S led to a reduction in the power output of MJPV cells.

- With increasing *CR*, I_{SC} and V_{OC} of MJPV cells increased, while η and *FF* decreased.

- The calculated results were validated using experimental data, yielding root mean square errors (RMSE) ranging from 0.45% to 3.79%

Chapter 7

Results and Discussion

7.1 Introduction

This chapter presents and discusses the results of indoor experimental testing and numerical simulation of the CPVT model. The CPVT model is an integrated system that combines point-focus Fresnel lens concentrators, high-efficiency GaInP/InGaAs/Ge MJPV cells, copper heat sinks and an absorber tube as an active cooling system. The main objective of this study is to design an efficient CPVT model that can reduce the MJPV module temperature and increase heat transfer to the HTF in the flow channel, resulting in high electrical and thermal energy production.

The results are analyzed in terms of various parameters that affect the thermal and electrical performance of the CPVT model, such as outlet HTF temperature, thermal and electrical efficiency, thermal and electrical energy, average solar cells temperature, pressure drop across the CPVT model, primary energy saving (PES) efficiency, heat transfer coefficient of the CPVT model, and convection and radiation losses of the CPVT model at average cell temperature.

The results are divided into two parts. The first part compares the indoor experimental and numerical simulation results under the same operation conditions. The experimental measurements, such as mass flow rates, the inlet temperature of the HTF, incident solar

radiation, and ambient temperature, have been exported to the CFD model to ensure a fair comparison of results under the same operating conditions.

Two additional CFD models have been developed to overcome the limitations posed by the experimental equipment, such as the maximum capacity of the flowmeter and radiation intensity from the solar simulator. These models are designed to extend the range of data covered in this study, which was previously constrained by these experimental limitations. Consequently, the second part of the results will encompass a broader scope, including laminar and turbulent flow regimes and various values of *CRs*, inlet HTF temperatures, and ambient temperatures. By incorporating these extended parameters, a more comprehensive understanding of the CPVT model's performance under diverse conditions can be attained.

7.2 Justification and Motivation of Using the CPVT Model

This section demonstrates the necessity and benefits of using the proposed CPVT model with an active cooling system for the MJPV solar cell. Figure 7.1 shows the variation in cell surface average temperature and electrical efficiency with time under no cooling conditions at an ambient temperature of 25 $°C$ and a *CR* of 500X. The simulation results indicate that the cell temperature rapidly increased from the initial temperature (ambient temperature) to 680 $°C$ in under 80 seconds and reached a steady state of 700 $°C$ in about 130 seconds. Moreover, Fig. 7.1 reveals the significant degradation of MJPV's electrical efficiency due to the high surface cell temperature. The electrical efficiency dropped from about 35% to less than 10% in about 90 seconds. By contrast, when using the proposed active cooling system, the generated heat was transferred from the MJPV cell solid layers

to the heat sink and copper pipe flow loop by conduction, dissipating mainly by forced convection. At a mass flow rate of 0.025 *kg/s*, the maximum temperature of the MJPV surface was significantly reduced from about 700 °*C* to 83.4 °*C*, below the maximum operating temperature, as explained later. Consequently, electrical efficiency experienced a substantial increase from approximately 10% to 34%.

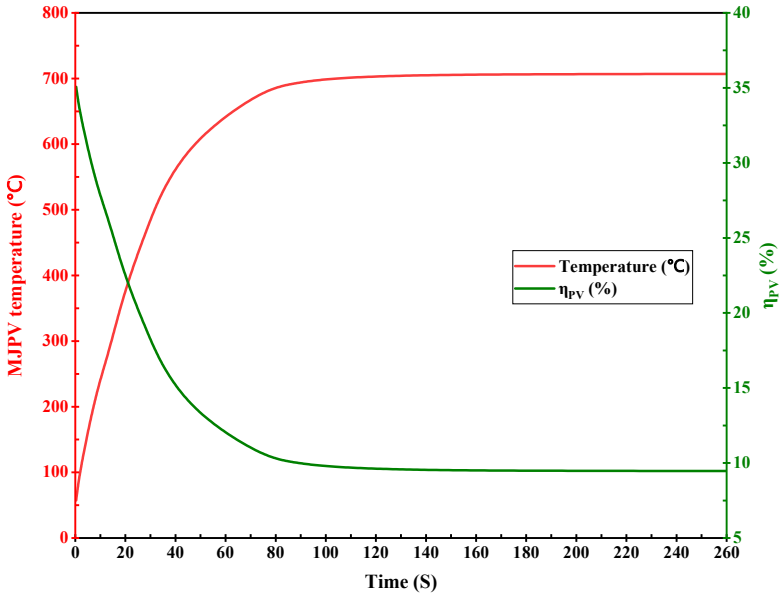

Fig. 7.1: Variation of cell temperature and electrical efficiency over time under no cooling conditions at a given ambient temperature

7.3 Experimental Results and Validation of Simulation

This section compares the results obtained from the experimental investigation and the numerical simulation of the 3D steady-state CPVT model. The CPVT model was tested and simulated under various design parameters to optimize its performance and identify its design limitations. The effects of these parameters on the thermal and electrical efficiencies of the CPVT model are discussed in detail. Moreover, the validity of the developed

computational model was examined by comparing it with the experimental results of the CPVT model. The following equation is used to calculate the percentage deviation between numerical simulation results and experimental results:

$$Dev\ (\%) = \left|\frac{EXP - SIM}{EXP}\right| \times 100 \tag{7.1}$$

7.3.1 Effect of Mass Flow Rate on Temperature Difference of the HTF

Figure 7.2 shows the effect of varying the mass flow rate of HTF on the temperature difference (ΔT) between the inlet and outlet of HTF, which was measured experimentally and predicted by simulation. The temperature difference decreases as the mass flow rate of HTF increases. The experimental and simulation results are in good agreement, with a maximum deviation of 11.0%. The slight discrepancy between the two results is attributed to the heat and optical losses in the experimental model and the nonuniformity of the irradiance distribution. The trend reveals that ΔT experiences a decline with increasing mass flow rate, ranging from 17.1 $°C$ at a flow rate of 0.0013 kg/s to approximately 1.15 $°C$ at a flow rate of 0.025 kg/s. These results underscore the significance of the HTF mass flow rate in regulating the temperature difference within the CPVT model, demonstrating its potential for influencing the system's thermal performance.

7.3.2 Effect of Mass Flow Rate on Average MJPV Cell Temperature

Figure 7.3 illustrates how the average temperature of the MJPV cells in the CPVT model changes with different mass flow rates. The figure shows that as the mass flow rate increases, the average temperature of the MJPV cells decreases in both experimental and numerical data. This phenomenon occurs because a higher mass flow rate enhances heat

transfer through convection, removing more heat from the CPVT model and consequently decreasing the average cell temperature.

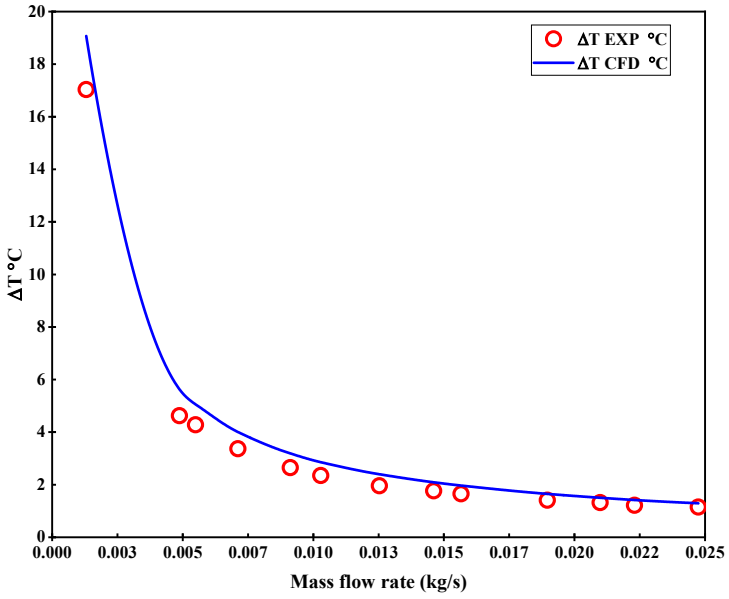

Fig. 7.2: The temperature difference between the inlet and outlet of the HTF at various mass flow rates

However, there is a discrepancy between the numerical and experimental values due to the nonuniformity effects. This is because achieving a uniform distribution of solar irradiance intensity on all MJPV cells in the CPVT model is complex. Specifically, MJPV cells located in the first and third paths receive less radiation flux than those in the central path, and this is even worse for the four MJPV cells placed in the corners, which receive about 56% less radiation flux than the cells in the center. Moreover, the inlet temperature of the HTF could not be controlled at a constant level in the experiment, unlike in the simulation. Figure 7.3 also indicates that the highest average cell temperature was recorded at the lowest mass flow rate. It is important to highlight that the simulation was conducted

under HTF inlet conditions (temperature and flow rate) and with input radiation values equal to those measured experimentally.

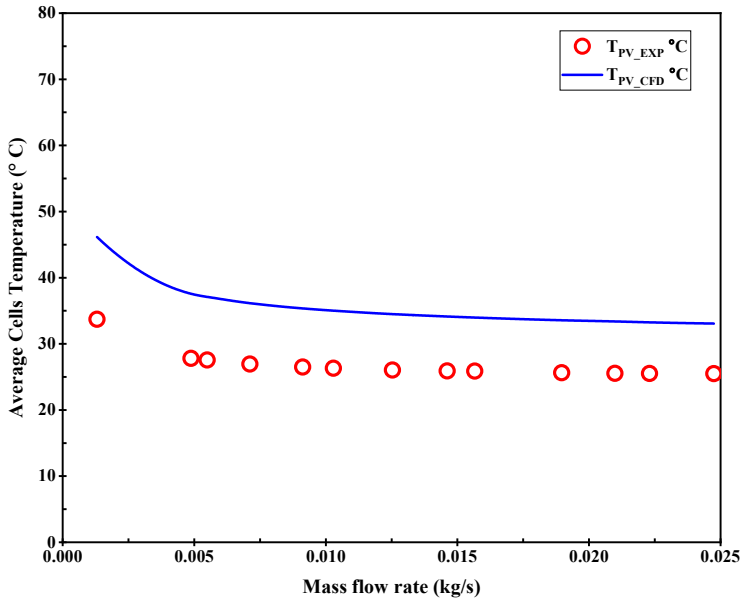

Fig. 7.3: Variation in average MJPV cell temperature versus mass flow rate

7.3.3 Effect of Mass Flow Rate on Efficiencies of the CPVT Model

The electrical and thermal efficiencies are significant parameters to evaluate the electrical and thermal performance of the CPVT model. In this section, we investigate the effect of the mass flow rate on these efficiencies. Figure 7.4 illustrates the changes in electrical and thermal efficiencies with the mass flow rates. We can observe that the electrical efficiency of the CPVT model increases significantly at low HTF flow rates and then levels off as the mass flow rate increases. The highest electrical efficiency is achieved at a mass flow rate of 0.025 *kg/s*; its value is 34.73% for experimental and 36.6% for numerical simulation. The experimental values of the electrical efficiency are comparable

with the corresponding numerical values over the entire range of the mass flow rate, with a maximum deviation of 5.4%. The slight difference is mainly due to the nonuniformity effects of the solar irradiance. Therefore, the experimental and numerical electrical efficiency curves in Fig. 7.4 agree well with each other qualitatively and quantitatively.

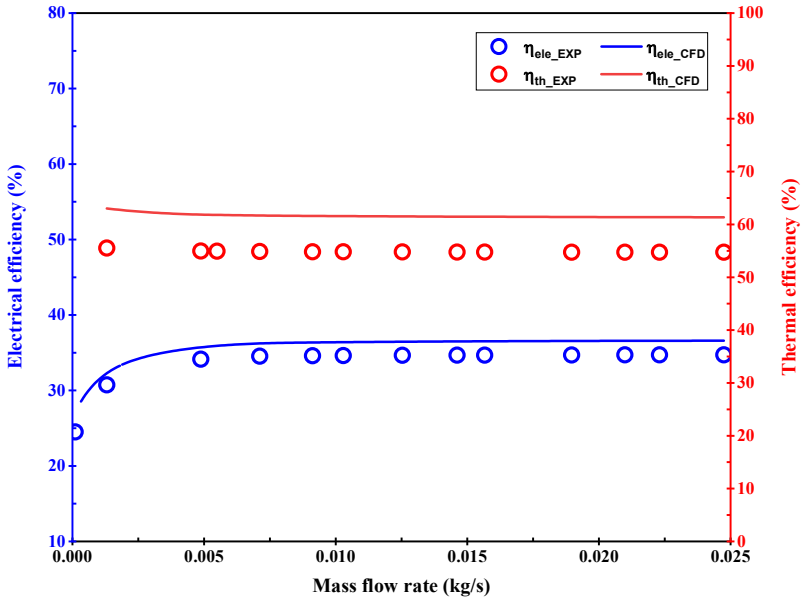

Fig. 7.4: Variation in the electrical and thermal efficiency versus mass flow rate

The thermal efficiency of the CPVT model decreases as the mass flow rate increases. However, this decrease is insignificant, and the thermal efficiency quickly reaches a plateau efficiency level after 0.005 *kg/s*. This flat behaviour is attributed to the low system temperatures. An increase in the mass flow rate of HTF would lead to better cooling of the MJPV solar cells, thereby increasing the photoelectric conversion efficiency. However, this rise in photoelectric conversion efficiency causes a decrease in thermal conversion. The average thermal efficiency of the experimental and numerical simulation was 54.7% and 61.4%, respectively. There was a maximum deviation of 12.1% between the two results.

As mentioned earlier, the slight discrepancy between the results is attributed to the nonuniformity effects, heat, and optical losses in the experimental model.

The electrical and thermal outputs of the CPVT system possess different qualities and values due to the principles outlined by the second law of thermodynamics. As a result, it is not appropriate to add them together to obtain a total energy output or overall energy efficiency as if they were equivalent based on the first law's perspective. Instead, the primary energy-saving (PES) efficiency is relied on as a meaningful metric to evaluate the CPVT system's performance. The concept of PES efficiency is explained in more detail in Chapter 4.

Figure 7.5 shows the PES efficiency plotted against the mass flow rate. The PES efficiency remains relatively unaffected by the mass flow rate and quickly reaches a plateau. The highest recorded PES efficiency is achieved at a mass flow rate of 0.025 *kg/s*, with values of 1.71 for the experimental model and 1.86 for the numerical simulation. The comparison between the experimental and numerical results shows a maximum deviation of 8.7%.

7.3.4 Effect of Mass Flow Rate on Power Output of the CPVT Model

The electrical and thermal power of the CPVT systems can be evaluated by calculating the output of the system. The output depends on the mass flow rate of the HTF that circulates through the system. Figure. 7.6 shows how the thermal and electrical power varies with the mass flow rate.

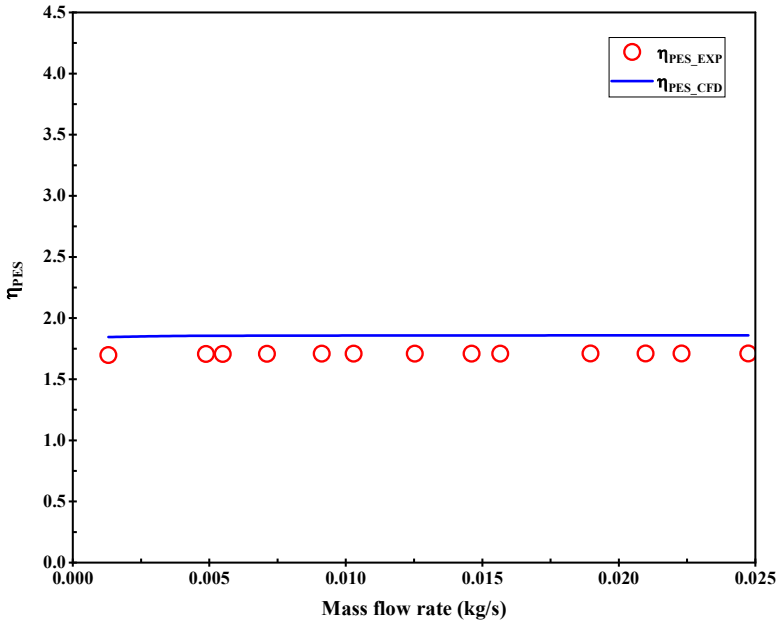

Fig. 7.5: Primary energy saving efficiency versus mass flow rate

The results show that the electrical power increases as the mass flow rate increases from 0.0013 to 0.01 *kg/s*. However, beyond this point, the electrical power only increases slightly with a further increase in the mass flow rate. On the other hand, the thermal energy decreases as the mass flow rate increases. The thermal energy is relatively insensitive to the mass flow rate and reaches a stable value after 0.005 *kg/s*. The maximum electrical and thermal power obtained from the CPVT model was 42.75 *W* and 67.89 *W*, respectively. The numerical simulation agreed with the experimental model, with a maximum deviation of 11.7% for the electrical power and 12.3% for the thermal energy.

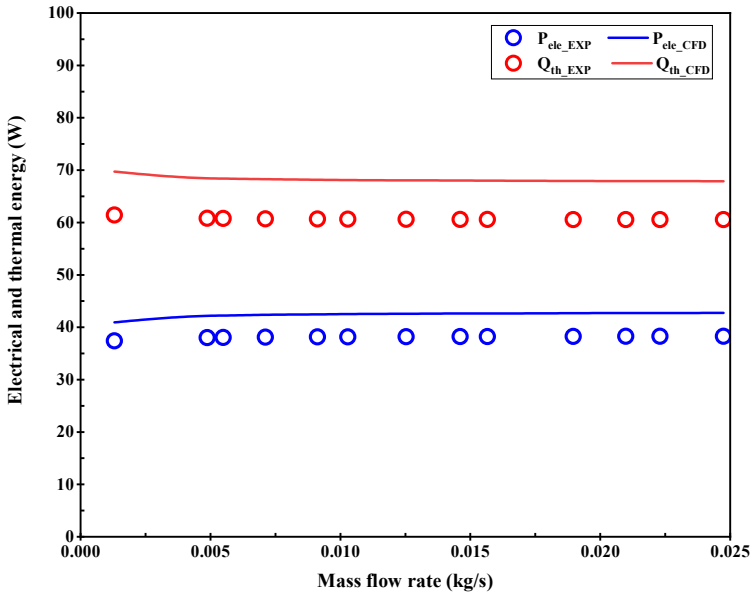

Fig. 7.6: Variation in the electrical and thermal energy versus mass flow rate

7.3.5 Variation of Convection Heat Transfer Coefficient in the CPVT Model

The heat transfer coefficient in CPVT systems is an essential indicator of attainable heat transfer rates. Qualitatively, the heat transfer coefficient tends to be higher in zones where flow is developing. Furthermore, improved temperature uniformity contributes to a more favourable heat transfer coefficient. Figure 7.7 illustrates the variation of the heat transfer coefficient in the CPVT model at different Reynolds numbers. The results indicate that the heat transfer coefficient increases with increasing Reynolds number, as higher fluid velocity enhances the heat transfer. The range of the heat transfer coefficient for Reynolds numbers up to 2000 was between 228 and 760 W/m^2K. The measured results showed good harmony with the predicted results, with minimal deviation.

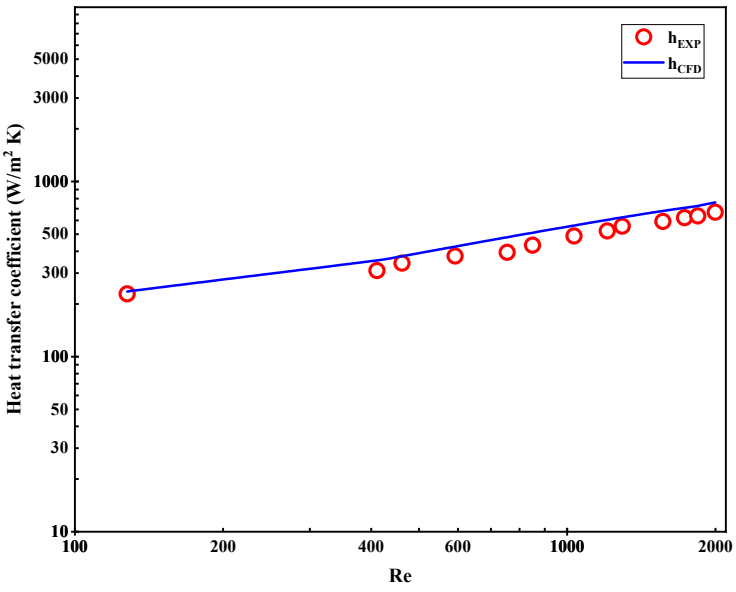

Fig. 7.7: Variation of convection heat transfer coefficient versus Reynolds numbers

7.3.6 Effect of Convection and Radiation Losses on the CPVT Model

Convection and radiation losses represent the primary sources of thermal inefficiency in CPVT systems, causing a reduction in the available energy for both thermal and electrical purposes. Convection losses occur due to the natural circulation of air around the upper surfaces of the MJPV cells and heat sinks, leading to heat dissipation from these areas. Conversely, radiation losses occur due to the emission of infrared radiation from the upper surfaces of the MJPV cells and heat sinks, which escapes to the surroundings. Notably, other outer surfaces of the CPVT model were fully isolated, resulting in negligible losses from these areas. The extent of convection and radiation losses is influenced by the temperature difference between the receiver and the ambient air and the geometry and orientation of the receiver itself. In this research, we experimentally investigated and numerically simulated the natural convection and radiation heat losses from the CPVT

model. Figure 7.8 illustrates the maximum radiation and natural convection heat losses for the CPVT system.

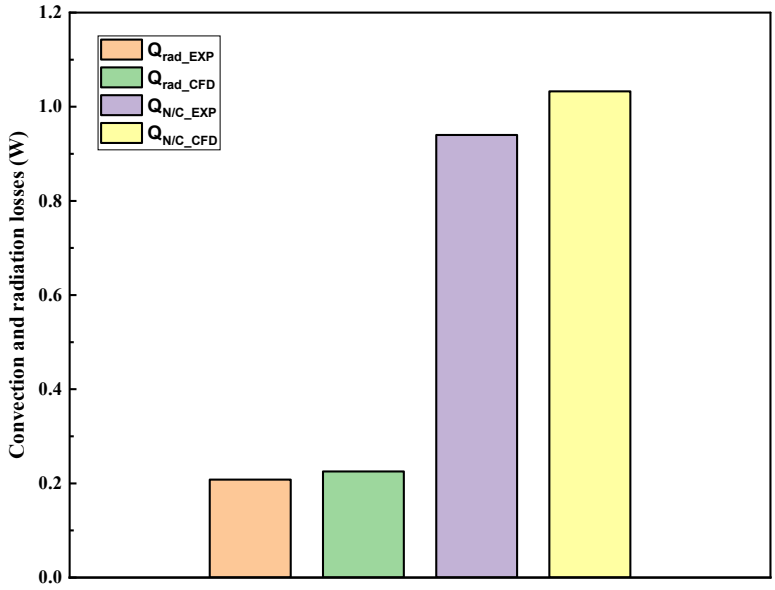

Fig. 7.8: Maximum radiation and natural convection heat losses for the CPVT model

It is evident from the graph that the natural convection heat losses are higher than the radiation losses. Still, the total losses are below 1.3 *W*. This is due to the small exposed area and the low temperature of the MJPV cells and heat sinks. The comparison between the experimental and numerical results reveals good agreement, further validating the accuracy of the numerical model.

7.3.7 Pumping Power for Different Flow Rates

Pressure drop is a crucial factor for thermal performance assessment, as it affects the overall efficiency of the CPVT systems by reducing the net power output. Therefore, the lower pressure drop is desirable to achieve higher efficiency. In this research, the pressure drop was measured using a differential pressure transducer and the pumping power was

calculated. Figure 7.9 illustrates the variation in pressure drop and pumping power with changes in the inlet mass flow rate.

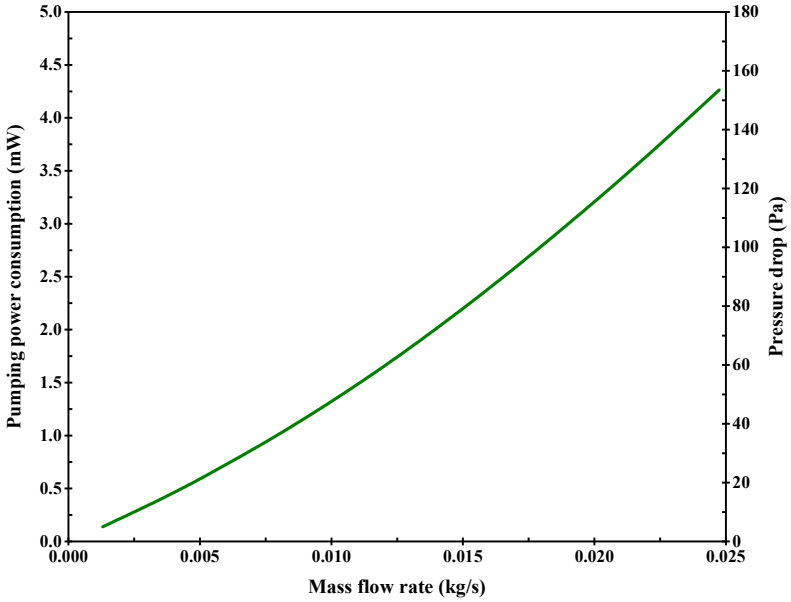

Fig. 7.9: Pressure drop and pumping power versus mass flow rates within the experimental range

The pressure drop and the pumping power increase with the increasing inlet mass flow rate. The pumping power required to overcome the pressure drop in the cooling channel is minimal, even at the maximum flow rate (4.5 mW), which is less than 0.011% of the produced electrical power under the same conditions. Therefore, this value is negligible compared to the output generated power.

7.3.8 Validation of the Numerical Model

CFD model validation aims to verify the accuracy and reliability of the simulation results of the CPVT model. As mentioned above, one of this experiment's challenges is obtaining a uniform concentrated irradiance on the surface of all MJPV cells. Efforts were dedicated to minimizing the losses due to non-uniform irradiance to an acceptable level.

An extra experiment was conducted to validate the CFD model. A uniform concentrated irradiance was obtained on the surface of the MJPV cells 6 and 7 located in the central path.

For the validation, a comprehensive comparison was made between the experimental and numerical results, ensuring that the same number of cells, geometry dimensions, material properties, operating, and boundary conditions were employed. The cell temperature at a steady state was considered a significant parameter for comparison. Figure 7.10 compares cell temperature between the CFD and experimental results. The analysis revealed a maximum deviation of approximately 4.58% between the experimental and CFD models. Conversely, the minimum deviation was a mere 1.14%, affirming that there is satisfactory agreement between the two sets of results. As such, the numerical model has been successfully validated and can now be confidently used to generate further results.

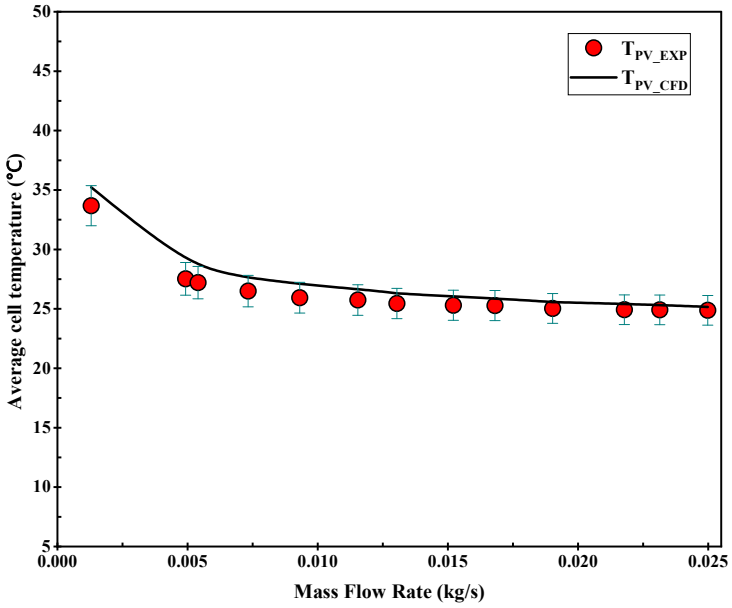

Fig. 7.10: Validation of the CFD model by comparing cell temperature with the experiment

7.4 Numerical Simulation Results

As discussed above, the experimental investigation of the CPVT model has validated the reliability of the computational code. To overcome the limitations posed by the experimental equipment, the same reliable model has now been extended to simulate a wider range of conditions, including laminar and turbulent flow regimes and various values of *CRs*, inlet HTF temperatures, and ambient temperatures. This part of the results will present and analyze the numerical simulation results.

7.4.1 Effects of Mass Flow Rate and *CRs* on HTF Outlet Temperature

Figures 7.11 and 7.12 display the variation of the outlet temperature versus mass flow rate of HTF and *CRs* for the laminar and turbulent flow regimes, respectively. From these figures, it can be seen that the outlet temperature decreases with increasing mass flow rate. The higher mass flow rate enhances the forced convection heat transfer and removes more heat from the HTF. However, the outlet temperature is very high at very low mass flow rates. This is because the heat removal rate through the flow channel is much lower than the heat gain from the heat sink and MJPV cells. Therefore, the HTF accumulates more thermal energy and reaches a higher temperature at the outlet. As the mass flow rate increases moderately, the outlet temperature drops sharply, as the increased volume of HTF takes away more heat in a shorter time. However, the outlet temperature becomes relatively stable at high mass flow rates as the heat removal rate reaches a maximum limit. The concentration ratio (*CR*) of the PFFL is another important parameter that affects the outlet temperature. A low *CR* can reduce the thermal performance of the CPVT system, while a

high *CR* can cause damage to the MJPV cells or boil the HTF inside the CPVT model, which is undesirable.

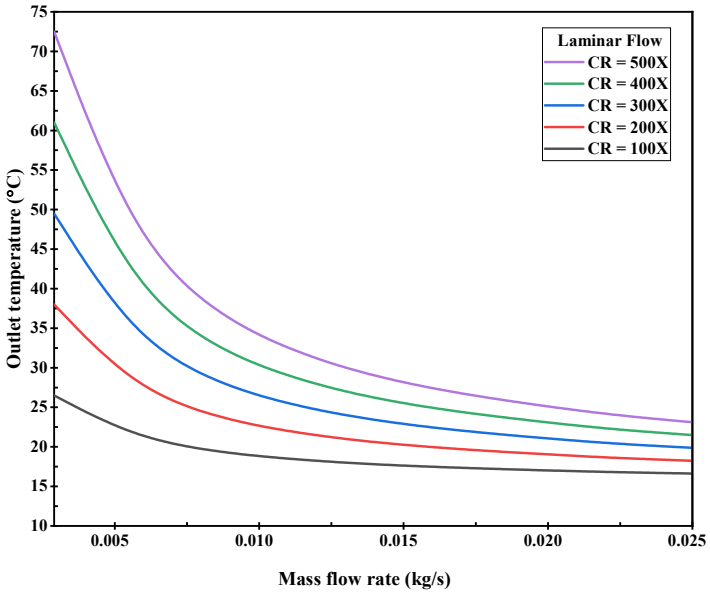

Fig. 7.11: Outlet temperature of the HTF at various mass flow rates and *CR* in the laminar flow

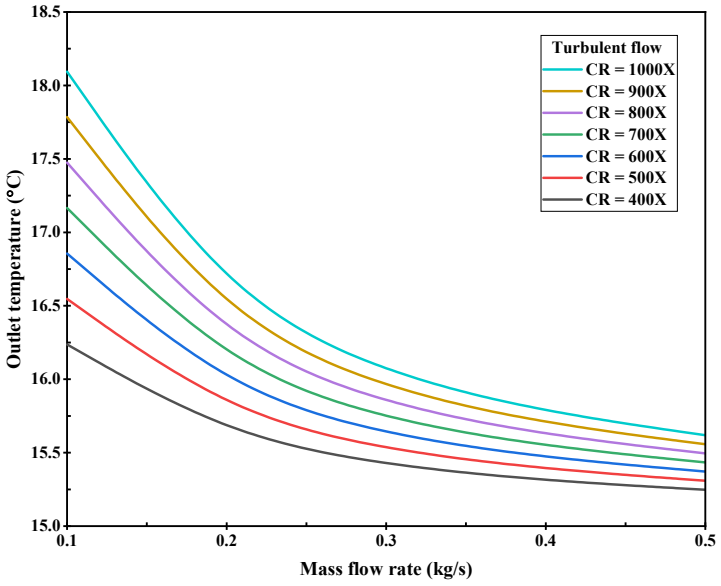

Fig. 7.12: Outlet temperature of the HTF at various mass flow rates and *CR* in the turbulent flow

Figures 7.11 and 7.12 show that the outlet temperature increases with increasing *CR* as more solar radiation is concentrated on the MJPV cells and heat sink. The highest outlet temperature in the laminar regime was observed at 72.5 *℃* at a mass flow rate of 0.0029 *kg/s* and a *CR* of 500X, while the highest outlet temperature in the turbulent regime was observed at 18.1 *℃* at a mass flow rate of 0.1 *kg/s* and a *CR* of 1000X.

7.4.2 Effects of Mass Flow Rate and *CRs* on MJPV Cell Temperature

Figure 7.13 shows the impact of mass flow rate and *CRs* on the average MJPV cell temperature for both laminar and turbulent flow regimes. The main findings from Fig.7.13 are that the cell temperature decreases with increasing mass flow rate, as the higher mass flow rate enhances the heat extraction by the coolant from the CPVT model. The cell temperature rises with increasing *CR* as more solar radiation is concentrated on the MJPV. This can cause damage to the solar cells or reduce their electrical output power. Therefore, some MJPV solar cell manufacturers have set a recommended operating temperature (ROT) for the MJPV at 110 *℃* to avoid overheating (AZURSPACE, 2014; Spectrolab, 2009). Additionally, the figure indicates that decreasing the MJPV cell temperature can be achieved by increasing the mass flow rate to a certain value beyond which it does not decrease further, as the thermal resistances of the CPVT model have reached their maximum limits.

In the laminar flow regime, the highest average cell temperature was observed at 179 *℃* at a mass flow rate of 0.0029 *kg/s* and a *CR* of 500X, while the lowest average cell temperature was observed at 38.9 *℃* at a mass flow rate of 0.025 *kg/s* and a *CR* of 100X. Similarly, the highest average cell temperature in the turbulent flow regime was observed

at 200.8 ℃ at a mass flow rate of 0.1 *kg/s* and a *CR* of 1000X. The lowest average cell temperature was observed at 86.9 ℃ at a mass flow rate of 0.5 *kg/s* and a *CR* of 400X.

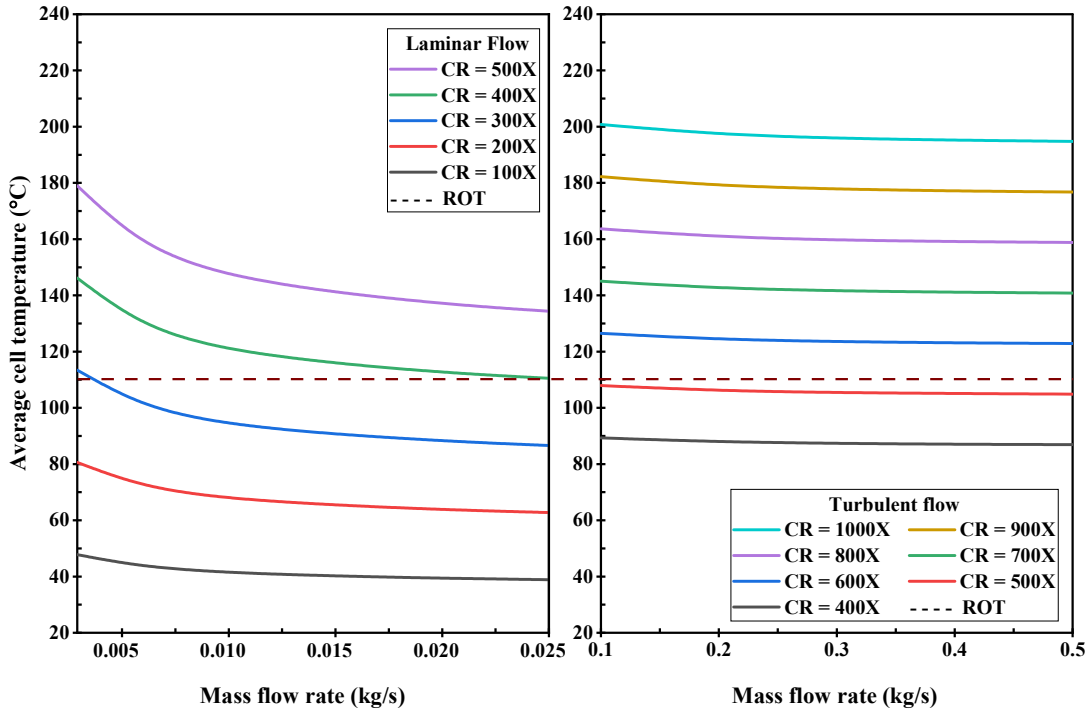

Fig. 7.13: Average solar cell temperature variation with mass flow rate and *CRs* for laminar and turbulent regimes

Figure 7.14 presents the variation of the average solar cell temperature with *CRs* at the maximum mass flow rate of the HTF for both laminar and turbulent flow regimes. It can be seen that the average cell temperature increases with increasing *CR* as more solar radiation is concentrated on the MJPV. In the laminar flow regime (left side of the graph), the highest average cell temperature was observed at 134.4 ℃ at a mass flow rate of 0.025 *kg/s* and a *CR* of 500X. In comparison, in the turbulent flow regime (right side of the graph), the highest average cell temperature was observed at 194.7 ℃ at a mass flow rate of 0.5 *kg/s* and a *CR* of 1000X.

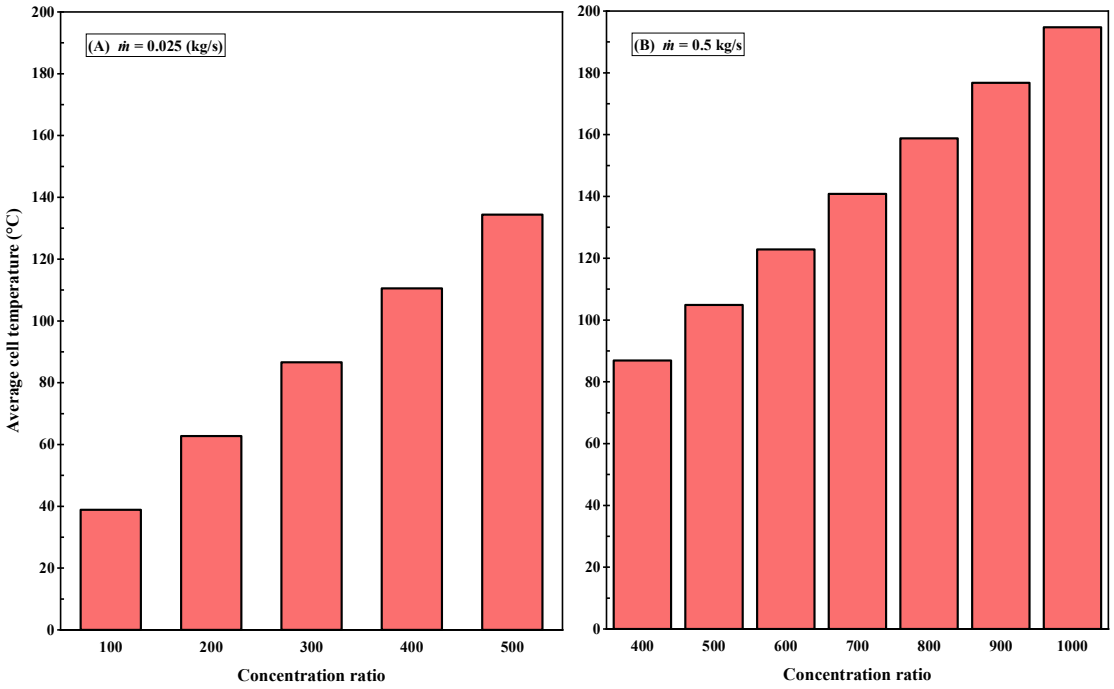

Fig. 7.14: Average solar cell temperature variation with *CRs* at a maximum mass flow rate for laminar and turbulent regimes

7.4.3 Effect of Mass Flow Rate on Average Pipe Wall Temperature

Figure 7.15 presents the average pipe wall temperature of the CPVT model at various *CRs* and mass flow rates for both laminar and turbulent flow regimes. As the figure shows, the average wall temperature experiences a significant decrease with an increased mass flow rate. This decline in temperature is attributed to the higher mass flow rate, which enhances heat extraction by the HTF from the pipe walls. Additionally, the figure highlights that the average pipe wall temperature increases with higher *CRs* due to the intensified concentration of solar radiation intensity, leading to increased heat generation through the MJPV solar cells. In the laminar flow regime, the highest average pipe wall temperature

was recorded at 57.7°*C*, occurring at a mass flow rate of 0.0029 *kg/s* and a *CR* of 500X. Conversely, the lowest average pipe wall temperature was observed at 17.2°*C* for a mass flow rate of 0.025 *kg/s* and a *CR* of 100X. Similarly, within the turbulent flow regime, the highest average pipe wall temperature was noted at 17.3°*C* with a mass flow rate of 0.1 *kg/s* and a *CR* of 1000X. On the other hand, the lowest average pipe wall temperature was observed at 15.3°*C* with a mass flow rate of 0.5 *kg/s* and a *CR* of 400X.

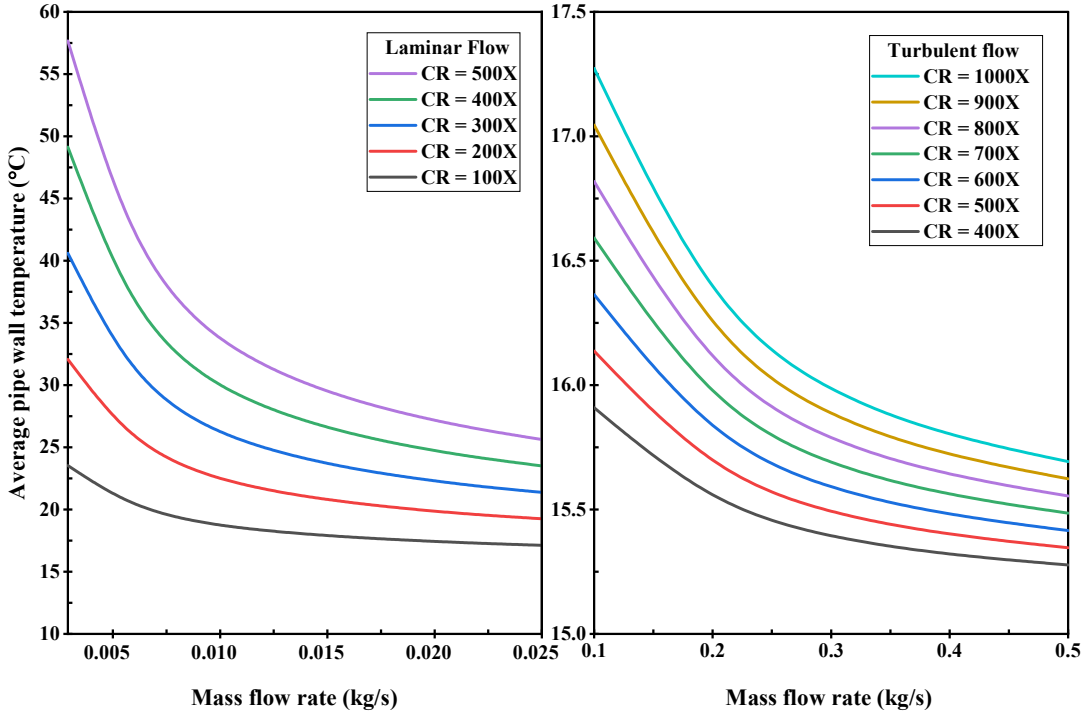

Fig. 7.15: Average pipe wall temperature variation with mass flow rate and *CRs* for laminar and turbulent regimes

7.4.4 Effect of Mass Flow Rate on the Efficiencies of the CPVT Model

The electrical and thermal efficiencies are significant parameters to evaluate the electrical and thermal performance of the CPVT model. Figure 7.16 shows the variation in the electrical efficiency of the CPVT model against increasing mass flow rate and *CRs* for both laminar and turbulent flow regimes. From this figure, it can be seen that the electrical efficiency increases with increasing mass flow rate, as the higher mass flow rate allows the evacuation of more heat from the MJPV, thereby decreasing the operating temperature of the solar cells. However, the electrical efficiency levels off at high mass flow rates, as the flow residence time in the flow channel is shorter and the temperature reduction of the solar cells is less significant. Moreover, the electrical efficiency decreases with increasing *CRs*, as more solar radiation is concentrated on the MJPV, thereby increasing the operating temperature of the solar cells. The electrical efficiency is inversely related to the cell temperature, as a higher temperature reduces the output voltage and increases the leakage current of the solar cells.

In the laminar flow regime, the highest electrical efficiency was recorded at 36.47%, occurring at a mass flow rate of 0.025 *kg/s* and a *CR* of 100X. The lowest electrical efficiency was observed at 25.56% for a mass flow rate of 0.0029 *kg/s* and a *CR* of 500X. In contrast, the highest electrical efficiency in the turbulent flow regime was 33.0% with a mass flow rate of 0.5 *kg/s* and a *CR* of 400X. The lowest electrical efficiency was observed at 25.72%, with a mass flow rate of 0.1 *kg/s* and a *CR* of 1000X.

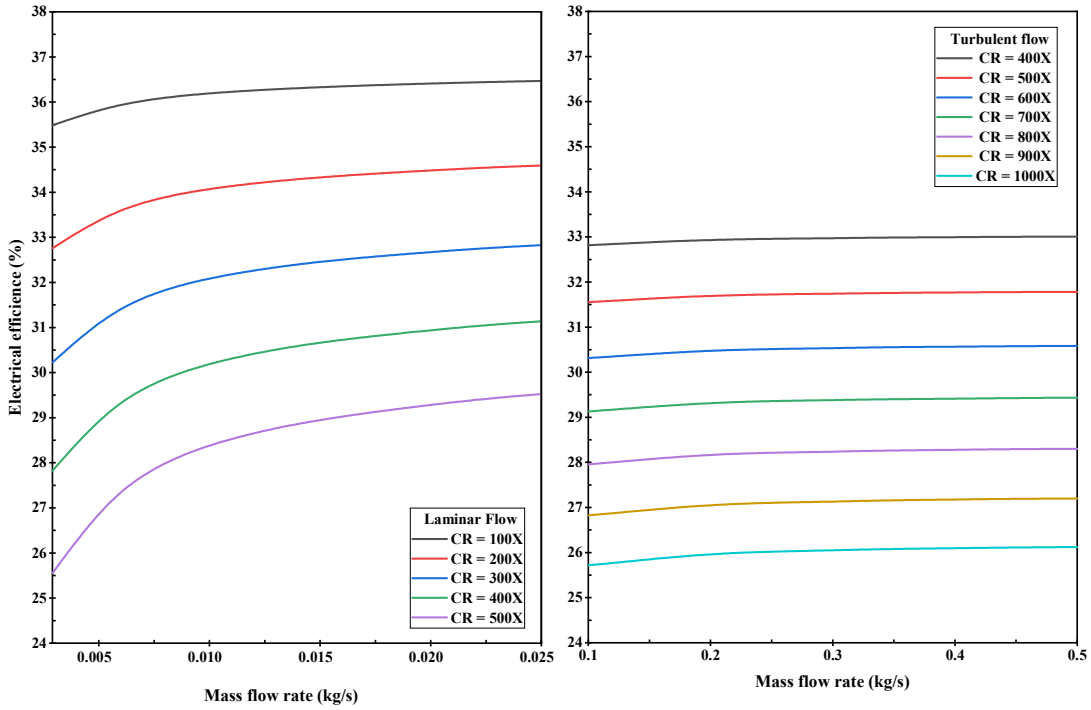

Fig. 7.16: Variation in electrical efficiency versus mass flow rate and *CRs* for laminar and turbulent regimes

Figure 7.17 shows the trend of thermal efficiency as a function of mass flow rate and *CRs* for both laminar and turbulent flow regimes in the CPVT model. This figure shows that the thermal efficiency decreases with increasing mass flow rate, as the higher mass flow rate cools the MJPV solar cells better, thereby increasing the photoelectric conversion efficiency. Consequently, it decreases the portion of irradiance converted into thermal energy. However, the thermal efficiency levels off at high mass flow rates as the heat removal rate reaches a maximum limit. Moreover, the thermal efficiency increases with increasing *CRs*, as more solar radiation is concentrated on the MJPV, causing an increase in the MJPV temperature, making more heat available for thermal conversion.

In the laminar flow regime, the highest thermal efficiency was recorded at 73.0%, occurring at a mass flow rate of 0.0029 *kg/s* and a *CR* of 500X, while the lowest thermal efficiency was observed at 61.5% for a mass flow rate of 0.025 *kg/s* and a *CR* of 100X. In contrast, in the turbulent flow regime, the highest thermal efficiency was 72.85%, with a mass flow rate of 0.1 *kg/s* and a *CR* of 1000X, while the lowest thermal efficiency was observed at 65.2%, with a mass flow rate of 0.5 *kg/s* and a *CR* of 400X.

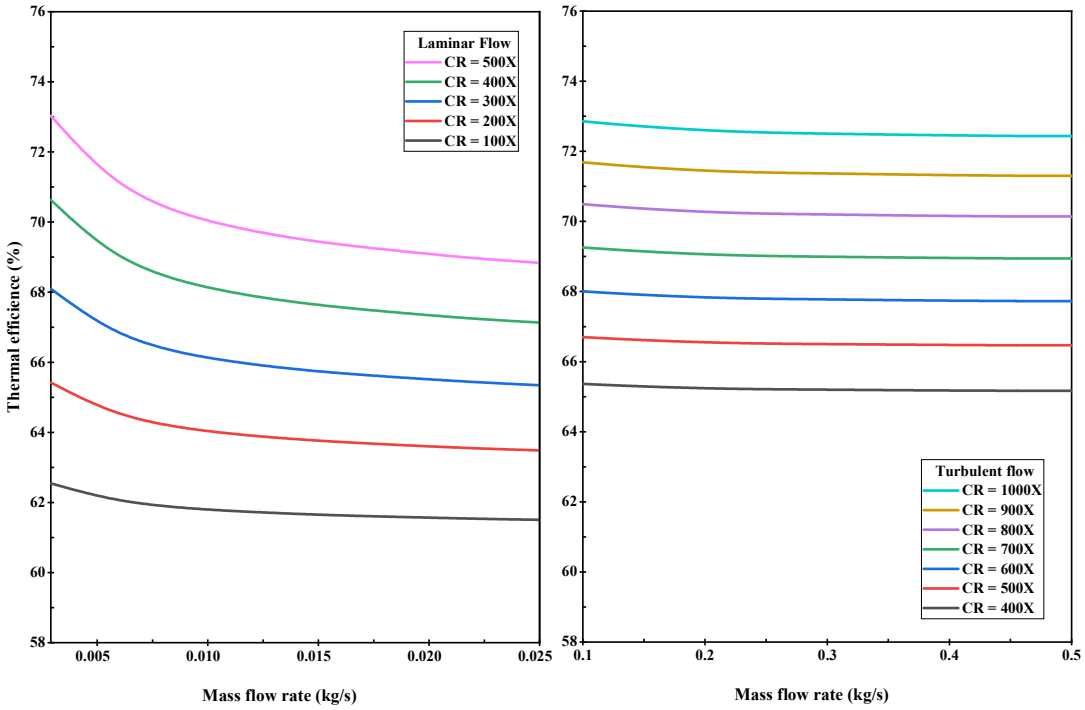

Fig. 7.17: Variation in thermal efficiency versus mass flow rate and *CRs* for laminar and turbulent regimes

Figure 7.18 provides an overview of the PES efficiency of the CPVT model at different *CRs* and mass flow rates for both laminar and turbulent flow regimes. The PES efficiency exhibits an increasing trend across both laminar and turbulent flow regimes with an increase in the mass flow rate.

The mass flow rate has a more pronounced influence on the PES efficiency in the laminar flow regime compared to the turbulent flow regime. This is attributed to the longer flow residence time in the laminar flow, allowing for more significant heat extraction and consequent improvement in efficiency. Furthermore, the PES efficiency decreases as the *CRs* increase. This is due to the concentration of more solar radiation on the MJPV cells, increasing their operating temperature. As the cell temperature rises, the electrical efficiency decreases, ultimately impacting the PES efficiency.

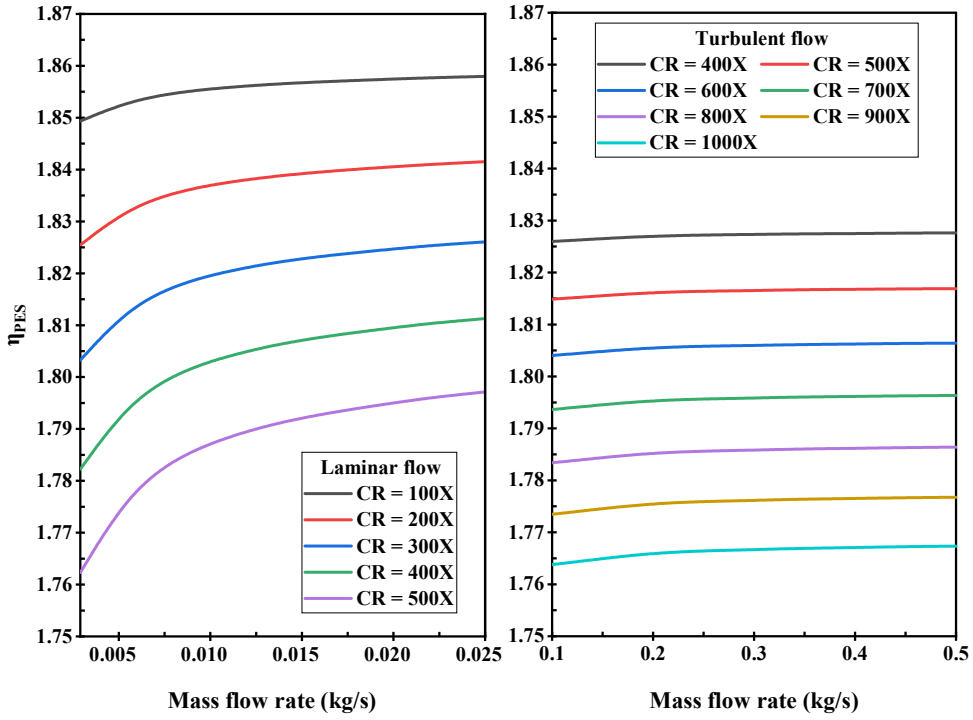

Fig. 7.18: Variation in PES efficiency versus mass flow rate and *CRs* in the CPVT model

Analyzing the results presented in Fig. 7.18, the highest recorded PES efficiency in the laminar flow regime was 1.858, observed at a mass flow rate of 0.025 *kg/s* and a *CR* of 100X. Conversely, the lowest PES efficiency was noted at 1.762, achieved with a mass

flow rate of 0.0029 *kg/s* and a *CR* of 500X. Similarly, the highest PES efficiency in the turbulent flow regime was 1.827, attained with a mass flow rate of 0.5 *kg/s* and a *CR* of 400X. On the other hand, the lowest PES efficiency was observed at 1.764, occurring with a mass flow rate of 0.1 *kg/s* and a *CR* of 1000X.

7.4.5 Effect of Mass Flow Rate on the Power Output of the CPVT Model

In this research, the extracted electrical and thermal energy of the CPVT model has been evaluated. Figures. 7.19 and 7.20 display the variation of the electrical power output versus the mass flow rate of HTF and *CRs* for the laminar and turbulent flow regimes in the CPVT model. As observed in the figures, the electrical power produced exhibits synchronization with the evolution of the mass flow rate and *CRs*. The results indicate that the electrical energy increases as the mass flow rate rises from 0.0029 to 0.01 *kg/s*. However, beyond this range, the electrical power only slightly increases despite further increases in the mass flow rate.

Additionally, Fig. 7.21 demonstrates the variation of electrical energy with *CRs* at the maximum mass flow rate of the HTF for both laminar and turbulent flow regimes. It becomes evident that the electrical power increases with higher *CRs*, as more solar radiation is concentrated on the MJPV cells. The highest recorded electrical energy in the laminar flow regime was 220 *W*, occurring at a mass flow rate of 0.025 *kg/s* and a *CR* of 500X. In comparison, in the turbulent flow regime, the highest electrical energy was observed at 389.3 *W*, achieved with a mass flow rate of 0.5 *kg/s* and a *CR* of 1000X.

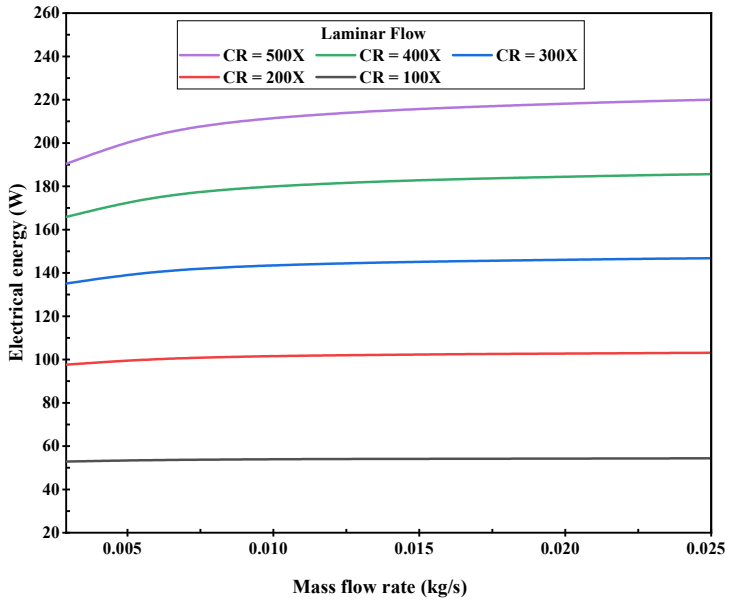

Fig. 7.19: Variation of the electrical energy against increasing mass flow rate and *CR* in the laminar flow

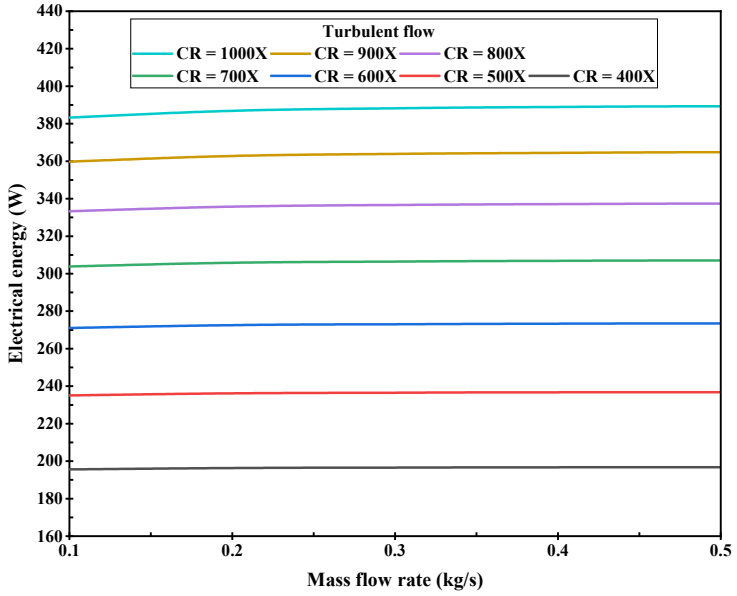

Fig. 7.20: Variation of the electrical energy against increasing mass flow rate and *CR* in the turbulent flow

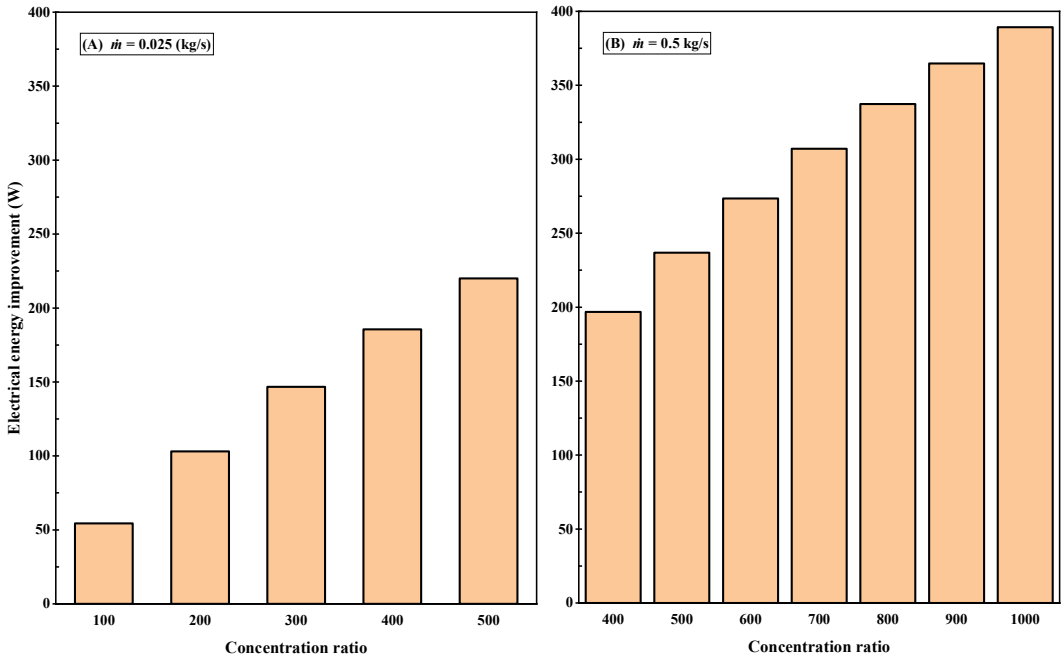

Fig. 7.21: Electrical energy variation with *CRs* at a maximum mass flow rate for laminar and turbulent regimes

Furthermore, Figures 7.22 and 7.23 illustrate the variation of thermal power output concerning the mass flow rate of HTF and *CRs* for both laminar and turbulent flow regimes in the CPVT model. The results reveal that the thermal energy decreases as the mass flow rate increases. After reaching a certain point, the thermal energy becomes relatively insensitive to further increases in the mass flow rate, stabilizing at a constant value. The highest thermal energy recorded in the laminar regime was 515.5 *W*, observed at a mass flow rate of 0.0029 *kg/s* and a *CR* of 500X. Similarly, in the turbulent flow regime, the highest thermal energy was observed at 1028.5 *W*, attained with a mass flow rate of 0.1 *kg/s* and a *CR* of 1000X.

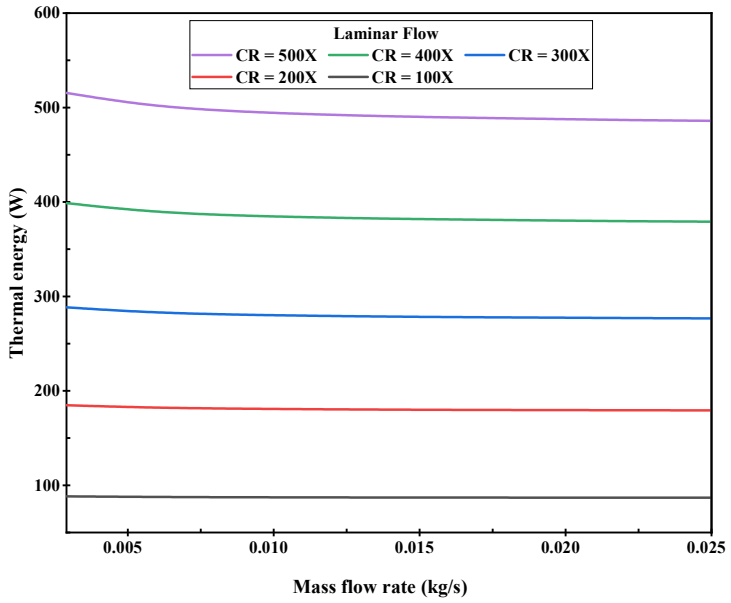

Fig. 7.22: Variation of the thermal energy against increasing mass flow rate and *CR* in the laminar flow

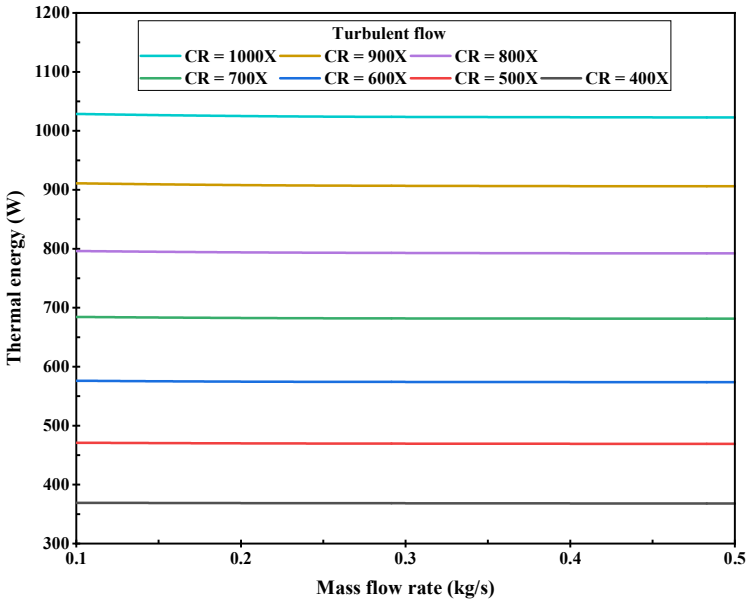

Fig. 7.23: Variation of the thermal energy against increasing mass flow rate and *CR* in the turbulent flow

Moreover, Fig. 7.24 shows how thermal energy changes with *CRs* at the maximum mass flow rate for both laminar and turbulent flow regimes. The figure demonstrates that the thermal energy increases with higher *CRs* as more solar radiation is concentrated on the

MJPV cells. In the laminar flow regime, the highest thermal energy was recorded at 485.9 *W*, occurring at a mass flow rate of 0.025 *kg/s* and a *CR* of 500X. Similarly, in the turbulent flow regime, the highest thermal energy was observed at 1022.5 *W*, achieved with a mass flow rate of 0.5 *kg/s* and a *CR* of 1000X.

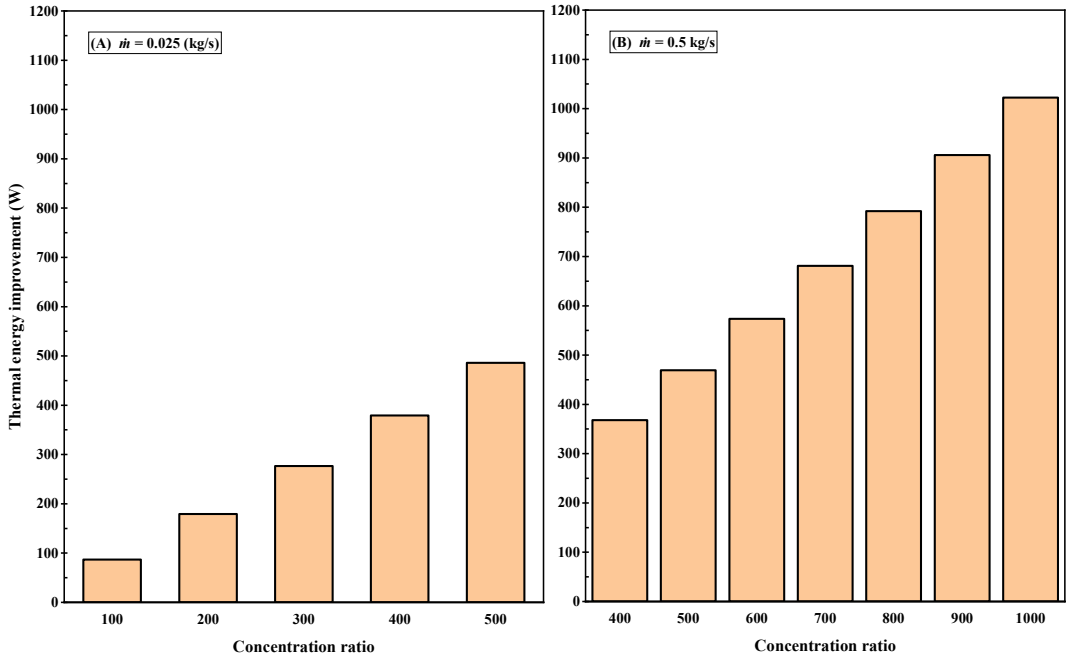

Fig. 7.24: Thermal energy variation with *CRs* at a maximum mass flow rate for laminar and turbulent regimes

7.4.6 Variation of Convection Heat Transfer Coefficient in the CPVT Model

The forced heat transfer coefficient in CPVT systems is an important parameter that affects the system's thermal performance. In this section, we numerically evaluate the forced heat transfer coefficient in CPVT systems under different conditions. Figure 7.25 shows the forced heat transfer coefficient variation in the CPVT model at different Reynolds numbers and *CRs* for the laminar and turbulent flow regimes.

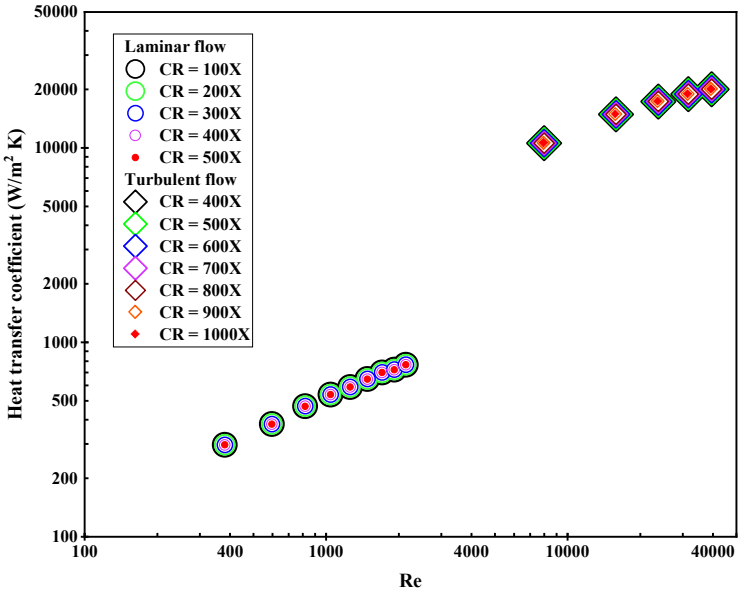

Fig. 7.25: Variation of convection heat transfer coefficient versus Reynolds numbers and *CRs*

It can be observed that the forced heat transfer coefficient in the CPVT model increases with the increase in the Reynolds number for both laminar and turbulent regions. A higher Reynolds number implies a higher fluid velocity, which enhances the heat transfer rate from the MJPV cells to the HTF. The heat transfer coefficient for the laminar flow ranged from 405 to 1044 W/m^2K, while the turbulent flow, the range was significantly higher, spanning from 14408 to 27310 W/m^2K. Interestingly, Fig. 7.25 reveals that *CRs* have no effect on the heat transfer coefficient.

7.4.7 Effect of Convection and Radiation Losses on the CPVT Model

Convection and radiation losses are the primary sources of thermal inefficiency in CPVT systems, as they reduce the energy available for both thermal and electrical purposes. Convection losses happen when air flows naturally around the upper surfaces of the MJPV cells and heat sinks, taking away some heat. Radiation losses occur when the upper surfaces

of the MJPV cells and heat sinks emit infrared radiation into the environment. Other outer surfaces of the CPVT model are assumed to be adiabatic surfaces, which means they do not lose any heat. In this research, we numerically evaluated the natural convection and radiation heat losses from the CPVT model.

Figure 7.26 shows the maximum and minimum radiation and natural convection heat losses for the CPVT system in the laminar flow under *CRs* 100X and 500X. The bar graph shows that the natural convection heat losses are higher than the radiation losses. The natural convection heat transfer coefficient is larger than the radiation heat transfer coefficient. The highest natural convection heat loss is 6.74 *W*, which occurs at a *CR* of 500X.

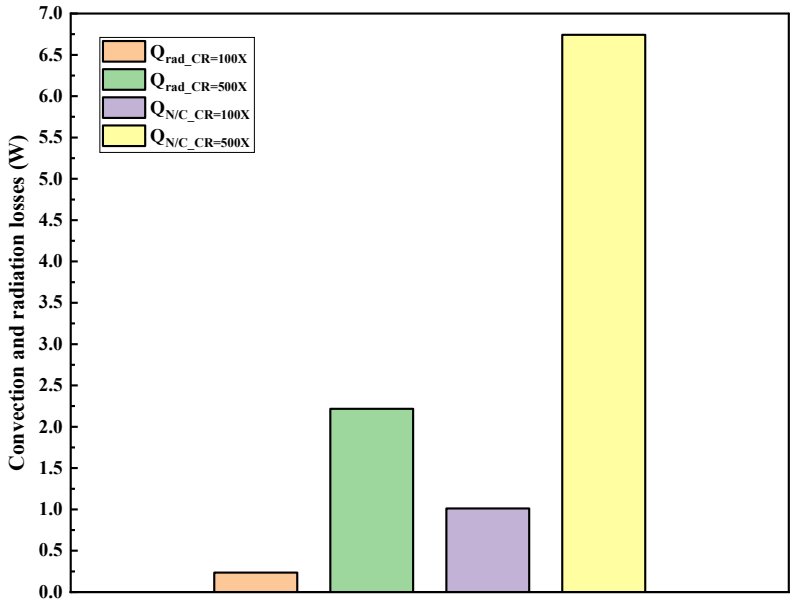

Fig. 7.26: Maximum and minimum radiation and natural convection losses in laminar flow

Figure 7.27 shows the maximum and minimum radiation and natural convection heat losses for the CPVT system in the turbulent flow under *CRs* 400X and 1000X. The bar graph shows that the natural convection heat losses are higher than the radiation losses for the same reason as in Fig. 7.26. The highest natural convection heat loss is 5.87 *W*, which occurs at a *CR* of 1000X.

Figure 7.28 compares the maximum radiation and natural convection heat losses for the CPVT system in both laminar and turbulent flow under the same *CR* of 500X. The bar graph shows that both types of heat losses are higher in laminar flow than in turbulent flow. This is because laminar flow has a thicker thermal boundary layer and slower heat transfer, which leads to a higher surface temperature and higher heat losses than turbulent flow. The highest radiation and natural convection heat losses in laminar flow are 2.22 *W* and 6.74 *W*, respectively. Moreover, all figures above show that both types of heat losses increase with higher *CRs*, as more solar radiation is concentrated on the MJPV cells, leading to higher surface temperature.

7.4.8 Effect of Inlet HTF Temperature on the Performance of the CPVT Model

The performance of the CPVT model depends on the inlet HTF temperature. In this research, we numerically investigated the influence of inlet HTF temperature on the performance of the CPVT model. We varied the inlet HTF temperature from 5 to 40 $°C$ while keeping the mass flow rate at 0.0112 *kg/s*, the ambient temperature at 15 $°C$, the irradiation level at 1000 W/m^2, and the *CR* at 300X.

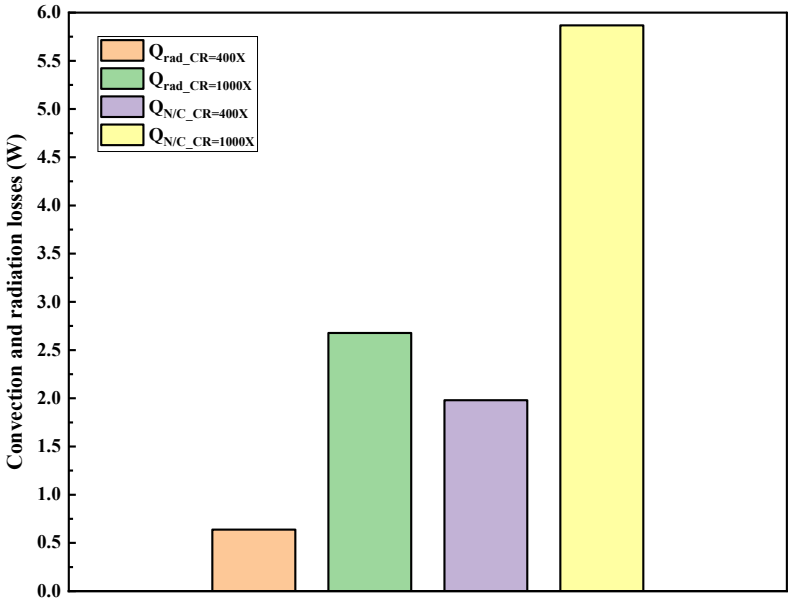

Fig. 7.27: Maximum and minimum radiation and natural convection losses in turbulent flow

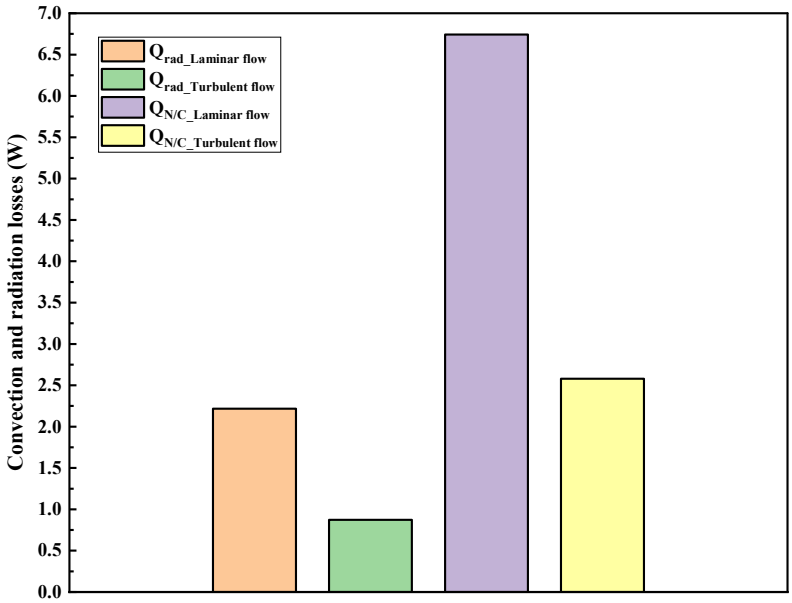

Fig. 7.28: Heat losses in laminar and turbulent flow under *CR* 500X

Figure7.29 shows how the inlet HTF temperature affects the average MJPV cell temperature. We can see that the MJPV cell temperature increases with increasing inlet

HTF temperature. This is because a higher inlet HTF temperature reduces the heat extraction by the HTF from the MJPV cells. Figure 7.29 also shows that the MJPV average temperature exceeds ROT (110 °*C*) at an inlet HTF temperature of 35 °*C*. Therefore, the inlet HTF average temperature should be 30 °*C* or less to maintain the MJPV cells within the safe operation limit.

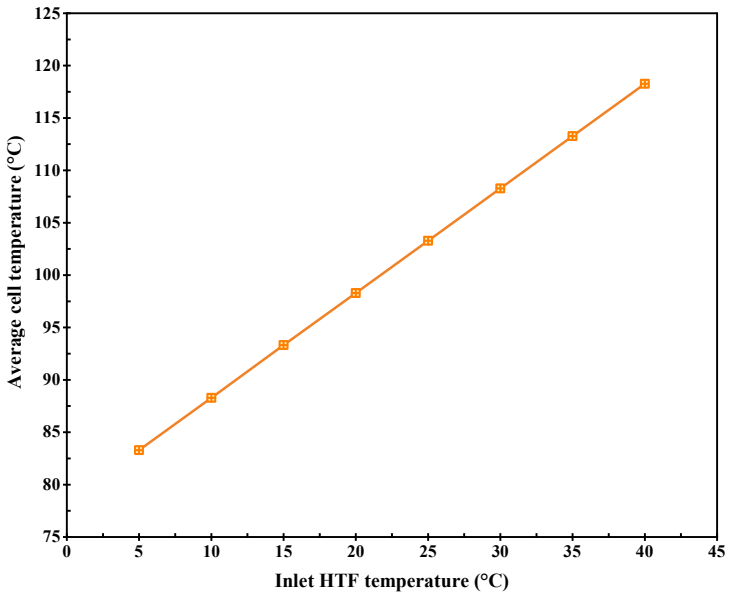

Fig. 7.29: Effect of inlet HTF temperature on the average MJPV cells temperature

Figure 7.30 displays the effect of the inlet HTF temperature on the electrical and thermal efficiency. It is evident that as the inlet HTF temperature increases from 5 °*C* to 40 °*C*, the electrical efficiency decreases from approximately 32.9% to about 30.6%, representing a reduction of 7%. Similarly, the thermal efficiency decreases from about 66.7% to around 64.3%, dropping 3.6%. This is because a higher inlet HTF temperature increases the MJPV cell temperature and reduces the heat transfer coefficient from the MJPV cells to the HTF, which lowers both electrical and thermal efficiency.

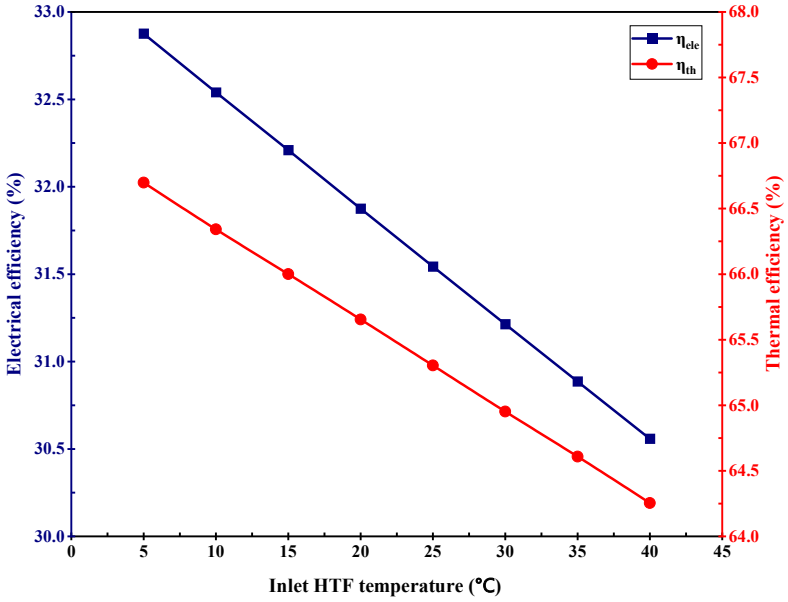

Fig. 7.30: Effect of inlet HTF temperature on the electrical and thermal efficiency of the CPVT model

Figure 7.31 shows how the inlet HTF temperature affects the electrical and thermal power output of the CPVT model. We can see that both power outputs decrease with increasing inlet HTF temperature. When the inlet HTF temperature increases from 5 to 40 $°C$, the electrical power decreases from about 147 W to about 136.6 W, with a reduction of 7.1 %, and the thermal power decreases from about 282.5 W to about 272.2 W, with a reduction of 3.65%. As explained above, the decrease in thermal power output can be attributed to the reduction in the heat transfer coefficient as the inlet HTF temperature rises.

Figure 7.32 illustrates the impact of the inlet HTF temperature on the Primary Energy-Saving (PES) efficiency of the CPVT model. The graph clearly shows that with an increase in the inlet HTF temperature from $5°C$ to $40°C$, the PES efficiency decreases from approximately 1.85 to 1.75, representing a reduction of 5.4%. The reason behind this behaviour lies in the fact that the PES efficiency of the CPVT model is directly derived

from both the electrical and thermal efficiencies of the system. Therefore, it exhibits a similar trend to these individual efficiencies. As the inlet HTF temperature increases, it leads to a decline in both electrical and thermal efficiencies, consequently decreasing overall PES efficiency.

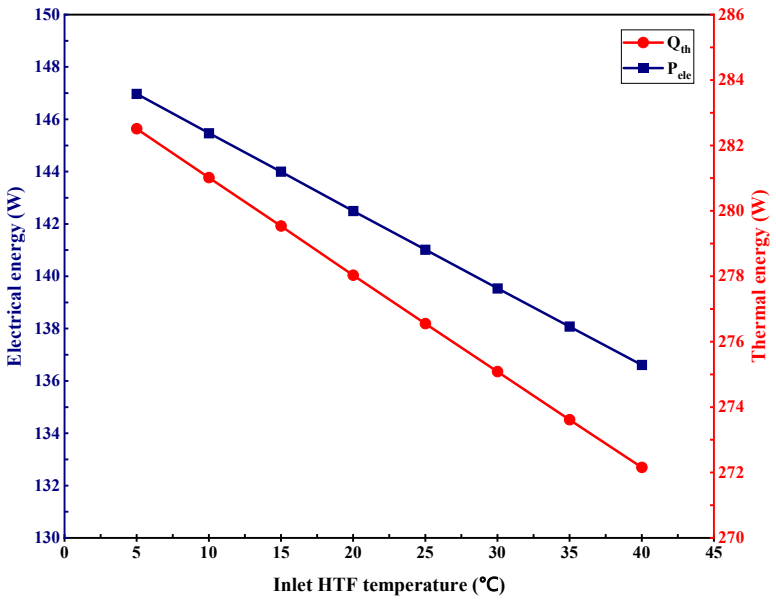

Fig. 7.31: Effect of inlet HTF temperature on the power output of the CPVT model

This research also studied the influence of inlet HTF temperature on the radiation and natural convection heat losses of the CPVT model. Figure 7.33 shows the relationship between the inlet HTF temperature and the heat losses due to radiation and natural convection. As the inlet HTF temperature increases, both heat losses also increase. When the inlet HTF temperature rises from 5 to 40 $°C$, the natural convection losses increase by 96 %, from about 2.02 W to about 3.96 W, and the radiation losses increase by 81 %, from about 0.58 W to about 1.05 W. These increases are attributed to the higher surface

temperature of the MJPV cells. Although these losses are relatively small, their magnitude is influenced by other parameters, such as mass flow rate and *CRs*.

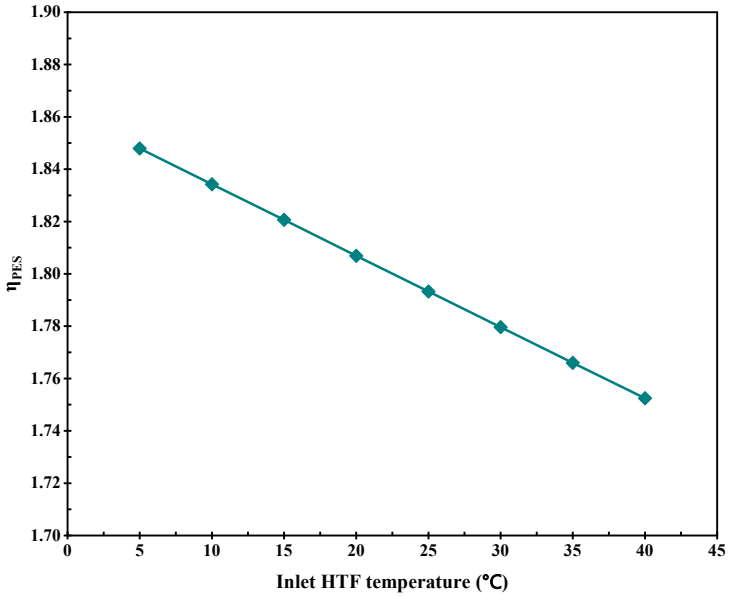

Fig. 7.32: Effect of inlet HTF temperature on the PES efficiency of the CPVT model

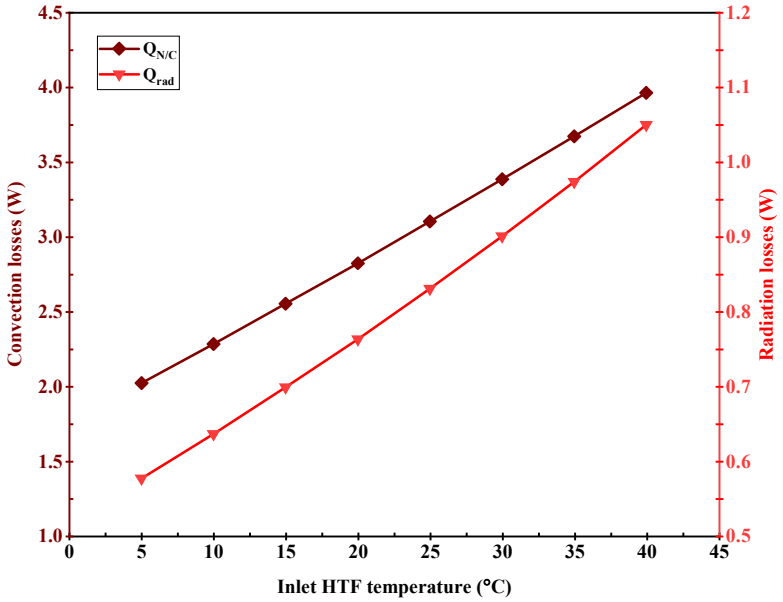

Fig. 7.33: Effect of inlet HTF temperature on the thermal losses of the CPVT model

7.4.9 Pressure Drop and Pumping Power Across the CPVT Model

Pressure drop is essential in the design of CPVT systems, as it can impact the system's overall efficiency by reducing the net power gain. This study assessed the pressure drop across the flow channel for both laminar and turbulent flow regimes. Figure 7.34 illustrates the pressure drop across the flow channel at various Reynolds numbers for both flow regimes in the CPVT model.

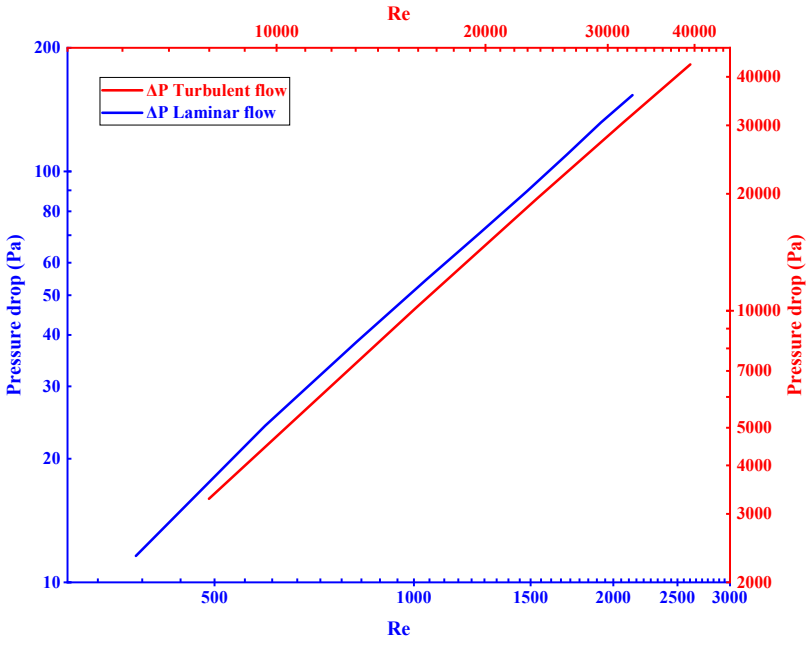

Fig. 7.34: Pressure drop across the CPVT model in laminar and turbulent flow

As expected, an increase in the Reynolds number leads to a corresponding increase in pressure drop for both laminar and turbulent flows. In the laminar flow, the highest pressure drop occurred at *Re* of 2137, measuring 153.4 *Pa*, while the lowest pressure drop was observed at *Re* of 380, measuring 11.6 *Pa*. Conversely, in the turbulent flow, the highest pressure drop was recorded at *Re* of 39458, measuring 43027 *Pa*, and the lowest pressure drop was observed at *Re* of 8000, measuring 3281 *Pa*. The turbulent flow exhibited a more

significant pressure drop than the laminar flow, leading to increased friction power. In addition, maintaining the MJPV cells at the desired working temperature requires additional power to circulate the HTF through the system. The numerical simulation extracted pressure drop values in the horizontal CPVT model, and the required pumping power to overcome the pressure loss was calculated using equation (4.37), with pump efficiency assumed to be 85%.

Figure 7.35 illustrates the variation in pressure drop and pumping power with changes in the inlet mass flow rate. The pumping power increases with increasing mass flow rate as more energy is needed to overcome the higher pressure drop. The maximum pumping power required to overcome the pressure drop in the cooling channel was observed at the maximum flow rate of 0.5 *kg/s*, measuring 26 *W*. This power requirement is available domestically, making additional pumping arrangements unnecessary.

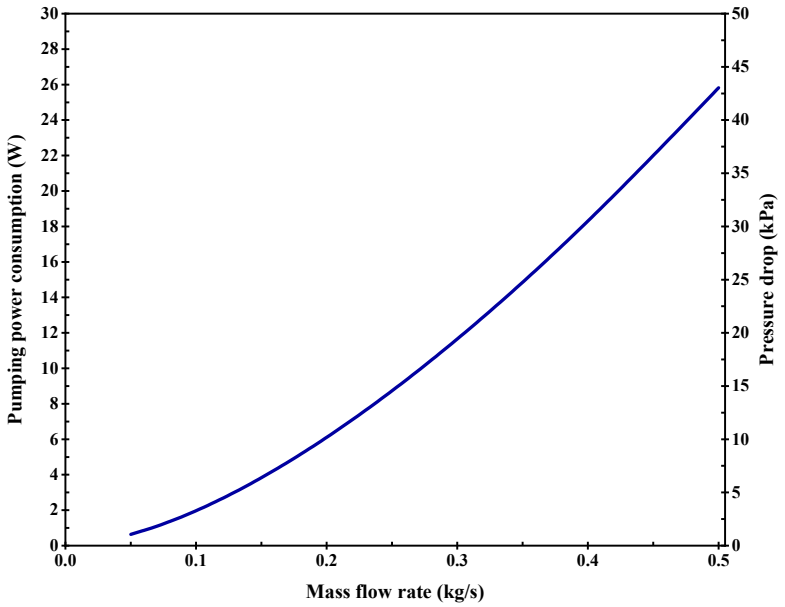

Fig. 7.35: Pressure drop and pumping power consumption versus mass flow rates

7.4.10 The Effect of the *CRs* on Power Gain and Material Reduction

The influence of *CRs* on the percentage power gain (*PPG*) and material reduction (*MR*) of the MJPV in the CPVT system was studied. The *PPG* of the CPVT system determines the percentage increase in electrical power output of the MJPV cells when using concentrators, compared to the reference power output of the MJPV cell without concentrators, typically obtained at the lowest or base concentration ratio available. The *MR* is the percentage decrease in the amount of MJPV cells needed for a given application when using concentrators, which can reduce the cost and environmental impact of the system. The *PPG* and *MR* are calculated using the following equations (Algareu, 2017):

$$PPG\ (\%) = \frac{P_{CR} - P_{ref}}{P_{ref}} \times 100 \tag{7.2}$$

$$MR\ (\%) = \left(1 - \frac{P_{ref}}{P_{CR}}\right) \times 100 \tag{7.3}$$

P_{CR} is the maximum power produced by the MJPV cell using concentrators, and P_{ref} is the reference power output of the MJPV cell. The *PPG* and *MR* of the MJPV cells in the CPVT system at different *CRs* are shown in Fig. 7.36 and Fig. 7.37, respectively. As seen in Fig. 7.36, the *PPG* increases with increasing *CR*, reaching 973.1% at *CR* = 500X. This means that the electrical power output of the MJPV cells is almost ten times higher when using concentrators. Figure 7.37 presents the possible *MR* of the MJPV cells under the same *CRs*. It is evident that The *MR* also increases with increasing *CR*, reaching up to 90.7% at *CR* = 500X. This means that only 9.3% of the original amount of MJPV cells is needed for the same application when using concentrators. This can significantly reduce the cost and

environmental impact of the system, as MJPV cells are expensive and require rare materials.

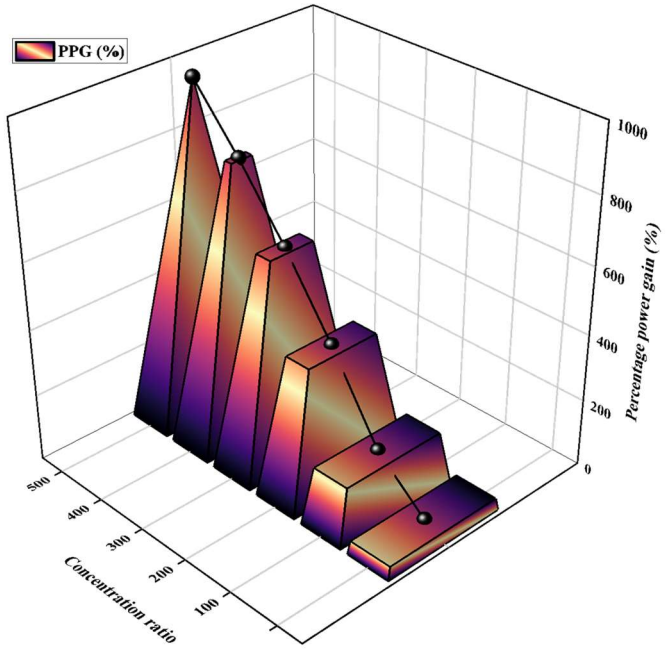

Fig. 7.36: Increase in percentage power gain of the CPVT model under various *CRs*

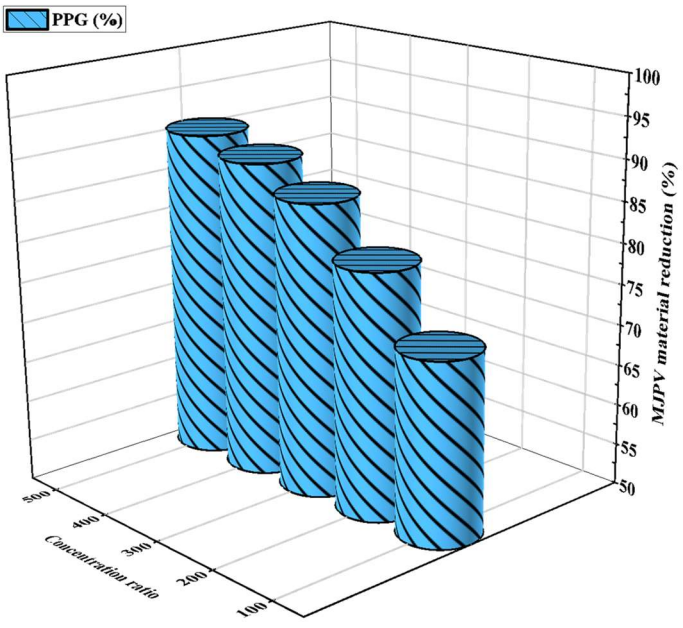

Fig. 7.37: MJPV material reduction under various *CRs*

Therefore, using concentrators can improve the performance and sustainability of CPVT systems by increasing the power gain and reducing the material consumption of MJPV cells. However, this also requires careful consideration of the cooling system and the optical losses that may occur at high *CRs*.

7.4.11 Effect of Pipe Curvature on Heat Transfer in the CPVT Model

In this research, the impact of pipe curvature (elbow bends) on heat transfer in the CPVT model at various mass flow rates within the laminar regime was numerically investigated. The flow channel in the CPVT model consists of four elbows, and to study the flow behaviour in elbows, we have to introduce the Dean number. This dimensionless group characterizes the effect of secondary flow on heat transfer in a curved pipe. The Dean number can be calculated from the following equation (Ghobadi & Muzychka, 2014):

$$De = Re\sqrt{\frac{D}{2R_C}} \tag{7.4}$$

Where Re is the Reynolds number, D is the tube diameter, and R_C is the radius of curvature of the curved tube. Figure 7.38 shows the temperature of the MJPV cells at different positions in the CPVT model at CR = 100X and various mass flow rates within the laminar regime. The upper part of the figure shows that at a low mass flow rate of the HTF, the cell temperature decreases with increasing mass flow rate; also, in all cases, cells 1 to 12 follow the same trend. However, when the Dean number reaches 112, the secondary flow starts to appear, as shown in the lower part of the figure, and the trend changes, with cell numbers

5 and 9 experiencing a decrease in temperature. Figure 7.39 further highlights the declining temperature of cell numbers 5 and 9 in the CPVT model.

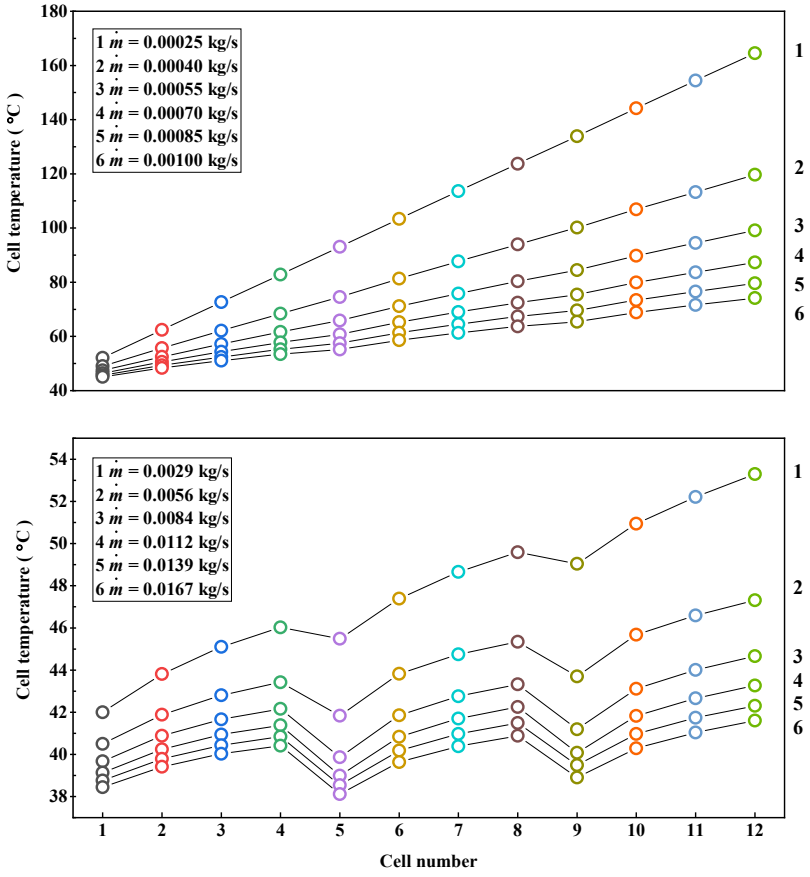

Fig. 7.38: The cell temperature according to its position in the CPVT model at CR = 100X and at different mass flow rates

This temperature decrease is attributed to the phenomenon of secondary flow that occurs in curved tubes, such as pipes with elbows. The secondary flow results from the centrifugal force caused by the curvature of the pipe, leading to the formation of vortices or swirling motion of the HTF within the pipe. When the HTF encounters a curved section or an elbow in the pipe, its direction changes. As it moves around the curve, the HTF

experiences inward acceleration towards the center of the curve due to the centrifugal force, creating vortices.

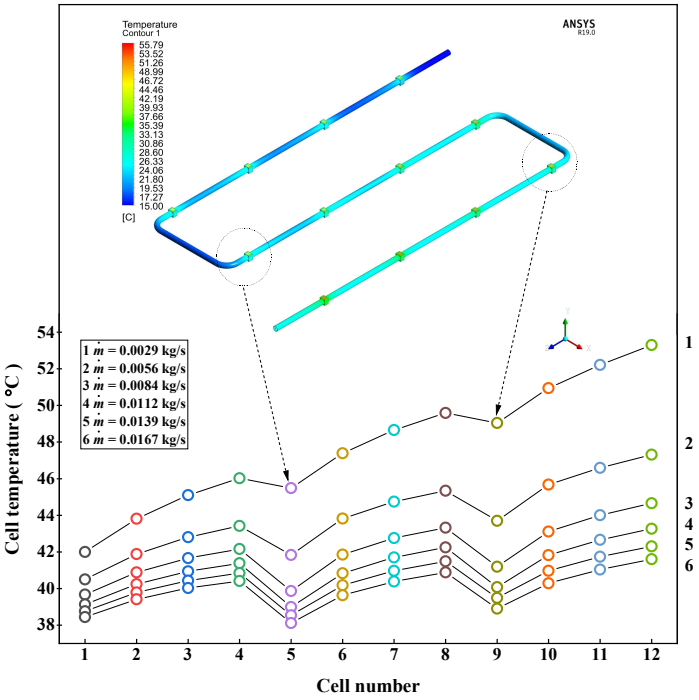

Fig. 7.39: The declining temperature of cell numbers 5 and 9 in the CPVT model

These vortices in the curved section of the pipe have several significant effects. Firstly, they mix the HTF in the cross-sectional plane of the pipe, enhancing convective heat transfer between the HTF and the pipe wall. This results in higher heat transfer efficiency in a curved pipe than in a straight pipe, especially in laminar flow conditions. Secondly, the secondary flow induces turbulence in the HTF, even in cases where the main flow is laminar. Turbulence further enhances the heat transfer rate by disrupting the HTF boundary layer and facilitating more efficient heat transfer between the HTF and the pipe wall. As a consequence of this enhanced heat transfer, cells 5 and 9 experience a higher overall heat

transfer rate, extracting more heat from these cells and consequently reducing their temperature.

7.4.12 Effect of Mass Flow Rate and *CRs* on Temperature Distribution

The CPVT model is a complex system comprising many components, such as MJPV cells, heat sinks, and concentrators. The system's performance depends on parameters such as mass flow rate, *CR*, and temperature. In this study, we investigated the effects of these parameters on the temperature distribution in the CPVT model. We considered a range of mass flow rates, from laminar to turbulent regimes, different *CRs*, and 12 MJPV cells. We generated numerous temperature contour plots, but we only present some representative ones in this thesis.

Figure 7.40 shows the three-dimensional temperature profile of the first and the last MJPV cells (number 1 and 12) at a mass flow rate of 0.0029 *kg/s* and 0.025 *kg/s*, respectively, and a *CR* of 100X. The top surface of the MJPV cell, where the constant heat flux is applied, has the highest temperature value. The temperature on this surface decreases in the middle and then increases at the edges, especially at the corners. This is because the backside of the heat sink has a curved shape that is thinner in the middle than at the edges. As a result, the thermal resistance in the middle is lower, allowing more heat to transfer. The maximum temperature recorded was 56°*C* on MJPV cell number 12. It was also observed that MJPV cell number 1 had a lower temperature than MJPV cell number 12 because it was closer to the inlet side.

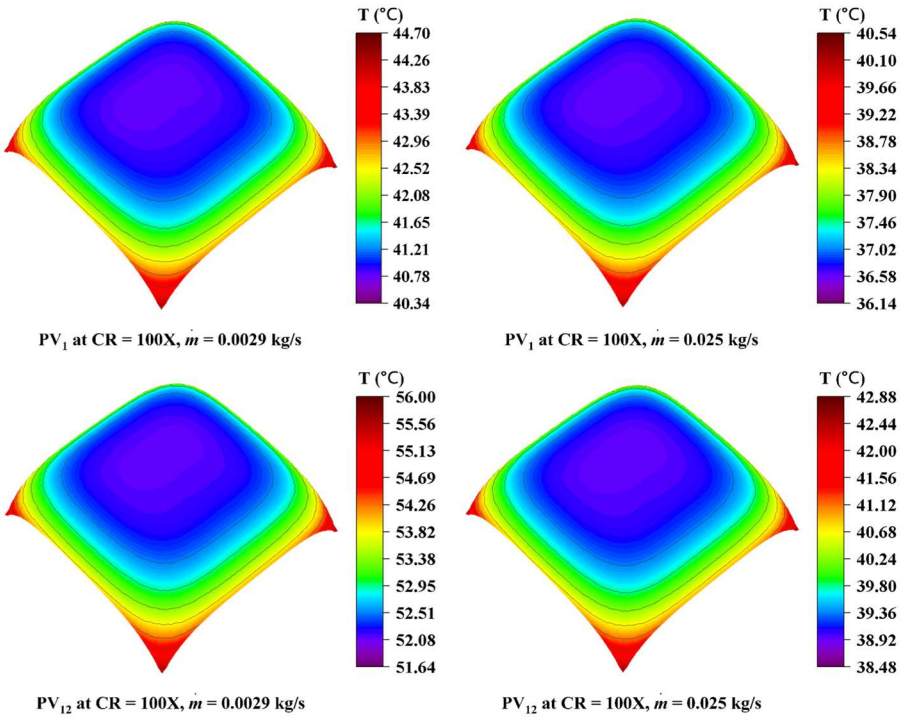

Fig. 7.40: Temperature profile of MJPV cells 1 and 12 at *CR* = 100X for laminar flow

Figure 7.41 shows the temperature profile of MJPV cells number 1 and 12 at a *CR* of 300X and a laminar flow with mass flow rates of 0.0029 *kg/s* and 0.025 *kg/s*, respectively. The general trend is similar to the previous contour plot. However, the maximum temperatures are higher due to the increased solar radiation. The maximum temperature recorded was 138°*C* on MJPV cell number 12 at a mass flow rate of 0.0029 *kg/s*, which exceeds the ROT of 110°*C*, as stated earlier. Increasing the mass flow rate to 0.025 *kg/s* reduced the maximum temperature to about 98.65°*C*, with a reduction of 28.5%.

Figure 7.42 depicts the temperature profile of MJPV cells number 1 and 12 at a *CR* of 500X and a laminar flow with mass flow rates of 0.0029 *kg/s* and 0.025 *kg/s*, respectively. The maximum temperatures are even higher than the case of *CR* of 300X due to the further

increased solar radiation. The maximum temperature recorded was 220.3 °*C* on MJPV cell number 12 at a mass flow rate of 0.0029 *kg/s*, which is far beyond the ROT of 110°*C*. Increasing the mass flow rate to 0.025 *kg/s* reduced the maximum temperature to approximately 154.4°*C*, with a reduction of 29.9%.

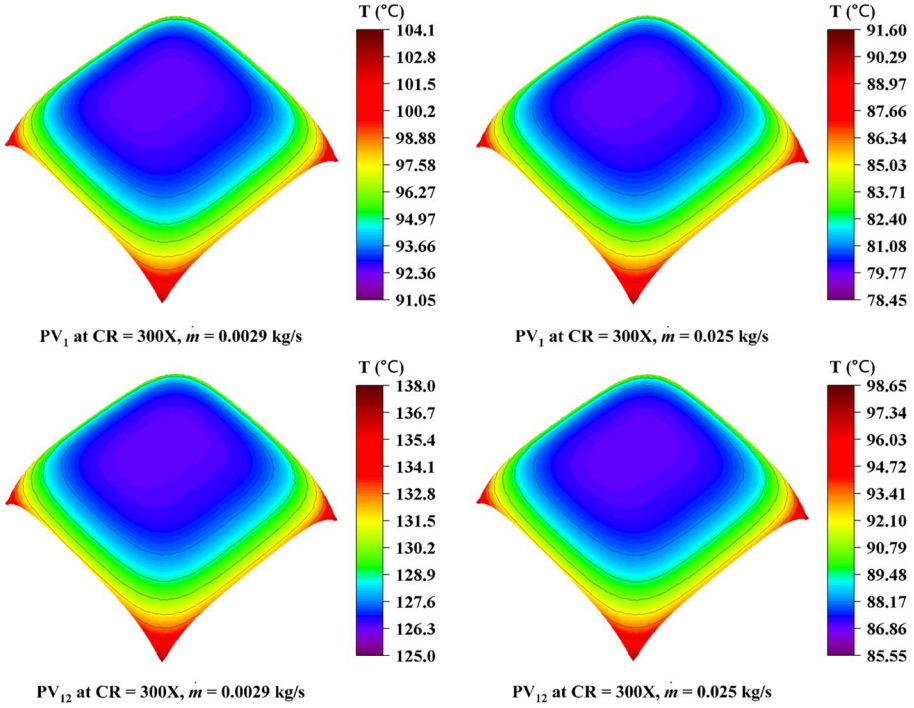

Fig. 7.41: Temperature profile of MJPV cells 1 and 12 at *CR* = 300X for laminar flow

Figure 7.43 displays the temperature profile of MJPV cells number 1 and 12 at a *CR* of 500X and a turbulent flow with mass flow rates of 0.1 *kg/s* and 0.5 *kg/s*, respectively. The maximum temperatures are lower than the case of laminar flow due to the enhanced heat transfer by turbulence. The maximum temperature recorded was 122.3 °*C* on MJPV cell number 12 at a mass flow rate of 0.1 *kg/s*, which is still above the ROT of 110°*C* but much lower than the case of laminar flow with the same *CR* and mass flow rate (220.3°*C*).

Increasing the mass flow rate to 0.5 *kg/s* reduced the maximum temperature to about 118.7 °*C*, with a reduction of only 2.94%. Comparing this with Fig. 7.42 at the same *CR*=500X, increasing the mass flow rate from 0.0029 *kg/s* to 0.1 *kg/s* reduced the maximum temperature by 44.5%.

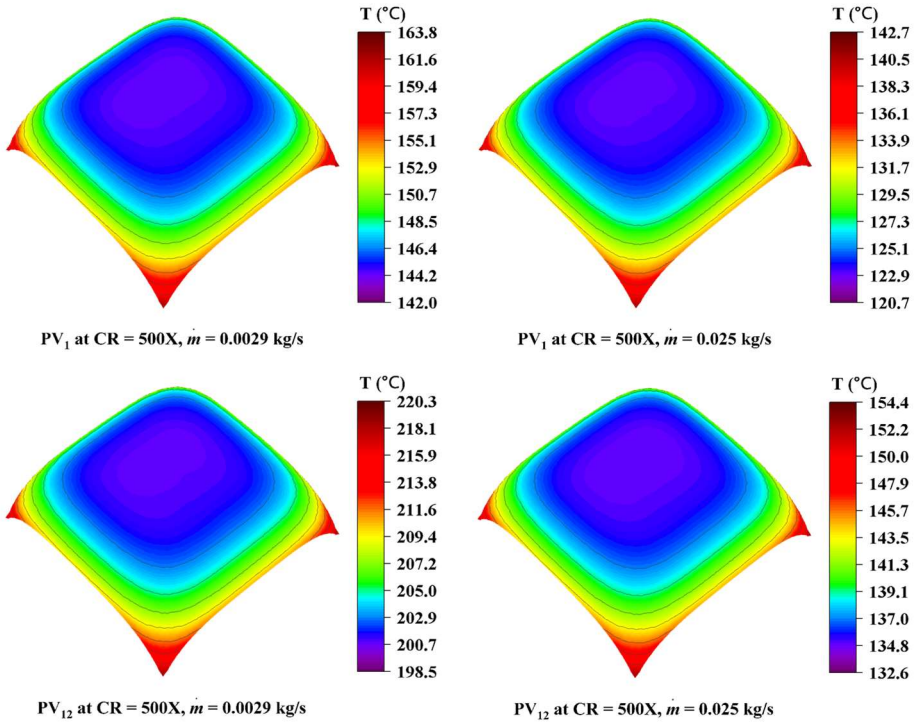

Fig. 7.42: Temperature profile of MJPV cells 1 and 12 at *CR* = 500X for laminar flow

Furthermore, Fig. 7.44 demonstrates the temperature profile of MJPV cells number 1 and 12 at a *CR* of 1000X and a turbulent flow with mass flow rates of 0. 1 kg/ s and 0. 5 kg/ s, respectively. The maximum temperatures are the highest among all cases due to the extremely high solar radiation. The maximum temperature recorded was 229.6 °*C* on MJPV cell number 12 at a mass flow rate of 0.1 *kg/s*, which is more than twice the ROT of 110 °*C*. Increasing the mass flow rate to 0.5 *kg/s* reduced the maximum temperature to 222.4

°*C*, with a reduction of only 3.14%. This reduction is insufficient to maintain the temperature within the desired ROT range due to the high thermal resistance.

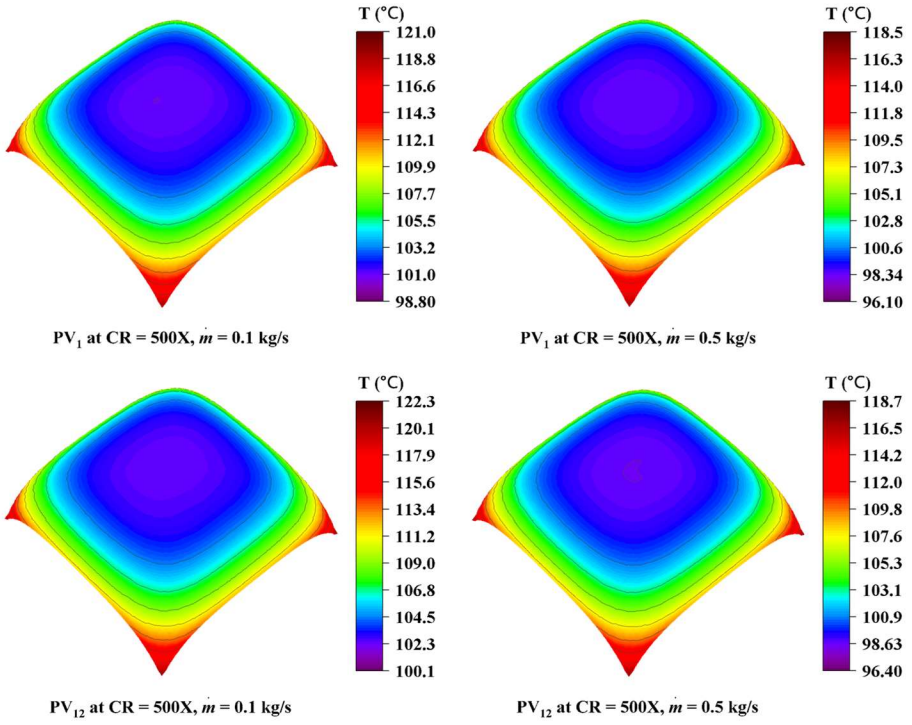

Fig. 7.43: Temperature profile of MJPV cells 1 and 12 at *CR* = 500X for turbulent flow

The HTF outlet temperature is a crucial parameter that significantly impacts the thermal and electrical performance of the CPVT system. This study investigated the effect of mass flow rate and *CRs* on the HTF outlet temperature. The research focused on laminar flow conditions with mass flow rates of 0.0029 *kg/s* and 0.025 *kg/s*. The HTF outlet temperature contours were predicted for *CRs* of 100X, 300X, and 500X, and the results were presented in Fig. 7.45, Fig. 7.46, and Fig. 7.47, respectively.

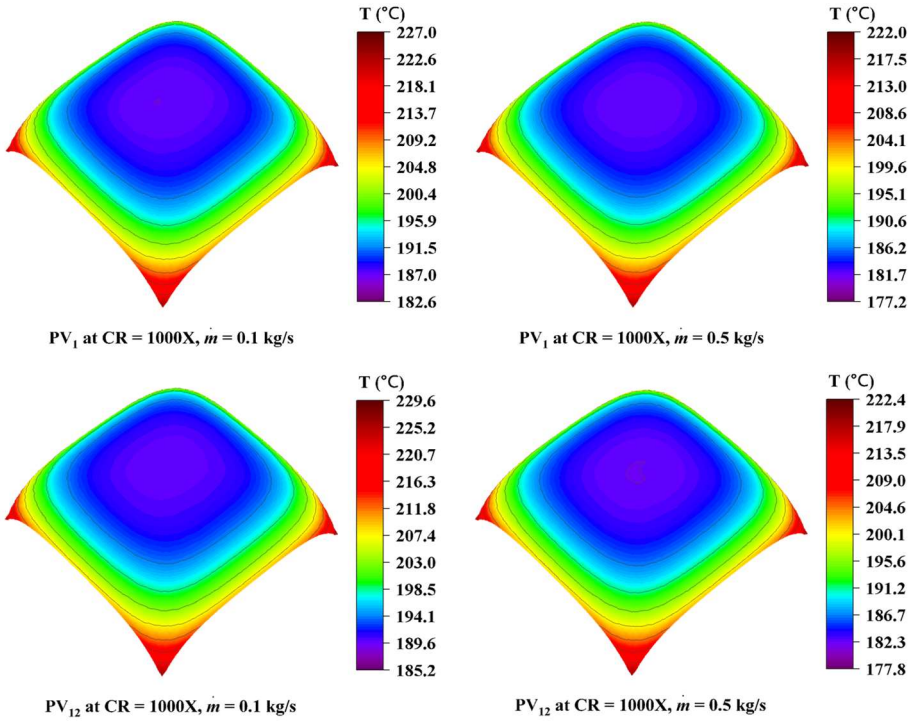

Fig. 7.44: Temperature profile of MJPV cells 1 and 12 at *CR* = 1000X for turbulent flow

From Fig. 7.45, it can be observed that the highest and lowest HTF outlet temperatures were 28.2 °*C* and 15.74 °*C*, respectively. Moreover, the HTF outlet temperatures decreased as the mass flow rate increased. This trend can be attributed to the increase in heat transfer as the mass flow rate increases. The temperature contours indicate that the highest temperature distribution occurs near the pipe wall. This temperature distribution near the wall is influenced by the constant heat flux applied to the MJPV cells, causing the wall to heat up. Consequently, heat is conducted from the wall into the adjacent HTF, creating a temperature gradient near the wall with higher temperatures. As the HTF moves away from the wall, conduction becomes less dominant, and heat transfer occurs mainly through convection. This leads to different HTF velocities, with the HTF near the wall moving

slowly due to the no-slip condition and the HTF in the center of the pipe moving more quickly. As a result, a velocity gradient is formed from the wall to the center of the pipe, influencing the temperature distribution.

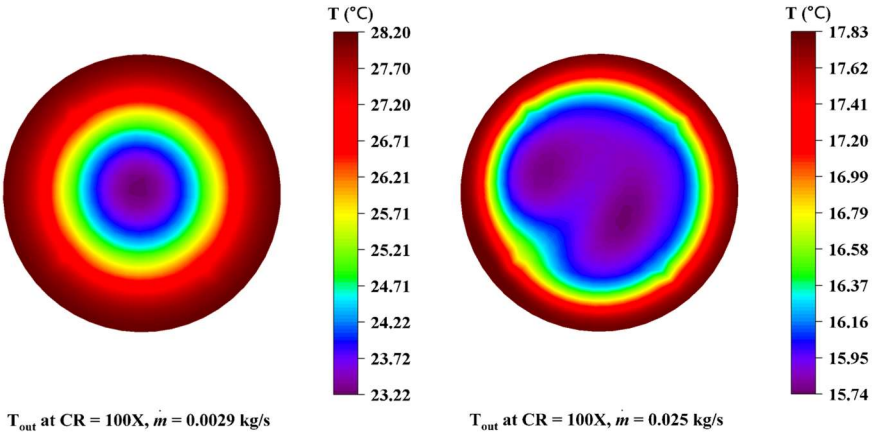

Fig. 7.45: Outlet temperature gradient of the HTF at *CR* = 100X for laminar flow

Figure 7.46 presents the HTF outlet temperature at a *CR* of 300X. At the same flow rate of 0.0029 *kg/s*, the maximum temperature increases to 54.6 °*C*, and the temperature distribution pattern remains similar to that observed at *CR* of 100X. Similarly, Fig. 7.47 displays the HTF outlet temperature at a *CR* of 500X, with the maximum temperature reaching 81.1°*C* at a mass flow rate of 0.0029 *kg/s*.

The study also considered turbulent flow conditions, with mass flow rates of 0.1 *kg/s* and 0.5 *kg/s*. The predicted temperature contours for the outlet HTF temperature were presented in Fig. 7.48 and Fig. 7.49, corresponding to *CRs* of 500X and 1000X, respectively. From Fig. 7.48, it can be observed that the maximum HTF outlet temperature was 16.69 °*C*. Additionally, the HTF outlet temperatures decreased as the mass flow rate

increased, thanks to the enhanced heat transfer resulting from higher mass flow rates. In turbulent flow, the temperature gradient is generally more uniform across the pipe's cross-section than in laminar flow.

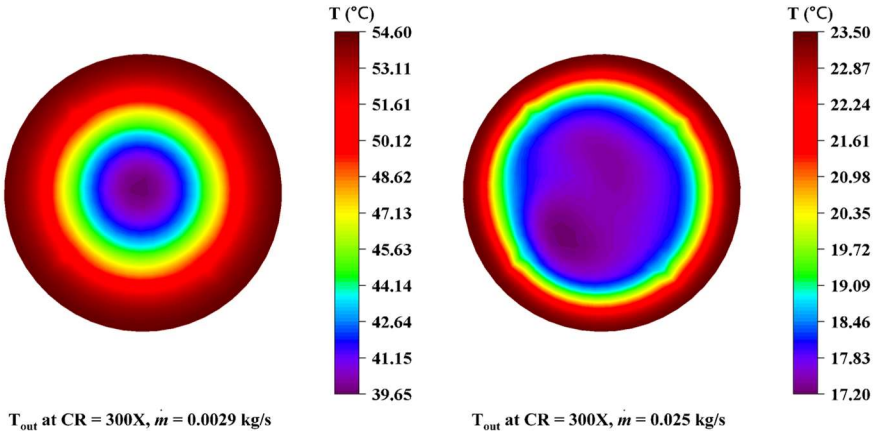

Fig. 7.46: Outlet temperature gradient of the HTF at *CR* = 300X for laminar flow

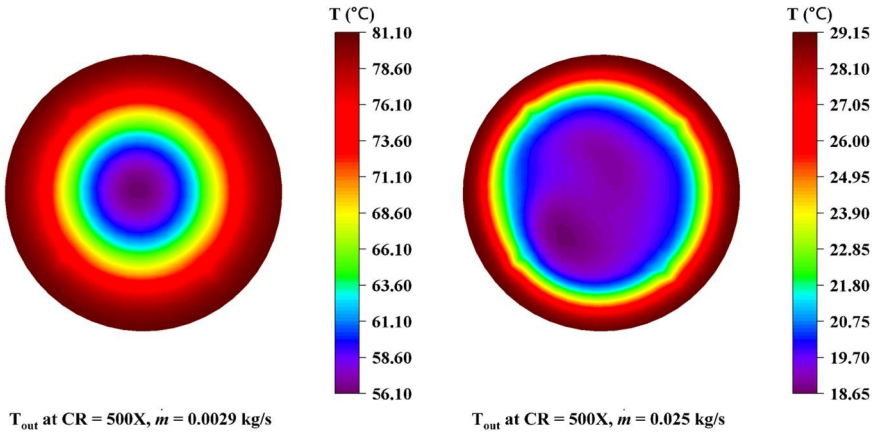

Fig. 7.47: Outlet temperature gradient of the HTF at *CR* = 500X for laminar flow

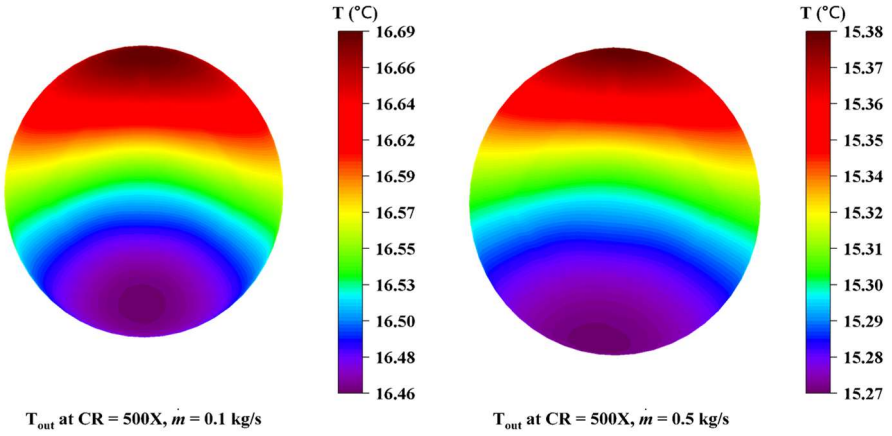

Fig. 7.48: Outlet temperature gradient of the HTF at *CR* = 500X for turbulent flow

Turbulent flow is characterized by highly chaotic and irregular fluid motion involving the formation of eddies and vortices. This turbulence promotes better mixing of the HTF and disrupts the thermal boundary layer near the wall, leading to enhanced heat transfer between the HTF and the pipe wall. As a result, the temperature distribution becomes more uniform, and the temperature gradient between the center and the pipe wall is reduced.

Finally, Fig. 7.49 shows that the maximum HTF outlet temperature was 18.37 *°C*. By increasing *CR* from 500X to 1000X, the HTF outlet temperature experiences only a slight increase, as the thermal resistances between the MJPV cells and HTF in the CPVT model have already reached their maximum limits. This indicates that further increasing the concentration ratio beyond 500X does not significantly improve the outlet temperature due to these thermal limitations.

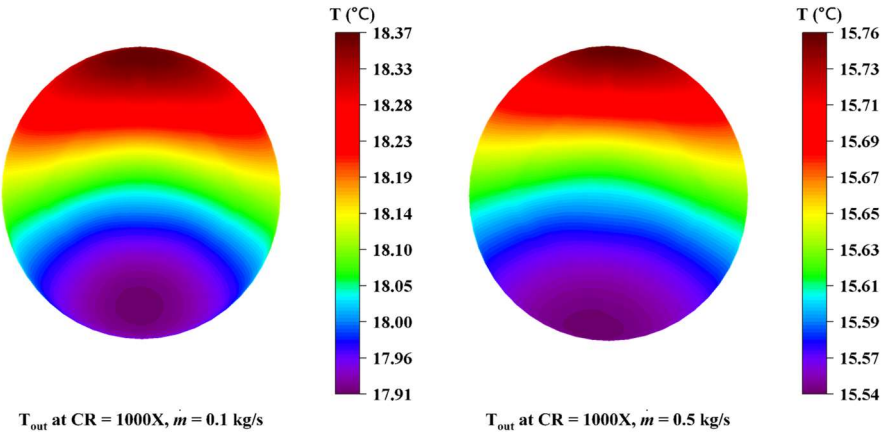

Fig. 7.49: Outlet temperature gradient of the HTF at *CR* = 1000X for turbulent flow

Appendix D contains additional figures depicting the effect of mass flow rates and *CRs* on various system performance aspects. These figures include temperature contours of the full module, temperature contours of the fluid domain, pressure contours of the fluid domain, velocity contours of the fluid domain, and temperature profiles on selected heat sinks. These visual representations provide further insights into the behaviour and characteristics of the CPVT system under different operational conditions.

Chapter 8

Conclusions and Recommendations

8.1 Conclusions

Solar energy is a promising and sustainable solution to meet the increasing global energy demand while reducing greenhouse gas emissions. However, existing solar energy technologies have limitations, such as low energy conversion efficiency, high cost, and land use requirements. One emerging technology that addresses these challenges is the CPVT system. This system combines MJPV solar cells and PFFL with active cooling.

Additional studies, analyses, and design considerations are still needed to advance the development of CPVT systems further. This study contributes to the research in this area by conducting systematic experiments using an indoor prototype model of CPVT and numerical simulations to investigate the feasibility of the proposed design. The laboratory real-scale prototype systems were designed and constructed, consisting of a sun simulator to emulate sunlight in an indoor environment. Copper heat sinks, machined to provide a flat surface for cell mounting and a round shape for attachment to a copper pipe flow loop, are also incorporated in the design. This design aims to reduce the MJPV cells' temperature and increase heat transfer to the HTF in the flow channel to produce electrical and thermal energy. The most important outcomes of this research are summarized in the following points:

- A comprehensive literature review on CPVT technologies, including their thermal and electrical performance, feasibility, and potential for sustainability and cost-effectiveness, has been presented: In addition, we summarized and compared more than twenty experimental and theoretical studies on CPVT systems based on the point focus in Table 2.1.

- All the technical challenges associated with developing the CPVT model were adequately addressed, and a full-scale prototype system was successfully manufactured and experimentally and numerically evaluated; the results showed that CPVT is a promising technology for simultaneously generating electricity and thermal energy. The CPVT model offers excellent opportunities to be used in several potential applications that cater to various sectors.

- The apparatus was benchmark tested to confirm its accuracy by comparing the pressure drop measurement with the laminar flow theory in a pipe. The results showed that the collected experimental data were within a ±10% range of the theoretical Fanning model. This precise measurement also showed insignificant effects of surface roughness on the results.

- The changes in electrical and thermal efficiencies of the CPVT model were investigated against increasing mass flow rate. The experimental results demonstrate that the prototype CPVT model achieved electrical and thermal efficiencies of 34.73% and 54.7%, respectively.

- Regarding the effect of mass flow rate and *CRs* on the electrical efficiency of the CPVT model: The CFD results show that in the laminar flow regime, the highest electrical

efficiency was recorded at 36.47%, occurring at a mass flow rate of 0.025 *kg/s* and a *CR* of 100X. On the other hand, the lowest electrical efficiency was observed at 25.56% for a mass flow rate of 0.0029 *kg/s* and a *CR* of 500X. In the turbulent flow regime, the highest electrical efficiency was 33.0% at a mass flow rate of 0.5 *kg/s* and a *CR* of 400X, while the lowest electrical efficiency was observed at 25.72% at a mass flow rate of 0.1 *kg/s* and a *CR* of 1000X.

- Regarding the effect of mass flow rate and *CRs* on the thermal efficiency of the CPVT model: The CFD results show that in the laminar flow regime, the highest thermal efficiency was recorded at 73.0%. This occurred at a mass flow rate of 0.0029 *kg/s* and a *CR* of 500X, while the lowest thermal efficiency was 61.5% observed at a mass flow rate of 0.025 *kg/s* and a *CR* of 100X. In the turbulent flow regime, the highest thermal efficiency was 72.85% at a mass flow rate of 0.1 *kg/s* and a *CR* of 1000X, while the lowest thermal efficiency was observed at 65.2% for a mass flow rate of 0.5 *kg/s* and a *CR* of 400X.

- Regarding the effect of mass flow rate on the PES efficiency of the CPVT model, the experimental results indicate that the highest recorded PES efficiency is achieved at a mass flow rate of 0.025 *kg/s*, with a value of 1.71.

- Regarding the effect of mass flow rate and *CRs* on the PES efficiency of the CPVT model, the CFD results indicate that the highest recorded PES efficiency in the laminar flow regime was 1.858, observed at a mass flow rate of 0.025 *kg/s* and a *CR* of 100X. Conversely, the lowest PES efficiency was noted at 1.762, achieved with a mass flow rate of 0.0029 *kg/s* and a *CR* of 500X. Similarly, the highest PES efficiency in the

turbulent flow regime was 1.827, with a mass flow rate of 0.5 *kg/s* and a *CR* of 400X. On the other hand, the lowest PES efficiency was observed at 1.764, occurring with a mass flow rate of 0.1 *kg/s* and a *CR* of 1000X.

- Regarding the power output of the CPVT model, the experimental results indicate that the maximum electrical and thermal power obtained from the CPVT model was 42.75 *W* and 67.89 *W*, respectively.
- Regarding the effect of mass flow rate and *CRs* on the power output of the CPVT model: The CFD results demonstrate that the highest recorded electrical energy in the laminar flow regime was 220 *W*, occurring at a mass flow rate of 0.025 *kg/s* and a *CR* of 500X. In comparison, in the turbulent flow regime, the highest electrical energy was observed at 389.3 *W*, achieved with a mass flow rate of 0.5 *kg/s* and a *CR* of 1000X. Furthermore, the highest thermal energy recorded in the laminar regime was 515.5 *W*, observed at a mass flow rate of 0.0029 *kg/s* and a *CR* of 500X. Similarly, in the turbulent flow regime, the highest thermal energy was observed at 1028.5 *W*, attained with a mass flow rate of 0.1 *kg/s* and a *CR* of 1000X.
- The CFD results indicate that the highest average cell temperature observed in the laminar flow regime was 179 ℃ at a mass flow rate of 0.0029 *kg/s* and a *CR* of 500X. The lowest average cell temperature recorded was 38.9 ℃ at a mass flow rate of 0.025 *kg/s* and a *CR* of 100X. Similarly, in the turbulent flow regime, the highest average cell temperature recorded was 200.8 ℃ at a mass flow rate of 0.1 *kg/s* and a *CR* of 1000X. The lowest average cell temperature observed was 86.9 ℃ at a mass flow rate of 0.5 *kg/s* and a *CR* of 400X.

- The experimental results demonstrate that the convection heat transfer coefficient range for Reynolds numbers up to 2000 were between 228 and 760 W/m^2K. In contrast, the CFD results show that for laminar flow, the heat transfer coefficient ranged from 405 to 1044 W/m^2K, while for turbulent flow, the range was significantly higher, spanning from 14408 to 27310 W/m^2K. Furthermore, the *CRs* did not affect the heat transfer coefficient.

- The experimental results show that the total natural convection and radiation heat losses are below 1.3 W. In contrast, the CFD results show that the highest radiation and natural convection heat losses in laminar flow are 2.22 W and 6.74 W, respectively. Moreover, the results indicate that both types of heat losses increase with higher *CRs*.

- Regarding the effect of inlet HTF temperature on the performance of the CPVT model, the CFD results demonstrate that the MJPV cell temperature increases with increasing inlet HTF temperature, whereas the electrical and thermal efficiencies decrease. This implies that a higher inlet HTF temperature leads to a lower quality of energy conversion and a higher risk of overheating and degradation of the MJPV cells. Therefore, an optimal inlet HTF temperature should be determined to balance the trade-off between electrical and thermal outputs.

- The flow channel design as a cooling system was highly effective as its incorporation in the CPVT system results in negligible thermal losses and parasitic pumping power.

- The results show that the PPG increases with increasing *CR*, reaching 973.1% at *CR* = 500X. This means that the electrical power output of the MJPV cells is almost ten times higher when using concentrators. The MR increases with increasing *CR*,

reaching 90.7% at *CR* = 500X. This means that only 9.3% of the original amount of MJPV cells is needed for the same application when using concentrators. This can significantly reduce the cost and environmental impact of the system, as MJPV cells are expensive and require rare materials.

- This proposed CPVT model can be used in various applications, depending on the HTF outlet temperature generated. The CFD results demonstrate that various outlet temperatures ranging from (18.1 to 72.5 ℃) were obtained depending on the mass flow rate and *CRs*. This temperature range is favourable for different applications such as swimming pool water heating, domestic hot water, and space heating.

- The numerical model has been successfully validated with indoor experimental results. The validation results for average cell temperature showed good agreement between the simulation and experimental model, with a maximum deviation of 4.58% at a mass flow rate of 0.0029 *kg/s* and a minimum deviation of 1.14% at a mass flow rate of 0.025 *kg/s*. These results confirm the numerical model's accuracy and reliability, demonstrating its potential for further optimization and analysis of the CPVT system.

- The mathematical model for MJPV cells accurately captured the temperature and radiation effects on their electrical characteristics. The model was based on a lumped diode model circuit and validated using experimental data from two MJPV cell manufacturers. The validation showed that the model agreed well with the experimental data, with root mean square errors (RMSE) ranging from 0.45% to 3.79%. The results showed that the performance of MJPV cells was highly dependent

on the *CR*, the cell temperature, and the series resistance. The model can be used to predict the behaviour of MJPV cells under various operating conditions.

8.2 Recommendations for Future Work

The project's primary objectives have been achieved and reported in detail in the present thesis. However, the present study suggests steps for further work in enhancing the performance of the CPVT model. The following research areas are recommended to be considered and addressed in future work:

Experimental aspects:

- It is essential to optimize the radiation output intensity and uniformity for the designed solar simulator by using reflectors, light guiding tunnel, and controllable high light intensity. This will ensure a more accurate and realistic simulation of the solar radiation conditions.
- Using a rectangular tube instead of a circular pipe is highly recommended to reduce thermal resistance and increase thermal performance. This will eliminate the thermal resistance caused by the heat sinks and improve the heat transfer efficiency between the MJPV cells and the HTF.
- Using a secondary optical element is preferable to improve the spectral homogeneity of the point-focus Fresnel lens and minimize the nonuniformity effects on the MJPV cells. This will enhance the electrical and thermal performance of the CPVT system by reducing the optical losses and increasing the concentration ratio.

- It is crucial to conduct the experimental tests outdoors under real solar radiation and weather conditions to evaluate the performance of the CPVT system in real-world operation. This will provide more reliable and valid results compared with other existing systems.

Numerical aspects:

- It is advisable to use line focus Fresnel lens (LFFL) instead of point focus Fresnel lens (PFFL) in the numerical simulation of the CPVT model. This will reduce the computational cost and time by simplifying the geometry and meshing of the model.
- Using a PV analyzer kit, which includes two main units: an I-V curve tracer and a wireless PV reference sensor, is beneficial. The I-V curve tracer can produce instant I-V and P-V curves for the solar cell and measure the following electrical parameters: V_{OC}, I_{SC}, I_m, V_m, P_m and FF. Simultaneously, the wireless PV reference sensor unit measures the following parameters: cell and ambient temperature, solar irradiance at the aperture and tilt angle of the system. This will enable a more comprehensive and accurate evaluation of the CPVT performance by considering various factors that affect it.
- Using a transient heat transfer model instead of a steady-state heat transfer model in ANSYS Fluent is desirable. This will allow a more detailed system behaviour to be studied at different solar hour angles and capture the dynamic changes in temperature, heat flux, and efficiency.

Economic aspects:

- It is important to assess the economic viability and environmental considerations of the CPVT system by conducting a cost-benefit analysis, a life cycle assessment, and a sensitivity analysis. This will provide information on the payback period, net present value, and internal rate of return, carbon footprint, energy payback time, and environmental impact factor of the system.

References

Abdelhady, S., Borello, D., & Tortora, E. (2014). Design of a small scale stand-alone solar thermal co-generation plant for an isolated region in Egypt. Energy Conversion and Management, 88, 872–882. https://doi.org/10.1016/j.enconman.2014.08.066

Ahmed, A., Shanks, K., Sundaram, S., & Mallick, T. K. (2020). Theoretical Investigation of the Temperature Limits of an Actively Cooled High Concentration Photovoltaic System. *Energies*, *13*(8), 8. https://doi.org/10.3390/en13081902

Al Siyabi, I. (2019). *Enhancing the performance of concentrating photovoltaics through multi-layered microchannel heat sink and phase change materials* [University of Exeter]. https://ore.exeter.ac.uk/repository/handle/10871/35932

Al-Amri, F., & Mallick, T. K. (2013). Alleviating operating temperature of concentration solar cell by air active cooling and surface radiation. *Applied Thermal Engineering*, *59*(1), 348–354. https://doi.org/10.1016/j.applthermaleng.2013.05.045

Aldossary, A., Mahmoud, S., & AL-Dadah, R. (2016). Technical feasibility study of passive and active cooling for concentrator PV in harsh environment. *Applied Thermal Engineering*, *100*, 490–500. https://doi.org/10.1016/j.applthermaleng.2016.02.023

AlFalah, G., Maatallah, T. S., & Al-Amri, F. G. (2022). Performance analysis of a single cell-ultra-high concentration photovoltaic thermal module based on pin-fins cooling microchannel. *International Journal of Energy Research*, *46*(3), 2947–2969. https://doi.org/10.1002/er.7356

Algareu, A. O. (2017). *Development of reflective low concentrated photovoltaic/ thermal system* [D_ph, University of Birmingham]. https://etheses.bham.ac.uk/id/eprint/7674/

Almonacid, F., Fernandez, E. F., Mellit, A., & Kalogirou, S. (2017). Review of techniques based on artificial neural networks for the electrical characterization of concentrator

photovoltaic technology. *Renewable and Sustainable Energy Reviews*, *75*, 938–953. https://doi.org/10.1016/j.rser.2016.11.075

Altuwairgi, A. (2022). *Full-spectrum solar energy harvesting for power and heat production using dichroic mirror* [Phd, Cardiff Uuniversity]. https://orca.cardiff.ac.uk/id/eprint/152295/

Alzahrani, M., Shanks, K., & Mallick, T. K. (2021). Advances and limitations of increasing solar irradiance for concentrating photovoltaics thermal system. *Renewable and Sustainable Energy Reviews*, *138*, 110517. https://doi.org/10.1016/j.rser.2020.110517

Amanlou, Y., Hashjin, T. T., Ghobadian, B., Najafi, G., & Mamat, R. (2016). A comprehensive review of Uniform Solar Illumination at Low Concentration Photovoltaic (LCPV) Systems. *Renewable and Sustainable Energy Reviews*, *60*, 1430–1441. https://doi.org/10.1016/j.rser.2016.03.032

Ansys. (2020b). Defining Boundary Conditions for Turbulent Flows in Ansys Fluent | Ansys Courses. *ANSYS Innovation Courses*. https://courses.ansys.com/index.php/courses/turbulence-modeling-in-ansys-fluent/lessons/defining-boundary-conditions-for-turbulent-flows-in-ansys-fluent-lesson-3/

Ansys. (2020a). How to Model Near-Wall Turbulence in Ansys Fluent | Ansys Courses. *ANSYS Innovation Courses*. https://courses.ansys.com/index.php/courses/turbulence-modeling-in-ansys-fluent/lessons/how-to-model-near-wall-turbulence-in-ansys-fluent-lesson-2/

ANSYS, Inc. (2017). *ANSYS Fluent User's Guide 18.1*. Southpointe 2600 ANSYS Drive Canonsburg, PA 15317.

Araki, K., Uozumi, H., & Yamaguchi, M. (2002). A simple passive cooling structure and its heat analysis for 500/spl times/ concentrator PV module. *Conference Record of the Twenty-Ninth IEEE Photovoltaic Specialists Conference, 2002.*, 1568–1571. https://doi.org/10.1109/PVSC.2002.1190913

Askari, I. B., Shahsavar, A., Jamei, M., Calise, F., & Karbasi, M. (2022). A parametric assessing and intelligent forecasting of the energy and exergy performances of a dish concentrating photovoltaic/thermal collector considering six different nanofluids and applying two meticulous soft computing paradigms. *Renewable Energy*, *193*, 149–166. https://doi.org/10.1016/j.renene.2022.04.155

ASTM-E927. (2019). *ASTM-E927 | Standard Classification for Solar Simulators for Electrical Performance Testing of Photovoltaic Devices | Document Center, Inc.* https://www.document-center.com/standards/show/ASTM-E927/history/2019%20EDITION

Atwater, H. A., & Polman, A. (2010). Plasmonics for improved photovoltaic devices. *Nature Materials*, *9*(3), 205–213.

AZURSPACE. (2014). *Enhanced Fresnel Assembly—EFA Type: 3C42A – with 10x10mm2 CPV TJ Solar Cell Application: Concentrating Photovoltaic (CPV) Modules 2014:0–3.* http://www.azurspace.com/images/products/0004355-00-01_3C44_AzurDesign_10x10.pdf

Bamisile, O., Huang, Q., Li, J., Dagbasi, M., Desire Kemena, A., Abid, M., & Hu, W. (2020). Modelling and performance analysis of an innovative CPVT, wind and biogas integrated comprehensive energy system: An energy and exergy approach. *Energy Conversion and Management*, *209*, 112611. https://doi.org/10.1016/j.enconman.2020.112611

Bar-Lev, A., Waks, S., & Grossman, G. (1983). Analysis of a Combined Thermal-Photovoltaic Solar System Based on the Spherical Reflector/Tracking Absorber Concentrator. *Journal of Solar Energy Engineering*, *105*(3), 322–328. https://doi.org/10.1115/1.3266385

Barrau, J., Rosell, J., Chemisana, D., Tadrist, L., & Ibañez, M. (2011). Effect of a hybrid jet impingement/micro-channel cooling device on the performance of densely packed PV cells under high concentration. *Solar Energy*, *85*(11), 2655–2665. https://doi.org/10.1016/j.solener.2011.08.004

Bauer, T. (2011). *Thermophotovoltaics: Basic principles and critical aspects of system design*. Springer Science & Business Media.

Ben Youssef, W., Maatallah, T., Menezo, C., & Ben Nasrallah, S. (2018). Assessment viability of a concentrating photovoltaic/thermal-energy cogeneration system (CPV/T) with storage for a textile industry application. *Solar Energy*, *159*, 841–851. https://doi.org/10.1016/j.solener.2017.11.058

Bergman, T. L., Lavine, A. S., Incropera, F. P., & DeWitt, D. P. (2020). *Fundamentals of Heat and Mass Transfer*. John Wiley & Sons.

Boese, F. K., Berghausen, K., Reich, A., & Spillekothen, H. G. (1983). Double purpose systems as an optimum solution for solar energy application. *Arab International Solar Energy Conference. 1*, 382–386.

Bos, K., & Gupta, J. (2018). Climate change: The risks of stranded fossil fuel assets and resources to the developing world. *Third World Quarterly*, *39*(3), 436–453. https://doi.org/10.1080/01436597.2017.1387477

Brogren, M. (2004). *Optical Efficiency of Low-Concentrating Solar Energy Systems with Parabolic Reflectors* [Doctoral thesis, comprehensive summary, info:eu-repo/semantics/doctoralThesis, text]. Acta Universitatis Upsaliensis.

Buffet, P. (1983). Hybrid Thermal and Photovoltaic Concentration Collector. In R. V. Overstraeten & W. Palz (Eds.), *Photovoltaic Power Generation* (pp. 251–256). Springer Netherlands. https://doi.org/10.1007/978-94-009-7136-3_34

Buonomano, A., Calise, F., Dentice d'Accadia, M., & Vanoli, L. (2013). A novel solar trigeneration system based on concentrating photovoltaic/thermal collectors. Part 1: Design and simulation model. *Energy*, *61*(Supplement C), 59–71. https://doi.org/10.1016/j.energy.2013.02.009

Buonomano, A., Calise, F., & Palombo, A. (2013). Solar heating and cooling systems by CPVT and ET solar collectors: A novel transient simulation model. *Applied Energy*, *103*, 588–606. https://doi.org/10.1016/j.apenergy.2012.10.023

Cai, Y., Wang, W.-W., Liu, C.-W., Ding, W.-T., Liu, D., & Zhao, F.-Y. (2020). Performance evaluation of a thermoelectric ventilation system driven by the concentrated photovoltaic thermoelectric generators for green building operations. *Renewable Energy*, *147*, 1565–1583. https://doi.org/10.1016/j.renene.2019.09.090

Calise, F., Dentice d'Accadia, M., Roselli, C., Sasso, M., & Tariello, F. (2014). Desiccant-based AHU interacting with a CPVT collector: Simulation of energy and environmental performance. *Solar Energy*, *103*, 574–594. https://doi.org/10.1016/j.solener.2013.11.001

Campos, C. S., Torres, J. P. N., & Fernandes, J. F. P. (2019). Effects of the Heat Transfer Fluid Selection on the Efficiency of a Hybrid Concentrated Photovoltaic and Thermal Collector. *Energies*, *12*(9), 9. https://doi.org/10.3390/en12091814

Cengel, Y. A. (2003). *Heat transfer: A practical approach* (2nd ed). McGraw-Hill.

Cengel, Y., & Cimbala, J. (2013). *Fluid Mechanics Fundamentals and Applications (SI units)*. McGraw Hill.

Chayet, H., Lozovsky, I., Kost, O., Loeckenhoff, R., & Rasch, K. (2010). High efficiency, low cost parabolic dish system for cogeneration of electricity and heat. *AIP Conference Proceedings*, *1277*(1), 175–178. https://doi.org/10.1063/1.3509183

Chen, H., Ji, J., Wang, Y., Sun, W., Pei, G., & Yu, Z. (2014). Thermal analysis of a high concentration photovoltaic/thermal system. *Solar Energy*, *107*, 372–379. https://doi.org/10.1016/j.solener.2014.05.043

Chen, H., Yang, J., Zhou, N., Chen, J., & Zhang, Y. (2019). Performance analysis of a high concentrating photovoltaic/thermal system with a water spray cooling device. *IOP Conference Series: Materials Science and Engineering*, *556*(1), 012034. https://doi.org/10.1088/1757-899X/556/1/012034

Chou, T., Shih, Z., Hong, H., Han, C., & Chiang, K. (2012). Thermal Performance Assessment and Validation of High-Concentration Photovoltaic Solar Cell Module. *IEEE Transactions on Components, Packaging and Manufacturing Technology*, *2*(4), 578–586. https://doi.org/10.1109/TCPMT.2011.2181165

Coventry, J. S. (2005). Performance of a concentrating photovoltaic/thermal solar collector. *Solar Energy*, *78*(2), 211–222. https://doi.org/10.1016/j.solener.2004.03.014

Coventry, J. S., & Lovegrove, K. (2003). Development of an approach to compare the 'value' of electrical and thermal output from a domestic PV/thermal system. *Solar Energy*, *75*(1), 63–72. https://doi.org/10.1016/S0038-092X(03)00231-7

Daneshazarian, R., Cuce, E., Cuce, P. M., & Sher, F. (2018). Concentrating photovoltaic thermal (CPVT) collectors and systems: Theory, performance assessment and

applications. *Renewable and Sustainable Energy Reviews*, *81*(Part 1), 473–492. https://doi.org/10.1016/j.rser.2017.08.013

David, L. (2023, April 16). What Are Ground Mounted Solar Panels? (2023 Guide). *EcoWatch*. https://www.ecowatch.com/solar/ground-mounted-solar-panels

Dey, C. J. (2004). Heat transfer aspects of an elevated linear absorber. *Solar Energy*, *76*(1), 243–249. https://doi.org/10.1016/j.solener.2003.08.030

Domínguez, C., Antón, I., & Sala, G. (2010). Multijunction solar cell model for translating I–V characteristics as a function of irradiance, spectrum, and cell temperature. *Progress in Photovoltaics: Research and Applications*, *18*(4), 272–284. https://doi.org/10.1002/pip.965

Duffie, J. A., Beckman, W. A., & Blair, N. (2020). Solar Engineering of Thermal Processes, Photovoltaics and Wind. In *Solar Engineering of Thermal Processes, Photovoltaics and Wind* (pp. 760–788). John Wiley & Sons, Ltd. https://doi.org/10.1002/9781119540328.ch23

Elliott, B. D. (2012). *Evaluation of an indirect solar assisted heat pump water heater in the Canadian environment* [M.A.Sc., Queen's University (Canada)]. http://search.proquest.com/docview/1886378591/abstract/D1E9998A7F4D49BCPQ/1

Esen, V., Sağlam, Ş., & Oral, B. (2017). Light sources of solar simulators for photovoltaic devices: A review. *Renewable and Sustainable Energy Reviews*, *77*, 1240–1250. https://doi.org/10.1016/j.rser.2017.03.062

European Commission. (2012). *Energy: Roadmap 2050*. Publications Office of the European Union. https://data.europa.eu/doi/10.2833/10759

Evans, D. L., Facinelli, W. A., & Otterbein, R. T. (1978). *Combined Photovoltaic/Thermal System Studies* (SAND-78-7031). Arizona State Univ., Tempe (USA). Dept. of Mechanical Engineering. https://www.osti.gov/scitech/biblio/6602074

Evans, D. L., & Florschuetz, L. W. (1977). Cost studies on terrestrial photovoltaic power systems with sunlight concentration. *Solar Energy*, *19*(3), 255–262.

Fresnel Factory. (2019). *CP330-280(CPV, F=330mm) Fresnel focus length 350mm 5T - Fresnel Factory.com*. https://www.fresnelfactory.com/cp330-280-cpv-f330mm.html

FULLSUN, G. (2020). *Triple junction concentrated gaas cell used for CPV system*. https://www.gaas.fullsuns.com/cpv/10-10mm-Gallium-Arsenide-40-Concertrator-Triple-Junction-Solar-Cell.html

Garboushian, V., Roubideaux, D., & Yoon, S. (1997). Integrated high-concentration PV near-term alternative for low-cost large-scale solar electric power. *Solar Energy Materials and Solar Cells*, *47*(1), 315–323. https://doi.org/10.1016/S0927-0248(97)00056-1

Ghobadi, M., & Muzychka, Y. S. (2014). Pressure drop in mini-scale coiled tubing. *Experimental Thermal and Fluid Science*, *57*, 57–64. https://doi.org/10.1016/j.expthermflusci.2014.04.011

Gibart, C. (1981). Study of and tests on a hybrid photovoltaic-thermal collector using concentrated sunlight. *Solar Cells*, *4*(1), 71–89. https://doi.org/10.1016/0379-6787(81)90038-7

Gottschalg, R., Betts, T. R., Infield, D. G., & Kearney, M. J. (2005). The effect of spectral variations on the performance parameters of single and double junction amorphous silicon solar cells. *Solar Energy Materials and Solar Cells*, *85*(3), 415–428. https://doi.org/10.1016/j.solmat.2004.05.011

Green, M. A., & Pillai, S. (2012). Harnessing plasmonics for solar cells. *Nature Photonics*, *6*(3), 3. https://doi.org/10.1038/nphoton.2012.30

Hamzat, A. K., Omisanya, M. I., Sahin, A. Z., Ropo Oyetunji, O., & Abolade Olaitan, N. (2022). Application of nanofluid in solar energy harvesting devices: A comprehensive review. *Energy Conversion and Management*, *266*, 115790. https://doi.org/10.1016/j.enconman.2022.115790

Helmers, H., Boos, A., Jetter, F., Heimsath, A., Wiesenfarth, M., & Bett, A. W. (2011). Outdoor Test Setup for Concentrating Photovoltaic and Thermal (CPVT) Systems. *AIP Conference Proceedings*, *1407*(1), 175–179. https://doi.org/10.1063/1.3658320

Helmers, H., & Kramer, K. (2013). Multi-linear performance model for hybrid (C)PVT solar collectors. *Solar Energy*, *92*(Supplement C), 313–322. https://doi.org/10.1016/j.solener.2013.03.003

Henry, C. H. (1980). Limiting efficiencies of ideal single and multiple energy gap terrestrial solar cells. *Journal of Applied Physics*, *51*(8), 4494–4500. https://doi.org/10.1063/1.328272

Holman, J. P. (2012). *Experimental Methods for Engineers, Eight Edition*. McGraw-Hill Companies, New York.

Hong, L., Yao, H., Wu, Z., Cui, Y., Zhang, T., Xu, Y., Yu, R., Liao, Q., Gao, B., Xian, K., Woo, H. Y., Ge, Z., & Hou, J. (2019). Eco-Compatible Solvent-Processed Organic Photovoltaic Cells with Over 16% Efficiency. *Advanced Materials*, *31*(39), 1903441. https://doi.org/10.1002/adma.201903441

Hosseini, S. E., & Butler, B. (2021). Design and analysis of a hybrid concentrated photovoltaic thermal system integrated with an organic Rankine cycle for hydrogen production.

Journal of Thermal Analysis and Calorimetry, *144*(3), 763–778. https://doi.org/10.1007/s10973-020-09556-4

Hovel, H. J. (1975). *Semiconductors and semimetals. Volume 11. Solar cells, CHAPTER 8 Temperature and Intensity*. Academic Press, Inc.,New York. https://www.osti.gov/scitech/biblio/7284142

Hu, L., & Mandelis, A. (2021). Advanced characterization methods of carrier transport in quantum dot photovoltaic solar cells. *Journal of Applied Physics*, *129*(9), 091101.

Huang, B. J., Lin, T. H., Hung, W. C., & Sun, F. S. (2001). Performance evaluation of solar photovoltaic/thermal systems. *Solar Energy*, *70*(5), 443–448. https://doi.org/10.1016/S0038-092X(00)00153-5

Hurley, S. (2021, October 18). Opportunities for solar energy. *Explaining Science*. https://explainingscience.org/2021/10/18/opportunities-for-solar-energy/

Hussain, M. I., & Lee, G. H. (2023). Concentrated solar powered agricultural products dryer: Energy, exergoeconomic and exergo-environmental analyses. *Journal of Cleaner Production*, *393*, 136162. https://doi.org/10.1016/j.jclepro.2023.136162

Ibn-Mohammed, T., Koh, S. C. L., Reaney, I. M., Acquaye, A., Schileo, G., Mustapha, K. B., & Greenough, R. (2017). Perovskite solar cells: An integrated hybrid lifecycle assessment and review in comparison with other photovoltaic technologies. *Renewable and Sustainable Energy Reviews*, *80*, 1321–1344. https://doi.org/10.1016/j.rser.2017.05.095

IEA. (2022a). *For the first time in decades, the number of people without access to electricity is set to increase in 2022 – Analysis*. IEA. https://www.iea.org/commentaries/for-the-first-time-in-decades-the-number-of-people-without-access-to-electricity-is-set-to-increase-in-2022

IEA. (2022b). *Renewable Electricity – Analysis*. IEA. https://www.iea.org/reports/renewable-electricity

Imenes, A. G., & Mills, D. R. (2004). Spectral beam splitting technology for increased conversion efficiency in solar concentrating systems: A review. *Solar Energy Materials and Solar Cells*, *84*(1), 19–69. https://doi.org/10.1016/j.solmat.2004.01.038

Imtiaz Hussain, M., & Lee, G. H. (2015). Experimental and numerical studies of a U-shaped solar energy collector to track the maximum CPV/T system output by varying the flow rate. *Renewable Energy*, *76*, 735–742. https://doi.org/10.1016/j.renene.2014.12.008

Imtiaz Hussain, M., & Lee, G. H. (2016). Thermal performance comparison of line- and point-focus solar concentrating systems: Experimental and numerical analyses. *Solar Energy*, *133*(Supplement C), 44–54. https://doi.org/10.1016/j.solener.2016.03.062

Jacob, J., Pandey, A. K., Rahim, N. A., Selvaraj, J., Samykano, M., Saidur, R., & Tyagi, V. V. (2022). Concentrated Photovoltaic Thermal (CPVT) systems: Recent advancements in clean energy applications, thermal management and storage. *Journal of Energy Storage*, *45*, 103369. https://doi.org/10.1016/j.est.2021.103369

Jamal, T., Urmee, T., & Shafiullah, G. M. (2020). Planning of off-grid power supply systems in remote areas using multi-criteria decision analysis. *Energy*, *201*, 117580. https://doi.org/10.1016/j.energy.2020.117580

Jean, J., Brown, P. R., Jaffe, R. L., Buonassisi, T., & Bulović, V. (2015). Pathways for solar photovoltaics. *Energy & Environmental Science*, *8*(4), 1200–1219. https://doi.org/10.1039/C4EE04073B

Jiang, S. L., Hu, P., Mo, S. P., & Chen, Z. S. (2009). Modeling for Two-Stage Dish Concentrating Spectral Beam Splitting Photovoltaic/Thermal System. *2009 Asia-*

Pacific Power and Energy Engineering Conference, 1–4. https://doi.org/10.1109/APPEEC.2009.4918499

Ju, X., Wang, Z., Flamant, G., Li, P., & Zhao, W. (2012). Numerical analysis and optimization of a spectrum splitting concentration photovoltaic–thermoelectric hybrid system. *Solar Energy*, *86*(6), 1941–1954. https://doi.org/10.1016/j.solener.2012.02.024

Kandilli, C. (2013). Performance analysis of a novel concentrating photovoltaic combined system. *Energy Conversion and Management*, *67*, 186–196. https://doi.org/10.1016/j.enconman.2012.11.020

Kaplan, G. M., Bowman, T. E., Raiford, M., & Ribot, J. (1985). *Understanding solar concentrators. Technical paper* (PB-86-143021/XAB; VITA/TP-30:6/85). Volunteers in Technical Assistance, Inc., Arlington, VA (USA). https://www.osti.gov/biblio/5905271

Karanasios, K. (2018). *Community choices: Pathways to integrate renewable energy into indigenous remote community energy systems* [UWSpace]. http://hdl.handle.net/10012/14200

Karathanasis, I. (2015). *Development and optimization of a concentrating photovoltaic/thermal cogeneration system* [Διδακτορική Διατριβή, Εθνικό Μετσόβιο Πολυτεχνείο (ΕΜΠ). Σχολή Μηχανολόγων Μηχανικών. Τομέας Ρευστών. Εργαστήριο Τεχνολογικών Καινοτομιών Προστασίας Περιβάλλοντος]. http://hdl.handle.net/10442/hedi/39465

Kashyap, S., Mishra, K., Sachdev, T., & Tiwari, A. (2022). Internal Characteristics of Double-base Array. In *Solar Thermal Systems: Thermal Analysis & its Application* (pp. 42–89). Bentham Science Publishers Pte.

Kilner, J. A., Skinner, S. J., Irvine, S. J. C., & Edwards, P. P. (2012). *Functional Materials for Sustainable Energy Applications*. Elsevier.

Kinsey, G. S., Hebert, P., Barbour, K. E., Krut, D. D., Cotal, H. L., & Sherif, R. A. (2008). Concentrator multijunction solar cell characteristics under variable intensity and temperature. *Progress in Photovoltaics: Research and Applications*, *16*(6), 503–508. https://doi.org/10.1002/pip.834

KLINE, S. J. & McClintock, F. A. (1953). Describing Uncertainty in Single Sample Experiments. *Mech. Engineering*, *75*, 3–8.

Kong, C., Xu, Z., & Yao, Q. (2013). Outdoor performance of a low-concentrated photovoltaic–thermal hybrid system with crystalline silicon solar cells. *Applied Energy*, *112*(Supplement C), 618–625. https://doi.org/10.1016/j.apenergy.2013.02.011

Kribus, A., Kaftori, D., Mittelman, G., Hirshfeld, A., Flitsanov, Y., & Dayan, A. (2006). A miniature concentrating photovoltaic and thermal system. *Energy Conversion and Management*, *47*(20), 3582–3590. https://doi.org/10.1016/j.enconman.2006.01.013

Krishna, Y., Faizal, M., Saidur, R., Ng, K. C., & Aslfattahi, N. (2020). State-of-the-art heat transfer fluids for parabolic trough collector. *International Journal of Heat and Mass Transfer*, *152*, 119541. https://doi.org/10.1016/j.ijheatmasstransfer.2020.119541

Kumar, V., Shrivastava, R. L., & Untawale, S. P. (2015). Fresnel lens: A promising alternative of reflectors in concentrated solar power. *Renewable and Sustainable Energy Reviews*, *44*(Supplement C), 376–390. https://doi.org/10.1016/j.rser.2014.12.006

Launder, B. E., & Spalding, D. B. (1974). The numerical computation of turbulent flows. In *Computer Methods in Applied Mechanics and Engineering* (Vol. 3, pp. 269–289). North-Holland.

Leutz, R., & Suzuki, A. (2001). *Nonimaging Fresnel Lenses: Design and Performance of Solar Concentrators* (Vol. 83). Springer. https://doi.org/10.1007/978-3-540-45290-4

Li, G., Pei, G., Yang, M., Ji, J., & Su, Y. (2014). Optical evaluation of a novel static incorporated compound parabolic concentrator with photovoltaic/thermal system and preliminary experiment. *Energy Conversion and Management*, *85*, 204–211. https://doi.org/10.1016/j.enconman.2014.05.082

Li, M., Li, G. L., Ji, X., Yin, F., & Xu, L. (2011). The performance analysis of the Trough Concentrating Solar Photovoltaic/Thermal system. *Energy Conversion and Management*, *52*(6), 2378–2383. https://doi.org/10.1016/j.enconman.2010.12.039

Lin, L., Tian, Y., Luo, Y., Chen, C., & Jiang, L. (2020). A novel solar system integrating concentrating photovoltaic thermal collectors and variable effect absorption chiller for flexible co-generation of electricity and cooling. *Energy Conversion and Management*, *206*, 112506. https://doi.org/10.1016/j.enconman.2020.112506

Liu, Y., Hu, P., Zhang, Q., & Chen, Z. (2014). Thermodynamic and optical analysis for a CPV/T hybrid system with beam splitter and fully tracked linear Fresnel reflector concentrator utilizing sloped panels. *Solar Energy*, *103*, 191–199. https://doi.org/10.1016/j.solener.2014.01.047

Lozano-Medina, A., Manzano, L., Marcos, J. D., & Blanco-Marigorta, A. M. (2019). Design of a concentrating solar thermal collector installation for a hotel complex in Gran Canaria. *Energy*, *183*, 803–811. https://doi.org/10.1016/j.energy.2019.06.165

Luque, A., & Hegedus, S. (2011a). *Handbook of Photovoltaic Science and Engineering*. John Wiley & Sons.

Luque, A., & Hegedus, S. (Eds.). (2011b). *Handbook of Photovoltaic Science and Engineering* (Second). John Wiley & Sons, Ltd.

Luque, A. L., & Viacheslav, A. (Eds.). (2007). *Concentrator Photovoltaics* (Vol. 130). Springer. https://doi.org/10.1007/978-3-540-68798-6

Lv, H., Sheng, F., Dai, J., Liu, W., Cheng, C., & Zhang, J. (2015). Temperature-dependent model of concentrator photovoltaic modules combining optical elements and III–V multi-junction solar cells. *Solar Energy*, *112*, 351–360. https://doi.org/10.1016/j.solener.2014.12.005

MacCormack, R. W., & Paullay, A. J. (1972). Computational efficiency achieved by time splitting of finite difference operators. *Aerospace Sciences Meetings*. 10th Aerospace Sciences Meeting, San Diego,CA,U.S.A. https://doi.org/10.2514/6.1972-154

Mbewe, D. J., Card, H. C., & Card, D. C. (1985). A model of silicon solar cells for concentrator photovoltaic and photovoltaic/thermal system design. *Solar Energy*, *35*(3), 247–258. https://doi.org/10.1016/0038-092X(85)90104-5

McDonald, P. W. (1971). *The Computation of Transonic Flow Through Two-Dimensional Gas Turbine Cascades*. ASME 1971 International Gas Turbine Conference and Products Show. https://doi.org/10.1115/71-GT-89

MCT, C. (2011, May 24). *The Chromasun Micro-Concentrator (MCT)*. Chromasun MCT. http://chromasun.com/MCT.html

Miles, R. W., Hynes, K. M., & Forbes, I. (2005). Photovoltaic solar cells: An overview of state-of-the-art cell development and environmental issues. *Progress in Crystal Growth and Characterization of Materials*, *51*(1), 1–42. https://doi.org/10.1016/j.pcrysgrow.2005.10.002

Mittelman, G., Kribus, A., & Dayan, A. (2007). Solar cooling with concentrating photovoltaic/thermal (CPVT) systems. *Energy Conversion and Management*, *48*(9), 2481–2490. https://doi.org/10.1016/j.enconman.2007.04.004

Motamedi, M., Chung, C.-Y., Rafeie, M., Hjerrild, N., Jiang, F., Qu, H., & A. Taylor, R. (2019). Experimental Testing of Hydrophobic Microchannels, with and without Nanofluids, for Solar PV/T Collectors. *Energies*, *12*(15), 15. https://doi.org/10.3390/en12153036

Mousazadeh, H., Keyhani, A., Javadi, A., Mobli, H., Abrinia, K., & Sharifi, A. (2009). A review of principle and sun-tracking methods for maximizing solar systems output. *Renewable and Sustainable Energy Reviews*, *13*(8), 1800–1818. https://doi.org/10.1016/j.rser.2009.01.022

Nakata, Y., Kobe, T., Machida, T., Shibuya, N., Takemoto, T., & Tsuji, T. (1982). A 30kwp Concentrating Photovoltaic/Thermal Hybrid System Application. *Conf. Rec. IEEE Photovoltaic Spec. Conf.; (United States)*. https://www.osti.gov/scitech/biblio/5489267

Nann, S., & Emery, K. (1992). Spectral effects on PV-device rating. *Solar Energy Materials and Solar Cells*, *27*(3), 189–216. https://doi.org/10.1016/0927-0248(92)90083-2

Nishioka, K., Takamoto, T., Agui, T., Kaneiwa, M., Uraoka, Y., & Fuyuki, T. (2006). Annual output estimation of concentrator photovoltaic systems using high-efficiency InGaP/InGaAs/Ge triple-junction solar cells based on experimental solar cell's characteristics and field-test meteorological data. *Solar Energy Materials and Solar Cells*, *90*(1), 57–67. https://doi.org/10.1016/j.solmat.2005.01.011

Niu, G., Guo, X., & Wang, L. (2015). Review of recent progress in chemical stability of perovskite solar cells. *Journal of Materials Chemistry A*, *3*(17), 8970–8980.

NREL. (2023). *NREL Best Research-Cell Efficiency Chart*. https://www.nrel.gov/pv/cell-efficiency.html

Oberkampf, W. L., DeLand, S. M., Rutherford, B. M., Diegert, K. V., & Alvin, K. F. (2002). Error and uncertainty in modeling and simulation. *Reliability Engineering & System Safety*, *75*(3), 333–357. https://doi.org/10.1016/S0951-8320(01)00120-X

Ohadi, M., Choo, K., Dessiatoun, S., & Cetegen, E. (2013). Force-Fed Microchannels for High Flux Cooling Applications. In M. Ohadi, K. Choo, S. Dessiatoun, & E. Cetegen (Eds.), *Next Generation Microchannel Heat Exchangers* (pp. 33–65). Springer. https://doi.org/10.1007/978-1-4614-0779-9_2

O'Neill, M. J. (1985). Measured performance for the first three years of operation of the DFW airport 27 kW (electric)/120 kW (thermal) photovoltaic and thermal (PVT) concentrator system. *Proceedings of the IEEE Photovoltaic Specialists Conference*, 1249–1254.

Osterwald, C. R., Wanlass, M. W., Moriarty, T., Steiner, M. A., & Emery, K. A. (2014). *Effects of Spectral Error in Efficiency Measurements of GaInAs-Based Concentrator Solar Cells* (NREL/TP-5200-60748). National Renewable Energy Lab. (NREL), Golden, CO (United States). https://doi.org/10.2172/1126836

Otanicar, T., Chowdhury, I., Phelan, P. E., & Prasher, R. (2010). Parametric analysis of a coupled photovoltaic/thermal concentrating solar collector for electricity generation. *Journal of Applied Physics*, *108*(11), 114907. https://doi.org/10.1063/1.3514590

Papis-Frączek, K., & Sornek, K. (2022). A Review on Heat Extraction Devices for CPVT Systems with Active Liquid Cooling. *Energies*, *15*(17), 17. https://doi.org/10.3390/en15176123

Pastuszak, J., & Węgierek, P. (2022). Photovoltaic Cell Generations and Current Research Directions for Their Development. *Materials*, *15*(16), 16. https://doi.org/10.3390/ma15165542

Pedrotti, F. L., Pedrotti, L. M., & Pedrotti, L. S. (2017). *Introduction to Optics*. Cambridge University Press.

POPIEL, C. O., & WOJTKOWIAK, J. (2007). Simple Formulas for Thermophysical Properties of Liquid Water for Heat Transfer Calculations (from 0°C to 150°C). *Heat Transfer Engineering*. https://doi.org/10.1080/01457639808939929

Renno, C., & De Giacomo, M. (2014). Dynamic Simulation of a CPV/T System Using the Finite Element Method. *Energies*, *7*(11), 11. https://doi.org/10.3390/en7117395

Renno, C., & Petito, F. (2013). Design and modeling of a concentrating photovoltaic thermal (CPV/T) system for a domestic application. *Energy and Buildings*, *62*, 392–402. https://doi.org/10.1016/j.enbuild.2013.02.040

Renno, C., & Petito, F. (2015). Choice model for a modular configuration of a point-focus CPV/T system. *Energy and Buildings*, *92*, 55–66. https://doi.org/10.1016/j.enbuild.2015.01.023

Renno, C., & Petito, F. (2016). Experimental and theoretical model of a concentrating photovoltaic and thermal system. *Energy Conversion and Management*, *126*, 516–525. https://doi.org/10.1016/j.enconman.2016.08.027

Ritchie, H., Roser, M., & Rosado, P. (2022). Energy. *Our World in Data*. https://ourworldindata.org/energy-production-consumption

Rizzi, A. W., & Inouye, M. (1973). Time-Split Finite-Volume Method for Three-Dimensional Blunt-Body Flow. *AIAA Journal*, *11*(11), 1478–1485. https://doi.org/10.2514/3.50614

Rosell, J. I., Vallverdú, X., Lechón, M. A., & Ibáñez, M. (2005). Design and simulation of a low concentrating photovoltaic/thermal system. *Energy Conversion and Management*, *46*(18), 3034–3046. https://doi.org/10.1016/j.enconman.2005.01.012

Salim, S. M., & Cheah, S. (2009). Wall y+ strategy for dealing with wall-bounded turbulent flows. *Proceedings of the International Multiconference of Engineers and Computer Scientists*, *2*, 2165–2170.

Sampaio, P. G. V., & González, M. O. A. (2017). Photovoltaic solar energy: Conceptual framework. *Renewable and Sustainable Energy Reviews*, *74*, 590–601. https://doi.org/10.1016/j.rser.2017.02.081

Santana, J. P., Rivera-Solorio, C. I., Chew, J. W., Tan, Y. Z., Gijón-Rivera, M., & Acosta-Pazmiño, I. (2023). Performance Assessment of Coupled Concentrated Photovoltaic-Thermal and Vacuum Membrane Distillation (CPVT-VMD) System for Water Desalination. *Energies*, *16*(3), 3. https://doi.org/10.3390/en16031541

Santbergen, R. (2008). *Optical absorption factor of solar cells for PVT systems* [Phd Thesis 1 (Research TU/e / Graduation TU/e), Technische Universiteit Eindhoven]. https://doi.org/10.6100/IR639175

Segal, A., & Epstein, M. (1999). COMPARATIVE PERFORMANCES OF `TOWER-TOP' AND `TOWER-REFLECTOR' CENTRAL SOLAR RECEIVERS. *Solar Energy*, *65*(4), 207–226. https://doi.org/10.1016/S0038-092X(98)00138-8

Segal, A., Epstein, M., & Yogev, A. (2004). Hybrid concentrated photovoltaic and thermal power conversion at different spectral bands. *Solar Energy*, *76*(5), 591–601. https://doi.org/10.1016/j.solener.2003.12.002

Shanks, K., Senthilarasu, S., & Mallick, T. K. (2016). Optics for concentrating photovoltaics: Trends, limits and opportunities for materials and design. *Renewable and Sustainable Energy Reviews*, *60*, 394–407. https://doi.org/10.1016/j.rser.2016.01.089

Sharaf, O. Z., & Orhan, M. F. (2015a). Concentrated photovoltaic thermal (CPVT) solar collector systems: Part I – Fundamentals, design considerations and current

technologies. *Renewable and Sustainable Energy Reviews*, *50*, 1500–1565. https://doi.org/10.1016/j.rser.2015.05.036

Sharaf, O. Z., & Orhan, M. F. (2015b). Concentrated photovoltaic thermal (CPVT) solar collector systems: Part II – Implemented systems, performance assessment, and future directions. *Renewable and Sustainable Energy Reviews*, *50*, 1566–1633. https://doi.org/10.1016/j.rser.2014.07.215

Singh, G. K. (2013). Solar power generation by PV (photovoltaic) technology: A review. *Energy*, *53*, 1–13. https://doi.org/10.1016/j.energy.2013.02.057

Skoog, D. A., Holler, F. J., & Crouch, S. R. (2017). *Principles of Instrumental Analysis*. Cengage Learning.

Skoplaki, E., & Palyvos, J. A. (2009). On the temperature dependence of photovoltaic module electrical performance: A review of efficiency/power correlations. *Solar Energy*, *83*(5), 614–624. https://doi.org/10.1016/j.solener.2008.10.008

Spectrolab. (2009). *Spectrolab. CDO-030-C3MJ Concentrator Solar Cell. Spectrolab, Inc 2009:2.* https://www.spectrolab.com/photovoltaics/C3P5_39.5_Point_Focus_Solar_Cells.pdf

Su, Y., Kulacki, F. A., & Davidson, J. H. (2014). Experimental and numerical investigations on a solar tracking concentrated photovoltaic–thermal system with a novel non-dimensional lattice Boltzmann method. *Solar Energy*, *107*, 145–158. https://doi.org/10.1016/j.solener.2014.05.033

Su, Y., Sui, P., & Davidson, J. H. (2022). A sub-continuous lattice Boltzmann simulation for nanofluid cooling of concentrated photovoltaic thermal receivers. *Renewable Energy*, *184*, 712–726. https://doi.org/10.1016/j.renene.2021.11.110

Swami, R. (2012). Solar Cell. *International Journal of Scientific and Research Publications*, *2*(7), 1–5.

Swanson, R. M. (2003). Photovoltaic Concentrators. In *Handbook of Photovoltaic Science and Engineering* (pp. 449–503). John Wiley & Sons, Ltd. https://doi.org/10.1002/0470014008.ch11

Tamilarasan, A. P. (2015). *Numerical modelling of heat transfer and evaporation characteristics of cryogenic liquid propellant* [Thesis]. https://digital.lib.washington.edu:443/researchworks/handle/1773/35255

Tawfik, M., Tonnellier, X., & Sansom, C. (2018). Light source selection for a solar simulator for thermal applications: A review. *Renewable and Sustainable Energy Reviews*, *90*, 802–813. https://doi.org/10.1016/j.rser.2018.03.059

The World Bank. (2022). *Report: COVID-19 Slows Progress Towards Universal Energy Access* [Text/HTML]. World Bank. https://www.worldbank.org/en/news/press-release/2022/06/01/report-covid-19-slows-progress-towards-universal-energy-access

Theristis, M., & O'Donovan, T. S. (2015). Electrical-thermal analysis of III–V triple-junction solar cells under variable spectra and ambient temperatures. *Solar Energy*, *118*, 533–546. https://doi.org/10.1016/j.solener.2015.06.003

Thinsurat, K. (2019). *Seasonal and Short-term Energy Storage Through the Integration of Solar PV/T with Thermochemical Sorption Technology for Domestic Applications* [PhD Thesis]. Newcastle University.

Tonui, J. K. (2006). *Hybrid photovoltaic/thermal solar energy systems* [Ph.D. Thesis, University of Patras]. http://hdl.handle.net/10442/hedi/27740

Tu, J., Yeoh, G. H., Liu, C., & Tao, Y. (2018). *Computational Fluid Dynamics: A Practical Approach* (Third Edition). Elsevier.

Vafai, K., & Zhu, L. (1999). Analysis of two-layered micro-channel heat sink concept in electronic cooling. *International Journal of Heat and Mass Transfer*, *42*(12), 2287–2297. https://doi.org/10.1016/S0017-9310(98)00017-9

van Dyk, E. E., Meyer, E. L., Vorster, F. J., & Leitch, A. W. R. (2002). Long-term monitoring of photovoltaic devices. *Renewable Energy*, *25*(2), 183–197. https://doi.org/10.1016/S0960-1481(01)00064-7

van Sark, W. G. J. H. M. (2013). Luminescent solar concentrators – A low cost photovoltaics alternative. *Renewable Energy*, *49*(Supplement C), 207–210. https://doi.org/10.1016/j.renene.2012.01.030

Vivar, M., Clarke, M., Pye, J., & Everett, V. (2012). A review of standards for hybrid CPV-thermal systems. *Renewable and Sustainable Energy Reviews*, *16*(1), 443–448. https://doi.org/10.1016/j.rser.2011.08.008

Vivar, M., Everett, V., Fuentes, M., Blakers, A., Tanner, A., Le, L., & Greaves, M. (2013). Initial field performance of a hybrid CPV-T microconcentrator system. *Progress in Photovoltaics: Research and Applications*, *21*(8), 1659–1671. Scopus. https://doi.org/10.1002/pip.2229

Vivar, M., Everett, V., Fuentes, M., Thomsen, E., Harvey, J., Ebert, M., le Lievre, P., Greaves, M., Tanner, A., & Blakers, A. (2012). Results from the first ANU-chromasun CPV-T microconcentrator prototype in Canberra. *AIP Conference Proceedings*, *1477*(1), 114–117. https://doi.org/10.1063/1.4753847

Vodret, S., Maio, D. V. D., & Caruso, G. (2014). Numerical simulation of turbulent forced convection in liquid metals. *Journal of Physics: Conference Series*, *547*(1), 012033. https://doi.org/10.1088/1742-6596/547/1/012033

Walter, D., Everett, V., Blakers, A., Vivar, M., Harvey, J., Muric-Nesic, J., Ratcliff, T., Surve, S., Scheppingen, R. V., Lievre, P. L., Greaves, M., & Tanner, A. (2010). A 20-sun hybrid PV-Thermal linear micro-concentrator system for urban rooftop applications. *2010 35th IEEE Photovoltaic Specialists Conference*, 000831–000836. https://doi.org/10.1109/PVSC.2010.5617182

Wang, X.-Q., Yap, C., & Mujumdar, A. S. (2008). A parametric study of phase change material (PCM)-based heat sinks. *International Journal of Thermal Sciences*, *47*(8), 1055–1068. https://doi.org/10.1016/j.ijthermalsci.2007.07.016

Warren M., R., James P. Hartnett, & Young I. Cho. (1998). NATURAL CONVECTION. In *Handbook of Heat Transfer* (3rd ed.). McGraw-Hill Education. https://www.accessengineeringlibrary.com/content/book/9780070535558/chapter/chapter4

Wiesenfarth, M., Philipps, S. P., Bett, A. W., Horowitz, K., & Kurtz, S. (2017). *CURRENT STATUS OF CONCENTRATOR PHOTOVOLTAIC (CPV) TECHNOLOGY*. *Version 1.3*(TP-6A20-63916). https://www.academia.edu/35797553/CURRENT_STATUS_OF_CONCENTRATOR_PHOTOVOLTAIC_CPV_TECHNOLOGY

Wolf, M. (1960). Limitations and Possibilities for Improvement of Photovoltaic Solar Energy Converters: Part I: Considerations for Earth's Surface Operation. *Proceedings of the IRE*, *48*(7), 1246–1263. https://doi.org/10.1109/JRPROC.1960.287647

Wong, K.-F. V., & Dorney, S. (1983). *A thermo-electric system using concentrated solar energy with photovoltaic cells*. 1103–1110. http://adsabs.harvard.edu/abs/1983thsc.conf.1103W

Wu, G., Yang, Q., Fang, H., Zhang, Y., Zheng, H., Zhu, Z., & Feng, C. (2019). Photothermal/day lighting performance analysis of a multifunctional solid compound parabolic concentrator for an active solar greenhouse roof. *Solar Energy*, *180*, 92–103. https://doi.org/10.1016/j.solener.2019.01.007

Wu, Y., Eames, P., Mallick, T., & Sabry, M. (2012). Experimental characterisation of a Fresnel lens photovoltaic concentrating system. *Solar Energy*, *86*(1), 430–440. https://doi.org/10.1016/j.solener.2011.10.032

Xia, X. W., Parfenov, A. V., Aye, T. M., & Shih, M.-Y. (2011). *Efficient hybrid electric and thermal energy generation*. *8108*, 81080F. https://doi.org/10.1117/12.894166

Xu, N., Ji, J., Sun, W., Han, L., Chen, H., & Jin, Z. (2015). Outdoor performance analysis of a 1090× point-focus Fresnel high concentrator photovoltaic/thermal system with triple-junction solar cells. *Energy Conversion and Management*, *100*, 191–200. https://doi.org/10.1016/j.enconman.2015.04.082

Xu, N., Ji, J., Sun, W., Huang, W., Li, J., & Jin, Z. (2016). Numerical simulation and experimental validation of a high concentration photovoltaic/thermal module based on point-focus Fresnel lens. *Applied Energy*, *168*(Supplement C), 269–281. https://doi.org/10.1016/j.apenergy.2016.01.077

Yamaguchi, M. (2003). III–V compound multi-junction solar cells: Present and future. *Solar Energy Materials and Solar Cells*, *75*(1), 261–269. https://doi.org/10.1016/S0927-0248(02)00168-X

Yastrebova, N. V. (2007). High-efficiency multi-junction solar cells: Current status and future potential. *Centre for Research in Photonics, University of Ottawa*.

Zhang, L., Jing, D., Zhao, L., Wei, J., & Guo, L. (2012). Concentrating PV/T Hybrid System for Simultaneous Electricity and Usable Heat Generation: A Review. *International Journal of Photoenergy*, *2012*, e869753. https://doi.org/10.1155/2012/869753

Zhang, Z., Hu, Z., & Xu, H. (2019). Theoretical analysis of a solar-powered multi-effect distillation integrated with concentrating photovoltaic/thermal system. *Desalination*, *468*, 114074. https://doi.org/10.1016/j.desal.2019.114074

Zhou, Y. (2015). *Eco- and Renewable Energy Materials*. Springer.

Zhu, L., Boehm, R. F., Wang, Y., Halford, C., & Sun, Y. (2011). Water immersion cooling of PV cells in a high concentration system. *Solar Energy Materials and Solar Cells*, *95*(2), 538–545. https://doi.org/10.1016/j.solmat.2010.08.037

Appendix A

Test Fixture Specifications

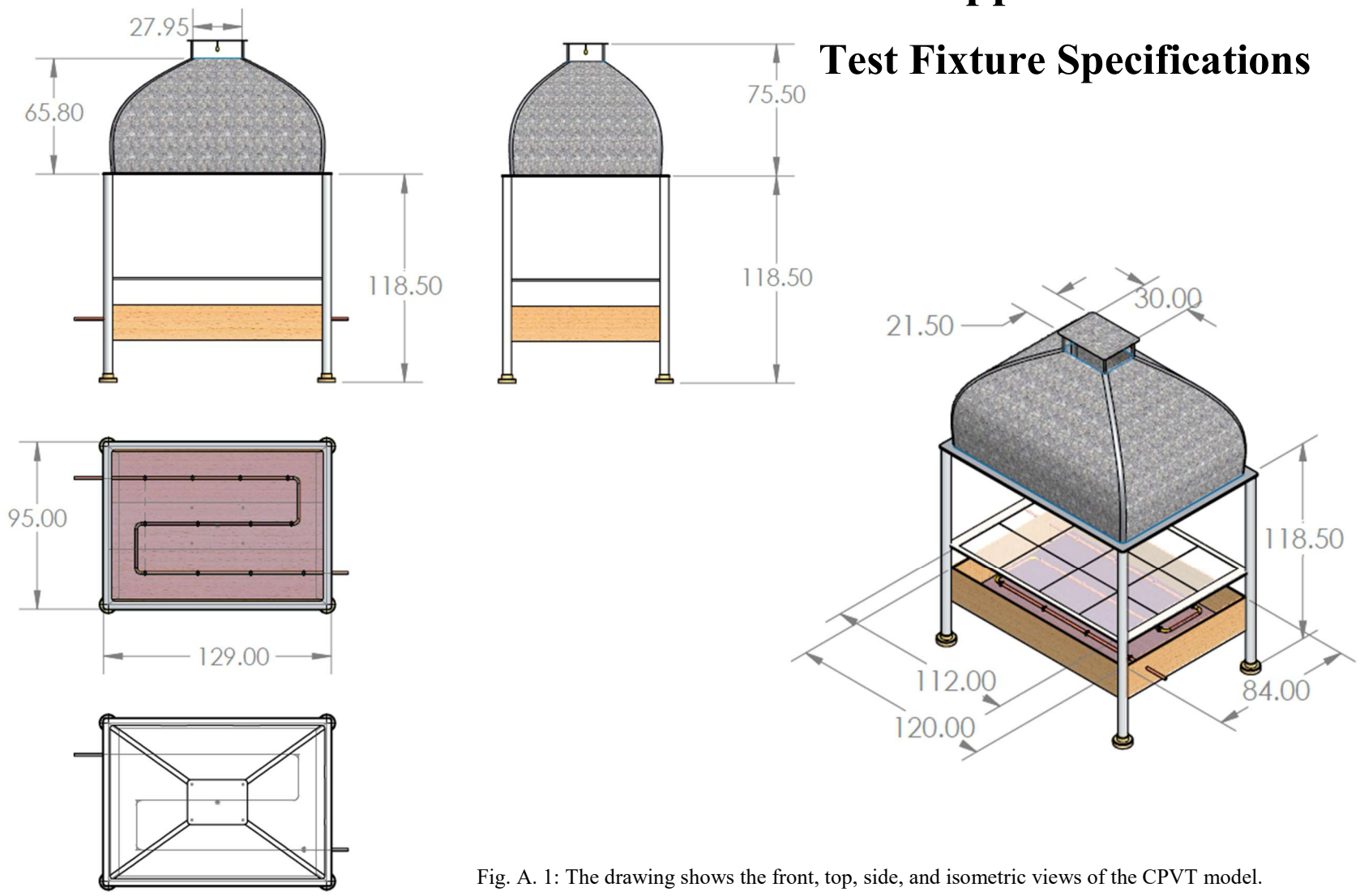

Fig. A. 1: The drawing shows the front, top, side, and isometric views of the CPVT model.

Dimensions in cm.

Appendix B

TES-1333/1333R Solar Power Meter

B.1 Product Features

- Light Transmittance of window film detection.
- Wide spectral range.
- Excellent long-term stability.
- Cosine corrected.
- Automatic transmission measurements.
- Select either power or transmission.
- Solar energy measurement.
- Current time setting function.
- User calibration factor setting function.
- End-mount light sensor.
- Select either W/m^2 or $Btu / (ft^2h)$ units.
- Data Hold/MAX/MIN/AVG modes.
- Data Memory and Read function. (99 sets)
- Auto Data Memory and RS232 interface to PC. (TES-1333R)

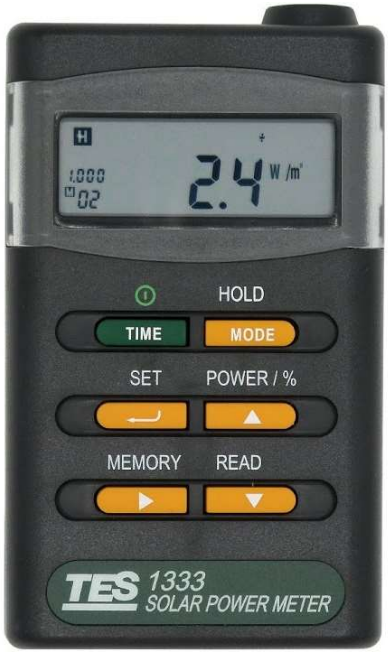

Fig. B. 1: TES-1333/1333R Solar Power Meter

B.2 Applications

- Meteorology.
- Agriculture.
- Solar radiation measurement.
- Solar power research.
- Physics and optical laboratories.
- Solar transmission measurement.
- Identify high performance windows.

B.3 Specification

Display	LCD display, 4-digit LCD reading
Range	2000 *W/m²*, 634 *Btu/(ft²h)*
Resolution	0.1 *W/m²*, 0.1 *Btu / (ft²h)*
Spectral response	400-1100*nm*
Accuracy	Typically, within ±10 *W/m²* [±3 *Btu/(ft²h)*] or ±5%, whichever is greater in sunlight; Additional temperature induced error ±0.38 *W/m²/℃* [±0.12 *Btu/(ft²h)/℃*] from 25 *℃*
Angular accuracy	Cosine corrected <5% for angles < 60°
Drift	< ±2% per year
Calibration	User recalibration available
Over-Input	Display shows “OL”
Sampling Rate	4 times/sec
Manu Data Memory and Read	99 sets
Auto Data Memory	43000 sets (TES-1333R)
Battery	4 pcs size AAA
Battery Life	Approx. 100 hours
Operating Temp and Humidity	0 *℃* to 50 *℃* (32 *℉* to 122 *℉*) below 80% RH
Storage Temp and Humidity	-10 *℃* to 60 *℃* below 70% RH
Weight	Approximately 158*g*
Dimension	110 (*L*) × 64 (*W*) × 34 (H) *mm*
Accessories Included	Manual, 4 pcs size AAA, (RS232 Cable, CD software →TES-1333R)

Appendix C

Uncertainty Analysis

C.1 Introduction

Uncertainty is an inevitable aspect of any experimental research, as it reflects the limitations and variability of the measurement process. Uncertainty can arise from various sources, such as the accuracy and precision of the instruments, the environmental conditions, the human errors, and the assumptions and approximations involved in the data analysis. Uncertainty affects the quality and reliability of the experimental results and can influence the interpretation and comparison of the data with other studies or theoretical models. Therefore, it is essential to estimate and report the uncertainty of the experimental measurements using appropriate methods and standards. We used the approach proposed by Kline and McClintock (1953) to calculate the uncertainty in our measurements. This technique is often called the root-sum squared (RSS) method. It allows us to estimate the uncertainty in our results from the uncertainties in our primary measurements. The uncertainty in a measurement propagates through other calculations that depend on that measurement. This kind is called uncertainty propagation. We computed the propagation of errors using the RSS method, which assumes that a result R is a function of a group of independent variables as follows:

$$R = R(x_1, x_2, x_3, \dots\dots\dots\dots, x_n) \qquad (\text{C. } 1)$$

Assume that w_1, w_2, w_3,.....,w_n are the uncertainties in the independent variables x_1, x_2, x_3,.....,x_n then the uncertainty in the results w_R can be determined from (Holman, 2012).

$$w_R = \left[\left(\frac{\partial R}{\partial x_1} w_1\right)^2 + \left(\frac{\partial R}{\partial x_2} w_2\right)^2 + \cdots + \left(\frac{\partial R}{\partial x_n} w_n\right)^2\right]^{1/2} \quad \text{(C. 2)}$$

Table C.1 summarizes the uncertainties of the experimental instruments, such as thermocouples, flowmeter, pressure transducer, solar power meter, digital multimeter, and thermal bath. The uncertainties in the properties of the working fluid are ± 0.5%.

Table C. 1: Uncertainties of experimental instruments

Equipment	Measurement	Uncertainty
Thermocouple	Temperature [℃]	± 0.1 ℃
Flowmeter	Flow rate [gpm]	± 1.0 %
Pressure transducer	Pressure [*Pa*]	± 0.08 %
Solar power meter	Radiation [W/m^2]	± 5.0 %
Digital multimeter	Voltage [*V*]	± 0.01 %
Digital multimeter	Ampere [*A*]	± 0.01 %
Thermal bath	Temperature [℃]	± 0.1 ℃

C.2 Uncertainty in ΔT and T_m

The uncertainty in the ΔT and T_m can be determined by employing Eq. (C.2) as follows:

$$w_{\Delta T} = \left[\left(\frac{\partial \Delta T}{\partial T_o} w_{T_o}\right)^2 + \left(\frac{\partial \Delta T}{\partial T_i} w_{T_i}\right)^2\right]^{1/2} \quad \text{(C. 3)}$$

$$w_{T_m} = \left[\left(\frac{\partial T_m}{\partial T_i} w_{T_i}\right)^2 + \left(\frac{\partial T_m}{\partial T_o} w_{T_o}\right)^2\right]^{1/2} \quad \text{(C. 4)}$$

C.3 Uncertainty in mass flow rate

The uncertainty in mass flow rate is calculated as follows:

$$\frac{w_{\dot{m}}}{\dot{m}} = \left[\left(\frac{w_\rho}{\rho}\right)^2 + \left(\frac{w_{\dot{V}}}{\dot{V}}\right)^2\right]^{1/2} \quad (C.5)$$

C.4 Uncertainty in Re and f

The uncertainty in the Reynolds number can be determined by employing Eq. (C.2) as follows:

$$\frac{w_{Re}}{Re} = \left[\left(\frac{w_{\dot{m}}}{\dot{m}}\right)^2 + \left(\frac{w_{D_i}}{D_i}\right)^2 + \left(\frac{w_{A_c}}{A_c}\right)^2 + \left(\frac{w_\mu}{\mu}\right)^2\right]^{1/2} \quad (C.6)$$

The uncertainty in the Fanning friction factor is determined from the following expression:

$$\frac{w_f}{f} = \left[\left(\frac{w_{\Delta P}}{\Delta P}\right)^2 + \left(\frac{w_{D_i}}{D_i}\right)^2 + \left(\frac{w_\rho}{\rho}\right)^2 + \left(\frac{w_L}{L}\right)^2 + \left(2\frac{w_U}{U}\right)^2\right]^{1/2} \quad (C.7)$$

C.5 Uncertainty in heat transfer measurements

The uncertainty in heat transfer measurements is calculated as follows:

$$\frac{w_Q}{Q} = \left[\left(\frac{w_{\dot{m}}}{\dot{m}}\right)^2 + \left(\frac{w_{C_p}}{C_p}\right)^2 + \left(\frac{w_{\Delta T}}{\Delta T}\right)^2\right]^{1/2} \quad (C.8)$$

For the heat transfer coefficient, the uncertainty is calculated using the following expression:

$$\frac{w_h}{h} = \left[\left(\frac{w_Q}{Q}\right)^2 + \left(\frac{w_{D_i}}{D_i}\right)^2 + \left(\frac{w_L}{L}\right)^2 + \left(\frac{w_{T_w}}{T_w - T_m}\right)^2 + \left(\frac{w_{T_m}}{T_w - T_m}\right)^2\right]^{1/2} \quad \text{(C. 9)}$$

Finally, the uncertainty in the Nusselt number is computed from:

$$\frac{w_{Nu}}{Nu} = \left[\left(\frac{w_h}{h}\right)^2 + \left(\frac{w_{D_i}}{D_i}\right)^2 + \left(\frac{w_k}{k}\right)^2\right]^{1/2} \quad \text{(C. 10)}$$

Table C.2 summarizes the calculated uncertainties in the temperature differentials (ΔT), mean temperature (T_m), flow rates, Reynolds numbers (Re), friction factor (f), heat transfer, and Nusselt numbers (Nu). The uncertainties in these parameters depend on the accuracy of temperature, flow rate, and pressure measurements, as well as uncertainties in the thermo-physical properties of the working fluids.

Table C. 2: Relative uncertainties of various parameters

Parameters	Uncertainty	Parameters	Uncertainty
ΔT	0.83/12.29 %	Re	4.64/5.48 %
T_m	0.30/0.41 %	f	5.15/12.90 %
Flow rate	2.55/12.93 %	Q	12.54/13.29 %
Nu	13.89/14.45 %	A_c	0.70 %

Appendix D

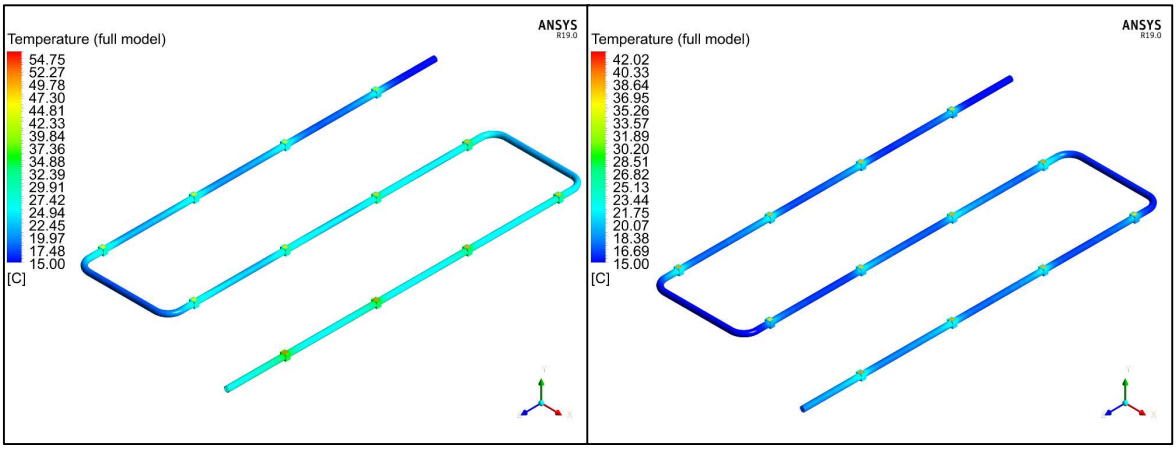

Fig. D. 1: Temperature contours of the full module at *CR* 100X, mass flow rates of 0.0029 *kg/s* on the left and 0.025 *kg/s* on the right (laminar flow).

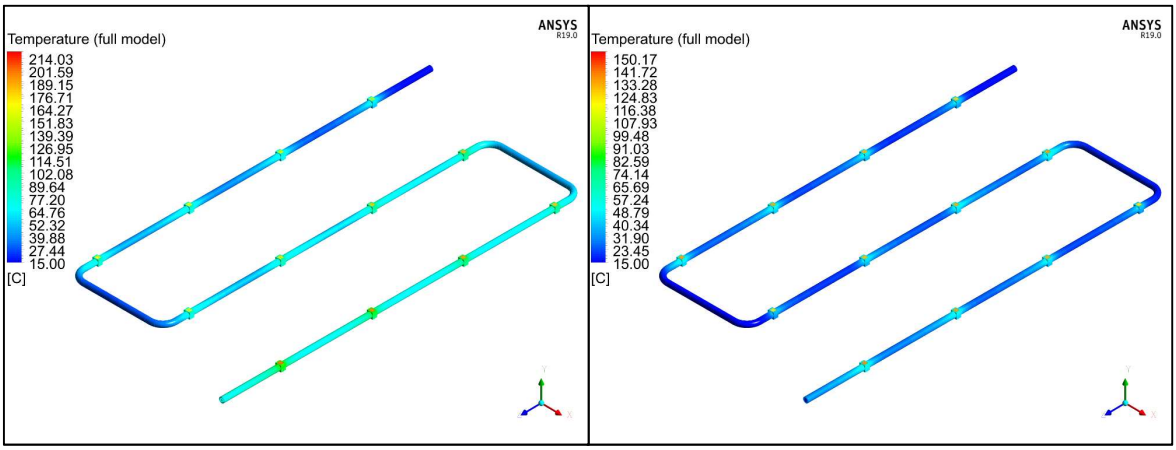

Fig. D. 2: Temperature contours of the full module at *CR* 500X, mass flow rates of 0.0029 *kg/s* on the left and 0.025 kg/s on the right (laminar flow).

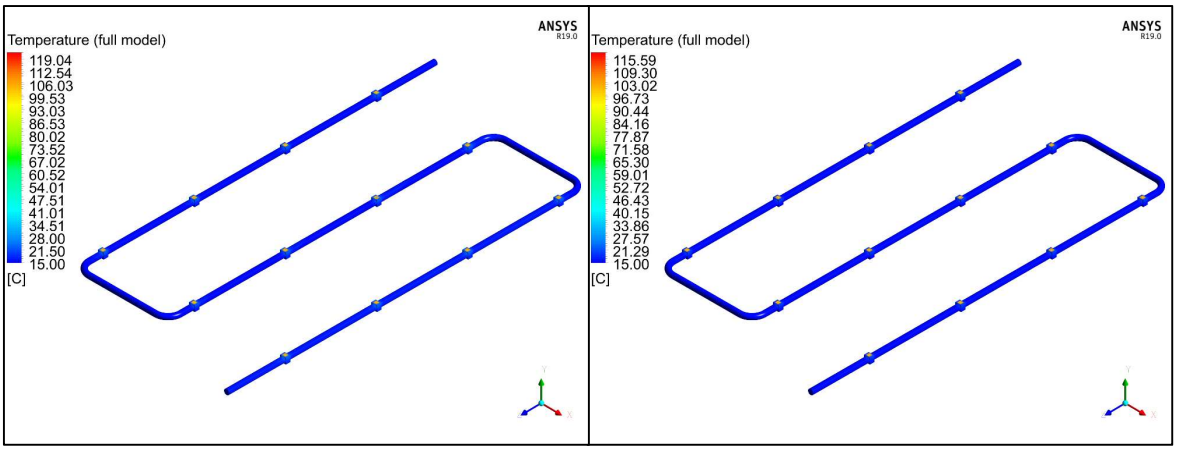

Fig. D. 3: Temperature contours of the full module at *CR* 500X, mass flow rates of 0.1 *kg/s* on the left and 0.5 *kg/s* on the right (turbulent flow).

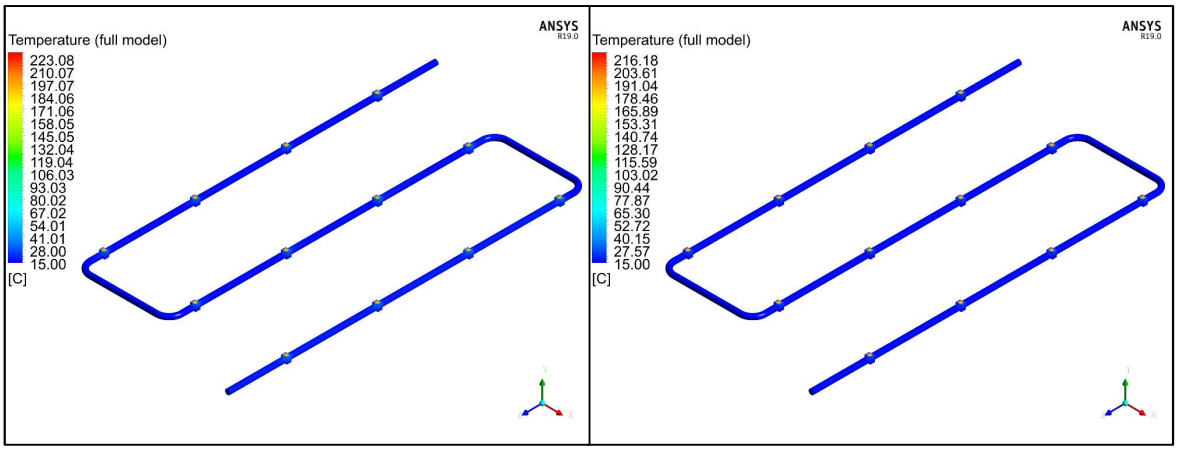

Fig. D. 4: Temperature contours of the full module at *CR* 1000X, mass flow rates of 0.1 *kg/s* on the left and 0.5 *kg/s* on the right (turbulent flow).

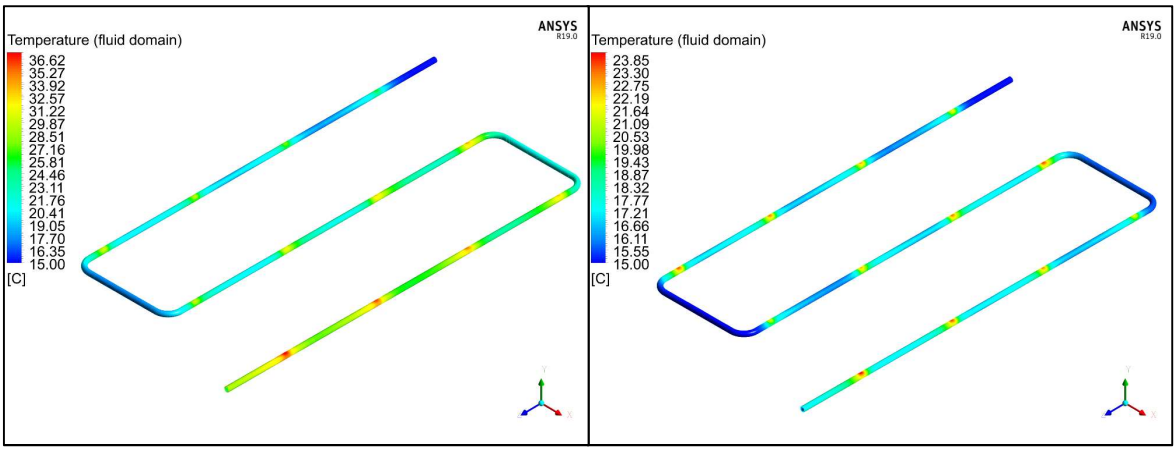

Fig. D. 5: Temperature contours of the fluid domain at *CR* 100X, mass flow rates of 0.0029 *kg/s* on the left and 0.025 *kg/s* on the right (laminar flow).

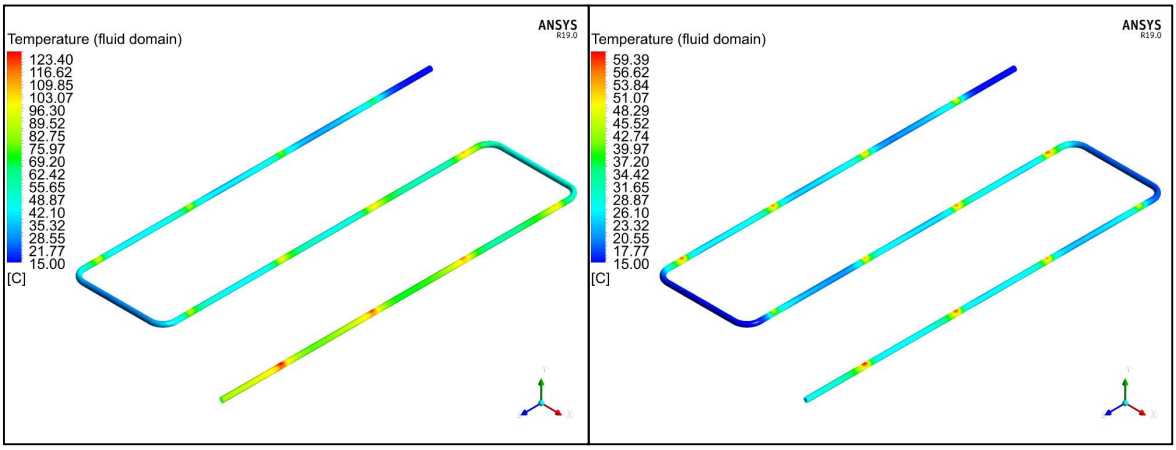

Fig. D. 6: Temperature contours of the fluid domain at *CR* 500X, mass flow rates of 0.0029 *kg/s* on the left and 0.025 *kg/s* on the right (laminar flow).

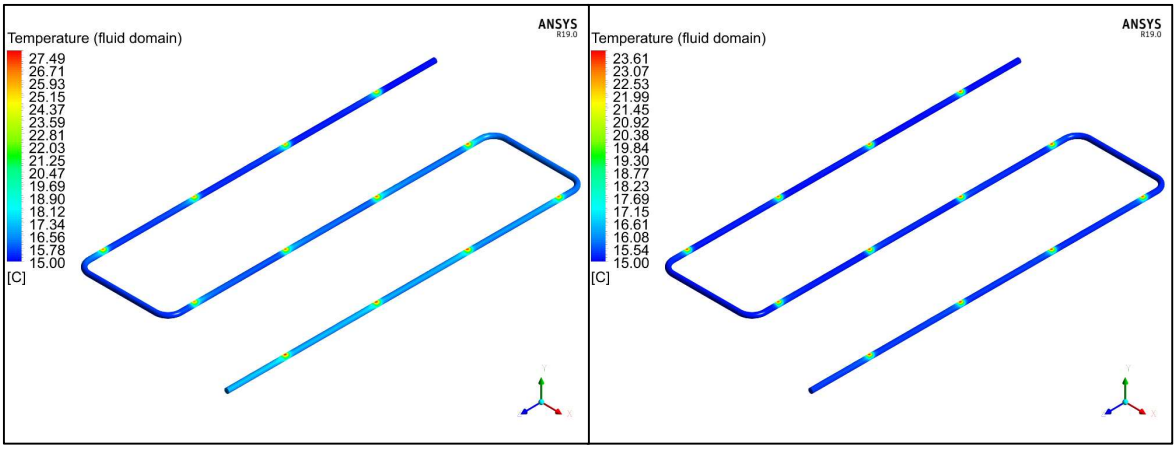

Fig. D. 7: Temperature contours of the fluid domain at *CR* 500X, mass flow rates of 0.1 *kg/s* on the left and 0.5 *kg/s* on the right (turbulent flow).

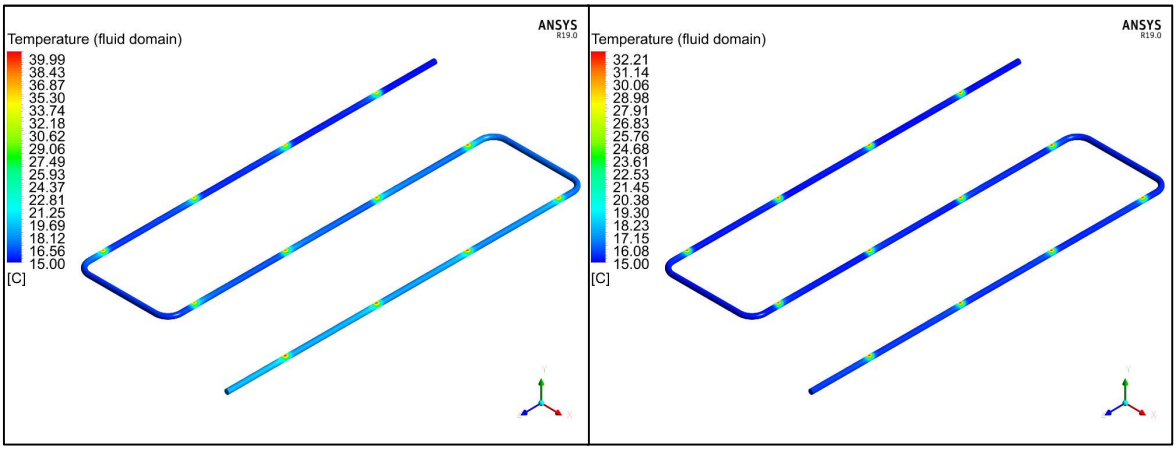

Fig. D. 8: Temperature contours of the fluid domain at *CR* 1000X, mass flow rates of 0.1 *kg/s* on the left and 0.5 *kg/s* on the right (turbulent flow).

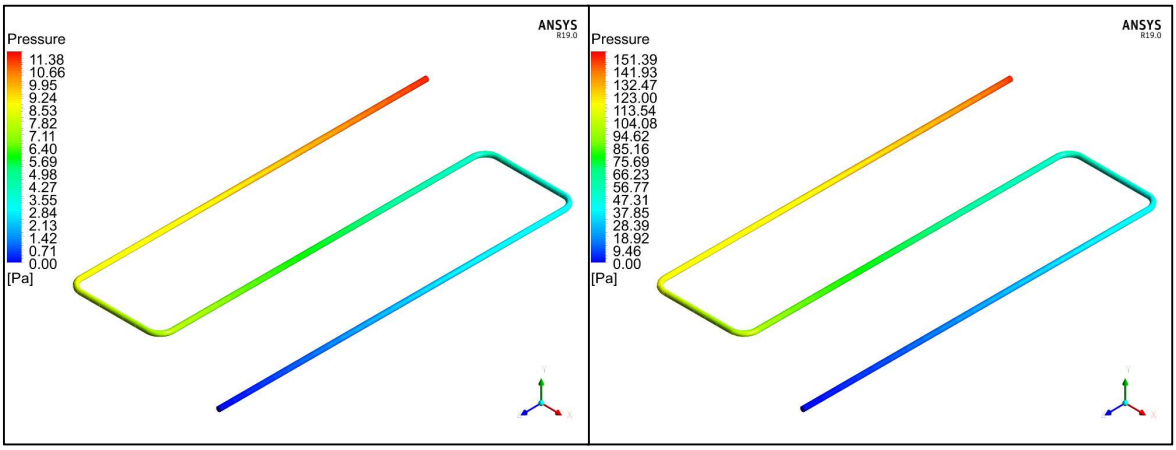

Fig. D. 9: Pressure contours of the fluid domain at mass flow rates of 0.0029 *kg/s* on the left and 0.025 *kg/s* on the right for all concentration ratios (laminar flow).

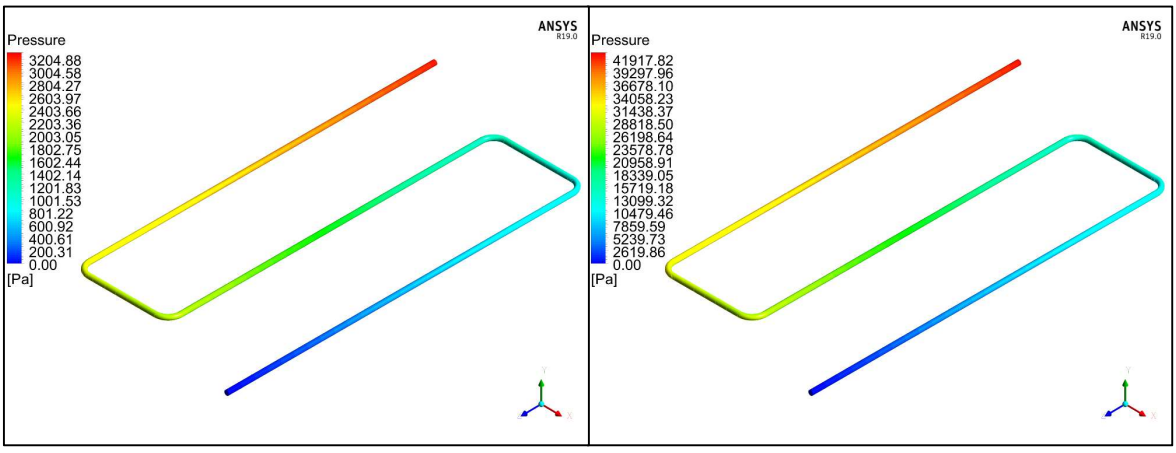

Fig. D. 10: Pressure contours of the fluid domain at mass flow rates of 0.1 *kg/s* on the left and 0.5 *kg/s* on the right for all concentration ratios (turbulent flow).

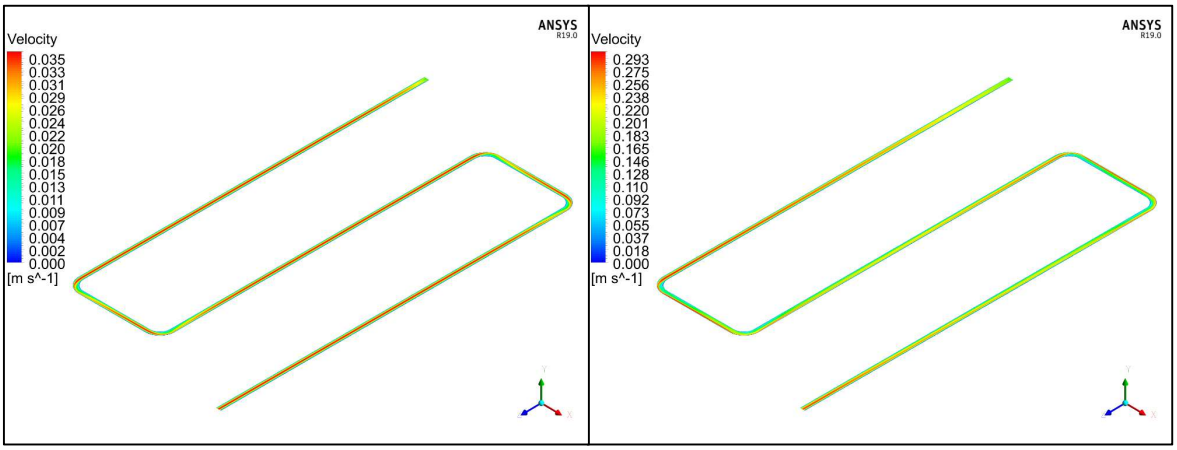

Fig. D. 11: Velocity contours of the fluid domain at mass flow rates of 0.0029 *kg/s* on the left and 0.025 *kg/s* on the right for all concentration ratios (laminar flow).

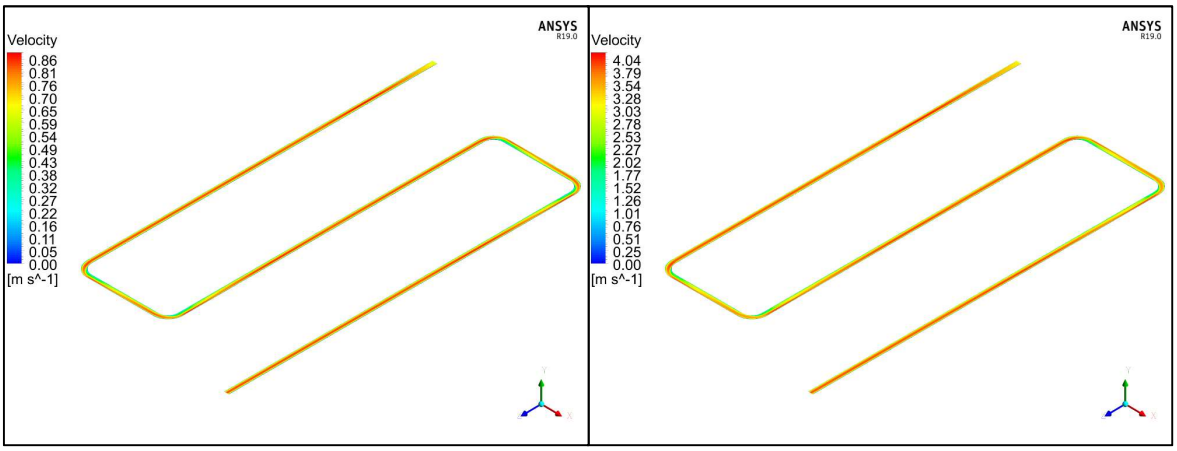

Fig. D. 12: Velocity contours of the fluid domain at mass flow rates of 0.1 *kg/s* on the left and 0.5 *kg/s* on the right for all concentration ratios (turbulent flow).

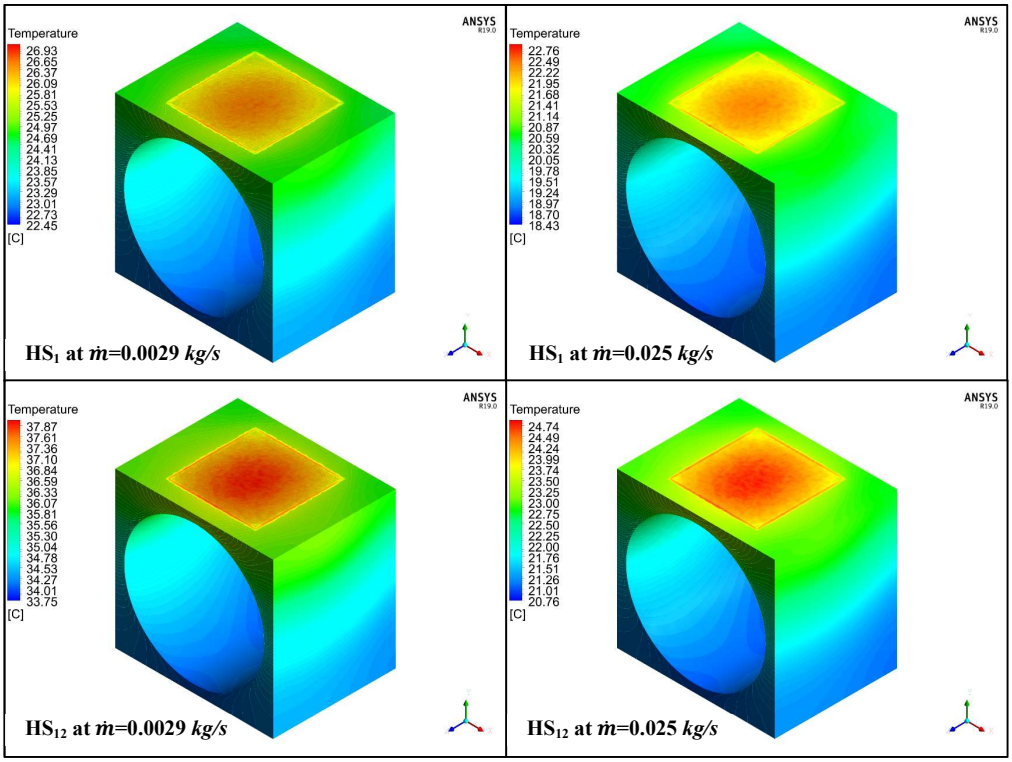

Fig. D. 13: 3-D temperature profile on selected heat sinks at *CR* = 100X for laminar flow

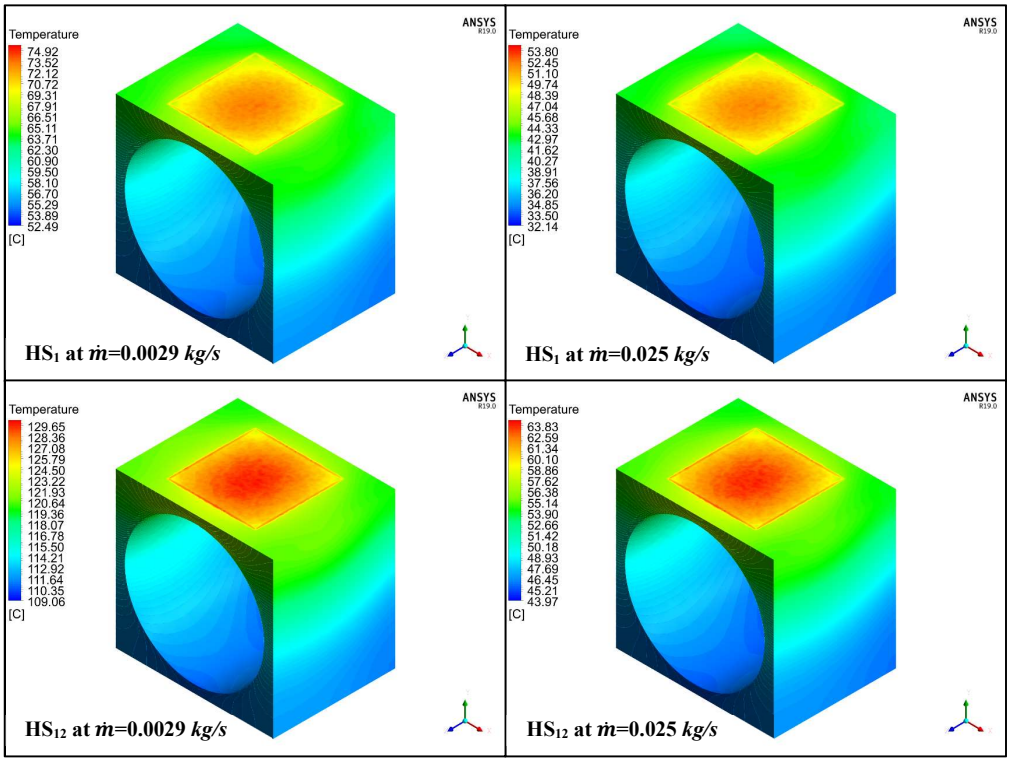

Fig. D. 14: 3-D temperature profile on selected heat sinks at *CR* = 500X for laminar flow

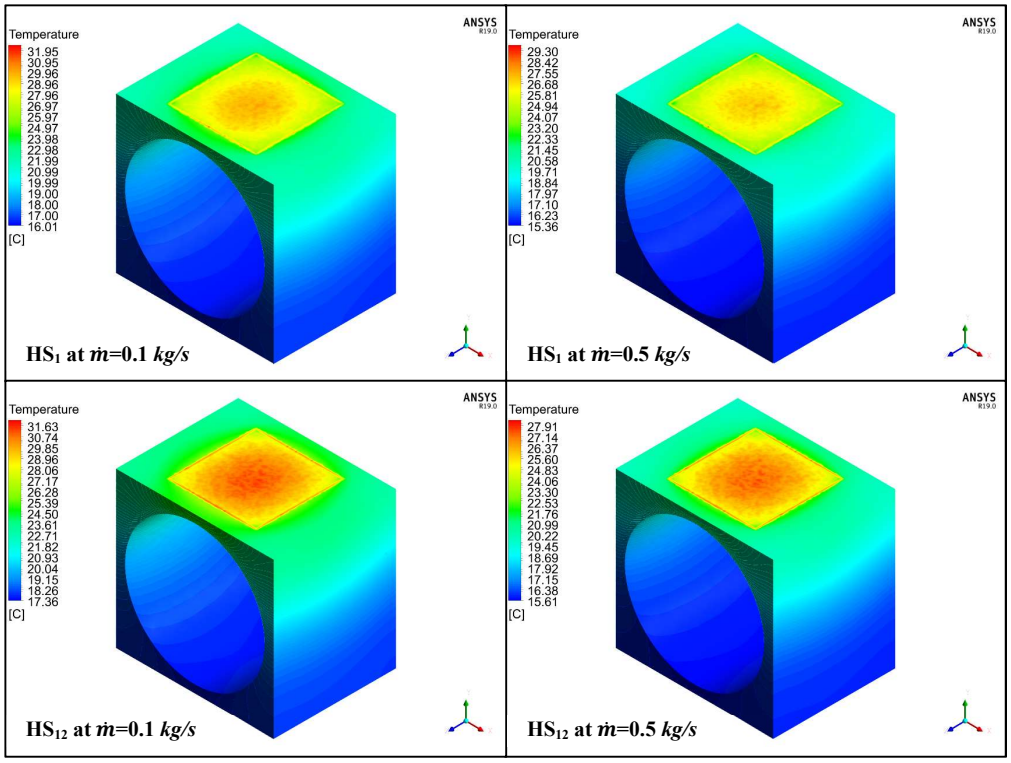

Fig. D. 15: 3-D temperature profile on selected heat sinks at *CR* = 500X for turbulent flow

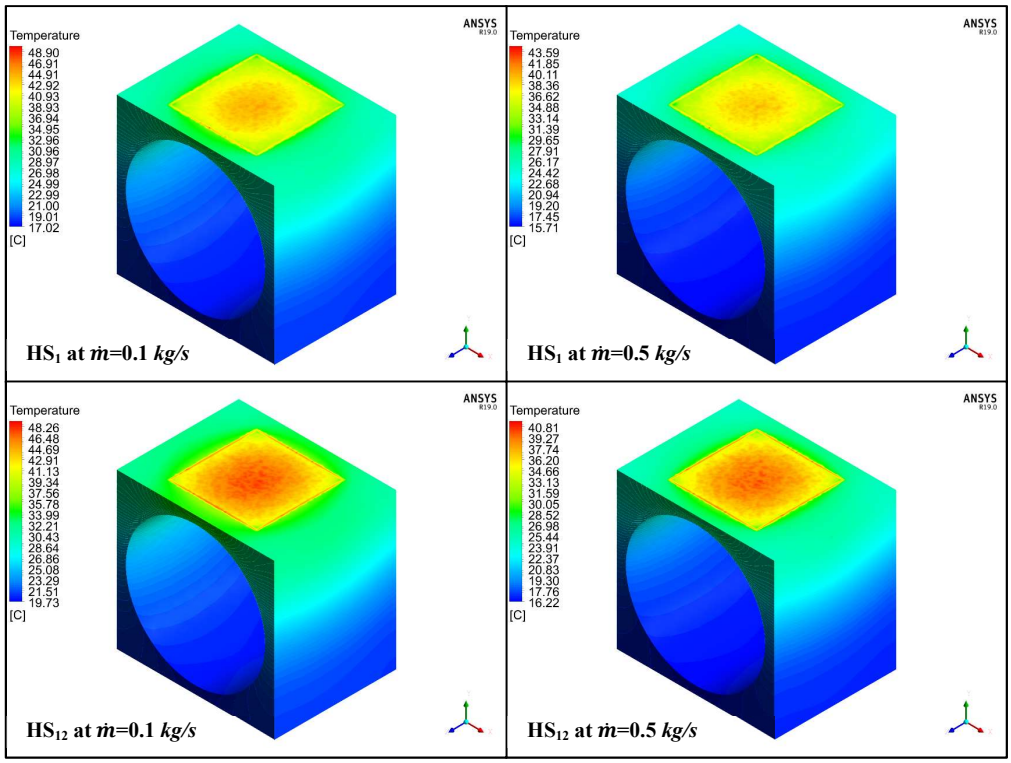

Fig. D. 16: 3-D temperature profile on selected heat sinks at *CR* = 1000X for turbulent flow